METAL AND MINERAL ZONING AND ORE PARAGENESIS AT THE KENSINGTON AU-TE DEPOSIT, SE ALASKA

By

Sarah H. Heinchon

A Thesis Submitted in Partial Fulfillment of the Requirements

For the Degree of

Master of Science

in

Geology

University of Alaska Fairbanks

May 2019

Approved:

Dr. Rainer Newberry, Committee Chair
Dr. Kenneth Severin, Committee Member
Dr. Mary Keskinen, Committee Member
Dr. Paul McCarthy, Chair
Department of Geosciences
Dr. Leah Berman, Dean
College of Natural Science and Mathematics
Dr. Michael Castellini, Dean
Graduate School

Abstract

The Kensington gold mine is a structurally controlled mesothermal gold deposit at the northern end of the Juneau Gold Belt. The Kensington is the only known gold deposit where over 90% of the gold occurs as calaverite ($AuTe_2$) rather than native gold (Au, Ag). Calaverite and native gold occur as microscopic inclusions in pyrite. Very little geochemical work had been performed on the ore at Kensington. This project generated a large geochemical data set of metals in sulfide concentrations of the ore.

To better understand this unique gold deposit I collected and analyzed 214 sulfide concentrates by X-ray fluorescence. The concentrates were collected from various locations, vein types, and sulfide textures to examine possible correlations between the different sample types and between trace metals associated with sulfides and tellurides.

Kensington sulfide concentrates have a consistent and strong correlation between Au and Te that indicates 90% of the gold occurs as calaverite. I surveyed 26 polished sulfide grain mounts. There are varying amounts of native gold and calaverite, depending on the presence of non-Au telluride minerals (petzite, hessite, coloradoite, altaite, tellurobismuthite, and melonite) and Cu sulfide minerals (chalcopyrite, tetrahedrite, and bornite). The corresponding sulfide concentrates still had a consistent Au to Te ratio despite the increased observed ratio of native gold to calaverite independent of Cu or non-Au telluride associated elements.

The consistent Au to Te ratio indicates a single Au-Te event, however the variable native gold to calaverite ratios and variable inclusion textures in pyrite and Cu-sulfides suggest two Au-Te events: a pre/syn-pyrite and a separate post-pyrite Au-Te event. I used an electron microprobe to generate Co maps of pyrite with varying gold and/or calaverite inclusion textures. There are multiple pyrite growth phases with two distinct pyrites: Co-rich pyrite generations (> 2 weight % Co) and Co-poor pyrite generations (< 10 ppm). Co maps distinctly show multiple generations of native gold and calaverite inclusions relative to pyrite growth. The majority of non-Au tellurides and Cu-sulfide are post-pyrite.

There are three main stages of metal mineralization in the Kensington ore:

Early barren pyrite

Calaverite, minor native gold, and more pyrite

Cu-sulfides and non-Au tellurides

Table of Contents

List of Figures

Page

List of Tables

Page

List of Appendices

Page

Acknowledgements

This thesis would not have been possible without funding and mine access provided by Coeur Alaska. Further funding was provided by the Society of Economic Geologists through their graduate student fellowship program. This work was performed at the Advanced Instrumentation Laboratory (AIL), University of Alaska Fairbanks. I received technical support from the talented Dr. Ken Severin, Karen Spaleta, and Dr. Maceij Sliwinski at the Advanced Instrumentation Laboratory (AIL), University of Alaska Fairbanks.

I would not have been able to finish this thesis without the abundant support from my friends and family, specifically my amazing husband, Kyle Heinchon, my parents, Holly and Richard Harrison, and my friends Amy Tuzzolino, Andrea Repetto, and Saundra Calderon.

Lastly I would like to thank my incredibly patient advisor and committee. Dr. Rainer Newberry, thank you for your hard work and persistence. Dr. Ken Severin, thank you for your instruction on the microprobe and your dry humor. Dr. Mary Keskinen, thank you for your kindness and moral support. Thank you for all of your encouragement and belief in my ability to finish.

1 Introduction

1.1 Overview of History and Setting

The Kensington gold deposit (Fig. 1.1) is near the north end of the 'Juneau Gold Belt' (JGB), a 150 km long zone of gold deposits and prospects spatially associated with the Coast Range megalineament in Southeastern Alaska. The region is close to tidewater and relatively accessible (by Alaskan standards) and was thoroughly explored in the late 1800s. The known prospects were identified by 1900, but only a handful proved large or continuous enough to generate even modest gold production. Outside of the immediate Juneau area (Fig. 1.1), the largest concentration of mined deposits is in the Berners Bay area, but even here, the historic gold production was only about 65,000 troy ounces (Redman et al., 1991). The Kensington deposit was briefly mined and produced a scant 2600 ounces (Fig. 1.2; Redman et al., 1991), less than 5% of the total output from the Berners Bay area. Although numerous attempts were made to re-start mining at Kensington (Fig. 1.2), the technical difficulties of producing gold from the ore proved insurmountable. Most of the gold at Kensington is present as calaverite ($AuTe_2$), which is considerably more expensive to extract than metallic gold (Au).

The oddity is that Kensington is the only known deposit of the entire Juneau Gold belt for which the ore is primarily calaverite. At the nearby Jualin deposit, for example (Fig. 1.3), a large fraction of the gold is as the native element (Leveille, 1991). The much higher historic production from other deposits in the Berners Bay area (Fig. 1.2) is largely due to this mineralogical oddity.

With the major rise in US gold prices in the 1970s, historic Alaskan deposits were systematically re-investigated. Because the vast bulk of the Kensington deposit was never mined, it had tremendous untapped potential. Since gold metallurgy has improved over the last century, the relatively high-grade ores became economic targets. Development of the resource was delayed due to environmental lawsuits that were eventually settled by the U.S. Supreme Court. Production began in 2010 with an initial mine life of 13 years.

The largest and most economically important gold district with commercially recovered Au tellurides is the Kalgoorlie Gold Field (Western Australia). The Kalgoorlie Gold Field is a group of orogenic deposits, similar to the Juneau Gold Belt (in which the Kensington is located), but gold tellurides only make up 20% of the gold ore (Shackleton et al., 2003). The Kensington Gold Mine is apparently unique among orogenic gold deposits and at least unusual among telluride bearing deposits (Saunders et al., 2014) in that the majority (over 90%) of gold at Kensington occurs as calaverite ($AuTe_2$) instead of native gold

(Casey, 2000). Gold tellurides are not common, and they rarely occur in major abundance in gold deposits.

The Kensington ore body is an early Tertiary quartz-pyrite vein system hosted in a weakly metamorphosed mid-Cretaceous pluton (Redman et al., 1991). The veins are structurally controlled by prominent shear zones in the Jualin pluton and are primarily quartz >> calcite, with 10-20% pyrite. The pyrite contains metallic gold, chalcopyrite, and telluride minerals, both as microscopic inclusions and filling fractures in the pyrite. Telluride-rich gold deposits are common in alkalic volcanic settings and rare in metamorphic settings (Saunders et al., 2014). Consequently, the Kensington deposit represents a unique opportunity to study an apparently unusual type of deposit, for which there are few (if any) direct comparisons.

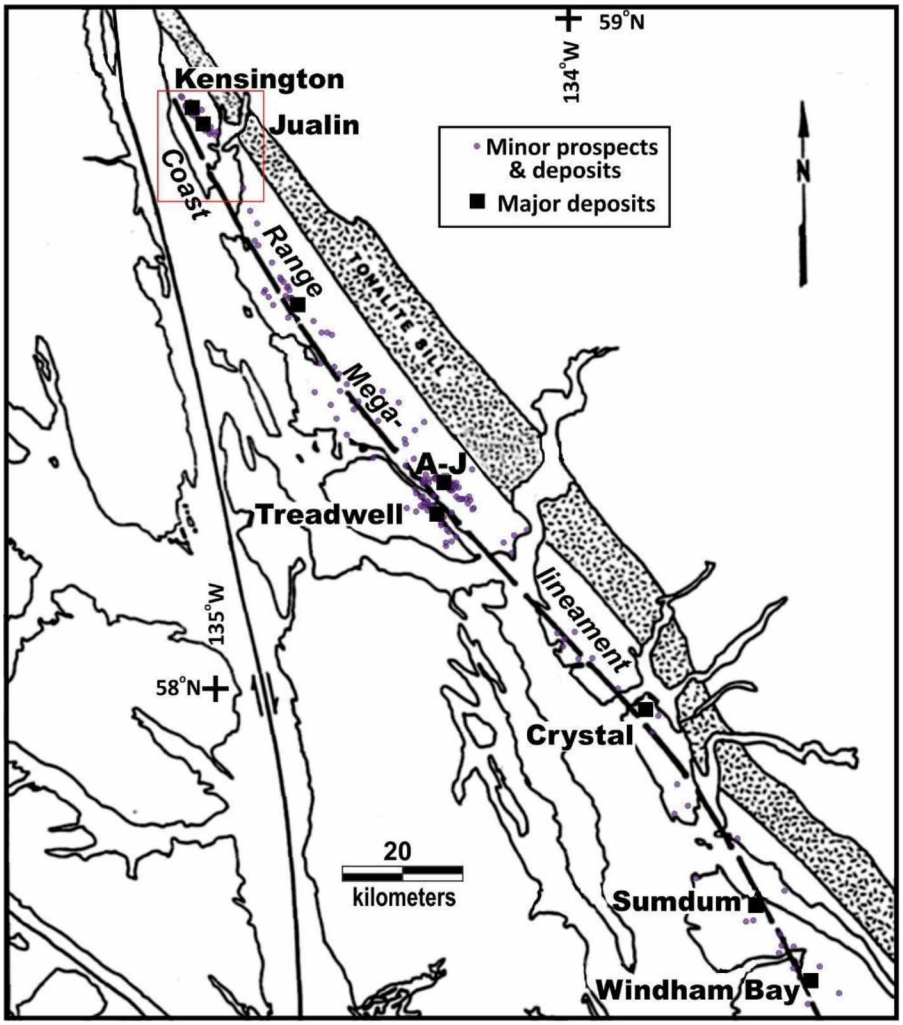

Figure 1.1. Map showing deposits and prospects of the Juneau Gold Belt (purple dots; major deposits = black squares) in relation to the Coast Range megalineament (thick dashed line). Red box outlines the area of Fig. 1.3. Modified from Leveille (1991)

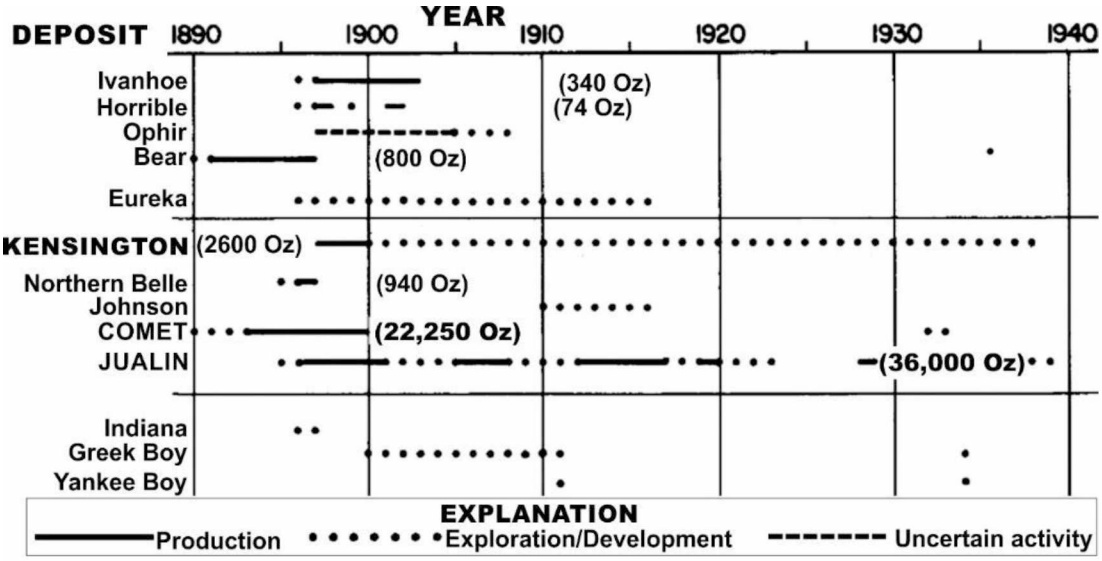

Figure 1.2. Overview of historic mining activity in the Berners Bay area, SE Alaska. Numbers in parentheses are the reported total gold production, in troy ounces. Modified from Redman et al. (1991).

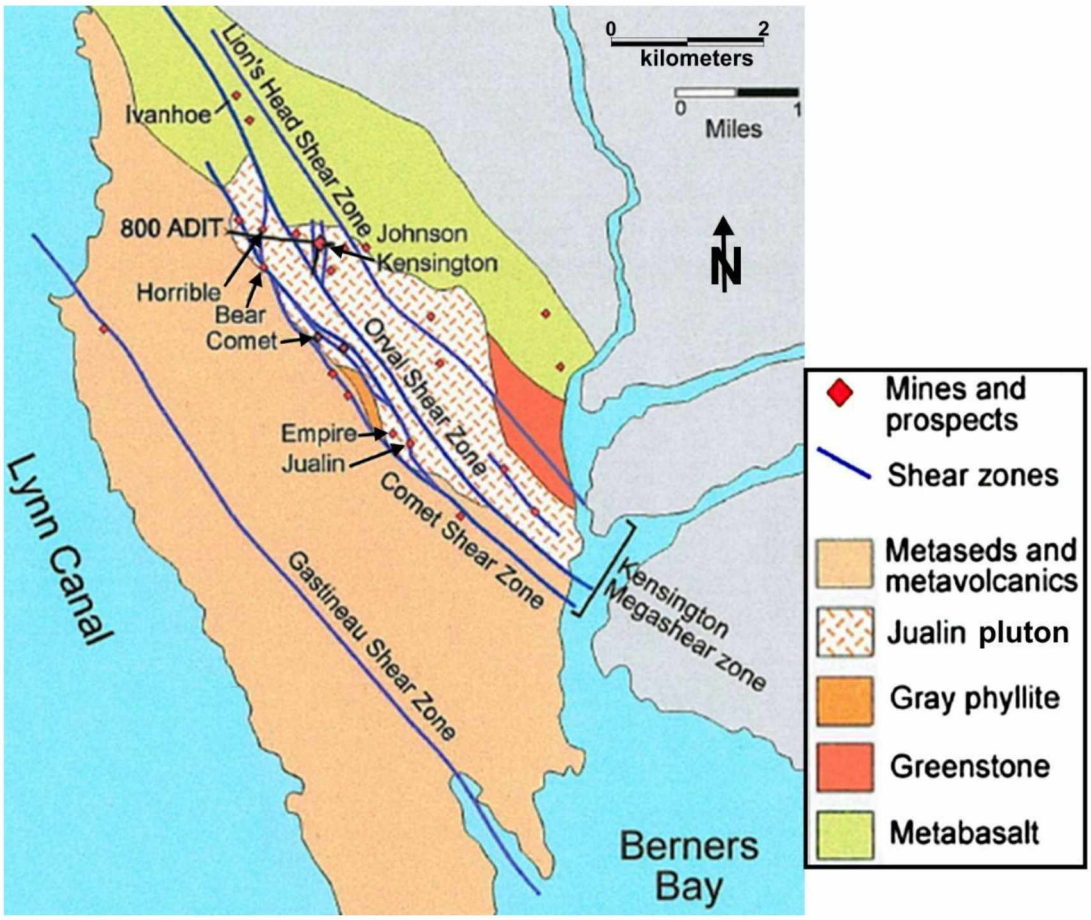

Figure 1.3. Simplified geology and major prospects and mines of the Berners Bay area, SE Alaska. The Gastineau Shear zone is the local name for the Coast Range megalineament. Modified from Redman et al. (1991).

The quartz-Au veins have varying concentrations of chalcopyrite as the second most abundant sulfide (Casey, 2000). It is unclear how (or if) chalcopyrite abundances affect the gold concentration (grade). Some quartz-Au veins display brittle deformation along the outer margins of veining and are sheeted within the vein. These are referred to as brecciated zones which are said to possess higher grades; no documentation of this exists, however. A rare ore type are massive pyrite bodies (MPBs) which are pluton-hosted pyrite masses outside of prominent shear zones and quartz-Au veins.

1.2 Thesis Objectives

The major objectives of this study are:

- Define the spatial distribution and zoning (if any) of ore-related elements
- Define the ore-related mineralogy, its paragenesis, and spatial patterns (if any)
- Relate metals and minerals to different types of ores in the mine

A priority is to determine if there are connections between multiple generations of pyrite and Au-Te mineralization. I hope to characterize this little-known type of deposit to enable future comparisons to other Au telluride bearing deposits, and the other occurrences in Berners Bay.

1.3 Juneau Gold Belt Geology

The JGB consists of mesothermal gold deposits located within a few kilometers of the Coast Range megalineament (Brew and Ford, 1978; Fig. 1.1). Such deposits are quartz veins formed by hot water several kilometers below the surface, typically hosted by metamorphic or metamorphosed rocks. The conventional explanation is that dewatering of metamorphic rocks during the greenschist to amphibolite transition released water that moved up along faults, cooled, and underwent chemical changes resulting in mineral deposition (Saunders et al., 2014).

Kensington is unique in the JGB because its ore is primarily a gold telluride called calaverite ($AuTe_2$) instead of native gold (AuAg solid solution). The ore also contains much higher Cu and less As, Pb, and Zn than other deposits of the JGB (Newberry et al., 1995). Despite the uniquely high tellurium (Te) at Kensington, it is otherwise broadly similar to other deposits in the belt, which formed at the same time under broadly similar conditions. This suggests a local source for the unique abundance of Te and Cu at Kensington.

Regional shearing along the Coastal Shear Zone generated localized shear zones within brittle bodies in the Berners Bay District such as the Jualin pluton (Redman et al., 1984). These shears

channeled the metamorphic fluids that deposited the Kensington vein system (Figs. 1.3, 1.4). There are several other historically mined deposits in the district; these are now also exploration targets.

1.4 Overall Kensington Ore Body Geology

Deposits of the Berners Bay district are early Tertiary veins hosted by the mid-Cretaceous Jualin pluton (Fig. 1.3, 1.4; Redman et al., 1984). A steeply-dipping, gold-bearing conglomerate containing Jualin plutonic rock clasts occurs along the western contact of the pluton (Fig. 1.4). The steep dip to this conglomerate (originally sub-horizontal) indicates (a) that the pluton has been turned on its side in the interval between intrusion (105 Ma) and formation of the main-stage, near-vertical, gold-quartz veins (55 Ma) and (b) that the pluton contained gold prior to main-stage veining (Redman et al., 1984).

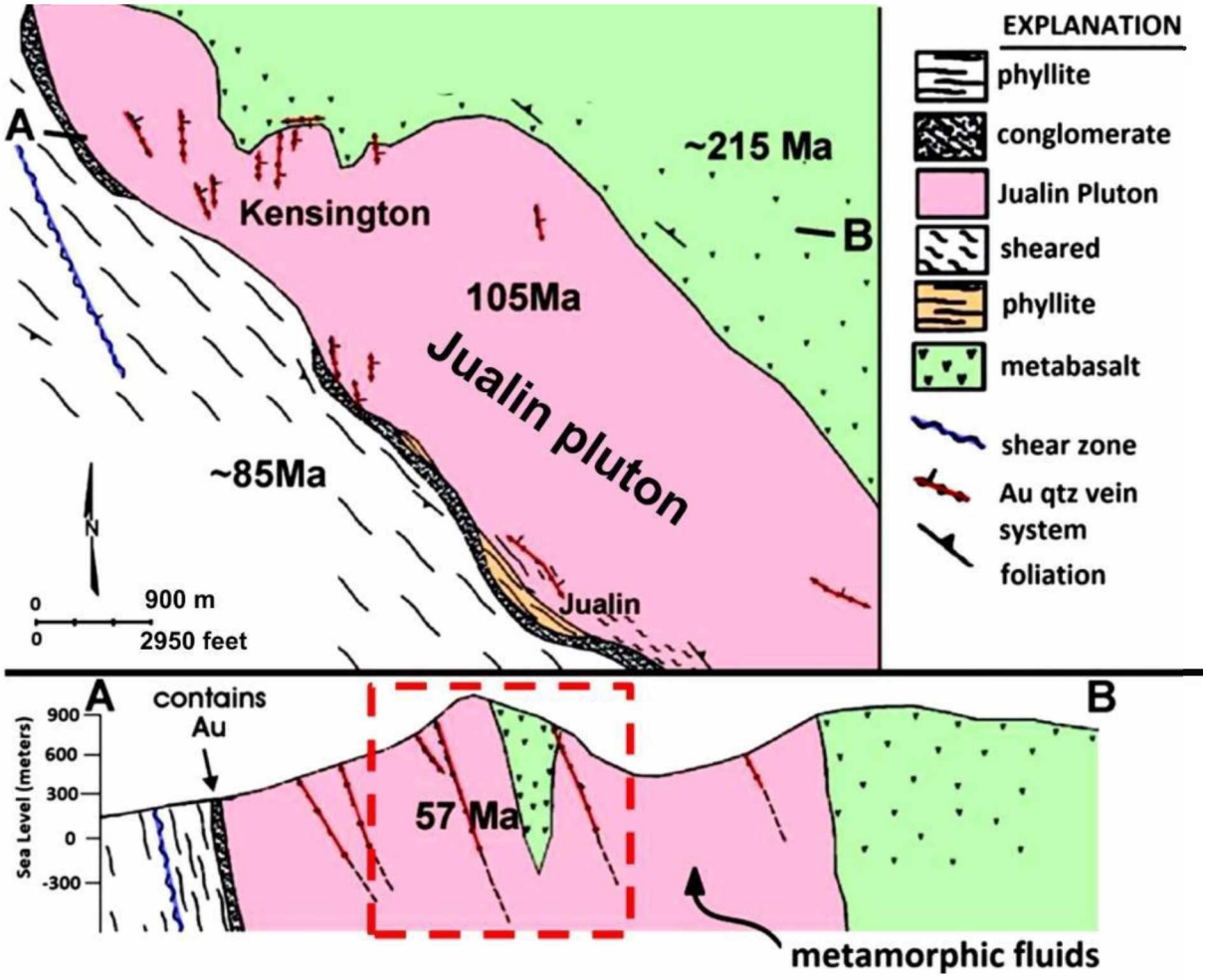

Figure 1.4. Simplified map of the Kensington-Jualin area (A) and cross-section through (B) the Kensington deposit, Berners Bay District, SE Alaska. The presence of gold in late Cretaceous conglomerate unconformably overlying the pluton (Redman et al., 1984) indicates the pluton contained gold prior to the main-stage vein event. The red dashed box shows the approximate area of Figure 1.5. Modified from Miller et al. (1995).

The veins within the Jualin pluton are of broadly two groups: Kensington to the north and Jualin to the south. These two groups have different structural orientations and somewhat different ore mineral assemblages (Redman et al., 1984; Miller et al. 1995; Casey, 2000). This study is restricted to samples from Kensington.

The Kensington ore body is comprised of multiple sub parallel vein sets that are broadly east dipping and strike north-south; they are confined to shear zones within the pluton (Fig. 1.5). At Kensington these can be subdivided into geologically similar sub-zones (Fig. 1.6; Beebe et al., 2018). As of the time I sampled (2011 – 2013), zone 10 was only subdivided into zone 10 and zone 10P with less overlap between upper zone 10 and zone 41.

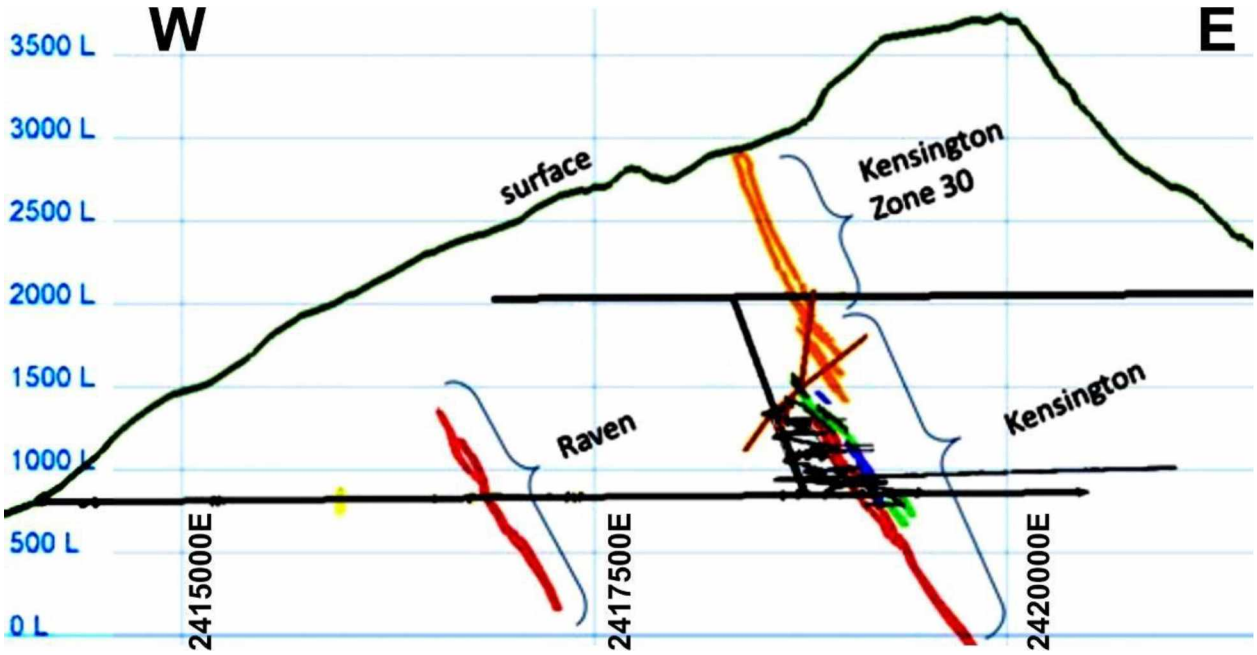

Figure 1.5. Simplified cross-section through the Kensington deposit, showing the upper parts (zone 30) and Raven (Horrible) vein systems that were not part of this study. Black lines show the extensive underground workings in the main Kensington mine area. Elevations are in feet above sea level. Modified from Beebe et al. (2018).

The ore zone strikes almost due north and dips steeply east (Fig. 1.5). The ore zones are not very wide, typically less than 30 meters (Fig. 1.6). However, the ore zones have significant strike lengths, usually 250-350 meters. Furthermore, the Kensington vein system is not a single massive vein, rather overlapping zones of veins (Fig. 1.6). This long-and-narrow geometry is best viewed as a long section or a plan view.

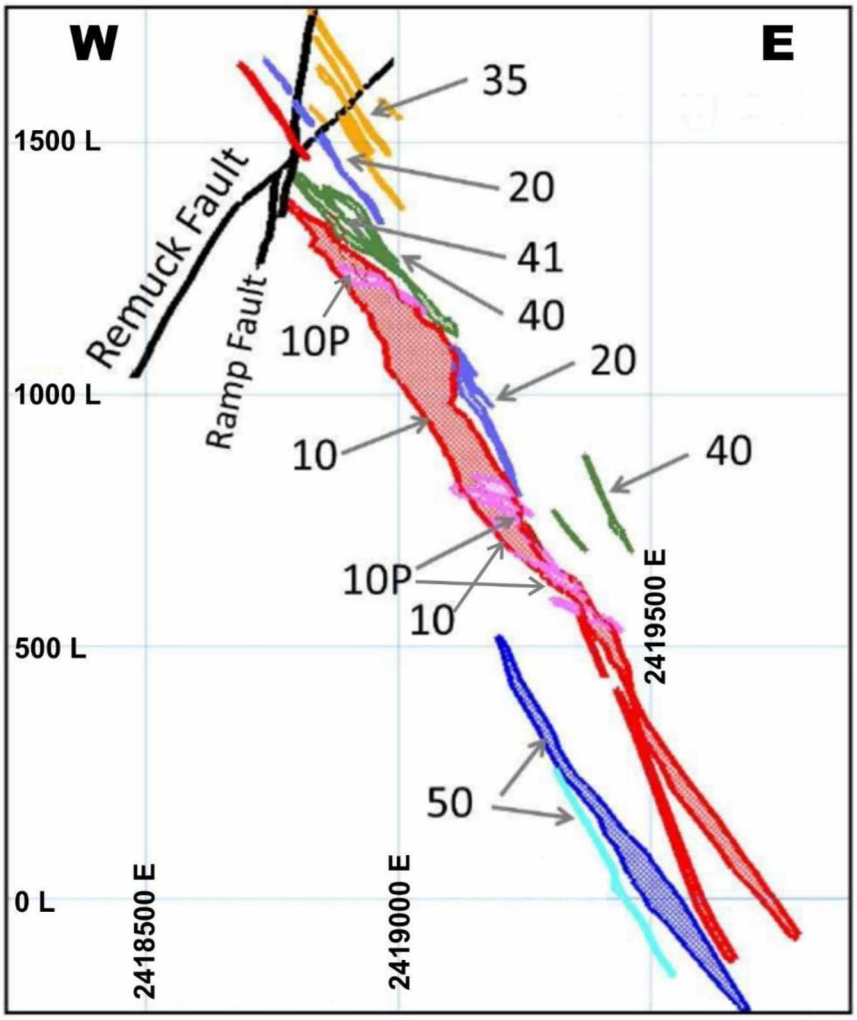

Figure 1.6. Detailed cross section through the main Kensington mine area, showing the complex current terminology for the various veins. Light blue lines are spaced 500' (152 meters) apart. My samples are entirely from below the Remuck and Ramp faults. Elevations are in feet above sea level. Modified from Beebe et al. (2018).

All elevations referred to in this study are in feet above sea level. Table 1.1 lists the different zones within the Kensington vein system, as of 2018. As the classification of veins has changed several times since my work there, and I anticipate further changes, I have kept designations as of 2013. That is, for the purpose of this study, I classify samples between 1250 ft. and 780 ft. elevations as zone 10 (Z10); samples from 1260' and above as Zone 41 (Z41); and samples below 780' as Zone 10P (10P). It's possible that a few samples have been misclassified, but, if so, they represent a small proportion. In particular, zone 20 (Table 1.1) is described as "… in the immediate hanging wall of zone 10" (Beebe et al., 2018). Some of my Z10 samples may belong to the current zone 20, but breaking out a small group that is compositionally indistinct seems an unnecessary complication for this study.

Table 1.1. Zone group descriptions at Kensington, modified from Beebe et al. (2018)

Number	Description of the Zone Group
10,10S,12	Main wide vein system; contains separately modeled splays (10S). Zone 12 is included as the southern extension of Zone 10.
10P	High grade pods, internal to Zone 10, but can extend outside of zone 10. More pronounced below 850 foot elevation.
20	Weak vein swarms in the immediate hanging wall of zone 10.
30	Upper wide vein system, similar to zone 10, but defined by lower vein density and grade.
35	Vein swarms with some discontinuous high angle shear veins; present in the hanging wall of the other zone groups.
41	Large high grade shear vein in the hanging wall of zone 10.
50	Vein swarms in the footwall of zone 10 and to the south; more E-striking than zone 10.

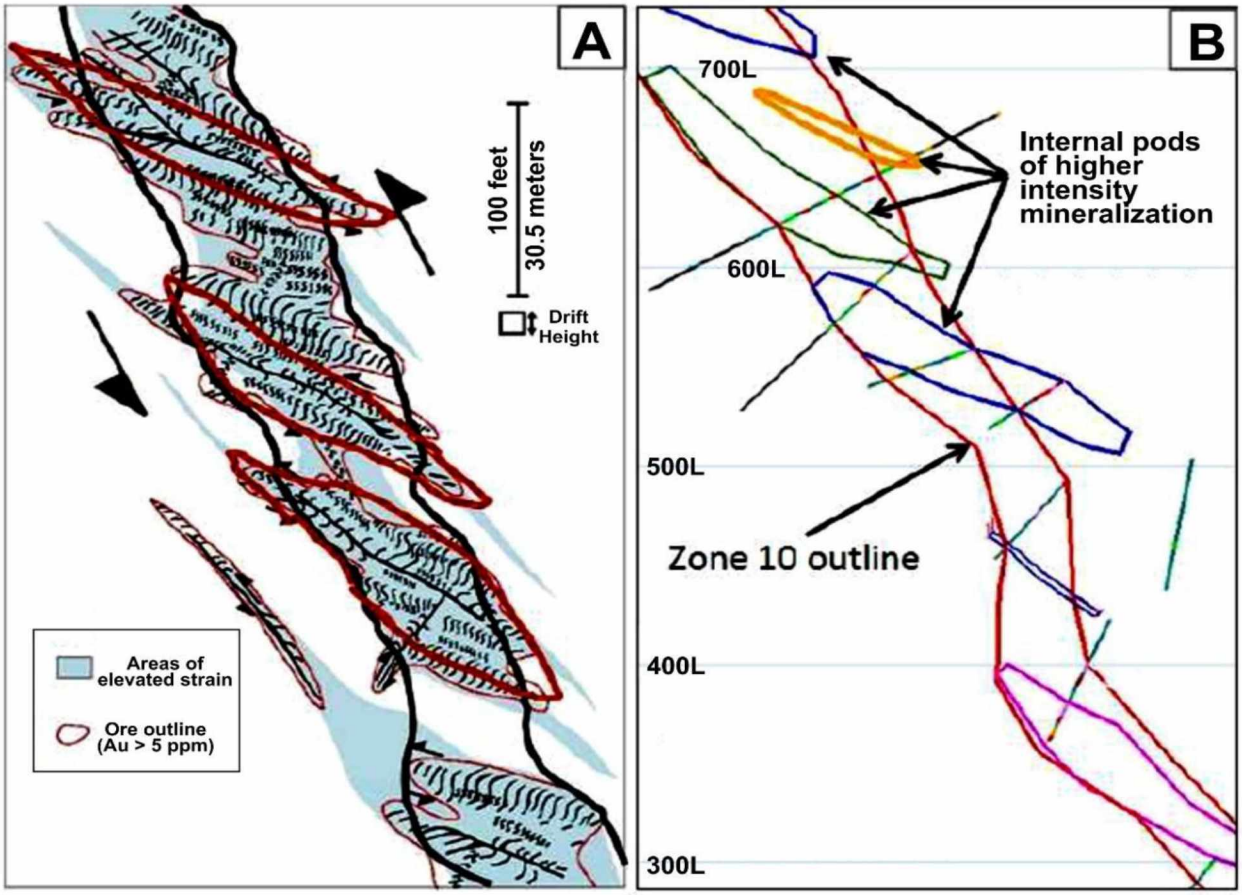

Figure 1.7. A) Schematic cross section (Rhys, 2010) through zone ten (outlined in black) with higher grade pods (outlined in red) reflecting higher concentration of dilatational structures. B) Actual zone 10 cross-section as modeled for the mine, with zone 10 outlined in red and higher-grade pods (10P) in various other colors. Modified from Beebe et al. (2018).

1.5 Previous Geochemical Studies

Prior to main stage veining, the Jualin pluton underwent weak Cu porphyry alteration, which variably enriched the pluton in Au, Cu, Te, and Mo (Fig. 1.7; Leveille, 1991; Newberry et al., 1995). This chemical alteration added significant amounts of potassium (as K-feldspar), which makes it difficult to determine the original composition of the Jualin pluton. The late Cretaceous conglomerate which unconformably overlies the Jualin Pluton (Fig. 1.3) contains anomalous Au (Redman et al., 1984), indicating that the pluton contained significant gold concentrations before the main-stage gold vein event.

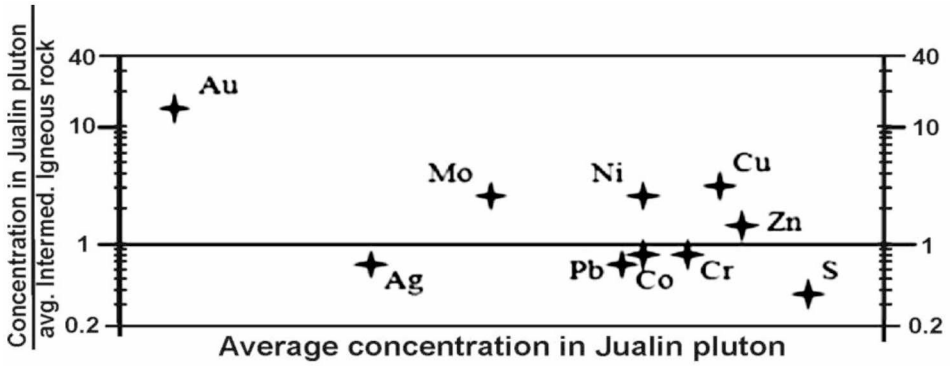

Figure 1.8. Average element concentration in Jualin pluton (outside of main-stage gold veins) /average concentration in intermediate igneous rocks vs. average concentration in Jualin pluton for several elements. Modified from Leveille (1991).

Table 1.2. Metallic minerals and their occurrences at Kensington as reported in Casey (2000)

Mineral	Occurrence	Size (mm)	Occurrence	Size (mm)	Occurrence
Au	Py inclusions	< .04	fractures in py & cp	<.1	py grain boundaries
$AuTe_2$	Py inclusions	< .04	Py fractures	<.1	py grain boundaries
Petzite	Py inclusions				py grain boundaries
Bi_2Te_3			fractured py		
HgTe			fractured py		
Tetrahedrite					py grain boundaries
$CuFeS_2$	Py inclusions				py grain boundaries
PbTe					py grain boundaries
ZnS	Py inclusions	< .01			
FeS	Py inclusions	< .01			

Gold is ubiquitously associated with (and invariably contained within) pyrite at Kensington. Gold is present as the telluride minerals calaverite ($AuTe_2$) and petzite (Ag_3AuTe_2), and as metallic Au. Table 1.2 (modified from data in Casey, 2000) lists the previously recognized sulfide and telluride minerals identified in the Kensington ore body and their textural relations. Tellurides and metallic Au occur as

inclusions in pyrite, along fractures in pyrite, and along pyrite grain boundaries. Other minerals are reported with restricted textural occurrences, possibly due to limited observations and sampling.

An additional possibility is that some of the metal elements in the Kensington ores occur as solid solution in pyrite. Pyrite is known to contain a wide range of elements in solid solution (Abraitis et al., 2004), most notably As, Co, Cu, Ni, Mo, Sb, and Se (Fig. 1.8a). Complete solid solution occurs in the series CoS_2-FeS_2-NiS_2 at temperatures > 600°C (Klemm, 1965). At lower (hydrothermal) temperatures, Co and Ni are still significantly soluble in pyrite, as demonstrated by microprobe analyses of natural pyrite (Fig. 1.8B; Vaughan and Craig, 1978). Leveille (1991), for example, notes modest concentrations of Co and Ni in pyrite-rich ores from the nearby Jualin deposit, yet no one has identified any Co or Ni mineral present at either Jualin or Kensington.

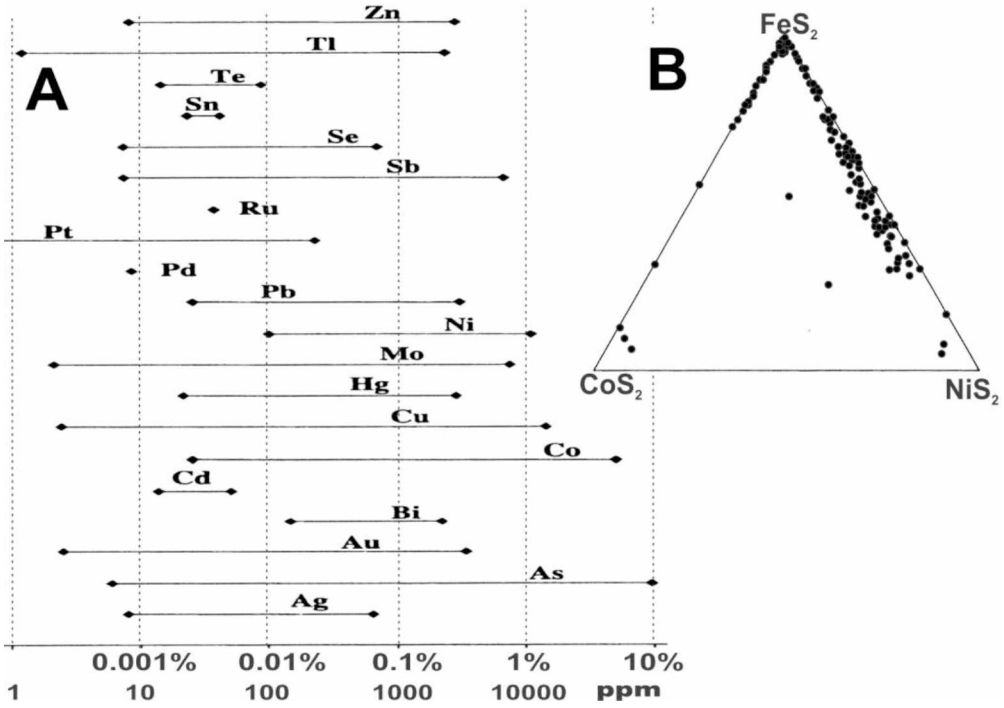

Figure 1.9. Compositional variability in pyrite, from analyses of natural materials. A) Compilation for 20 elements in pyrite, modified from Abraitis et al. (2004). B) Compilation of compositions in the (Co-Ni-Fe)S_2 system, modified from Vaughan and Craig (1978).

Redman et al. (1998) summarized Hydrothermal Vein stages at Kensington as:

Stage 1: Late Magmatic: Epidote-quartz-calcite-chlorite

Stage 2: Pre-gold-bearing hydrothermal: calcite-chlorite ±quartz ±pyrite—mostly west-dipping and

Stage 3: Gold-bearing hydrothermal

Previous workers, e.g. Leveille (1991), Caddey et al. (1995), Miller et al. (1995), Redman et al. (1998), and Casey (2000), have classified vein types in the Kensington-Jualin area based on crosscutting relationships, vein orientations, and vein compositions. There is some disagreement concerning the timing of gold mineralization and how many vein types there are. However, all recognized early barren quartz-pyrite veins, main stage gold-bearing quartz-carbonate-pyrite veins, and late barren quartz-carbonate veins. Previous workers have not described massive pyrite bodies.

1.6 Overall Characteristics and Approaches

A primary focus of this thesis concerns spatial elemental and mineralogical patterns and variations between different ore types (categories). I examine differences between types of veining, sulfide minerals, and sulfide textures of the ore in the Kensington deposit. To accomplish this I employed six analytical tools: X-Ray Fluorescence (XRF); Electron Microprobe Energy dispersive analysis (EDS), back-scattered electron imaging (BSE) and Cobalt mapping; reflected light petrography; X-Ray Diffraction (XRD), and the hand held XRF (niton). The multiple analytical tools I use produce overlapping results, which allows for some confirmation of observations. Table 1.3 lists the tools employed and the types of results produced by each. Appendix A provides the sampling and analyses procedures I followed.

Table 1.3. Types of results generated by different analytical techniques

Type of Results	Analytical Tool					
	XRF	Microprobe		Ref. Light	XRD	Hand-Held XRF
		EDS + BSE	Co Maps			
Metal Associations	X	X				X
Mineral Associations	X	X		X	X	X
Mineral Compositions	X	X				
Mineral Zoning		X	X			
Mineral Textures		X	X	X		
Paragenetic Sequence		X	X	X		

XRF was my primary analytical tool. I used the XRF results to identify samples with anomalous metal concentrations, to be investigated further with other tools. XRF yields metal concentration distributions, at the mine (> 400 m2) and heading (40 - 50 m2) scale. The XRF data are also used in calculating sulfide mineral abundances, to determine metal associations and, in some cases, mineral composition. I infer mineral associations where they are easily derived from the XRF data.

I utilized the electron microprobe to generate three types of data: EDS, BSE, and Co maps. BSE images are employed as the starting point in identifying different minerals: BSE image brightness is proportional to mineral mean atomic number. EDS analysis was then performed on different minerals as identified by the BSE image. Thus, BSE and EDS together yielded mineralogy, mineral composition, and mineral associations and textures.

Reflected light petrography yielded similar information, but is less quantitative ("what is that five micron grain?") although considerably cheaper. I employed Co mapping to examine zoning in selected pyrite grains, with the aim of relating such to the timing of Au-Te deposition. I employed hand-held XRF to quickly determine metal concentrations in hand samples and polished sections. Finally, I employed XRD to identify minerals in a few, very fine grained, brecciated samples.

Confirmation of optically-identified minerals using the microprobe (EDS/BSE) allowed me to confidently identify these minerals with reflected light petrography. Mineral identification via EDS is also important to interpreting the XRF data. Mineral assemblages for the majority of my samples are derived from using the XRF data in that manner. For example, samples with significant Hg are assumed to contain coloradoite (HgTe) because I observed no other Hg-bearing mineral with EDS (chapter 4.5).

1.7 Methodology and Analytical Techniques

A major goal was to determine trace metal variations in the ore at Kensington. Previous studies indicated that ore-related minerals are always within or attached to sulfides, especially pyrite. To ensure that measured concentrations are as high as possible, I maximized the pyrite content of the samples. I eventually collected 214 pyrite-rich samples, the distribution of which is shown on the long section Fig. 1.10 (a vertical section along the length of the vein, instead of across the vein). Long sections looking west are the best portrayal of the data due to the long strike and thin 'width' of the vein systems. Each hand sample weighed 0.5 – 5 kg and includes samples from:

- Massive pyrite bodies independent of veining
- Brecciated sections of a quartz-Au veins
- Undeformed sections of a quartz-Au veins

1.8 Sampling Techniques and Mine Access

Samples were collected from easily accessible underground workings located in Zone 41, Zone 10 and Zone 10P. Samples were directly chiseled out from either the drift ribs or faces except for 480N-3, which was a muck pile sample. There are few samples from the 900 level because it is the main

haulage access and a high traffic area. Other gaps in the sample locations are due to the backfill method Kensington utilizes to store tailings and increase the structural integrity of the mine.

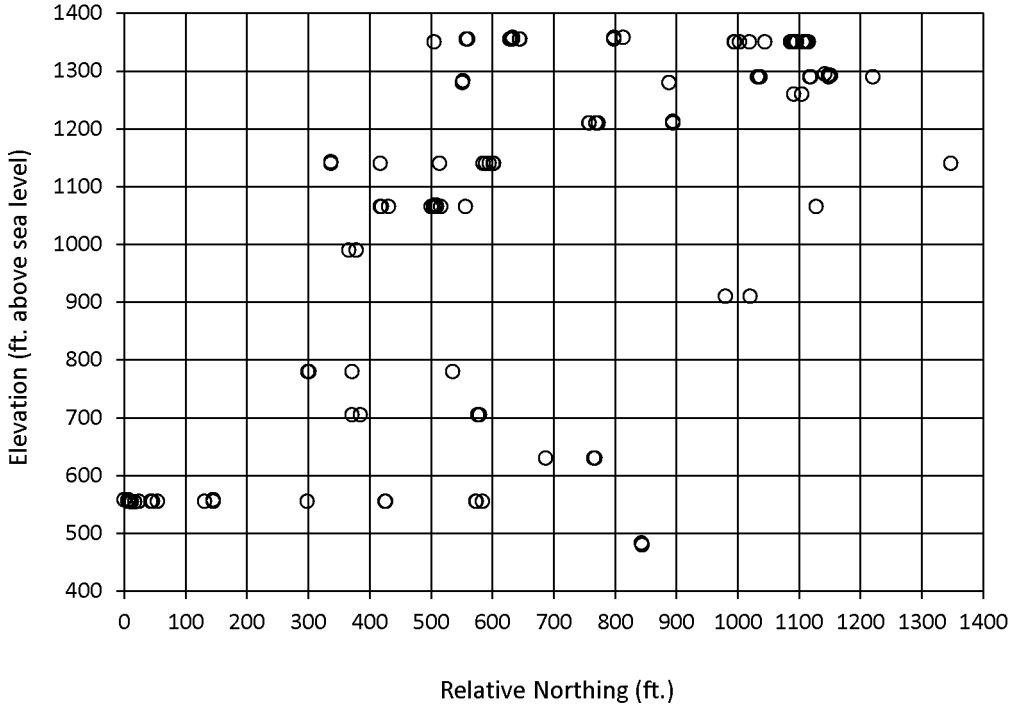

Figure 1.10. West-facing long section through the Kensington deposit showing sample locations. Each point represents 1-20 samples. Gridlines are spaced 100 ft. (30.5 m) apart.

I actively sought brecciated veins and chalcopyrite-rich areas. Chalcopyrite is difficult to consistently identify underground because surfaces are coated by oxidation tarnish and diesel fume films. These make pyrite and chalcopyrite indistinguishable unless the surface was fresh or the signature blue-green oxidation from copper was present.

There are different vein orientations, vein sizes, and sulfide textures within and adjacent to veins. I collected samples from the typical Kensington veins, but also from disseminated pyrite adjacent to veins, disseminated pyrite within highly altered plutonic inclusions in veins, and unusual blobs of pyrite not associated with quartz-calcite veins. I made a point of collecting sulfide rich samples along strike of well exposed veins as well as along the width of these veins.

Appendix B details the sample locations, the type of sample, and the analysis used on each sample. Samples KEN-01 through KEN-07 were crushed at Kensington. After crushing, I handpicked pyrite-rich material (all samples) and also panned material from KEN-01. Other samples were not crushed, but consisted of multiple pieces broken during sampling. These were subsequently

handpicked to concentrate sulfides. Some samples were sub-sampled based on different pyrite grain sizes and host-rock contacts, as well as to test for homogeneity of trace minerals in a sample.

1.9 Analytical Techniques

Multiple analysis methods were used to collect a variety of data. The primary data were generated from X-ray florescence (XRF) due to the relatively low cost and sensitivity to trace metals. Electron dispersive spectroscopy (EDS) produced my second largest data set. EDS was not used as much as XRF due to time and cost restraints. Reflected light microscopy produced limited results due to the difficulty of identifying tiny (< 5 micron) grains. X-ray diffraction was used on three samples to determine the mineralogy of very fine-grained material.

1.9.1 X-Ray Fluorescence

The main analysis method used was wavelength dispersive *X-ray fluorescence* (XRF) to identify samples for further analysis via reflected light and microprobe. I pulverized the samples made from hand concentrated sulfide-rich material using a steel-ball mill and pressed them into 37mm pellets. Appendix C gives the XRF pellet recipe used. The pellets were analyzed with a PanAlytical Axios XRF analyzer. The lids of the steel-ball mill were analyzed to determine composition of the mill steel. Based on the elemental composition of that steel, and the elemental ratios, I ruled out significant sample contamination from the mill. I created and standardized a customized XRF routine for analyzing elements known and suspected to correlate with elemental gold (Au) at Kensington.

The brecciated quartz-Au vein pressed pellets contained significantly more quartz than the other pellets because it was extremely difficult to separate the fine grained sulfide-rich matrix from the quartz. This resulted in analyzed samples with significantly lower pyrite contents than those of the other vein types.

Table 1.4 lists the elements measured in the XRF routine along with the lower limit of detection (LLD) and median concentrations. I employed well-characterized natural standards and certified artificial gold standards (1 - 30 ppm Au, Appendix D). In addition, I created four XRF standards with variable concentrations of Au, Hg, Ag, and Te, by adding measured amounts of ICP solution standards to a pulverized pyrite-quartz mixture. These were pressed into 37mm pellets. Appendix D gives the calculated and measured compositions of these four artificial standards, using several different XRF routines.

I processed the XRF data in a multi phased process (see Appendix E), due in part to some peak overlap problems. Tungsten XRF peaks overlap those from several ore-related elements, including Au, Hg, and Bi. Small amounts of tungsten are not a problem but even a few percent of the mineral scheelite ($CaWO_4$), variably present in the ore veins, is enough to overwhelm the peaks due to a few ppm of the ore and associated elements. Once I recognized this problem, I created a second specialized routine that employed alternate XRF lines for several elements suffering from W interference. I found that I also needed to make additional background corrections for As, Ag, Te, Bi, W, Mo, Zn, Sb, and Hg, as my XRF calibrations were designed to maximize accuracy at moderate (not extremely low) concentrations. These corrections were calculated by analyzing several low trace element standards with both KEN2 and the W routine.

Table 1.4. Elements and components analyzed by XRF

Element	**LLD* (ppm)**	**Median** (ppm)
Cu	1	108
As	2	BDL**
Ag	10	BDL
Te	9	172
Bi	2	BDL
Au	2	131
W	2	11
Mo	1	7
Pb	5	BDL
Zn	1	12
Sb	7	BDL
Ni	3	20
Hg	2	BDL
Co	7	137
Se	2	25

Component	**LLD (%)**	**Median (%)**
S	0.01	35
Al_2O_3	0.01	0.5
CaO	0.80	2.1
K_2O	0.00	0.2
MgO	0.00	0.3
Na_2O	0.00	0.1
SiO_2	0.42	19
MnO	0.00	BDL
TiO_2	0.00	BDL
P_2O_5	0.00	BDL
Fe	0.00	32

*LLD = lower limit of detection; BDL = below detection limit

Because all of the known ore and ore associated minerals occur with sulfide minerals, the trace element concentrations of a sample depend on the amount of sulfide present and the abundance of trace minerals in the sulfide. In order to more 'fairly' compare concentrations from samples with widely varying sulfide contents, I normalized the concentrations to 100% sulfide. This is equivalent to converting data originally expressed as parts per million to grams of element per ton of sulfide.

The % pyrite was calculated from Fe and S concentrations. The % pyrite calculated with Fe and S were compared. Samples with ≥ 5% deviation between the two calculated pyrite values were flagged for closer inspection. Most of these samples had elevated CaO, K_2O, and MgO. Both ankerite (Ca $(Fe,Mg,Mn)(CO_3)_2$) and chlorite are present in the Kensington veins. These additional Fe-bearing minerals artificially increase the % pyrite calculated from %Fe. In these ankerite and chlorite-bearing samples %, pyrite was calculated from %S.

Fahlore (tetrahedrite-tennantite solid solution) is present in high enough concentrations to effect the relative abundances of chalcopyrite and pyrite, so I started by calculating % fahlore based on Sb and As concentrations. I then calculated chalcopyrite abundance using the leftover % Cu, and finally calculated % pyrite from S and Fe left over from calculation of fahlore and chalcopyrite abundance. Appendix E contains the various sulfide equations employed.

Once the % pyrite, % chalcopyrite, and % fahlore were calculated with the appropriate equations, the various elements were normalized to 100% sulfide (% pyrite + % chalcopyrite + % fahlore). Analyzed samples with ≤ 20% total sulfide were rejected, as the concentrations would be enhanced by a factor of at least five.

1.9.2 Reflected Light Microscopy and Electron Dispersive Spectroscopy

After all of the samples were analyzed, those with elevated Au, Ag, Mo, Sb, As, Co, Hg, Cu, and Ni were identified for further study. I made 26 polished sections from the set of samples with anomalous metal concentrations. The polished sections were created by hand selecting sulfide grains, mounting in epoxy, trimming to approximately 5 mm thickness and then hand polishing with diamond paste. I optically identified major minerals in reflected light (pyrite, chalcopyrite, tetrahedrite, coloradoite, calaverite, and Au) and identified other telluride minerals with energy dispersive spectroscopy (EDS) on a CAMECA SX-50 electron microprobe. I also employed EDS to evaluate gold fineness and tetrahedrite compositions.

1.9.3 Co Mapping of Pyrite

Pyrite can accommodate up to several weight percent of several elements in solid solution, especially Co, Ni, and Se. Sulfide-normalized Se and Ni concentrations are low (74 and 98 grams/ton sulfide, respectively, chapter 2), but Co concentrations are < 25 to > 1000 grams/ton sulfide. These concentrations are sufficiently high to be detected by the electron microprobe. A dozen samples with elevated Co concentrations were identified for elemental mapping. Co concentrations were crudely

calculated by measuring X-Ray counts at the Co Ka peak position for 30 seconds at a minimum of 500 points for each Co map. Backgrounds were not measured at each point, but rather were measured on a pyrite standard that contains low (below detection) Co. All 3 LiF spectrometers were set up to measure the Co Ka1 line.

The Co maps were post processed by adding all three LIF maps using the map addition feature in the JEOL EPMA software. Minerals containing heavy elements such as Au, Te, Ag, and Hg produce a false Co high in the maps due to their higher x-ray backgrounds. This was accounted for by overlapping the EDS image of the Au^0 and telluride inclusions over the Co map. The resulting composite maps show the zoned pyrite grains in relation to their inclusions.

1.9.4 X-Ray Diffraction

X-ray diffraction was used solely on the fine grained sulfide component from brecciated samples. This method was utilized because of the low volume of material and relatively low sulfide content (< 10%). I only used XRD on 3 samples to verify the presence of molybdenite. This was the only method that produced this data because the fine grained material was gouged out in the polishing process (even with epoxy impregnation).

1.10 Constraints of Data Sets

All of the ore (gold and calaverite), non-Au tellurides, and accessory sulfides in the Kensington mine are opaque. This restricts microscopy to reflected light only. Samples analyzed by EDS were selected based on unidentifiable opaque minerals (optical) and (or) high metal concentrations based on XRF data. Not all polished sections have associated EDS data. I made 23 polished sections and generated extensive EDS data for half of them, have no data for about a third, and minimal data for the rest. I did not identify accessory telluride minerals (reflected light microscopy) in samples for which I acquired little EDS. These slides may or may not have accessory telluride minerals and (or) calaverite grains too small to identify optically. Based on the samples I did examine thoroughly, I think I identified the vast bulk of these minerals in my samples by reflected light microscopy.

2 Mine-Scale Elemental and Mineralogical Patterns

This chapter contains the majority (but not all) of the XRF results. Because most of the elements occur as inclusions associated with sulfide and because the sulfide contents of my samples vary considerably, the XRF values are typically given as parts per million (ppm) normalized to 100% sulfide. For trace elements, this is equivalent to grams element per ton of sulfide. These concentrations do not directly equate to metal grades at the mine, because the sulfides are diluted by other minerals in the veins and associated wallrocks. In this chapter I start by examining the quality and reproducibility of the XRF analyses, which are based on first creating a sulfide-rich fraction from a vein sample. I then give correlation coefficients among the various elements analyzed and use these as a basis for systematically addressing the mine-wide metal abundances, gross mineralogy, and zoning.

2.1 Hand Sample Compositional Homogeneity

The basis of all of my data is hand samples of sulfide rich material from different vein types, sulfide textures, and major sulfide mineralogy. The vast bulk of opaque minerals occur as microscopic inclusions in pyrite (occasionally chalcopyrite); hence, grade is generally proportional to pyrite abundance. However, pyrite is not uniformly endowed with mineral inclusions, and at the scale of individual pyrite grains, inclusion density varies widely. With enough pyrite grains, the average is approximately constant; however, is a hand specimen large enough to accurately average out such inhomogeneity? Establishing the degree of hand specimen compositional uniformity is a critical first step.

I established hand specimen compositional homogeny by subsampling hand samples, preparing them identically, and then analyzing them with XRF. Rather than crushing a sample, concentrating pyrite, and then creating splits of the pyrite concentrate, I treated each subsample as a separate sample and concentrated the pyrite in each. All 25 subsampled rocks (Table 2.1) are pyrite-rich and represent a variety of sulfide textures, vein types, and zones. Of the 25, 4 hand samples were subsampled based on variations in sulfide texture, grain size, or sulfide mineralogy. (These 4 samples are excluded this section because they deliberately do not represent identical splits).

Because metal abundance is proportional to pyrite abundance, and no effort was made to make the pyrite abundance in each subsample identical, I started the analysis of the data (following XRF

analysis) by normalizing the metal concentrations to 100% sulfide (i.e., multiplying concentrations by a factor of approximately 1 (pure sulfide) to 5 (20% sulfide). I then calculated the arithmetic mean and standard deviation for each set of subsamples. Finally, I calculated the relative standard deviation (RSD) for each split sample as (100* standard deviation/average value).

Most data exhibit a pattern similar to that seen for Pb, As, Bi, and Sb (Fig. 2.1): at low concentrations relative standard deviation varies widely. For concentrations significantly above detection limits (5-20 ppm, depending on the element) relative standard deviation is typically 5-50% and does not vary appreciably with concentration. I consequently excluded data for concentrations close to detection limits.

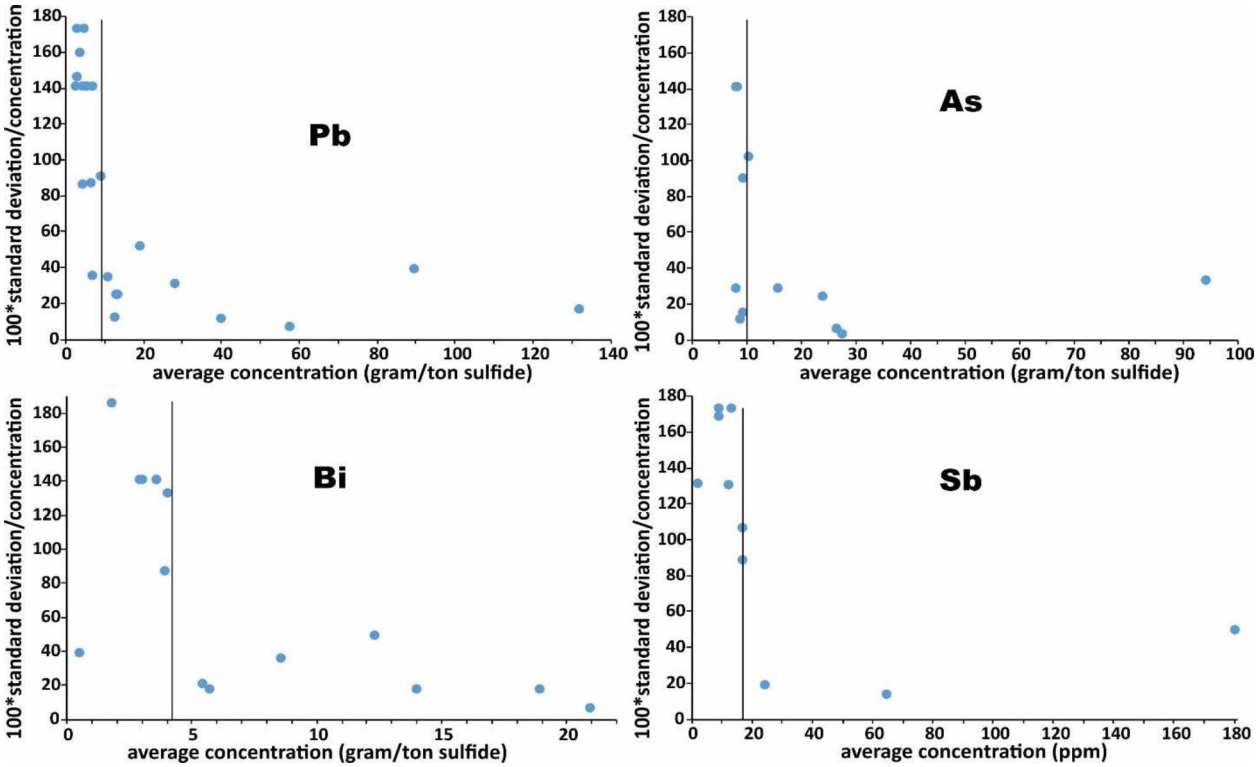

Figure 2.1. Relative standard deviations vs. average concentration for Pb, As, Bi, and Sb from 21 duplicate samples. Data is only plotted if all of the sub-samples yielded concentrations above detection limits.

Individual and average percent relative standard deviation (RSD) for 11 elements are shown in Table 2.1. Elements not shown are those for which only 2 or 3 of the duplicates possessed concentrations above the 'random noise' threshold. The average relative standard deviations are 20-30%, suggesting that for concentrations significantly above detection, the concentrations are precise to

± 20-30% of the amount present. This results in sparse data for most of the metals that typically occur at low concentrations at Kensington (i.e., those outside of Au, Te, Cu, Zn, Ni, and Co).

Table 2.1. Percent relative standard deviations for replicated (split) samples

Zone	Sample#	# Splits	Cu	As	Ag	Te	Bi	Au	Pb	Zn	Ni	Hg	Co
41	1280-235-10	**2**	2			4		11		33	2		20
	1350-12	**3**	74			72			25	20	13		28
	1350-13	**3**	10	6	6	5	7	7	12	19	16		28
	1350-2	**2**	13			34	39	31		35	2		12
	1350-21	**2**	22	15		68		71	52	45	1		4
	1350-3	**2**				23	36	19		17	33		42
	1350-4	**3**	59			21	21	23		14	4		17
	1355-201-12	**3**	10	4	38	48	49	53	7				29
	1355-201-14	**4**	50	34		43	18	50	17	38	17	51	17
	K12-5	**2**	3			33		28		4	4		14
	K13-16	**3**	11	29		15		16	35	57	26		6
	KEN-04	**2**	18	29	6	6		17	31	32	27	10	9
10	1065-189-2	**3**	15			62		72		52	6		16
	1065-189-8	**2**	5			7		8		28	1		7
	1140-189-4	**2**	19			21		13		11	31		2
	1140-197-6	**3**	10	11		13		10		6	2		34
10P	480N-3	**3**	7		36	22	18	19	12	16	10	33	7
	555-152-1	**3**	5	24	7	25	18	29	39	36	12	20	12
	555-160-1	**2**	23			5		2		12			7
	555-160-6	**2**	32	35	35	75		43	25	32	27		15
	555S-6	**3**	23					50		16	10	11	14
Average			**21**	**21**	**21**	**30**	**26**	**29**	**26**	**26**	**13**	**25**	**16**

Notes: % relative standard deviation = (100*standard deviation/mean)
Blank entries = elements present at concentrations at or near the detection limit

Of the 11 elements shown, Co and Ni display the smallest individual and average % relative standard deviations (13% and 16%, respectively). Data shown ahead indicate that in these samples the bulk of both elements are present in solid solution in pyrite—rather than as inclusions of Co- or Ni-rich minerals. Consequently, I infer that the elemental variations represent a combination of analytical uncertainties and actual variations in abundances of trace inclusion minerals in the sulfides. The data appear to indicate that at the hand specimen scale, ore-related mineral inclusions are homogeneously distributed in pyrite and that single hand specimens are large enough to characterize the trace mineral abundances at a single sampling site.

2.2 Heading-scale Compositional Variability

Samples from the north end of the 480' level (480N, zone 10) are from a sulfide band that occurs in a discrete vein (Fig. 2.2, vein types are described in chapter 3). Sample 480N-1 and 480N-3 were taken approximately 10 cm from each other along strike of the band. Sample 480N-3 was then subsampled into 3 parts (A, B, and C). The relative standard deviations (RSDs) of the 480N-3 subsamples are remarkably low, even for elements with relatively low concentrations (<50 grams per ton sulfide; Table 2.2). The RSD does not increase appreciatively for any element (except Mo) when sample 480N-1 is included, indicating generally uniform distribution of metals in this sulfide band. (As, W, and Sb were never above detection limit (5 ppm, un-normalized), so they are not listed in Table 2.2).

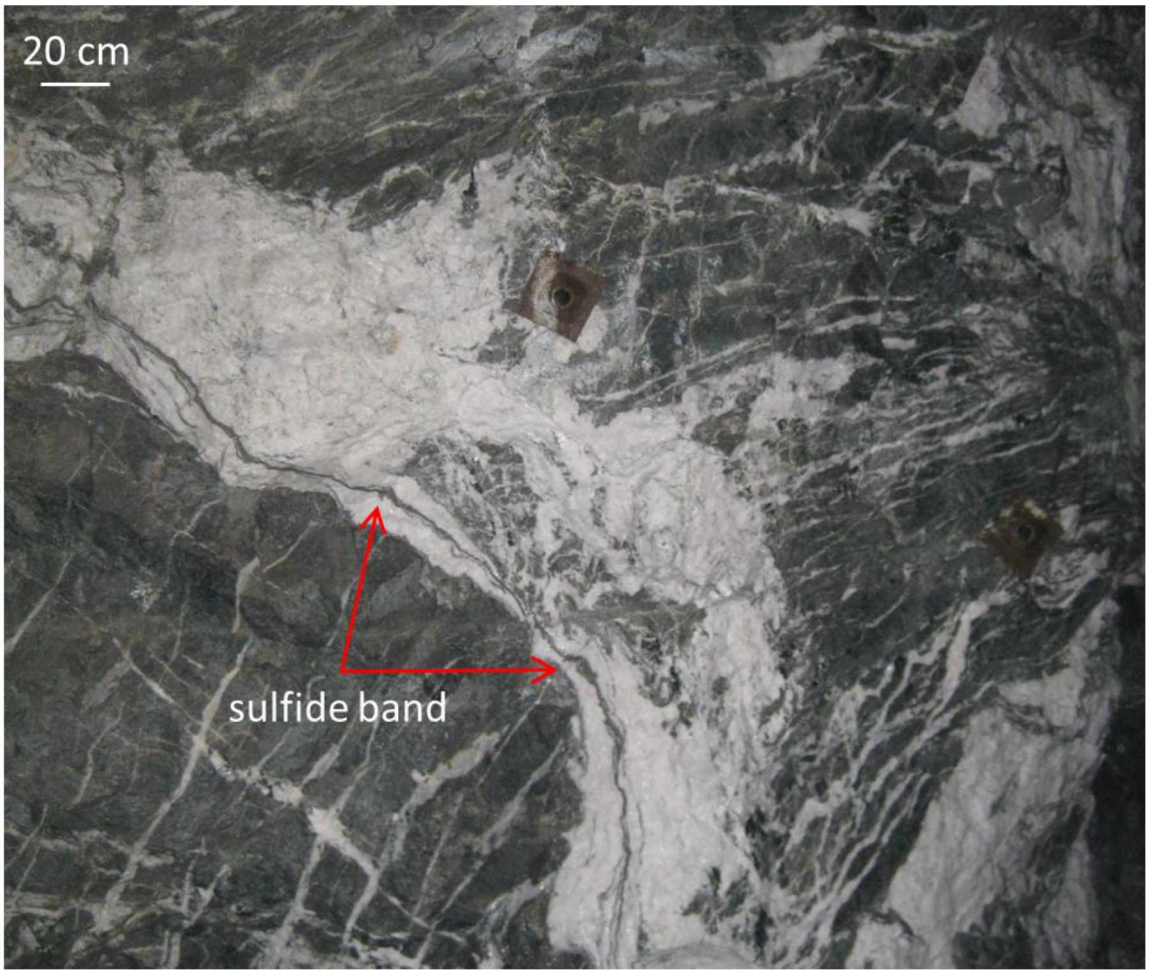

Figure 2.2. Underground photo of a small (< 5 cm thick) sulfide band within a discrete vein. This image is from the lowest mine level sampled (480 elevation, zone 10P).

Table 2.2. Trace metal concentrations and related statistics, 480' level, g per ton sulfide

Sample	Cu	Ag	Te	Bi	Au	Mo	Pb	Zn	Ni	Hg	Co	Se	%Sulfide
480N-1	124	39	485	44	371	14	33	23	44	15	609	24	38
480N-3A	154	58	994	50	744	33	41	39	30	18	676	23	27
480N-3B	136	77	1133	62	799	63	53	40	26	30	582	26	24
480N-3C	139	36	717	44	543	31	45	30	25	17	636	27	31
480N-1&3, avg*	138	53	832	50	614	35	43	33	31	20	626	25	30
480N-1&3, RSD*	9	36	35	17	32	58	19	24	28	34	6	7	

*avg = average; RSD = relative standard deviation

Another example of compositional homogeneity for a single sulfide texture and vein type is given by samples from the 1290 ft. level at the 260 heading (1290-260). This heading contains a very large (> 4m wide) discrete vein from zone 41. I sampled two separate sulfide clots from the lower section of this vein (Fig. 2.3). The two samples are approximately 1m apart along the strike of the vein. Sample K12-5 was sub-sampled; those and K12-4 have very similar sulfide-normalized metal concentrations (table 2.3). Only the Cu concentrations exhibit significant variations.

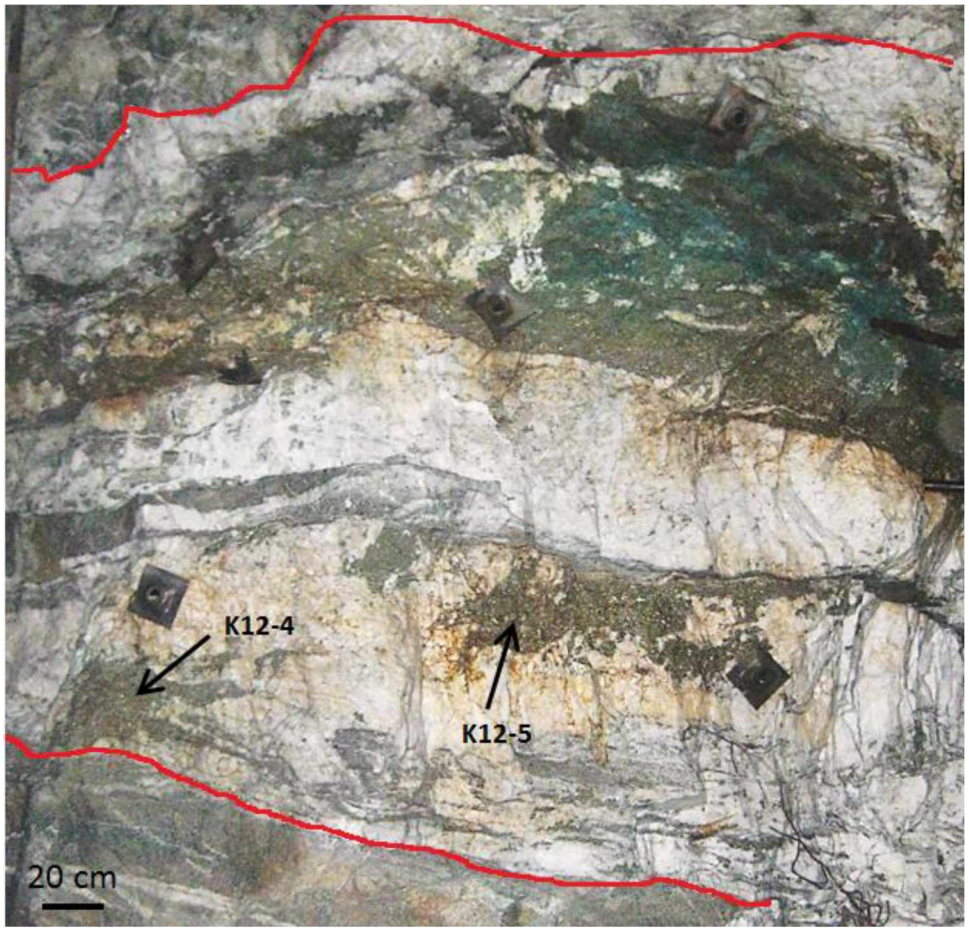

Figure 2.3. Image from heading 1290-260, showing locations of samples K12-4 and 12-5. These two sulfide clots (identified with arrows) have very similar metal concentrations (Table 2.3).

Table 2.3. Metal concentrations (g/ton sulfide) and statistics for samples from 1290-260

Sample	Cu	Ag	Te	Bi	Au	W	Mo	Zn	Ni	Co	Se	%Sulfide
K12-4	230	8	850	7	617	18	13	11	53	194	36	76
K12-5A	809	-	595	-	499	8	10	11	40	242	37	79
K12-5B	780	8	955	7	741	14	14	11	38	294	31	75
K12- 4&5avg*	606	8	800	7	619	13	12	11	44	243	35	77
K12- 4&5 RSD*	54	0	23	0	20	38	17	0	19	21	9	

* avg = average, RSD = Relative standard deviation, - = concentration below detection;
Concentrations for Pb, Sb, As, and Hg are uniformly below detection.

In sum, the low RSDs for most elements in most subsamples, and the very low RSD of nearby samples from the 480N and the 1290-260 indicate that nearby samples with the same texture and location relative to veining have consistent metal concentrations. This allows me to use small (generally < 1 kg) samples to characterize mineralization in a specific location.

2.3 General Compositional Patterns

The complete XRF data are given in Appendix F. After removing data with < 20% sulfide, I have 182 multi-element XRF analyses. Inter-element correlation coefficients (Table 2.4) indicate three major elemental associations: (1) Au-Te, (2) Ag-Bi-Pb-(Ni, Te) and (3) Sb-As-Zn-(Ag,Pb). The higher the R^2 value, the stronger a correlation is between the two variables. $R^2 = 1$ is a perfect correlation.

A Bi-Mo association also appears present, but inspection of the data indicates it is likely due to a small number of samples with high sulfide-normalized concentrations of each. Due to the large number of samples with 'below detection limit' concentrations for Bi, I have only 41 samples (22% of the total) with data for both Mo and Bi.

Based on these correlations, I present compositional data for the three groups above plus other elements (Co, Cu, Se) which do not appreciably correlate with the others. These are presented as 'Au-Te', 'non-Au Te-associates', and 'other elements'. I include Ni with the non-Au Te-associated elements because I have found (rare) $NiTe_2$ and compositional data (see ahead) suggest that several additional samples likely contain this mineral.

Table 2.4. Correlation coefficients for sulfide-normalized Kensington XRF data

	Bi	Ag	Te	As	Mo	Pb	Zn
Ag	**0.61**						
As		**0.39**					
Au			**0.82**				
Mo	**0.36**	0.17					
Pb	0.13	0.17	0.12	**0.27**	0.15		
Zn		**0.60**		**0.88**		**0.23**	
Sb		**0.64**		**0.79**		0.18	**0.97**
Hg			**0.25**				

Note: R^2 values < 0.1 have been omitted; bolder red values are more significant

2.4 Au-Te Elemental Abundance Patterns and Mineralogy

Sulfide rich Kensington samples contain > 2000 to < 25 grams Au per ton sulfide; the majority contain >100 grams Au per ton sulfide (Fig. 2.4). The Au concentrations display an approximately log normal distribution, which is common for trace elements in a variety of rock types and settings. Similar patterns are shown for all trace elements in the Kensington samples for which there are a sufficient

number of samples with concentrations above the detection limits (5 ppm for most, equivalent to 5 to 25 grams/ton sulfide).

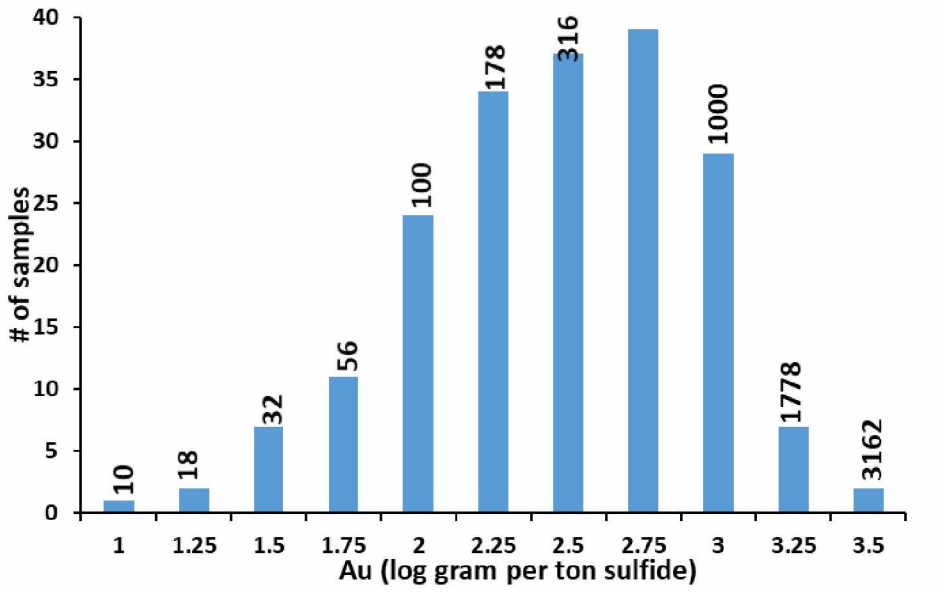

Figure 2.4. Histogram of Au log concentrations (grams/ton sulfide) from XRF results. Each interval is labeled with the actual Au concentration in that interval.

The most obvious and important metal association at Kensington is that of Au and Te (Fig. 2.5). The majority of elemental Au at Kensington occurs as calaverite ($AuTe_2$) as indicated by the strong correlation between Au and Te (Fig. 2.5) at an atomic ratio of approximately 1:2. (I found very small (average size ≈10µm) grains of petzite (Ag_3AuTe_2) in four samples. I consider petzite an accessory telluride even though it is technically a gold-bearing mineral.) However, non-Au telluride minerals also occur, including those with Ag, Bi, Hg, Ni, and Pb (see ahead); their influence is diminished by separating data for which atomic Au/(Au+Ag+Bi+Hg+Ni+Pb) is <75%. Such points generally fall on or below the atomic Au=2Te line due to their 'extra' Te. Similarly samples with low Au or Te (< 50 gram per ton sulfide) can also skew the data, due to analytical uncertainties at low concentrations. Samples that fall into either of these categories are excluded from the following results.

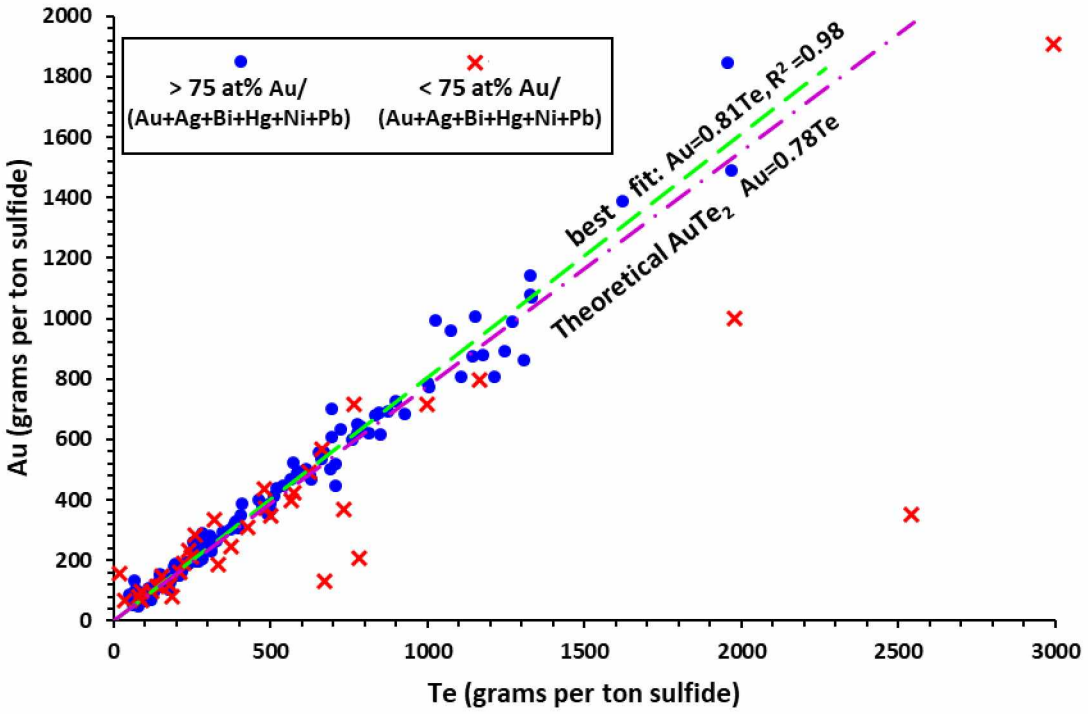

Figure 2.5. Au vs. Te for sulfide normalized XRF data. Samples with < 50 grams Au and/or Te per ton sulfide are excluded. Samples with < 75% atomic Au/(Au+Ag+Bi+Hg+Ni+Pb) generally fall below the theoretical Au to Te ratio of calaverite. The miniscule deviation between the theoretical and calculated trend lines show that the majority of Au present at Kensington is as calaverite, not native gold.

The best fit line (fig 2.4) for analyses with > 75% atomic Au/(Au+Ag+Bi+Hg+Ni+Pb) is nearly identical to line drawn for ideal $AuTe_2$, with a 3% difference in their slopes. Samples that fall above the trend line have excess Au (relative to 100% calaverite) while samples that fall below have excess tellurium. The best fit line falls slightly on the 'excess Au' side of ideal $AuTe_2$, indicating a small amount of native gold is present in addition to calaverite.

A histogram of atomic Au:Te ratios for samples with atomic Au/(Au+Ag+Bi+Hg+Ni+Pb) > 75% show a normal distribution skewed towards higher Au ratios (Fig. 2.6). An Au:Te ratio greater than 0.5 indicates the presence of native gold as well as calaverite; higher ratios indicate more native gold. Two thirds (66%) of the samples have an Au:Te ratio of 0.45 to 0.55, i.e., approximately calaverite (within analytical errors). However 29% of all samples have atomic Au:Te ratios greater than 0.55. There appears to be a slight tendency for zone 41 to yield lower Au:Te ratios (i.e., less native gold) and for zone 10 to yield higher Au:Te ratios (more native gold).

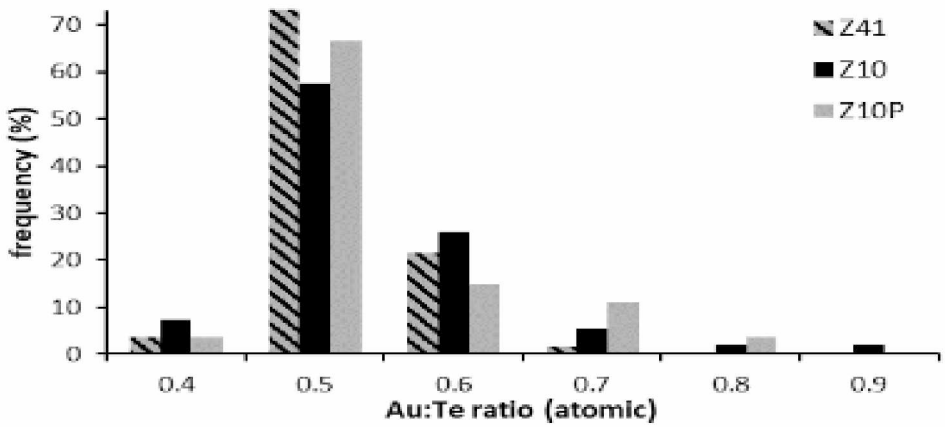

Figure 2.6. Histogram of atomic Au:Te ratios for Kensington samples. Only samples with > 50 Au grams per ton sulfide and with > 75% atomic Au/(Au+Ag+Bi+Hg+Ni+Pb) are included.

A plot of Au vs. atomic Au:Te ratios for samples with > 50 g/ton sulfide Au and Te shows that very high Au concentrations are not due to an abundance of native gold (Fig. 2.7). Higher Au:Te ratios are characteristic of samples with low concentrations of Ag+Bi+Pb+Ni+Hg, that is, for samples with low concentrations of elements that form telluride minerals (outside of Au). However, a few samples with elevated Ag+Bi+Pb+Ni+Hg still possess high Au:Te ratios (Fig 2.7). This is odd, because they presumably contain 'excess' Te due to the non-calaverite telluride minerals present. This oddity suggests that either non-equilibrium assemblages are present or that Ag, Bi, Pb, Ni, and Hg are more strongly attracted to Te than is gold.

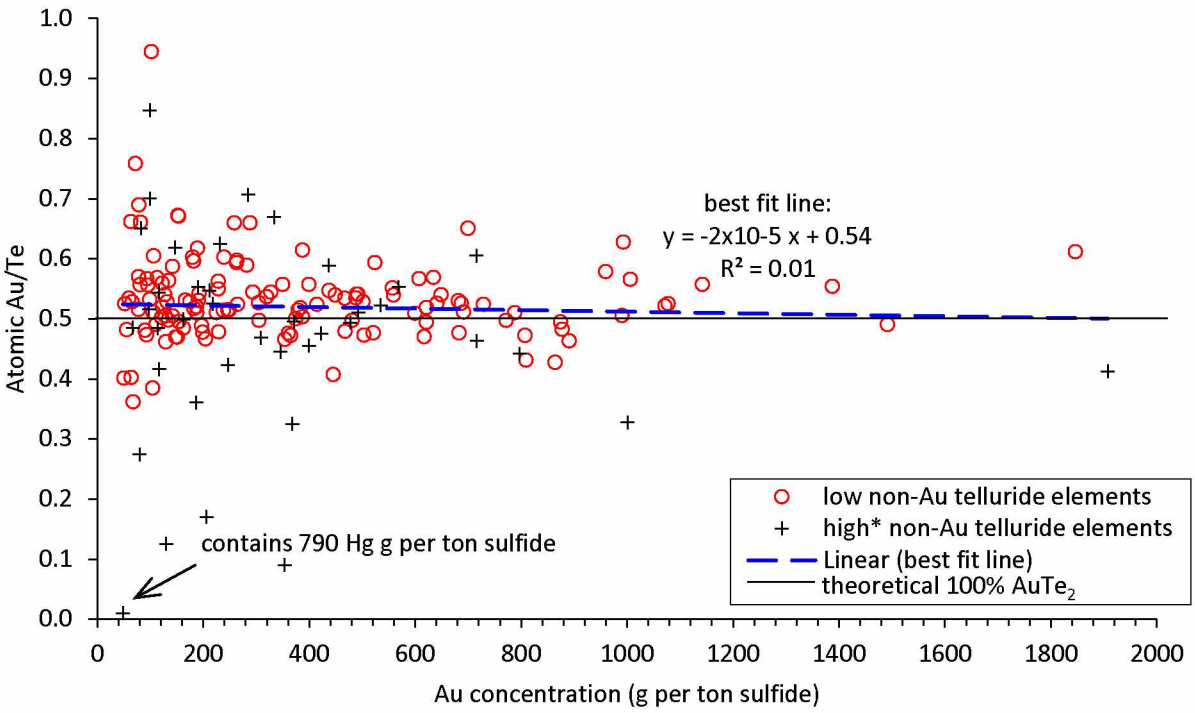

Figure 2.7. Atomic Au:Te ratios for Kensington samples, broken into sets with relatively low and high concentrations of non-Au Te-associated element. Only samples with > 50 Au grams per ton sulfide are included. Best fit line to the majority of data plots very close to Au/Te = 0.5.

Spatial patterns of elemental and mineral abundances are best shown by long sections through the deposit, as described in Chapter 1. A long section view of sulfide-normalized Au concentrations (Fig. 2.8) shows that higher Au concentrations are most common near (a) the south end and (b) the north end of my sampling (Fig. 2.8). The northern high-Au zone might—or might not-- continue through zone 10 to zone 10p. If so, it has a near-vertical orientation in the long section. The southern Au-rich zone is better defined as a 100 foot (30 m) wide zone characterized by samples with grades higher than 600 grams/ton sulfide. Samples outside of this southern zone commonly have grades of < 400 grams/ton sulfide. Unlike the northern zone, this zone plunges about 60° S across the long section. Both higher-grade zones could be viewed as higher-grade "pipes" within the overall vein system.

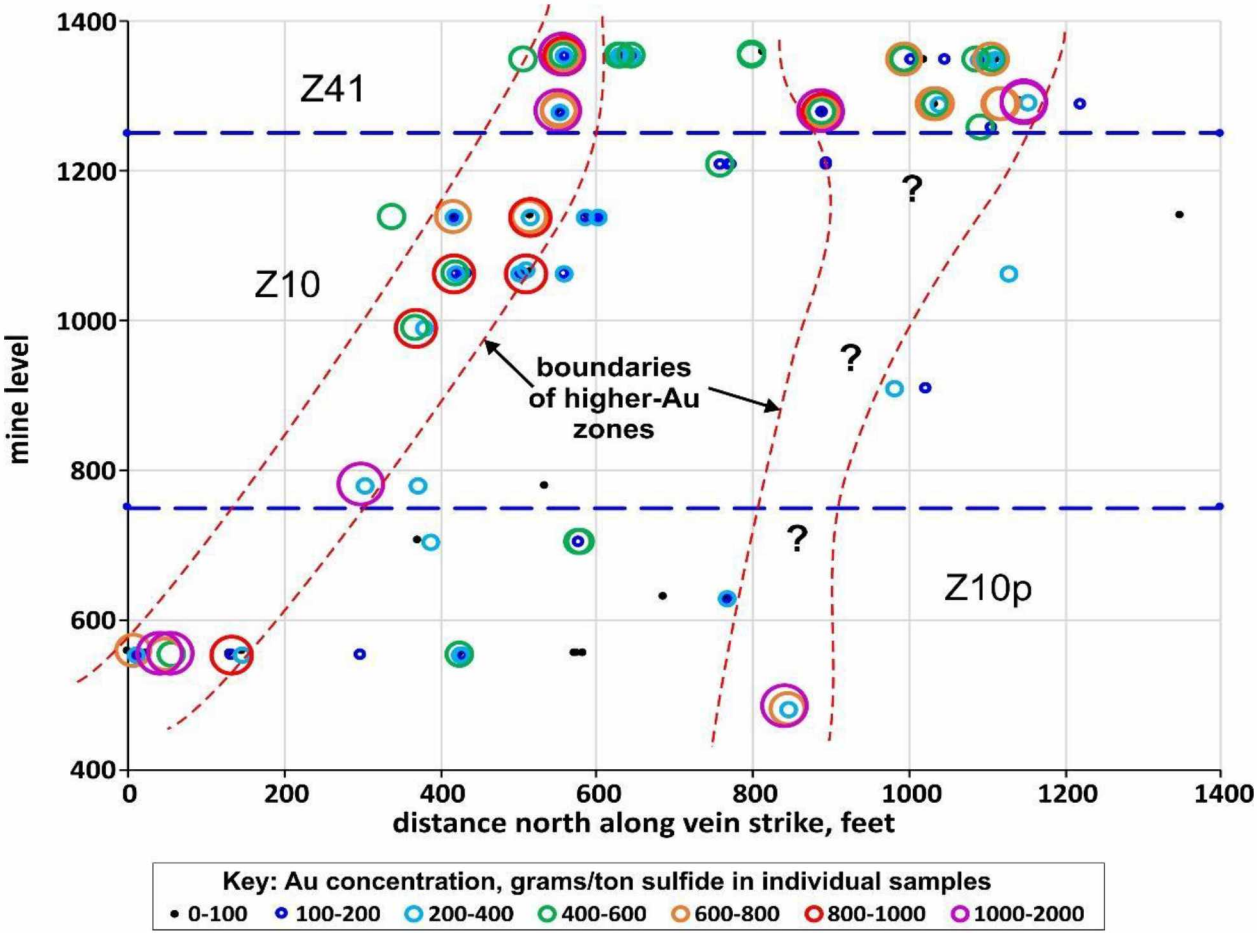

Figure 2.8. Long section showing Au concentrations in my samples, expressed as grams/ton sulfide. Actual mining grades would depend on the concentrations of sulfide at a given site. Higher Au concentrations appear to define two 'pipes' with vertical continuity, especially the southern one.

A long section with distribution of Au: Te ratios (Fig. 2.9) appears to show that samples with lower Au: Te ratios (calaverite only, black dots) and with a relatively high abundance of non-Au telluride (black **+**) appear to be more common in and adjacent to the Au-rich zones (Fig. 2.8). Oddly, samples with high Au/Te (possessing native gold) are not particularly associated with the high-gold zones, and if anything, are more common outside of the high-Au zones. The absence of a spatial overlap between high Au:Te (i.e., native gold presence, Fig. 2.7) and the two high gold 'pipes' (Fig. 2.6) indicates abundant native gold does not produce higher Au grades.

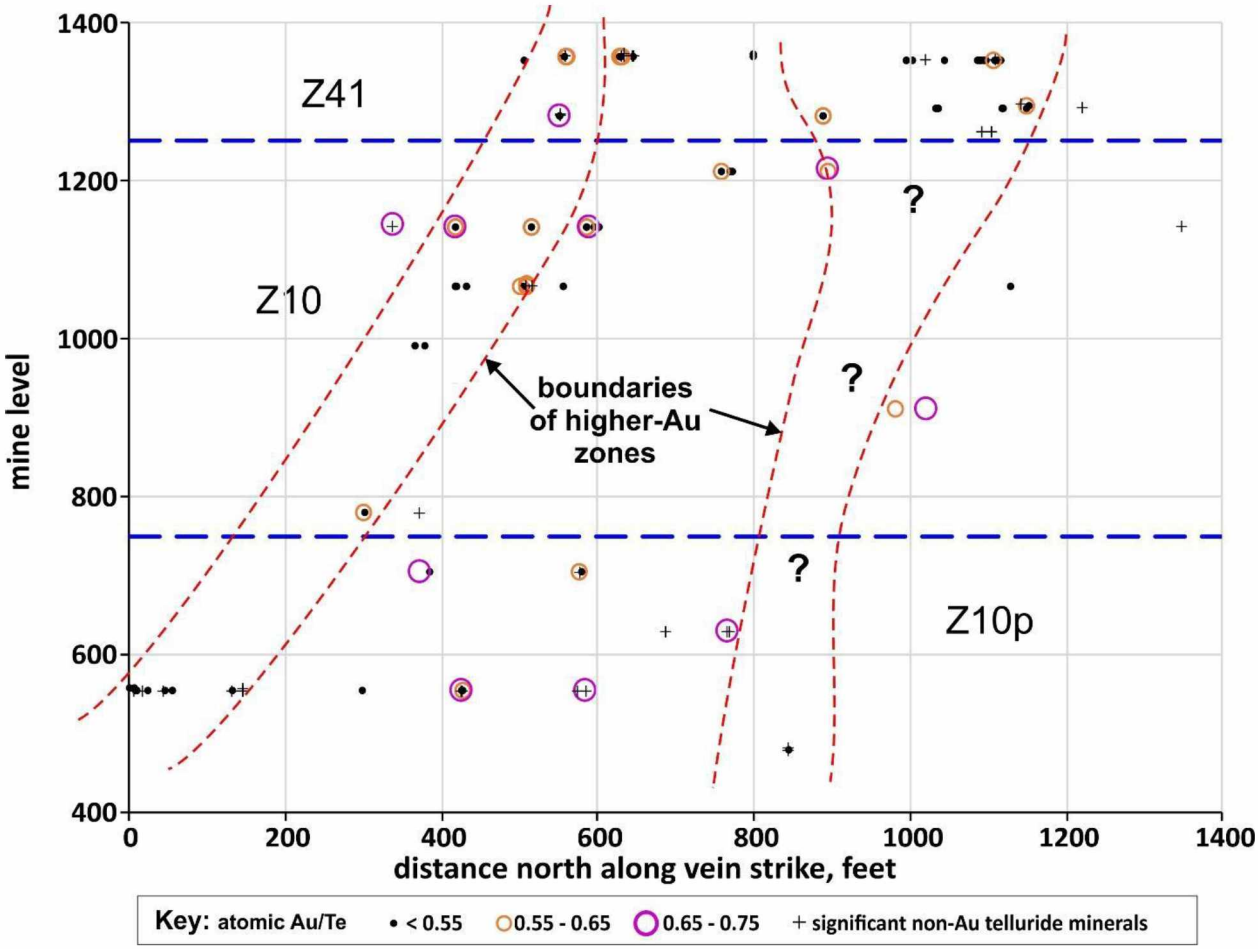

Figure 2.9. Kensington long section with ranges of atomic Au:Te ratios plotted for samples with Au/(Au+Ag+Bi+Hg+Ni+Pb) >75%; samples with lower ratios depicted with + symbols. Boundaries of Au-rich zones from fig. 2.8.

2.5 Abundance patterns and mineralogy of other Te-associated elements

I have observed a variety of telluride minerals in Kensington samples, including: Hessite (Ag_2Te), petzite (Ag_3AuTe_2), and coloradoite (HgTe). I have also identified Bi-Te-(S) minerals, altaite (PbTe), and rare melonite ($NiTe_2$). To the limit of my observations, Hg and Bi are the only elements at Kensington that are exclusively present as tellurides. Ag occurs in solid solution (with native gold and calaverite), however, samples with high Ag to Au ratios contain Ag tellurides. Ni and Pb also don't exclusively occur as telluride minerals. Based on polished section data, Pb occurs both at PbTe and as PbS.

Ni appears to be a special case (Fig. 2.10): a plot of raw Ni concentration vs. wt% sulfide shows strong correlations except for those samples with the highest Ni contents. Three main populations can be identified: (a) most of the samples (average 30 grams/ton sulfide), (b) higher Ni samples (average 45

grams/ton sulfide), and (c) samples with > 50 ppm Ni (no Ni-% sulfide correlation). I interpret most of the data to represent solid solution of Ni in pyrite (and lesser chalcopyrite). Because group 'c' shows (if anything) a negative correlation between Ni and % sulfide and because I identified melonite ($NiTe_2$) in one of the group 'c' samples, I infer that all the group 'c' samples contain melonite in addition to Ni in solid solution in pyrite. The group 'c' sample with lowest Ni contains 51 ppm, equivalent to 70 grams Ni/ton sulfide. Hence, samples with > 70 grams Ni/ton sulfide likely contain at least some $NiTe_2$. A histogram of sulfide-normalized Ni (Fig. 2.10b) clearly illustrates the 'anomalous' Ni population.

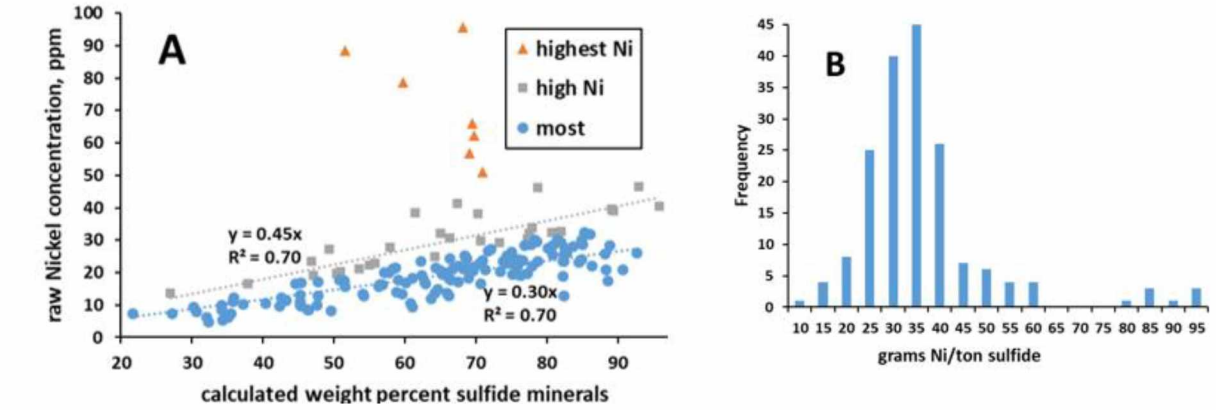

Figure 2.10. Ni concentration populations. A) Raw Ni concentration (ppm) vs. calculated wt% sulfide minerals shows 3 different populations. B) Histogram of sulfide-normalized Ni, clearly illustrating the 'anomalous' population. The group with the highest ppm Ni shows no correlation between % sulfide and Ni and most likely represents Ni at least in part due to Melonite ($NiTe_2$) inclusions. The other samples likely contain most of their Ni as solid solution in pyrite (and lesser chalcopyrite).

Kensington contains elevated and varied concentrations of the Te-associated elements Ag, Hg, Bi, Ni, and Pb (Fig. 2.11). I compare the 'averages' using geometric means (geomean) rather than the normal arithmetic means due to the presence of a few very elevated outliers. Given that the distributions are log-normal (e.g., Au, Fig. 2.4), a geometric mean is more appropriate than the mean. The geomean concentrations of the telluride-forming elements are well below the geomean concentration of Au, 241 g per ton sulfide (fig 2.11); however individual samples from zone 10P contain higher Hg and Ag than Au. The geomeans are calculated for concentrations above detection limits, so that in most cases a true 'mean' concentration would be significantly lower, as concentrations of these elements are commonly below detection.

Zone 10 is conspicuously barren of non-Au tellurides except for one slide with coloradoite. The XRF data reflect the low occurrence of non-Au tellurides in the low Ag, Hg, Pb, Bi, and Ni concentrations

in zone 10 (Fig. 2.11). Zone 10P contains higher geomean concentrations for Bi and Hg than zone 41; given the large number of samples from zone 10P with > 200 grams Hg/ton sulfide, this difference is probably real. Conversely, the Bi concentrations of zones 41 and 10P are likely similar (Fig. 2.11).

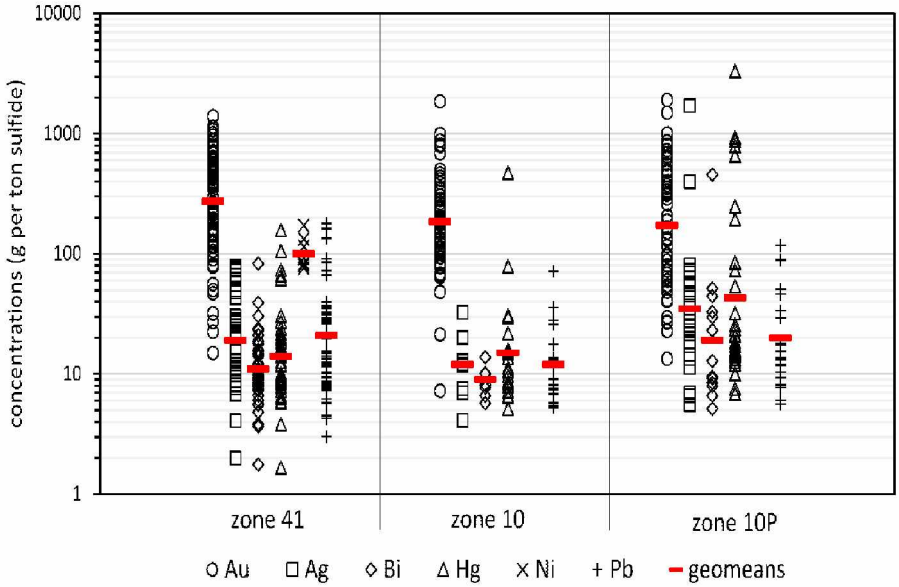

Figure 2.11. Concentration ranges of telluride forming elements arranged by zone. Concentrations below detection limits are excluded. Only those Ni concentrations that likely represent $NiTe_2$ (Fig. 2.9) are plotted. The two very high Pb concentrations have been excluded. The associated samples contain visible galena. Zone 10 contains lower mean concentrations of Ag and Bi. Zone 10P contains the highest absolute and mean Hg concentrations.

Calculation of correlation coefficients for the non-Au telluride elements (Table 2.4) is complicated by the fact that almost all samples contain concentrations below detection for at least one of the elements. A long section showing spatial distribution of samples with elevated Ag, Bi, Ni, Hg, and Pb (Fig. 2.12), however, shows some clustering of these elements. Melonite ($NiTe_2$) exclusively occurs in zone 41 along with the highest concentrations of Ag and Hg (Fig. 2.12). Elevated Hg concentrations are restricted to the southern margin of all three zones, whereas elevated Bi is restricted to the northern margin. That is, elevated Bi and Hg practically never occur together. In contrast elevated Pb and Ag (seen as blue circles with + symbols) are common associates. Finally, Zone 10 essentially lacks higher concentrations of the non-Au Te-associated elements (Fig. 2.12). Individual long sections showing concentrations of Hg, Ni, Bi, and Ag are given in Appendix G.

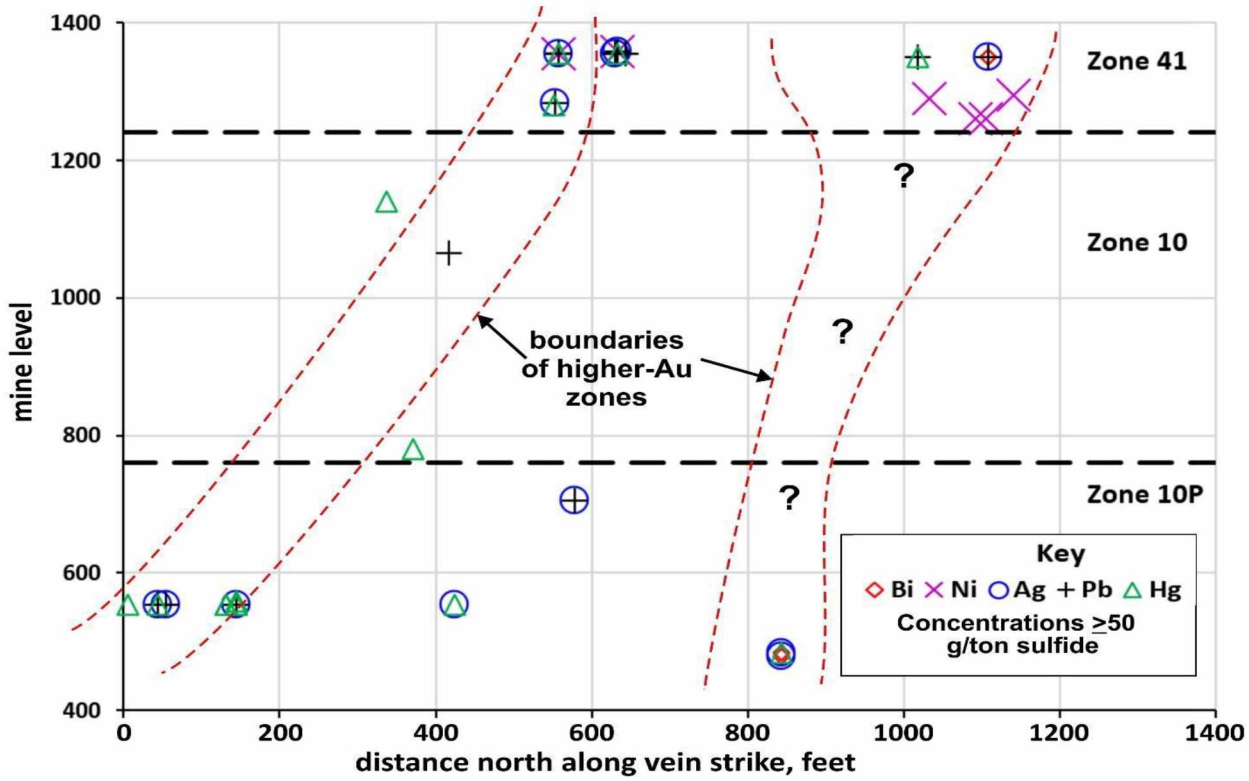

Figure 2.12. Long section showing spatial distribution of samples with elevated concentrations of non-Au telluride-associated elements. These are almost exclusively located in zones 41 and 10P.

2.6 Lead

Lead represents a (mostly) Te-associated element for which I have the largest proportion of samples with concentrations above detection (48%). I found galena (± PbTe) in one of the samples with the highest Pb concentrations (> 700 grams/ton sulfide). Given the high mean atomic weight of Pb, PbS and PbTe stand out as very bright spots in back-scattered electron (BSE) images. I checked each of these for major elements by EDS and invariably found PbTe. Consequently, I am certain that PbS is quite rare.

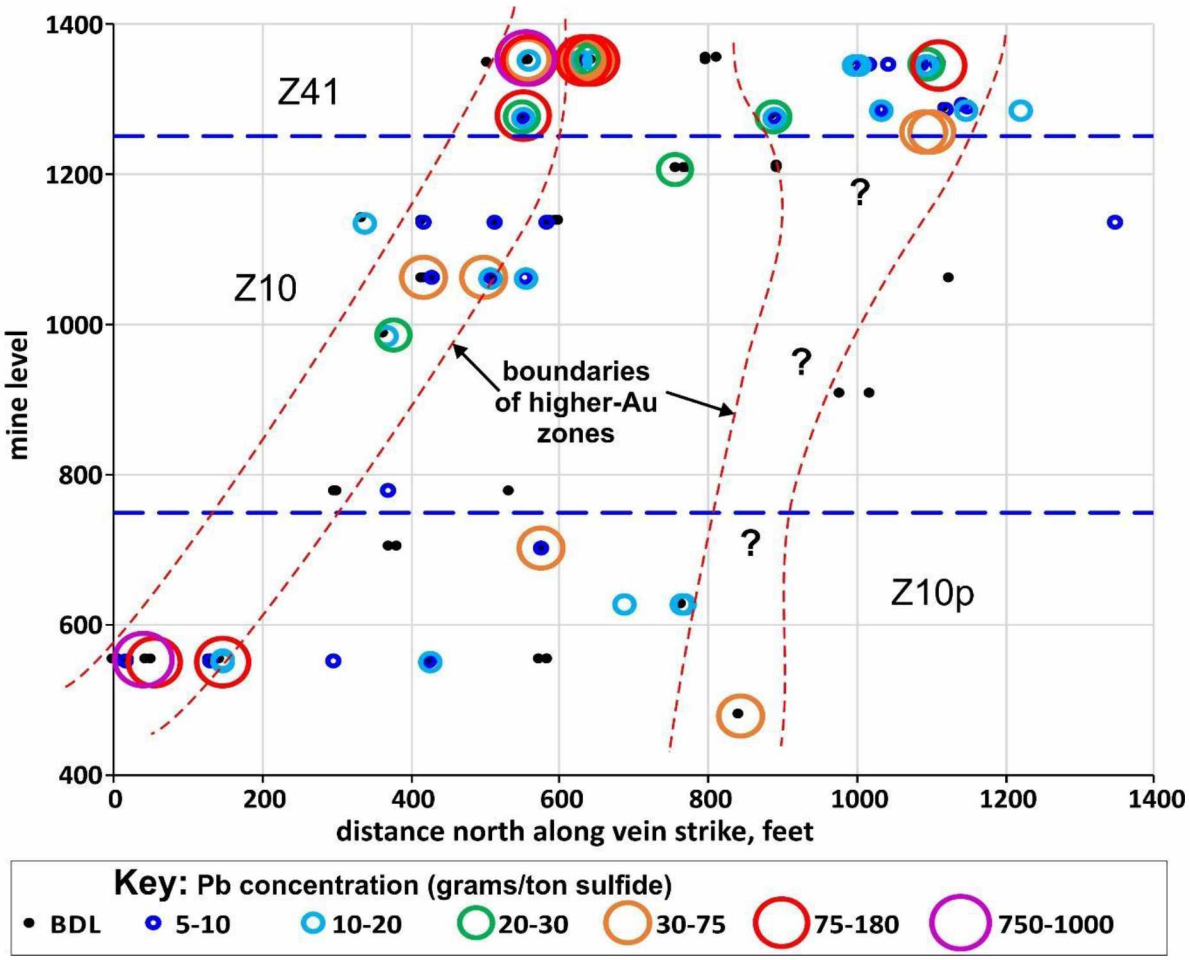

Figure 2.13. Long section showing spatial distribution of sulfide-normalized Pb concentrations relative to the Au-rich zones identified in Fig. 2.8. The samples with highest Pb also contain galena (PbS).

The spatial distribution of Pb in long section (Fig. 2.13) shows that significant concentrations (> 30 grams/ton sulfide) are almost entirely restricted to within or adjacent to the higher-Au zones of Fig. 2.8. However, many of the samples within the high-Au zones contain low (< 25 grams/ton sulfide) Pb. That is, on a sample-by-sample basis, there is a poor correlation between Pb and Au (Table 2.4). However, a heading that contains high sulfide-normalized Au concentrations is also likely to contain high sulfide-normalized Pb (Fig. 2.13). Further, headings outside of the 'higher-gold zones' invariably contain low sulfide-normalized Pb. In terms of general spatial patterns, Pb seems to be associated with Au, and much more strongly than the other Te-associated elements.

2.7 Abundance Patterns and Mineralogy of Non-Te-Associated Elements

These elements include Cu, Mo, Co, As, Sb, and Zn. The latter 3 occur together in the mineral tetrahedrite and are treated together. The former three seemingly occur mostly independently and are all treated separately.

2.7.1 Cu Distribution and Mineralogy

The spatial distribution of Cu concentrations at Kensington is complicated by the fact that chalcopyrite abundance varies tremendously within and between sampling sites. Clean sulfide aggregates from Kensington seemingly vary from nearly pure chalcopyrite to nearly pure pyrite. Further, identifying copper-rich samples underground proved problematic due to the discoloration of sulfides from diesel exhaust residue. Consequently, I rely on XRF analyses to determine copper contents of my samples. Plotting such sulfide-normalized Cu concentrations (Fig. 2.14) reveals a compositional gap between 1.6 and 3 wt% Cu, equivalent to about 5-8 wt% chalcopyrite. This seems a logical place to break between 'Cu-rich' (> 2% Cu) and 'normal' (pyrite-rich) samples. Consequently, I define Cu-rich samples as those with at least 3 wt% Cu normalized to 100% sulfide.

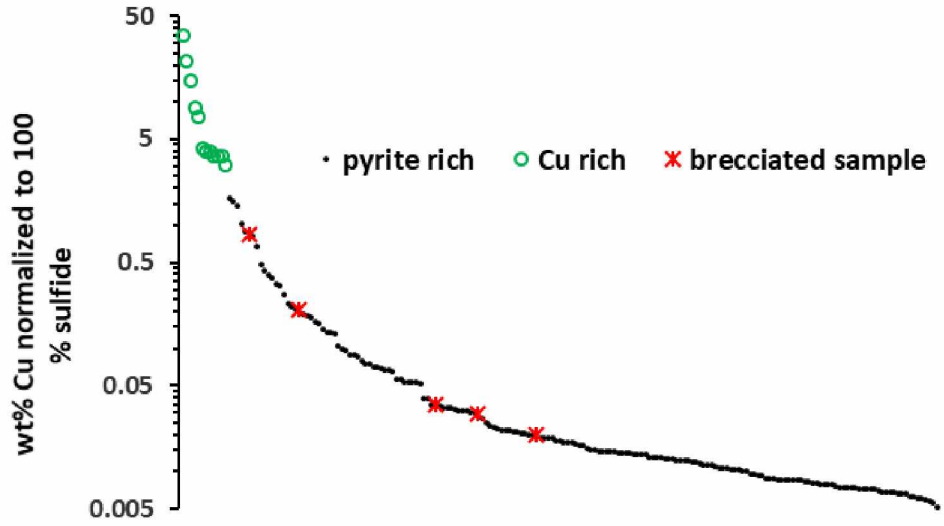

Figure 2.14. Cumulative sulfide-normalized wt% Cu for Kensington samples, showing Cu-rich samples distinguished from others. Brecciated samples are described in chapter 3.

The typical predominant Cu sulfide mineral at Kensington is chalcopyrite. Tetrahedrite-Tennantite ('fahlore') is more abundant than chalcopyrite in a handful of samples (see ahead), but all samples contain at least traces of chalcopyrite. Further, Cu-rich samples exclusively contain chalcopyrite. I found rare bornite in only 2 polished sections, and given its easy identification, I am confident that it's rare. Consequently I use the terms 'Cu-rich' and 'chalcopyrite-rich' interchangeably.

Zone 41 contains half of the Cu-rich (> 3% Cu, sulfide normalized) samples and 60% of the samples with >.08 % sulfide-normalized Cu. The Cu-rich samples are sub-equally present in zones 10 and 10P. However, samples with appreciable (>.08%) Cu are present at 6 general areas (2 in each zone; Fig. 2.15), which seemingly define 3 main sub-vertical regions: northern, central, and southern.

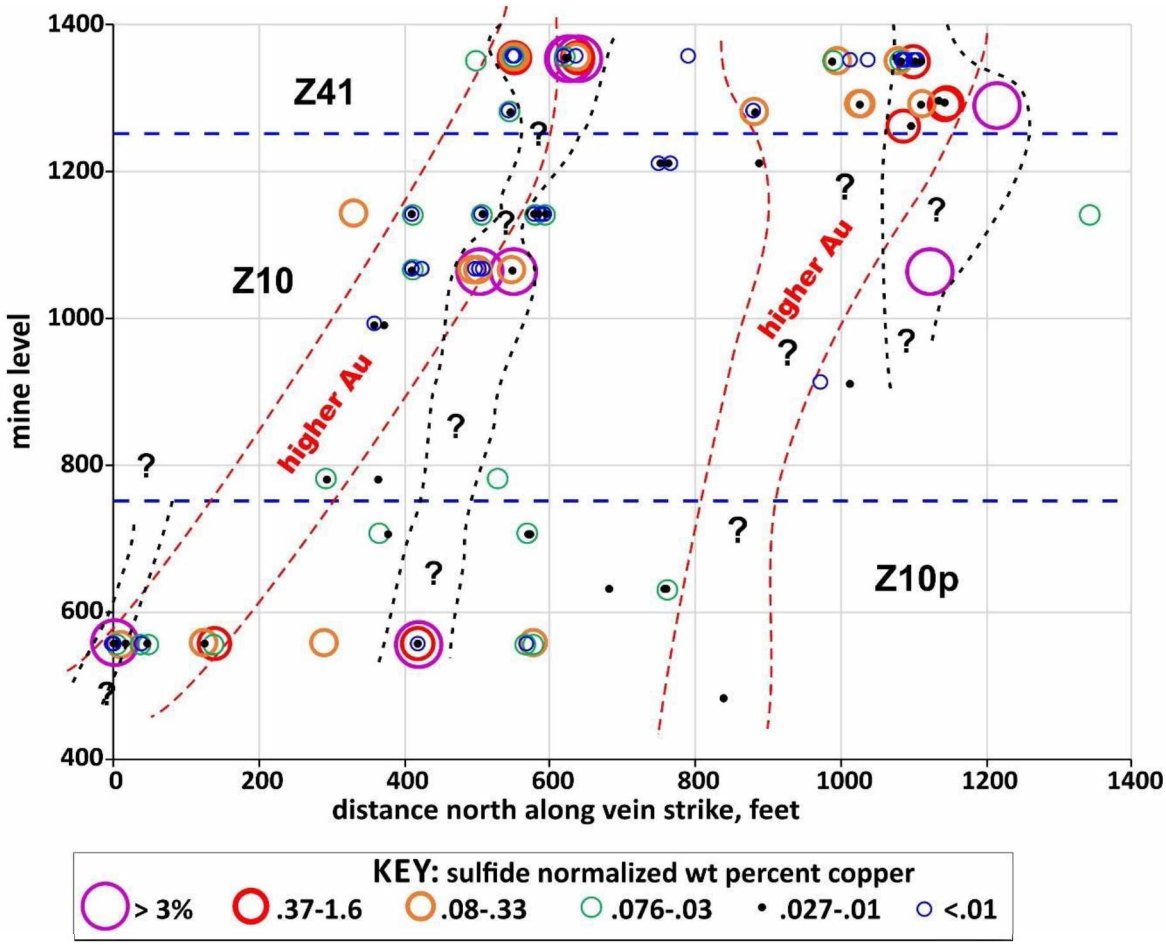

Figure 2.15. Long section view looking west showing distribution of sulfide-normalized wt % Cu. Three possibly sub-vertical, Cu-enriched zones are outlined by the black dotted lines. Gold-rich zones are taken from Fig. 2.8. Samples containing > 3% Cu are considered 'Cu-rich'.

The northern Cu-rich region is mostly defined by Cu-rich samples at three different levels in zone 41, with a single Cu-rich sample underneath in zone 10. This region somewhat overlaps with the northern gold-rich zone of Fig. 2.8. The central Cu-rich region contains Cu-rich and high-Cu samples from the lowest to the highest mine levels (Fig. 2.15) separated by sampling gaps. Thus, it might (or might not) represent continuous Cu enrichment. It overlaps the southern gold-enriched pipe in zone 41, but takes a different trend with depth than the southern high Au zone—it's practically vertical whereas the southern Au-rich zone rakes about 60° south. The southern Cu-enriched region is defined by a single Cu-

rich sample at the south end of lower zone 10p. If it has the same near-vertical trend as the others, then it also barely overlaps the southern Au-rich zone (Fig. 2.8). The general lack of correlation between Cu and Au is emphasized by Fig. 2.15; Cu-rich samples usually contain < 400 grams Au/ton sulfide and Cu-poor samples show a wide range in Au concentrations.

2.7.2 Tetrahedrite Solid Solution (Fahlore)

Tetrahedrite is a complex solid solution mineral with an approximate formula of $(Cu,Ag)_{10}(Zn,Fe)_2(Sb,As)_4S_{13}$. I used tetrahedrite to refer to the Sb end-member and Sb-fahlore to indicate the solid solution mineral with atomic Sb>As. With a very small number of exceptions, all the fahlore I've examined compositionally has atomic Sb>As (Chapter 5), so I will refer to all as Sb-fahlore. My compositions (chapter 5) also show that the Ag content is very low, usually below detection limits. Further, atomic Zn/(Zn+Fe) is always > 0.85, and commonly > 0.95, so elemental Zn concentrations in my samples are simply proportional to concentrations of Sb+As (Fig. 2.16). This compositional characteristic also explains the very high As-Sb-Zn correlation coefficients (Table 2.4). Further, I've only found traces of sphalerite in one sample, suggesting that the bulk of Zn in my samples is dissolved in Sb-fahlore.

Given these relations, it makes more sense to show the distribution of calculated Sb-fahlore abundance, than to separately show the distribution of the elements Sb, As, and Zn. I've calculated Sb-fahlore abundance using the XRF As and Sb data (wt% Sb x 3.43 = wt% tetrahedrite; wt % As x 4.94 = wt% tennantite; wt% fahlore = wt% tetrahedrite + wt% tennantite.) I then calculated % chalcopyrite abundance using the Cu 'left over' from making fahlore and % pyrite, using 'left over' Fe and S. Sulfide normalized wt% fahlore is thus 100*(wt% fahlore/total wt % sulfide minerals).

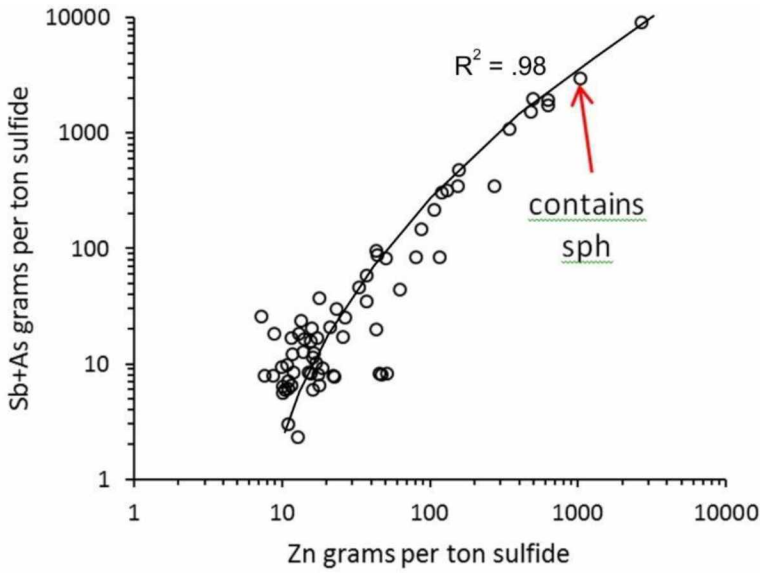

Figure 2.16. Sulfide-normalized Zn vs. Sb + As concentrations from XRF data. The strong correlation between these elements indicates that the vast bulk of Zn in my samples substitutes into Sb-fahlore.

Based on these calculations, several regularities emerge (Fig. 2.17). First, Cu-rich samples do not contain significant abundances of fahlore. That is, high % Cu does not result in high % fahlore. Second, all samples with fahlore contain at least some chalcopyrite, whereas most chalcopyrite-bearing samples contain little or no fahlore. Finally, only a handful of samples contain more calculated fahlore than chalcopyrite (Fig. 2.17).

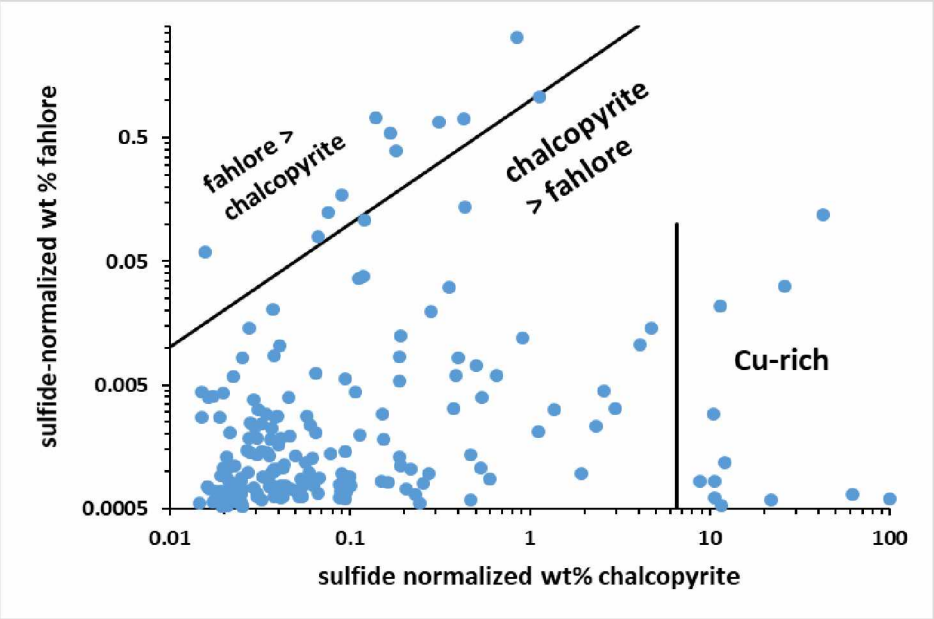

Figure 2.17. Sulfide normalized wt % chalcopyrite vs wt % fahlore, from XRF data. Almost all samples have more chalcopyrite than fahlore.

The relative scarcity of fahlore at Kensington is emphasized by the long section showing sulfide-normalized wt% fahlore in my samples (Fig. 2.18). All of the samples with > 0.1% calculated sulfide-normalized fahlore are at the south ends of zones 41 and 10P, corresponding to the southern high-Au zone. This very restricted area of significant fahlore is in considerable contrast to the multiple areas of high Cu (Fig. 2.15). The absence of fahlore in the northern high gold zone also indicates that fahlore is not uniquely associated with high Au. The most fahlore-rich sample in southern zone 41 also contains very high Pb (Fig. 2.13); but fahlore-rich samples in southern zone 10P are only in the general vicinity of the highest Pb sample. These spatial relations cause the weak correlations between Pb and Sb-As-Zn (Table 2.4).

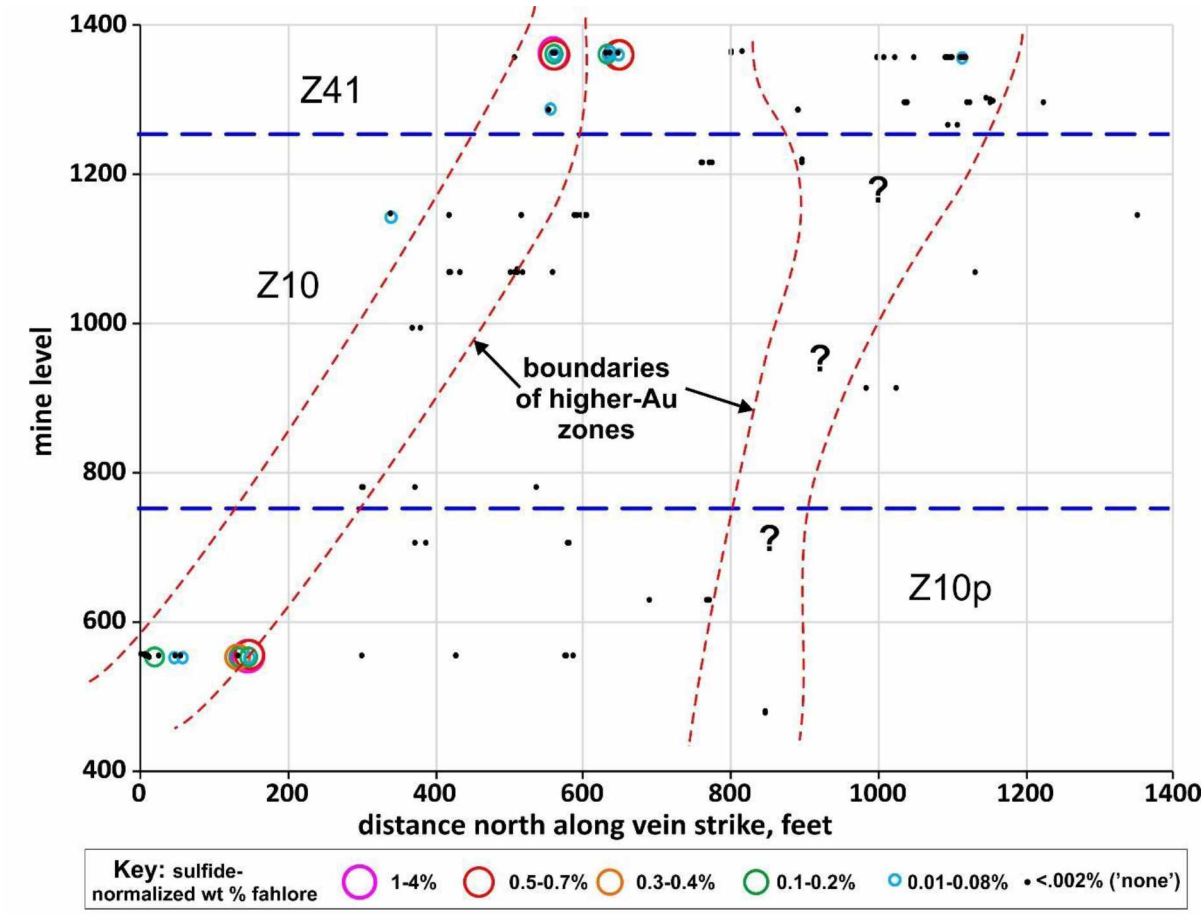

Figure 2.18. Long section showing calculated sulfide-normalized % fahlore (tetrahedrite-tennantite) (from XRF data) with outlines of the Au-rich zones from Fig. 2.8. See text for calculation methods.

2.7.3 Molybdenum Distribution and Mineralogy

My samples are generally low in molybdenum (Mo) but most yield concentrations (barely) above detection. However, two samples contain > 1000 g Mo per ton sulfide and 12 samples contain > 100 g Mo per ton sulfide (Appendix F). Given this abundance, I found it frustrating that I have almost never seen molybdenite (MoS_2) in reflected light or microprobe BSE images. However, based on consistent relations between Mo concentration and calculated % pyrite for 6 Kensington pyrite concentrates (Fig. 2.19a), it would appear that some/much of the Mo is in solid solution in pyrite, rather than as MoS2. A plot of raw Mo concentrations vs. calculated % sulfide minerals for all but the two most Mo-rich (Fig. 2.19b) can be broken into 4 groups: very high, high, moderate, and low-Mo. The high- and moderate-Mo groups yield strong correlations between Mo and % sulfide, consistent with Mo present in solid solution. The very high Mo group probably contains at least some MoS_2, hence, shows little correlation with % sulfide. The low-Mo group could represent sulfides with very little Mo in solid solution.

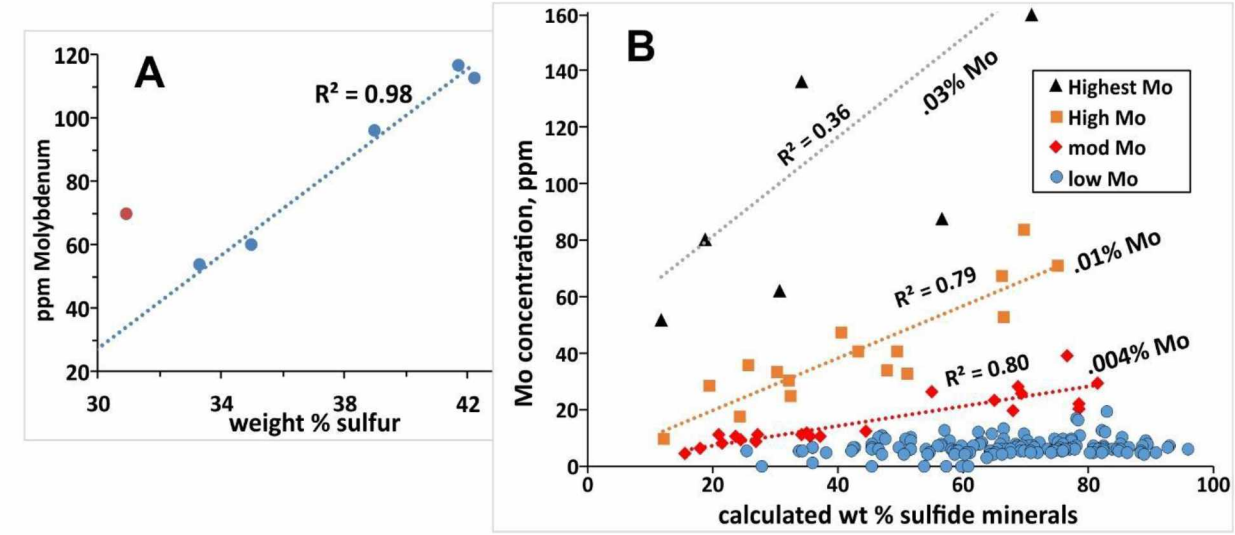

Figure 2.19. A) Mo concentration vs. wt % sulfur for 6 Kensington pyrite concentrates, analyzed by a commercial laboratory. **B)** Raw Mo concentration vs. calculated wt% sulfide minerals for all but the two highest-Mo samples. Mo concentrations > 100 ppm probably represent MoS_2 inclusions; lower concentrations likely represent Mo solid solution in pyrite.

To better understand Mo behavior in high-Mo samples, I prepared polished surfaces from two samples and performed numerous hand-held XRF analyses on each. Doing so showed two contrasting patterns (Fig. 2.20): an association with pyrite and an assocation with muscovite. Repeated analyses of sample 1350-13 show that Mo concentration increases with wt% sulfide minerals (almost entirely

pyrite). However, the sulfide-normalized Mo concentrations are approximately 600-700 grams Mo/ton sulfide, too high to be accomodated by solid solution in pyrite. Instead, these likely reflect inclusions of MoS_2 in pyrite. In contrast, repeated analyses of sample 705-Paste 3 shows that Mo concentration increases with decreasing % sulfide minerals but increased muscovite (Fig. 2.20b). In this case MoS_2 was precipitated outside of pyrite and sulfide-normalizing isn't really appropriate. I believe, however, that this applies to only a handful of samples.

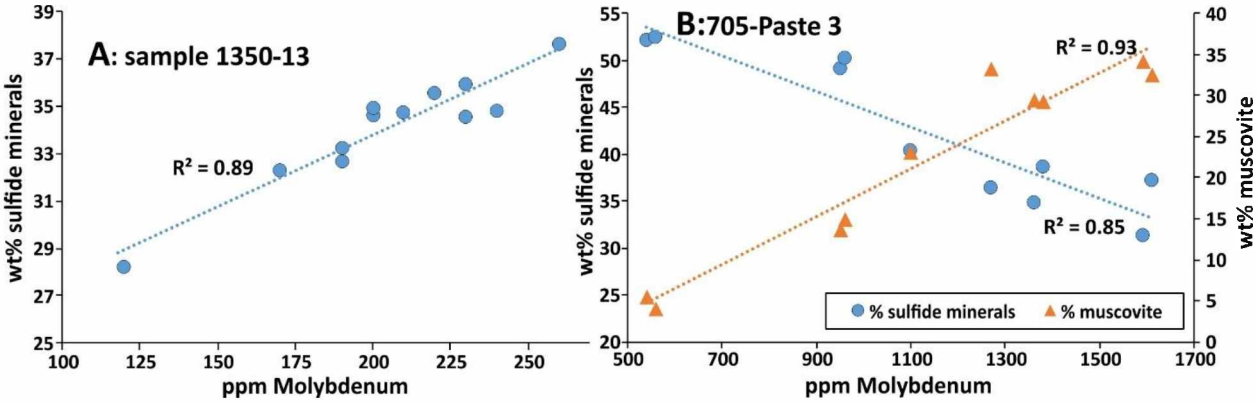

Figure 2.20. Relations between Mo and total sulfide concentrations for two relatively Mo-rich samples, based on hand-held XRF data. Abundances of sulfide minerals and of muscovite were calculated based on the measured Fe, S, and Cu concentrations and on the measured Kensington concentrations, respectively.

The spatial pattern of Mo concentrations in long section (Fig. 2.20) shows highest concentrations in zone 41 but not much correlation between high Mo and the high Au zones. In particular, Mo concentrations in zones 10 and 10P are as high outside the Au zones as inside them. It's difficult to see a spatial pattern in the data. This might be due to 'noise' from background Mo as variable amounts of solid solution in pyrite, and to the fact that sulfide-normalizing the Mo isn't always appropriate.

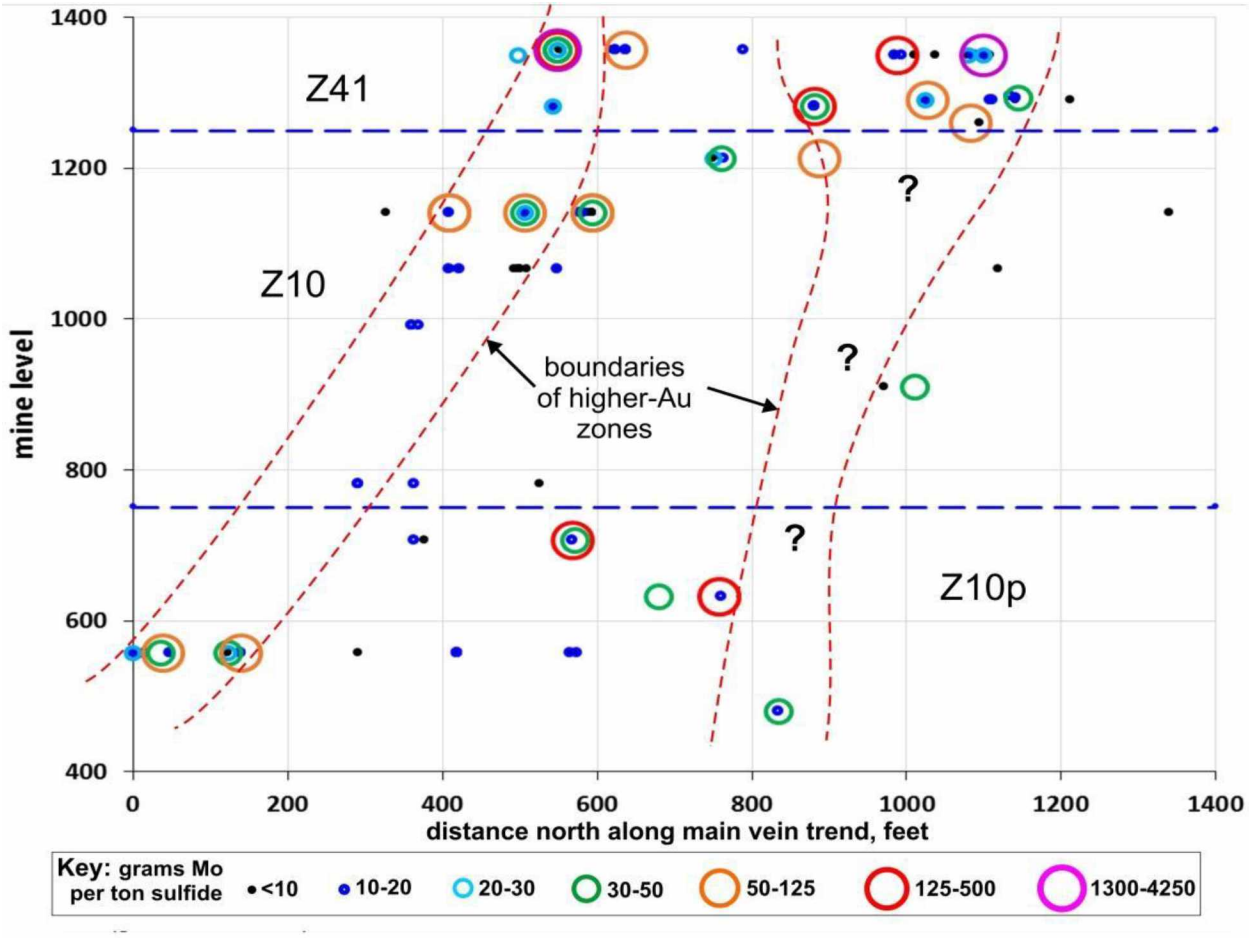

Figure 2.21. Long section showing distribution of Mo concentrations (grams/ton sulfide).

2.7.4 Se and Co Distribution and Mineralogy

Both of these elements are known to occur in solid solution in sulfides and are discussed separately. Due to its close fit in size and chemistry, Se simply and easily substitutes for S. The XRF Se data (Figs. 2.20a) can be interpreted as indicating three different pyrite types, one averaging about 80, one about 50 ppm and one about 35 grams/ton Se. Similarly, the histogram of sulfide-normalized Se concentrations (Fig. 2.20b) can be approximated by Gaussian distributions for those 3 different concentration populations. The highest Se population is least abundant, accounting for about 15% of the analyses; the lowest-Se group is most abundant.

The long section (Fig. 2.21) shows that higher Se concentrations are more common in the south and that Zone 41 contains few of the higher-Se sulfide samples. This is the only case where elemental concentrations are higher in zone 10 than in the overlying zone 41. The two highest Se concentrations

are both in the southern higher-Au zone (Fig. 2.21), but otherwise there does not appear to be a correlation between Se concentration and Au abundance.

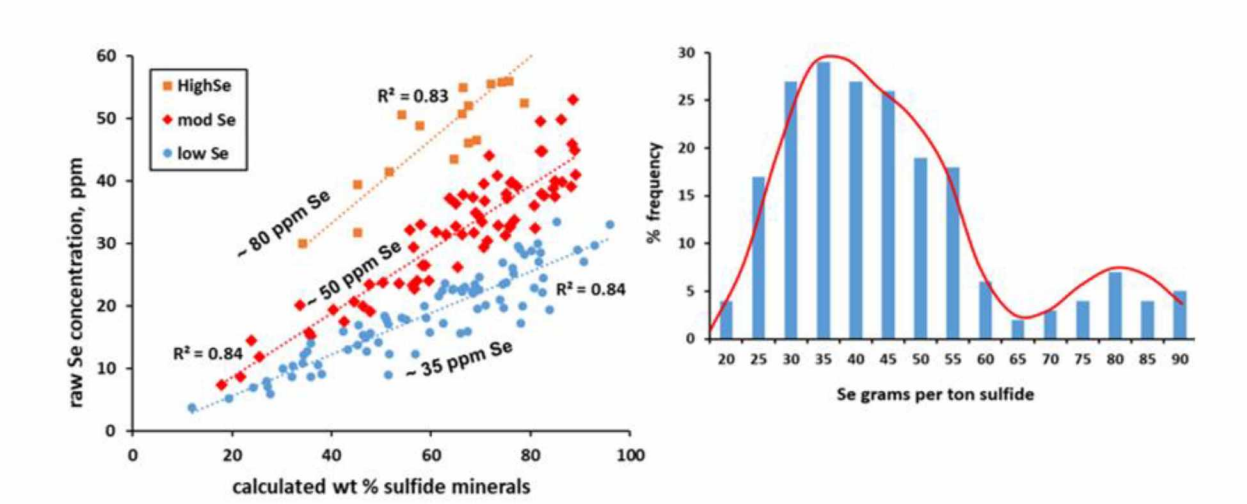

Figure 2.22. A. (left) raw Se concentrations vs. calculated % sulfide minerals for all XRF data. **B.** (right) a histogram of sulfide-normalized Se concentrations (grams Se/ton sulfide) for all XRF data. The red line is the Gaussian cumulative frequency distribution calculated for populations with 80, 50, and 35 grams/ton Se.

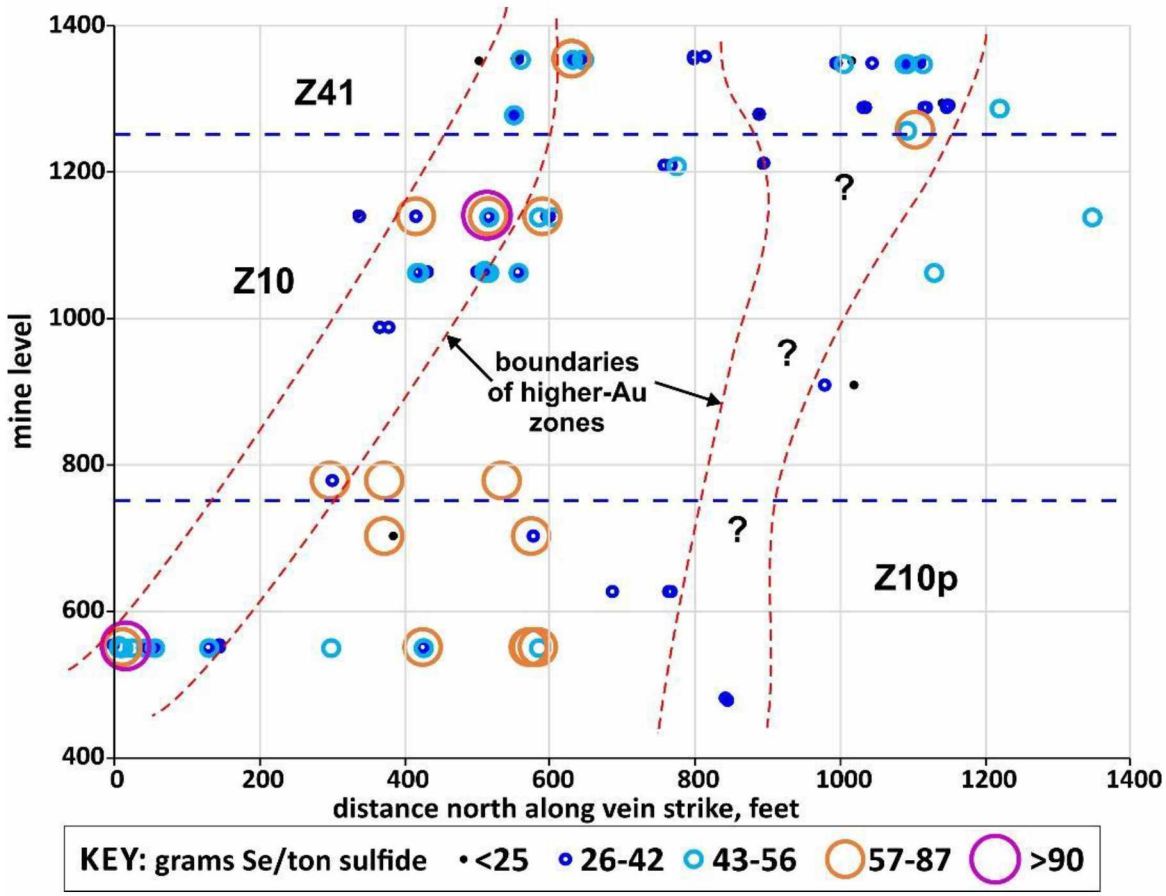

Figure 2.23. Kensington long section showing distribution of Se concentrations, broken into groups that approximate the 3 populations shown in Fig. 2.20. Zone 41 generally lacks higher Se concentrations.

Co is the most abundant (> 0.1 wt% sulfide normalized) of the trace elements for which no host mineral (outside of pyrite) has been identified at Kensington. Lack of an obvious host mineral (e.g., carrollite, $CuCo_2S_4$) makes pyrite the logical host. Unlike Ni and Se, there is no general correlation between raw Co concentration and pyrite abundance (Fig. 2.22a). Given the strong affinity of Co for pyrite, it is most likely that Co occurs exclusively as solid solution in pyrite at Kensington, but includes at least 5 different populations with average wt% Co of ~ 0.1% to ~ 0.01% (Fig. 2.22a). Modeling the Co concentration histogram as a series of Gaussian distributions requires at least 7 different populations (Fig. 2.22b). The histogram shows a large population with approximately 150 g Co/ton sulfide and several additional populations, e.g., with mean concentrations at 550, 650, 750 and 850 grams Co per ton pyrite.

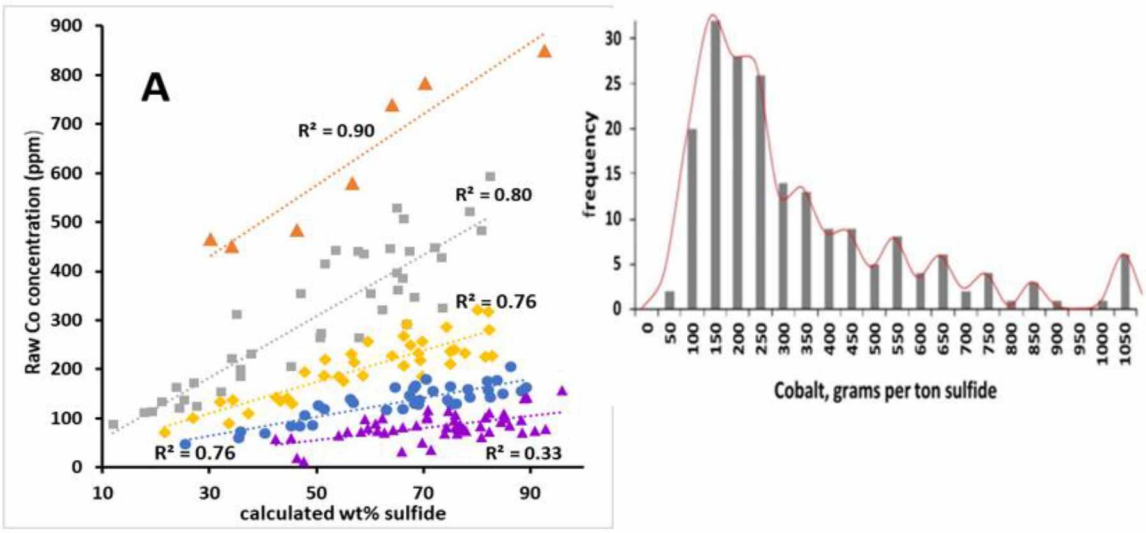

Figure 2.24. Co-sulfide abundance relations. **A.** (left) raw cobalt concentrations (ppm) vs. calculated sulfide mineral %, showing that the data require at least 5 different populations to adequately describe the variations. **B.** (right) Histogram of sulfide-normalized Co concentrations, with red line the calculated cumulative distribution for multiple Gaussian distributions. These data require that pyrite at Kensington averages >0.1% Co to <0.01% Co.

The spatial pattern of Co concentrations in Long section (Fig. 2.23) is simply quite unlike that for any other element presented. There is clearly no relation between Co concentrations and high Au zones, and instead, virtually all the samples from the north third of the long section (and from the north half of zone 41) have low (< 300 gram Co/ton pyrite) average concentrations. The highest Co concentrations are in zone 10P, but high concentrations are also present in zone 10. Both also contain very low concentrations as well (Fig. 2.23). There's no sense of a vertical or horizontal concentration gradient.

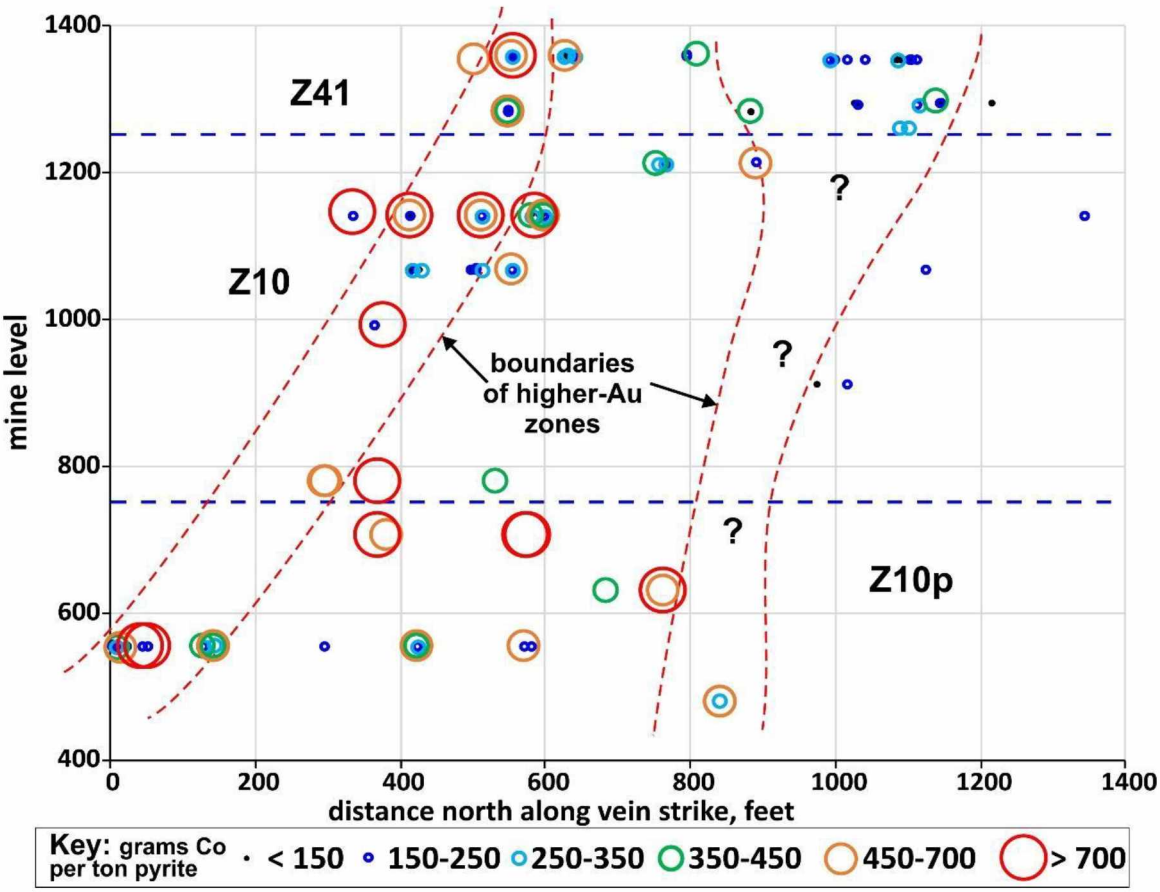

Figure 2.25. Long section, showing distribution of calculated Co concentrations (grams Co/ton pyrite) based on XRF analyses.

2.8 Discussion

By-and-large, there aren't many elemental correlations in the XRF data (Table 2.4). I ascribe this to variably-complex elemental-mineralogical relations. I group these into 5 major categories: (a) elements in only one mineral, with limited variability, (b) elements mostly in 2 minerals, with limited variability, (c) elements present in many minerals, (d) elements present in 1 mineral, but with major compositional variability, and (e) minerals present as inclusions.

2.8.1 As-Sb-Zn-(Ag) Correlations

The only example of group (a) behavior is Sb-As-Zn largely restricted to Sb-rich fahlore. The very strong correlations between Sb, As and Zn (R^2 of 0.79-0.97) suggest that Sb, As, and Zn almost entirely occur in 'tetrahedrite' and that this mineral is of relatively constant composition, despite the fact that it can vary from the As to the Sb-end members. What's

striking about the calculated abundance of Sb-fahlore at Kensington is that it's independent of the rock total Cu content (Fig. 2.17) and if anything, Sb-fahlore is more abundant in relatively Cu-poor rocks. That is, the limiting factor for precipitating Sb-fahlore was the abundance of Sb and As, not Cu.

The 'more complicated' formula for fahlore is $(Cu, Ag)_{10}(Fe,Zn)_2(As,Sb)_4S_{13}$, that is, it contains variable amounts of Fe and Zn. Because Zn has been (rarely) reported as sphalerite at Kensington (Casey, 2000) whereas As- and Sb-bearing minerals (outside of tetrahedrite) haven't, I assume that it's the availability of Sb and As that dictate Sb-fahlore occurrence and abundance. What's striking about the spatial distribution of my fahlore-bearing rocks (Fig. 2.18) is that it's almost entirely restricted to the southern higher-Au zone and immediate vicinity. Only one sample from zone 41 with a trace of calculated fahlore falls outside that region. Further, only one sample from zone 10 contains a trace of calculated fahlore: this mineral is almost entirely restricted to zones 41 and 10P (Fig. 2.18). These various restrictions suggest that veins in the southern part of zone 41 and 10P have received 'extra' Sb-As-Zn. If so, there should be textural evidence for such, at least on the micro-scale.

The lack of correlation between fahlore and Au abundance is obvious: while there's some overlap in the southern 'elevated Au' zone, there's none at all in the northern one (Fig 2.18). If additional Au was deposited with the As-Sb-Zn, it wasn't consistently so.

The correlations between As-Sb-Zn and Ag (R^2 = .39-.64) are more problematic, as they suggest that some Ag is present as solid solution in fahlore. First, the much higher R^2 for Ag-Sb (.64) than Ag-As (.39) is consistent with the fact that Ag^+ (much larger than Cu^+) only appreciably substitutes into tetrahedrite (Sb) and not tennantite (As). Further, a plot of sulfide-normalized Ag concentration vs. calculated wt% fahlore (tetrahedrite + tennantite) shows a strong correlation for the 12 samples with the highest fahlore abundances (Fig. 2.24). There is essentially no correlation for the other samples, as Ag concentrations vary tremendously despite the presence of < 0.05 wt% calculated fahlore. In contrast, Zn displays a much stronger correlation with % fahlore (R^2 = 0.98), and over the entire range of fahlore abundances. Based on the slope of the Zn-fahlore best fit line, the estimated average Zn concentration is about 8%,

which matches the theoretical composition of $Cu_{10}Zn_2(As,Sb)_4S_{13}$. Certainly the fact that most of the data points show no correlation between Ag and % fahlore indicates that multiple Ag phases are present. Only considering the most fahlore-rich samples, the correlation between Ag and % fahlore is good, but poorer than that for Zn, and is really anchored by the single high-fahlore point. Without it the Ag-fahlore correlation drops to $R^2 = 0.6$. Such a correlation could be due to inclusions of an Ag-rich mineral in the fahlore, rather than solid solution. In sum, the moderate correlation between Ag and the Sb-As-Zn group is compatible with Ag present in solid solution in fahlore, but doesn't require such. Additional data (chapter 4) are needed to clarify.

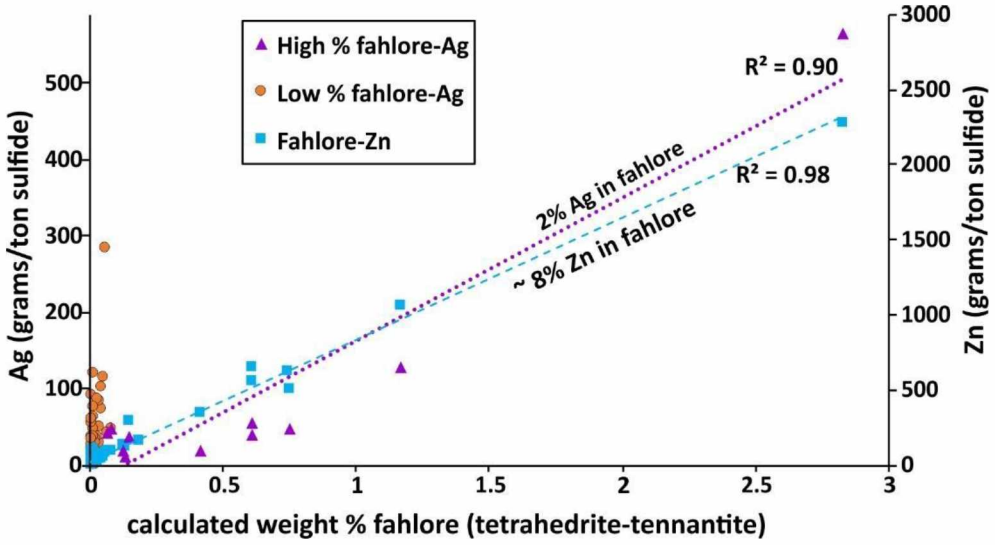

Figure 2.26. Calculated fahlore concentration vs sulfide-normalized Ag (most points) and Zn (blue squares). The 12 most fahlore-rich samples yield a strong correlation with Ag; the remaining data are very poorly correlated.

2.8.2 Au-Te-(Hg,Ag,Pb,Bi)

The second-best correlation ($R^2 = 0.82$) is between Au and Te (Table 2.4). This is impressive because (a) not all Au at Kensington is in the form of Calaverite ($AuTe_2$) and (b) many additional telluride minerals occur. Given that, one might expect a poorer correlation between the two. However, except for a handful of analyses, samples with less than 75% atomic Au/(Au+Hg+Ni+Pb+Bi) (i.e., a major proportion of non-Au tellurides) follow the same Au-Te trend as do samples with higher proportions of gold (Fig. 2.5,2.7). In order for this to be true, samples with higher proportions of non-Au telluride minerals must also contain higher

proportions of native gold. I speculate that much of the Au at Kensington was initially precipitated as $AuTe_2$, and was subsequently partly remobilized in the presence of elements like Hg, Pb, Bi, and Ag, to make gold + non-Au telluride, conserving both initial Au and Te. If this is true, there ought to be some textural evidence for such, at least at the microscopic scale.

Most of the non-Au telluride-associated elements yield poor inter-element correlations (Table 2.4). The exception is Ag-Bi, with R^2 of 0.61. This correlation is somewhat suspicious, as both elements are mostly present at concentrations below detection and the R^2 decreases to 0.36 by simply removing the highest Bi sample. Nevertheless, there is some correlation between the two. Other correlations are much lower, 0.25-0.12. Such poor correlations indicate non-uniform enrichment in these elements. That is, for samples with high concentrations of Hg+Bi+Pb+Ag+Ni relative to Au, at best one or two of these are similarly enriched in any given sample.

However, although individual samples show poor inter-element correlations, there are considerable similarities in 10 m areas where the elements are enriched. I have compiled 10 m areas in the long section where the elements Ag, Bi, Ni, Pb, and Hg are present in anomalous concentrations (Figure 2.25); here elemental overlaps are more obvious. In particular, all but Ni are present in anomalous concentrations in lower S and N zone 10P and all are present in anomalous concentrations in upper south zone 41. I think it not coincidental that fahlore is present in southern zone 10P and 41 in these same areas. Similarly, anomalous concentrations of Ag and Pb exactly overlap in zone 10P where viewed at 10 m areas, not samples *per se*. Furthermore, areas of anomalous Ag, Bi, and Pb almost exactly coincide in zone 41 (Fig. 2.25). This makes sense if elements are inhomogeneously distributed on the heading scale (meters) even if relatively homogeneous on the hand specimen scale. Finally, given the similarities in distribution of fahlore and of Bi, Ag, Pb, Hg, and Ni, I speculate that these components were added more-or-less together, with the latter elements 'spreading out' farther to the north than those required to make fahlore (As and Sb). Although speculative, these suggestions can be tested by examining the detailed mineralogy and textures of samples. I will present such results in Chapter 4.

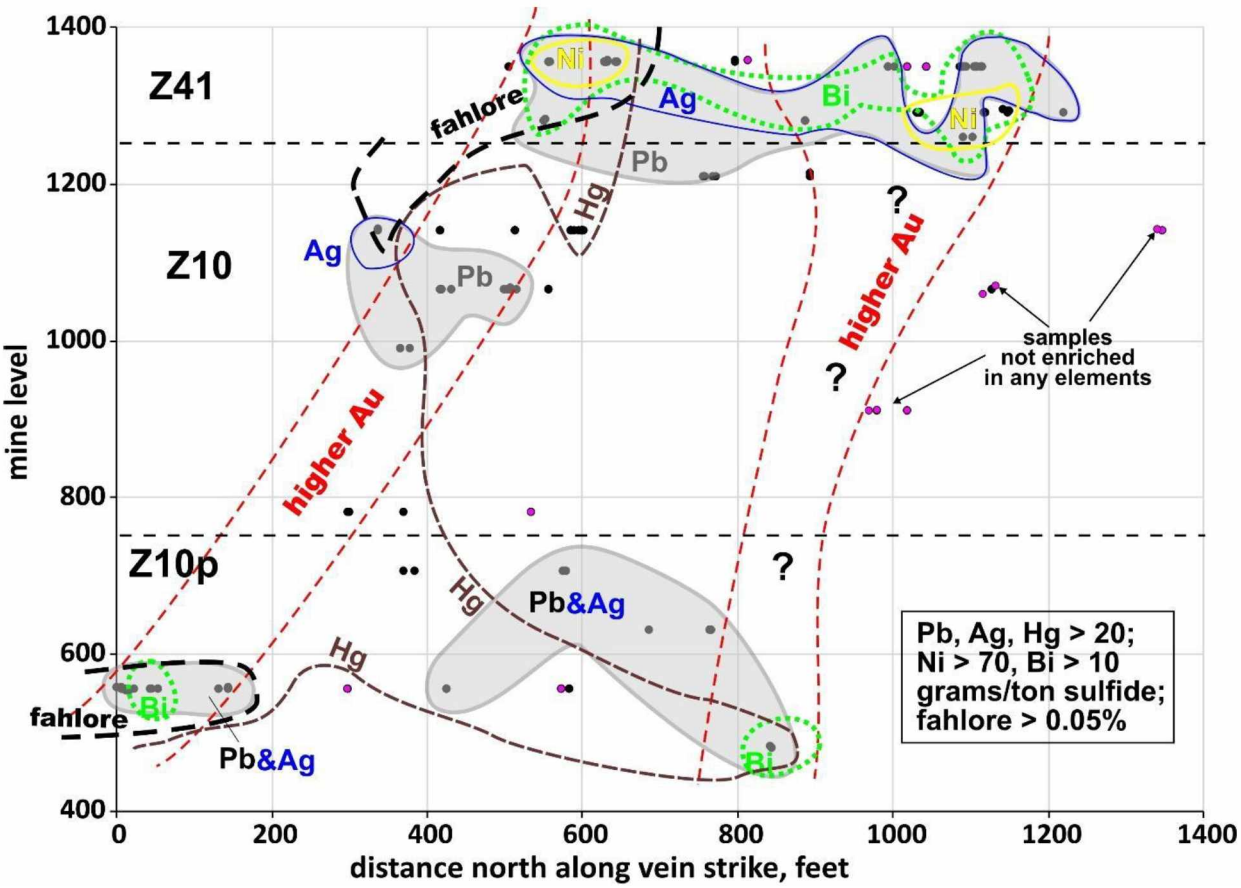

Figure 2.27. Compiled data for anomalous concentrations of elements and fahlore as present in 10 m areas of the Kensington long section. Black dots are sample locations, magenta ones are those for which no elements are present in anomalous concentrations. Boundaries of anomalous metals are color coded: red = Au, grey = Pb (± Ag), blue = Ag, yellow = Ni, green = Bi, brown = Hg. The thick black dashed line outlines the areas where sulfide-normalized fahlore concentrations are > 0.05%.

2.8.3 Co, Ni, Mo, Se: Pyrite-Associated Elements

All four of these elements (and additional ones) are known to occur in solid solution in pyrite (e.g., Abraitis et al., 2004). In addition, Keith et al. (2018) focused specifically on pyrite from gold deposits of several types. Their data for 'orogenic' deposits (Table 2.5) which are the closest analogue to deposits of the Juneau gold belt, indicates that very high concentrations of these elements can be present. Such values are compatible with inferred concentrations based on the XRF data (e.g., Figs. 2.10, 2.19, 2.20, 2.22). This doesn't prove that these elements are largely present as solid solution in pyrite, but certainly indicates such is possible. I include Cu, even though I have no way to assess from the XRF data whether Kensington pyrite contains appreciable Cu, to show that it is also possible. That such wide variations are apparently

present suggests that either pyrite trace element compositions uniformly change across the mine or else that there are different generations of pyrite—otherwise identical-looking, but with different trace element contents—variably present in different parts of the mine.

I find it distressing that none of these elements yield significant correlations with each other at Kensington (Table 2.4), but recognize that they each show somewhat different patterns. Se substitutes for S, whereas the others substitute for Fe, and consequently there's no reason why Se enrichments should correlate with the others. Inferred Ni concentrations in most Kensington pyrites are quite uniform (Fig. 2.10), approximately 30-45 grams/ton sulfide; higher concentrations reflect some additional Ni present as $NiSe_2$ inclusions in pyrite. Co is much more complicated, as the XRF data require 5-9 different populations, with average Co of 100 to > 1000 gram/ton sulfide. It's conceivable that the Ni concentrations are actually as complex, but the concentrations are too low to accurately tease much from the data.

Table 2.5. Concentrations of trace elements in pyrite of orogenic gold deposits*

	Co	Ni	Cu	Se	Mo
minimum (ppm)	<1	<1	<1	2	<1
maximum (wt %)	6.4	2.6	4.7	0.02	0.01
*Data from Keith et al. (2018)					

The apparent concentrations of Mo in pyrite resemble a combination of the Co and Ni patterns. Most (approximately 2/3) Kensington pyrites contain an average of about 10 grams/ton sulfide Mo, with two additional populations averaging about 40 and 100 grams/ton sulfide (Fig. 2.19). This range is proportionally as great (factor of 10) as that for Co. Higher apparent concentrations are associated with visible MoS_2 (at least in some cases, and implicitly the rest) similar to the Ni pattern. Very high Mo concentrations are rare (1000-4000 grams/ton sulfide) and are definitely associated with MoS_2. These high concentrations play havoc with attempts to correlate concentrations, but even with those removed, Mo simply does not appreciably correlate with either Ni or Co.

The most troublesome aspect of the proposed Mo substitution into Kensington pyrite is the problem of charge balance. Abraitis et al. (2004) suggest that Mo substitutes into pyrite as Mo^{3+} (and not Mo^{4+}, as in molybdenite), which makes both the size and charge of the Mo closer to that of Fe^{2+}, but doesn't eliminate the problem. I propose that a coupled substitution of $Cu^{+} + Mo^{3+} = Fe^{2+} + Fe^{3+}$ could account for the charge problem. Of course, given the enormous amount of chalcopyrite present at Kensington, it would be impossible to determine if such is feasible based on XRF data.

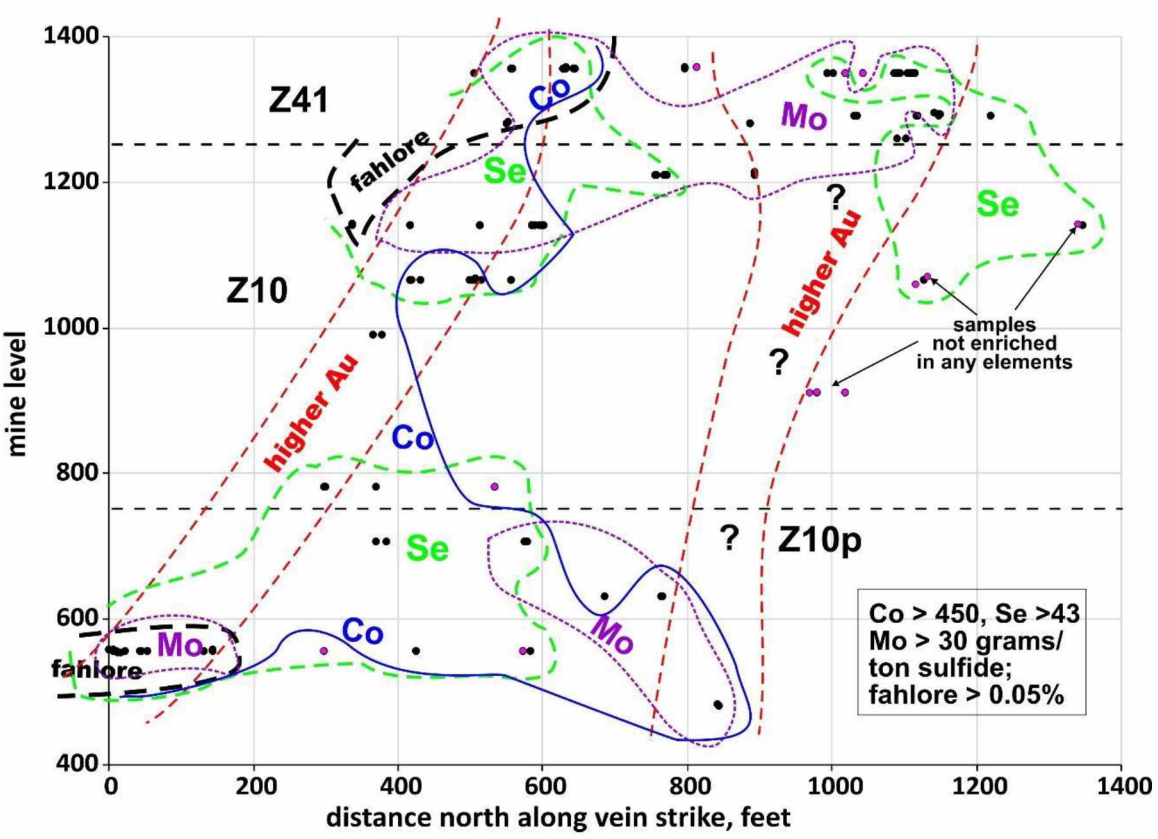

Figure 2.28. Compiled data for anomalous concentrations of elements and fahlore as present in 10 m areas of the Kensington long section. Black dots are sample locations, magenta ones are those for which no elements are present in anomalous concentrations. Boundaries of anomalous metals are color-coded: red = Au, blue = Co, green = Se, purple = Mo. The thick black dashed line outlines the areas where sulfide-normalized fahlore concentrations are > 0.05%.

The compiled long section with anomalous Co, Se, Mo, and fahlore (Fig. 2.26) fails to show much in common, except that all are anomalous in areas with appreciable fahlore (the

south end of the long section). Oddly, the areas of anomalous Co resemble that for Hg (Fig. 2.25): most of zone 10P is anomalous as are only the southernmost parts of zones 41 and 10. Similarly, the pattern of Mo anomalies is similar to those of Ag and Pb, with high values only in the far southern and northern parts of zone 10P but extensive high values across zone 41. If Co and Mo are (for the most part) truly dissolved in pyrite, then there may be different pyrite 'generations'—identifiable by their trace element compositions—that correlate with higher HgTe, PbTe, and AgTe inclusion abundances.

2.9 Summary and Conclusions

I have shown that the concentrations of Au and of other trace elements in sulfides at Kensington vary considerably, as depicted in long section. These differences—especially in trace elements—had not been previously detected because most of these elements are at very low concentrations in typical rocks. They only become apparent if employing sulfide-rich samples and if analyses are normalized to 100% sulfide. I have found two steeply-plunging 'pipes' of higher Au (grams/ton sulfide). The calculated abundance of fahlore (tetrahedrite-tennantite solid solution) based on very strong As-Sb-Zn correlations, is coincident with the southern higher-Au 'pipe' in Zones 41 and 10P, but not in zone 10. The fact that many trace elements are present in anomalous concentrations in these same areas suggests that the fahlore was 'added' to the pre-existing veins, and accompanied by other identifiable minerals. Anomalous concentrations of Co (for sure) and Mo (possibly) as solid solution in pyrite suggest that there may be multiple generations of pyrite with different mineral inclusion abundances. I intend to test some of these ideas by examining more thoroughly the specific characteristics of veins and vein types—and their relationship to metal patterns—and by examining selected samples via reflected light microscopy and microprobe analyses to look for patterns in how inclusion minerals occur in pyrite. These topics will be addressed in the next several chapters.

3 Macroscale Ore Characteristics and Their Relations to Metal Abundances

The purpose of this chapter is to define macroscale characteristics and then examine the various metal concentrations and patterns introduced in Chapter 2 in light of these characteristics. In particular I attempt to find any aspects of the samples at the meter to centimeter scale that can help explain features like the 'higher gold' zones and the asymmetry to many metal and fahlore abundances (higher to the south). In this chapter I define 3 main categories of characteristics: vein type, sulfide texture, and primary sulfide type. These categories are largely based on macroscale observations of the mine ribs, from fieldwork summers 2011 to 2013, and some subsequent study of sample hand specimens.

3.1 Primary Sulfide Types

Samples fall into one of three sulfide types: 1) pyrite-rich, 2) chalcopyrite-rich (Cu-rich), and 3) brecciated. Pyrite-rich and Cu-rich samples are determined by their Cu concentrations (measured via XRF) while brecciated is both a texture and grain size. (Note that "brecciated" is both a vein type and a sulfide type.) Pyrite-rich samples are the most common and comprise 91% of the total samples. Twelve samples (6%) are chalcopyrite-rich and five samples (3%) are brecciated.

3.1.1 Pyrite-rich Samples

Pyrite-rich samples contain at least 20 wt% total sulfide with no more than 2 wt% Cu (normalized to 100% sulfide). Pyrite-rich samples were collected from throughout the mine and represent the main source of ore at Kensington. The vast majority of gold and calaverite grains occur as inclusions in pyrite grains or immediately adjacent to pyrite grains.

3.1.2 Cu-Rich Samples

The predominant Cu sulfide mineral at Kensington is chalcopyrite, both calculated from XRF concentrations (Chapter 2) and seen in reflected light (Chapter 4). All polished sections contain chalcopyrite, usually as the second most abundant sulfide. I previously defined (section 2.7.1) Cu-rich as containing > 3% (sulfide-normalized) Cu, based on a break in the cumulative Cu abundance plot (Fig. 2.14).

Copper contents of samples can vary tremendously over short distances, e.g., as seen in the 1355-210 heading, zone 41 (Fig. 3.1). Cu-rich samples can include both massive sulfide and sulfide clots (Table 3.1; see section 3.3 for textural definitions); sample 16 is a very Cu-poor pyrite clot about 40 cm from the nearest Cu-rich sample. (See ahead for descriptions of different sulfide textures.) Relative % chalcopyrite changes from nearly 100% to 0.03% (sample 16) to 26%, over a distance of about 1 meter.

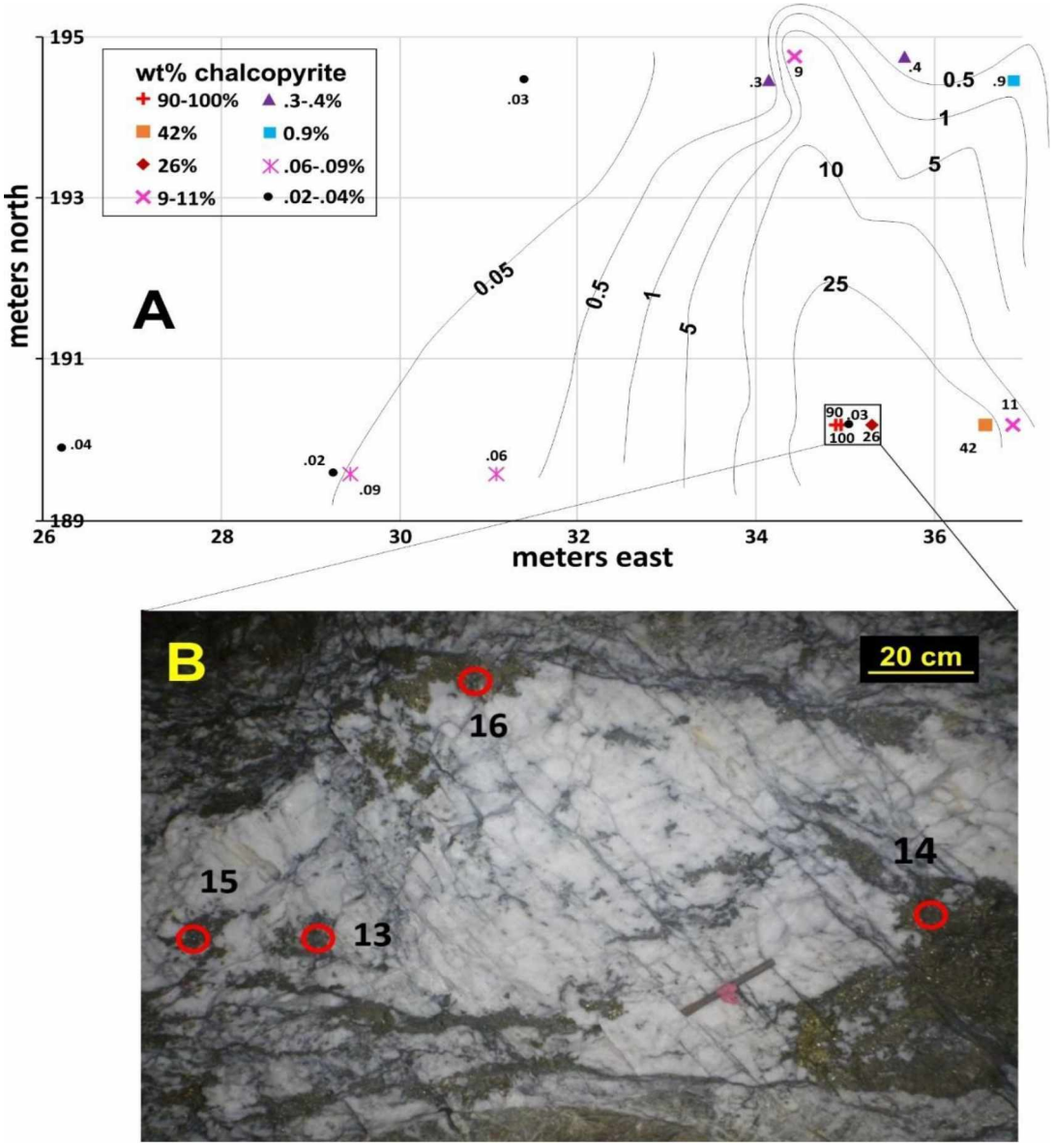

Figure 3.1. Map and rib views of the 1355-210 heading (zone 41) A) Map view, showing wt % chalcopyrite for individual samples and generalized contours. Note that higher-Cu samples are restricted to the E end of the drift. The location of the rib image (B) is indicated by the black box. B) Image of the south rib, facing N. The 4 samples shown are identified by abbreviated sample numbers (e.g., 16 = 1355-210-16).

As they are on opposite sides of a sub-horizontal discreet vein, one could argue that the Cu-rich and Cu-poor sulfide clots in the large vein (Fig. 3.1b) formed at different times, under different

conditions, as an explanation to the widely varying Cu abundances. Note, however, that one can broadly contour % chalcopyrite in that heading (Fig. 3.1a), if one is willing to average the concentrations of nearby samples and ignore the extreme variations within a meter.

Table 3.1 gives data for the 4 samples shown on Fig. 3.1b. It illustrates the typical differences between Cu-rich and pyrite-rich samples: the latter contain much higher Au and Co. These differences are caused by solid solution of Co predominantly in pyrite (not chalcopyrite) and a much higher inclusion density (Chapter 4) in pyrite than in chalcopyrite.

Table 3.1. Data for samples on figure 3.2b (all but % sulfides are sulfide-normalized)

Sample	Type	Cu wt%	ppm Au	ppm Co	%py	%cp	%sulfides*
1355-210-13	clot	34.7	157	11	0	100	54
1355-210-14	massive	9.0	114	81	74	26	87
1355-210-15	clot	29.9	234	--	14	86	16
1355-210-16	clot	0.02	524	527	>99.5	0.03	66

On a much smaller scale, sample 480Access -1 (zone 10P) and was sub-sampled based on apparent variations in chalcopyrite concentrations. Subsample MG is the finer grained pyrite-rich material circled in blue, while subsample CG is the coarser chalcopyrite-rich material circled in red (Fig. 3.2). CG contains nearly 3 times as much sulfide-normalized chalcopyrite as subsample MG; however MG contains nearly 5 times as much Au (table 3.2). MG is also significantly more enriched in non-Au telluride elements. Table 3.2 also illustrates the pitfalls of using sulfide-normalized data: raw concentrations have been enhanced by a factor of 5 (MG) -7.5 (CG), which enhances the uncertainties in concentrations by the same amounts. I doubt the validity of either and have rejected analyses like 'cg' that yielded less than 20% calculated sulfide.

Figure 3.2. Close-up photo of a sample from the 480Access ramp, showing two different sulfide mineral abundances seen in one hand sample.

Table 3.2. Sulfide-normalized metal concentrations for 480access-1 subsamples

Sample	%Cu	Ag	Te	Bi	Au	Mo	Zn	Sb	Ni	Hg	Co	Se	%cp	%sulf*
MG	0.81	1700	3000	455	1910	36	80	--	33	84	327	40	2.3	22
CG	2.25	478	680	--	425	--	82	60	--	--	82	67	6.5	**13**

*all but % sulfide are sulfide normalized values; units are grams/ton sulfide unless indicated otherwise;
-- = below detection limit

The subsamples from 480Access-1 represent exceptional samples. I normally concentrated sulfide from original samples much larger than either mg or cg. However, they do illustrate the inhomogeneous distribution of chalcopyrite that can be seen on the centimeter scale.

3.1.3 Brecciated Samples

Brecciated samples are defined by texture and grain size rather than by composition and are restricted to zone 41. I define them as quartz rich sections that have been mechanically fractured; only the brecciated section is considered a 'brecciated sample' (Fig. 3.3).

Very fine grained dark gray material is usually located along the margins of the fractured sections as well as between and within fractures (Fig. 3.2). XRD and XRF analysis indicate that this very fine grained material contains up to 17% chlorite, 35% sericite and 50% pyrite. I have separated these from 'normal' pyrite-rich samples, based both on textures and on their very contrasting metal abundances (see ahead).

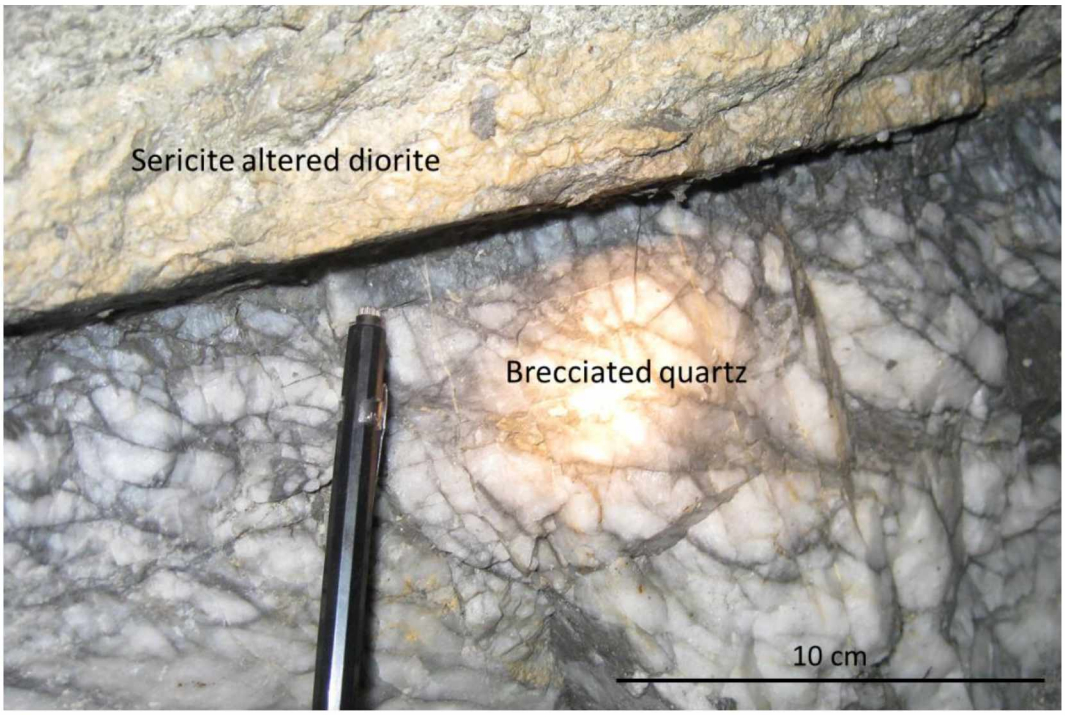

Figure 3.3. A close up image of the upper margin of a brecciated section of a discrete vein from the 1365 level (zone 41).

Brecciated veins represent < 3% of my XRF samples. I attempted to collect samples with high sulfide abundances, but of my 14 brecciated samples, only half contained enough sulfide (≥ 20 wt %) to be used in XRF comparisons. I also found it impossible to produce polished sections from the fine grained material, as it readily plucked out during polishing.

3.1.4 Sulfide Type Summary

Pyrite-rich samples are the most common by far (> 91%), followed by chalcopyrite-rich (6%), and then brecciated samples (< 3%). Chalcopyrite-rich samples are found in all zones; however half are located in zone 41 with ¼ in each of zones 10 and 10P (Fig. 3.4). All of the Cu-rich samples in zone 10 are located at the 1065 level and the Cu-rich samples in zone 10P are restricted to the 555 and 480 levels. Brecciated samples are restricted to the highest sampled levels of zone 41 and are within or immediately adjacent to the higher-Au zones.

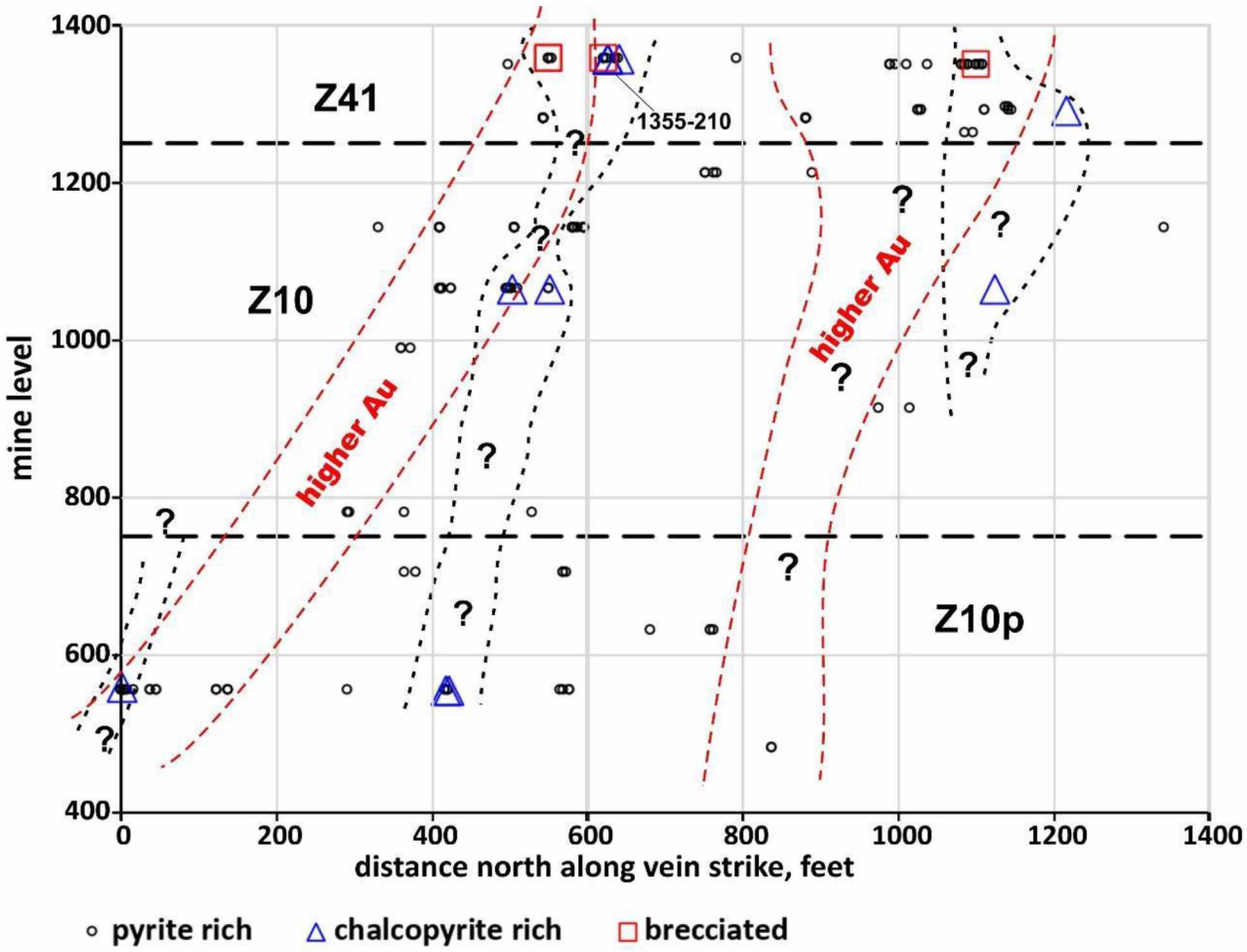

Figure 3.4. Locations of pyrite-rich, Cu-rich, and brecciated sample on the Kensington long section. The location of the 1355-210 heading (Fig. 3.1) is also shown. Red dashed lines show the locations of the higher-Au zones (from Fig. 2.8) and black short dashes show the elevated Cu zones (from Fig. 2.15).

3.2 Controls on Elemental Concentrations by Sulfide Type

3.2.1 Tellurium-Associated Elements

Figure 3.5 shows the sulfide-normalized concentrations and geometric means (geomeans) for the Te-associated elements Au, Ag, Bi, Hg, and Pb sorted by sulfide type. (Concentrations below detection were not incorporated into the geomean calculations.) Brecciated samples have the highest geomean concentrations for all the elements shown. Cu-rich samples have only slightly lower geomean Au concentrations than pyrite-rich samples (192 vs. 212 grams Au per ton sulfide); however they do not have as large a range (Fig. 3.5). In fact they have a remarkably restricted range (82 – 333 grams per ton sulfide with 1 higher value from zone 10P) compared to pyrite-rich samples (below detection to nearly 2000 grams/ton sulfide). The restricted range in all concentrations for both Cu-rich and brecciated samples is probably related to the small sample size, especially for the brecciated samples.

For all but Hg, the geomean elemental concentrations in pyrite-rich and Cu-rich samples are practically identical (Fig. 3.5), particularly Ag and Bi. The geomeans for Pb are slightly higher for Cu-rich samples; the maximum concentration of Hg is much higher in pyrite-rich samples. The maximum Hg in Cu-rich samples is 43 grams per ton sulfide; 15 pyrite-rich samples have higher Hg concentrations, with a maximum of nearly 0.4% (sulfide-normalized) Hg. The large number of low Hg (but above detection limits) concentrations in pyrite-rich samples makes the Hg geomean for pyrite-rich samples only slightly higher than that for Cu-rich samples. This contrasting behavior of Hg and Pb is puzzling.

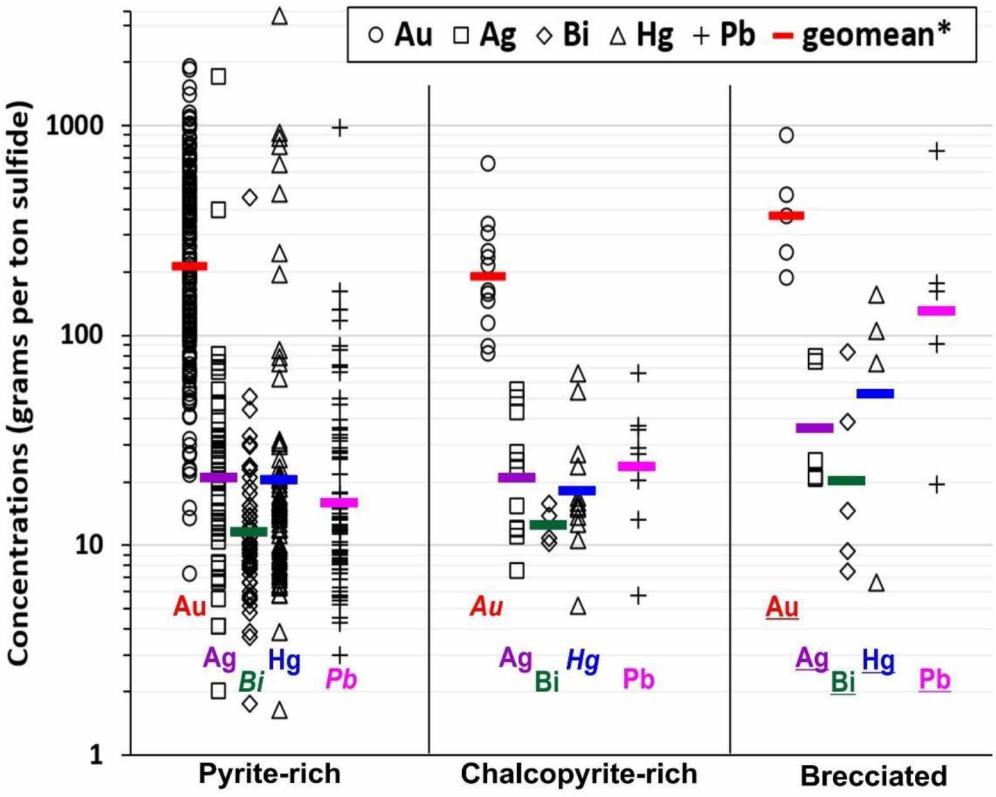

Figure 3.5. Concentration ranges of telluride forming elements by sample type. *geomean = geometric mean, concentrations below detection limits are excluded. Nite2 is only in pyrite-rich samples, consequently, Ni concentrations are not shown. Underlined = highest geomean concentration, italics = lowest geomean. Note that the brecciated samples have higher concentrations of all these elements.

Figure 3.6 shows no relationship between sulfide normalized gold and relative percent chalcopyrite, particularly for samples from zone 41. There are insufficient samples from zones 10 and 10P (3 from each) to draw definitive conclusions, but these also appear to show no correlation between gold and chalcopyrite abundance.

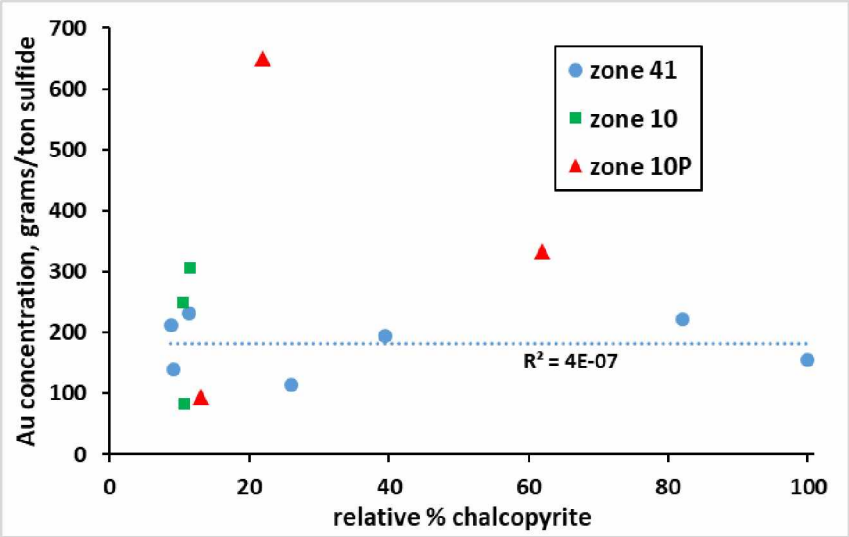

Figure 3.6. Au concentrations of chalcopyrite-rich samples vs. relative % chalcopyrite, by zone.

Brecciated samples contain higher geomean concentrations of all the telluride-related elements shown. However, except for Bi, pyrite-rich samples have higher maximum concentrations. The higher geomean values for brecciated samples might be related to the small sample size, but they might also be real.

3.2.1 Non-Tellurium-Associated Elements

Figure 3.7 shows the sulfide-normalized concentrations and geometric means for Mo, Co, Se, and fahlore sorted by sulfide type. (Concentrations below detection were not incorporated into the mean calculations.) For Mo, both geomean and maximum concentrations are in the order brecciated >> pyrite-rich > Cu-rich. The former two have some concentrations sufficiently high as to indicate MoS_2. The very low maximum and geomean concentrations for Cu-rich samples indicate both Mo is not significantly present in solid solution and not present as MoS_2 inclusions. Similarly, the low geomean Co concentrations for Cu-rich samples indicates that Co is preferentially incorporated into pyrite (rather than chalcopyrite). In contrast, the slightly higher geomean concentration of Se for Cu-rich samples suggests that Se may have a preference for chalcopyrite over pyrite. Small sample numbers are likely responsible for the lowest geomean concentrations of fahlore in pyrite-rich samples, despite 7 of the 8 highest fahlore concentrations in this sulfide type.

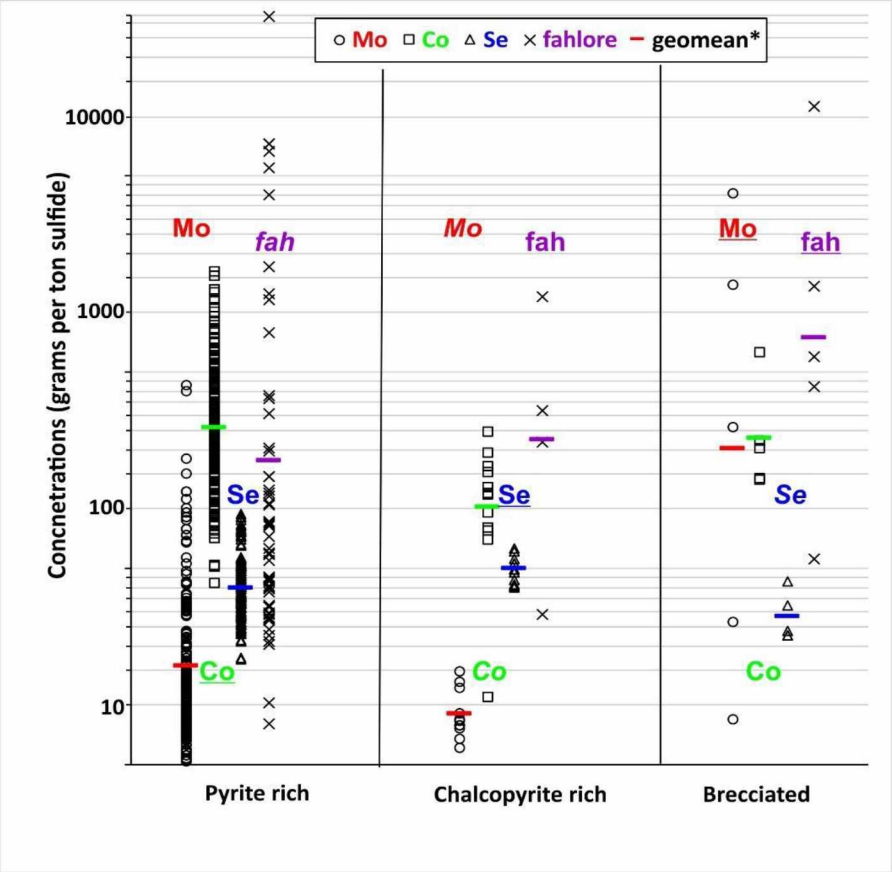

Figure 3.7. Concentration ranges of fahlore and elements not associated with Te by sulfide type. *Geomean = geometric mean, concentrations below detection limits are excluded. Underlined = highest geomean concentration, italics = lowest geomean. Geomeans and labels are color coded.

3.3 Vein Types

The ore at Kensington is vein hosted and extent of veining is a primary indicator of grade (Au concentration). Two primary vein types occur: discrete and network. Both are structurally controlled by shear zones and network stringers commonly splay from the larger discrete veins. I define three main vein types: 1) discrete, 2) network, and 3) brecciated. These vein types are defined and their relations to elemental abundances are described in the following sections

3.3.1 Discrete Veins

Discrete veins are continuous for distances of > 10 meters and are 0.5 to >2m wide. They are present in all zones. Prominent discrete veins are located in zones 41 and 10P. Zone 41 contains the largest discrete veins, some more than 2 m wide. Zone 10P discrete veins are slightly narrower, 0.5 to 1m wide. Zone 10 discrete veins are generally accompanied by a dense series of network veins (e.g., Fig.

3.8). Discrete veins commonly display sigmoidal geometries and commonly have shallow dips; in contrast, network veins are both west- and east- dipping.

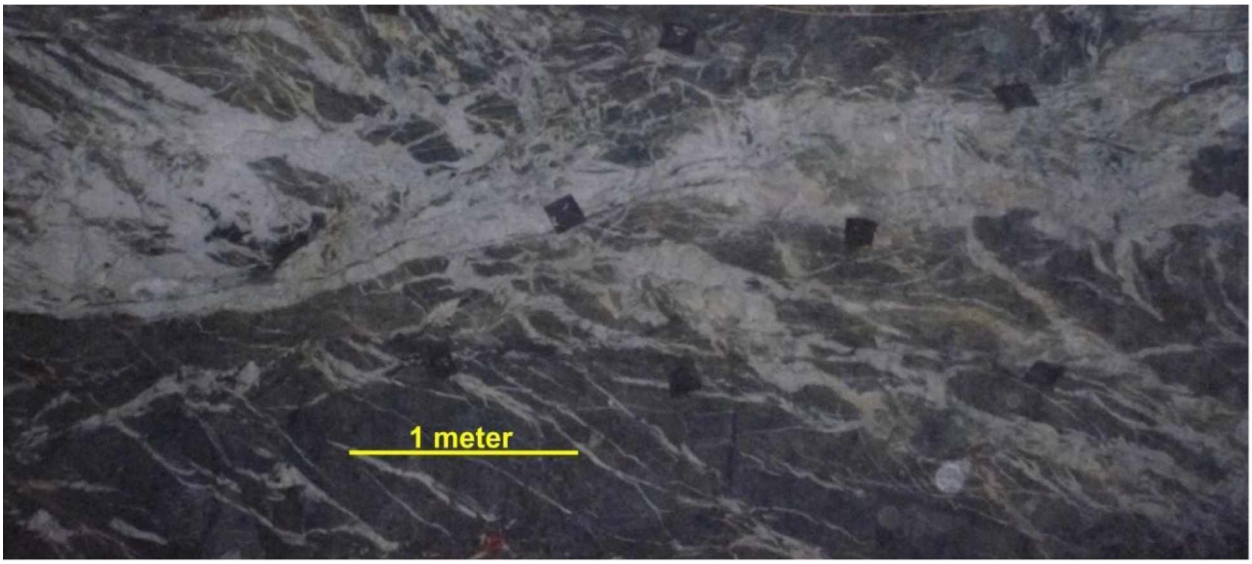

Figure 3.8. Underground image of mine rib showing a discrete vein with associated network veins.

In addition to sulfides, discrete veins contain quartz > calcite ± ankerite ± chlorite ± fluorite ± scheelite. Discrete veins commonly contain clasts of altered diorite. Discrete veins can be vuggy, but this texture is uncommon (and may be due to loss of carbonate mineral from weathering).

3.3.2 Network Veins

Network veins are the most common vein type observed in all zones. Generally speaking, denser zones of network veins generally contain higher Au grades than do low-density zones. Network veins are much narrower (<1 cm -50 cm) than discrete veins. Network veins can be shallow or steeply-dipping and can dip in a variety of directions (e.g., Fig. 3.9). They commonly cut each other and can form *en echelon* structures. Network veins contain the same minerals as discrete veins, except that they lack fluorite.

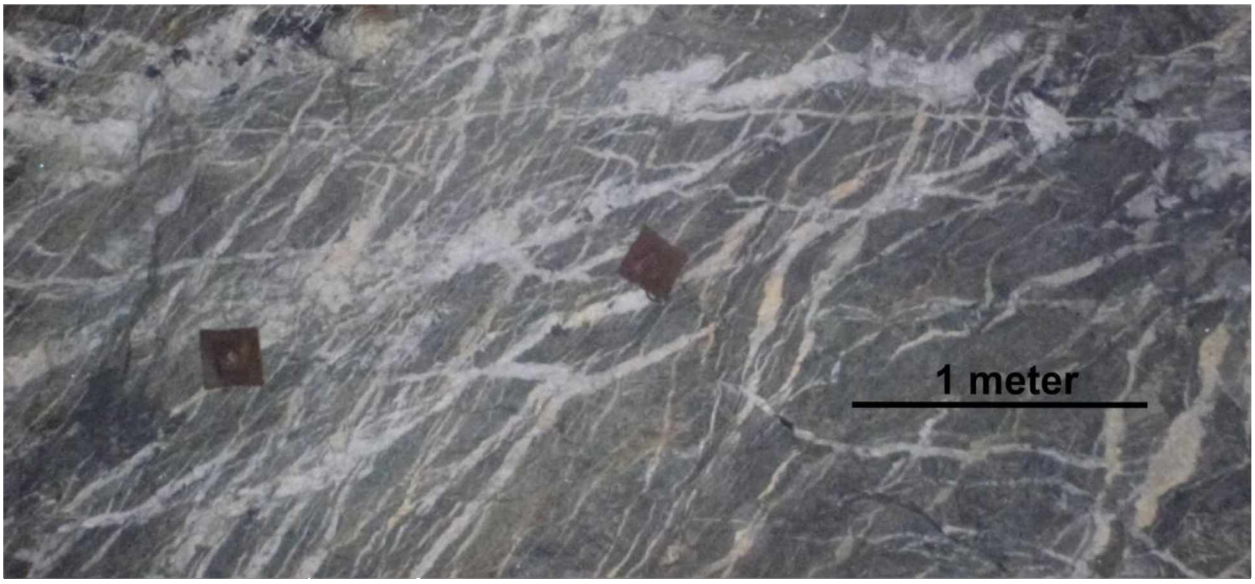

Figure 3.9 Underground image of network veins from zone 10.

3.3.3 Brecciated Veins

I have previously defined them as quartz rich sections that have been mechanically fractured; only the brecciated section is considered a 'brecciated vein' (Fig. 3.2). Brecciated sections occur as bands parallel to strike within discrete veins. The brecciated sections have formed at the top, bottom, and (or) middle of the hosting veins, usually accompanied by clots and/or bands of undeformed pyrite within the same vein. Several Cu-rich samples were taken from undeformed clots of sulfide near brecciated sections (e.g., Fig. 3.10). Although texturally fascinating, I was only able to secure a small number of suitable samples of these for analysis.

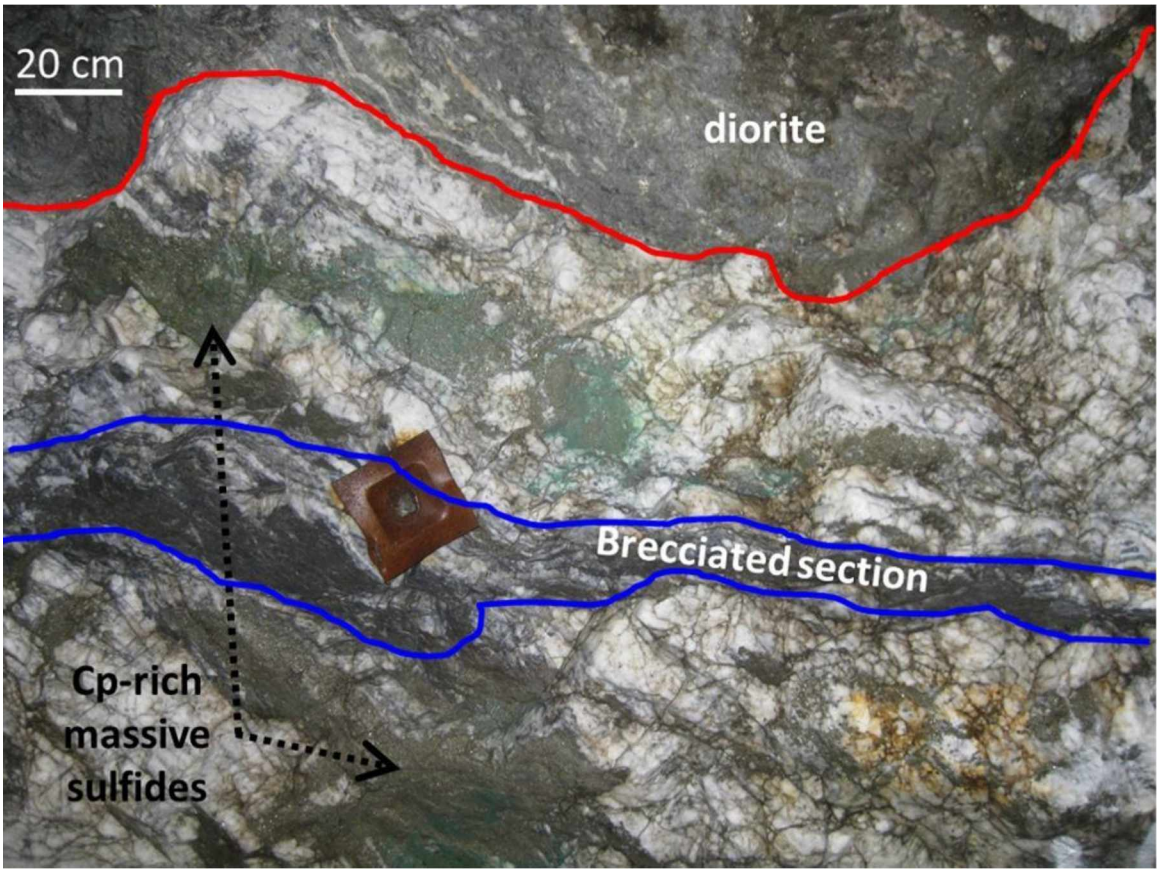

Figure 3.10. Image of a discrete vein from the 1260S heading, the lower section of zone 41, containing a brecciated section. This image shows a brecciated, Mo-rich section of a discrete vein with chalcopyrite-rich massive sulfides above and below the brecciated section.

3.3.4 Massive Pyrite Bodies

I recognized a new sulfide type in 2011: massive pyrite with almost no quartz. Such massive pyrite bodies (MPBs) are within the Kensington ore system but do not form along or near prominent shear or vein zones. They simply occur as pyrite masses hosted by diorite (e.g., Fig. 3.11). The origins, characteristics, and tonnages of the MPBs are not known, but they appear to be uncommon, as I only observed MPBs in the 1140 level. Since I have only four MPB samples (KEN-01, 02, 08, and 1140-206-7) and only two contained > 20% sulfides, they have been grouped with the pyrite-rich sample category (sections 3.1-3.2), and have largely been excluded for the vein type comparisons.

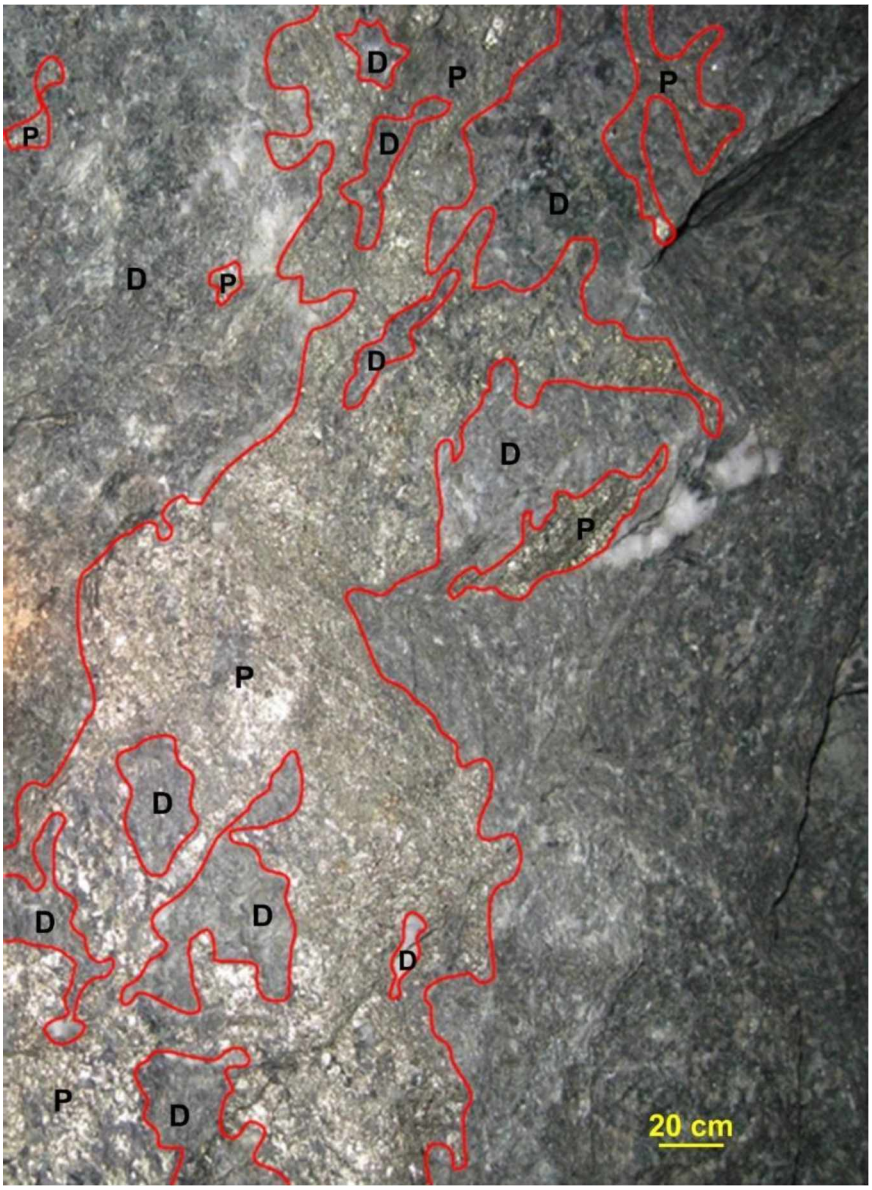

Figure 3.11. Image from the 1140 level in zone 10, showing massive pyrite (P) bodies (MPBs) in altered diorite (D). Massive pyrite areas are amorphous blobs outlined in red, with no associated veining.

3.3.5 Vein Type Summary

Table 3.3 summarizes my macroscale observations of ore types. Network and discrete veins are located throughout the mine and in all zones. Brecciated veins are restricted to the highest elevations in zone 41. Known MPBs are restricted to the 1140 elevation in zone 10.

Table 3.3. Summary characteristics of Kensington vein types

Ore Type		Notes	Width (m)	Orientation	Locations		
					Z41	Z10	Z10P
massive pyrite bodies		no veining	.001 – 0.2	NA		X	
veins	discrete	largest in Z41	0.5 - >2	multiple	X	X	X
	network	most common	0.01 - 0.5	multiple	X	X	X
	brecciated	always w discrete veins	<0.2	sub-horizontal	X		

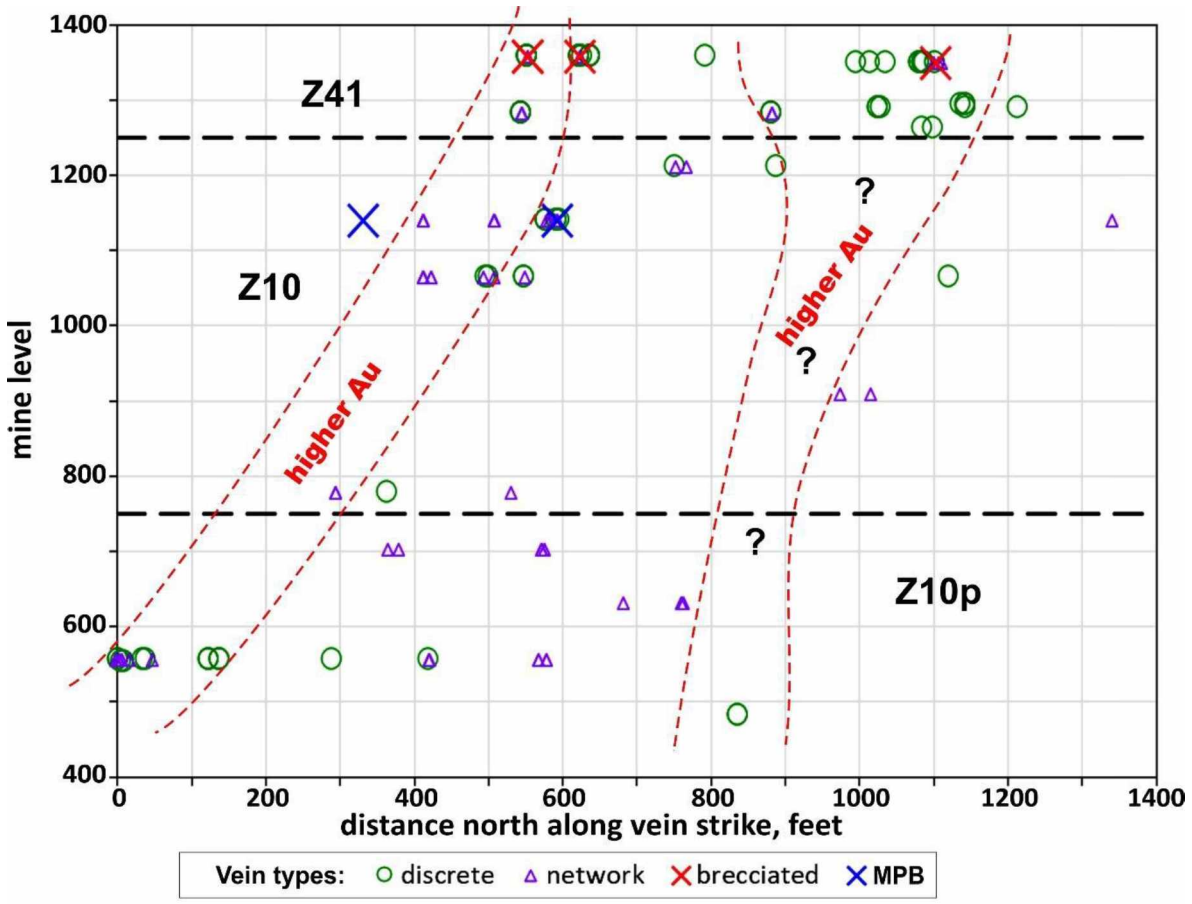

Figure 3.12. Long section showing locations of different vein types which I sampled combined with the zones of higher Au (red dashed, from Fig. 2.8) and of higher Cu (black short dash, from Fig. 2.15), and significant fahlore (thick black dashed lines, from Figure 2.27). The relative abundances of discrete and network veins may not be representative of the deposit. MPB = massive pyrite body.

Figure 3.12 shows the distribution of ore types on the long section, combined with the zones of higher Au and Cu and the zones of significant fahlore. A few patterns emerge. Fahlore is restricted to the south end and to samples from discrete veins (or massive pyrite bodies). The zones of higher gold, however, don't include the MPBs but include areas with the other vein types and combinations of them.

The southern two Cu-enriched 'pipes' are restricted to sites where both network and discrete veins are present. Finally, discreet veins are much more common in zone 41 than the other zones.

3.3.6 Vein Types and Elemental Associations

Figure 3.13 shows ranges and geomean concentrations for the Te-associated elements, sorted by vein type. I have excluded the massive pyrite bodies due to having only 2 samples. Brecciated veins again have the highest geomean concentrations, again possibly related to the small number of samples. Discrete veins have by far the highest concentrations of Hg (Fig. 3.13) and the second-highest geomean for Hg, as well as for Au. In contrast, the Ag and Bi distributions and geomeans for discrete and network veins are practically identical. In other words, discrete veins appear to host sulfides with concentrations equal to or higher than those of the network veins.

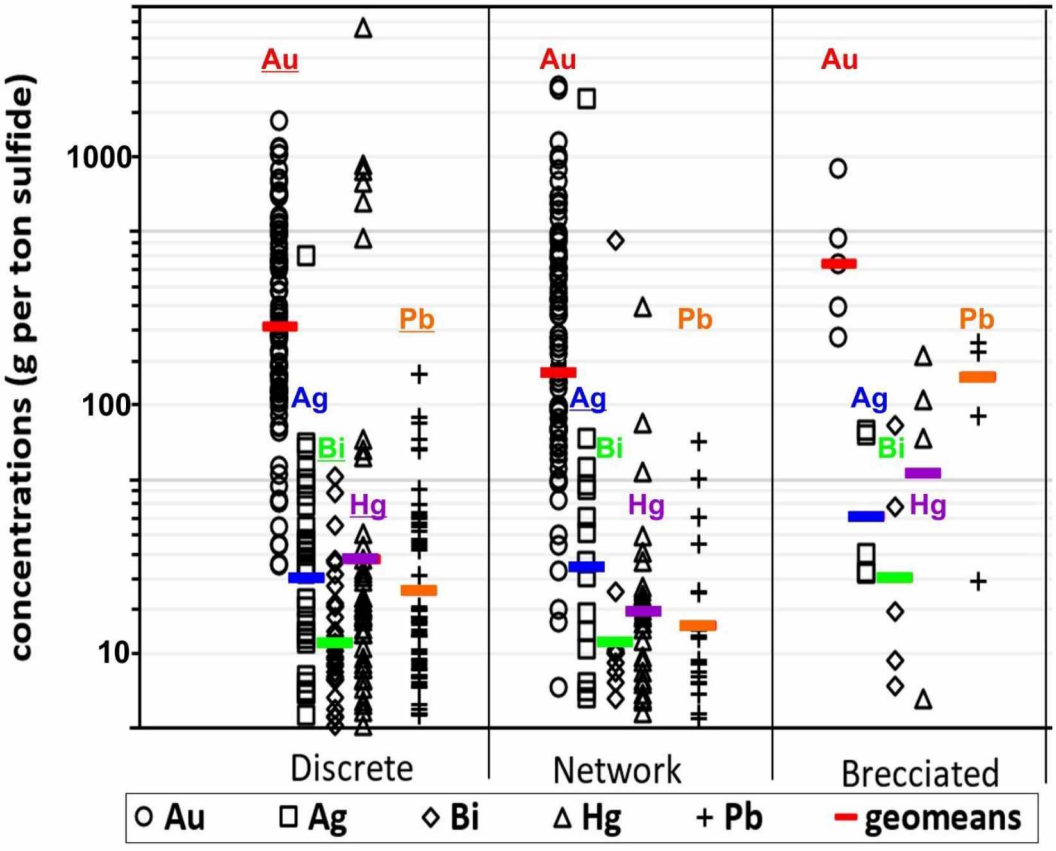

Figure 3.13. Concentration ranges of telluride forming elements by vein type. Samples below detection limits are excluded. Element labels are color-coded for easier comparison. Brecciated samples have the highest geomean concentrations; elements underlined have the second highest geomeans.

Table 3.4 gives geomean concentrations for non-Te-associated elements sorted by the various vein types. I have included data from massive pyrite bodies for comparison. The breccia veins have enormously higher Mo concentrations, reflected in the geomean > 10 times higher than the others. Discrete and breccia veins contain similar (and high) geomean Cu concentrations, nearly 4 times those of the network veins. Ni, Co, and Se geomean concentrations are very similar, perhaps reflecting approximately equal relative abundances of pyrite in each. In terms of raw abundances, the differences are also striking, with much higher chalcopyrite and fahlore geomean concentrations in the discreet and network veins. This is emphasized by Figure 3.14, which shows sulfide-normalized fahlore abundances for samples from the various vein types. Dozens of samples from discrete veins contain appreciable (> .01%) fahlore; none of the samples from network veins do. Although the number of brecciated veins with calculated fahlore is small, most contain appreciable amounts. Oddly, one of the two samples from massive pyrite bodies also contains a small amount of fahlore.

Finally, the relatively high geomean pyrite concentrations for all show that I was generally successful in generating sulfide-rich samples. The massive pyrite body samples contained the greatest amounts of silicates, as I was unable to completely separate (by hand) pyrite from altered diorite in these samples.

Table 3.4. Geometric mean data for non-Te associated elements and calculated minerals by vein type

		grams/ton sulfide						calculated wt% in original sample*						
	n	Cu	Mo	Ni	Co	Se		Sil	qtz	calc	py	cp	fah	tot
Discrete	**81**	**751**	**16**	**32**	**211**	**39**		2	**27**	**4**	**65**	**0.11**	**0.07**	**98**
network	**81**	238	**15**	**29**	**275**	**43**		**6**	**33**	**8**	**53**	**0.04**	0.003	**100**
breccia	**5**	**811**	**201**	**37**	**225**	**28**		**6**	**32**	1	**59**	**0.05**	**0.05**	**99**
MPB#	**2**	**318**	6	**32**	144	**39**		**20**	**20**	**6**	**55**	**0.05**	**0.01**	**101**

Notes: elements/minerals underlined if especially high, non-bold if especially low; mineral abbreviations: Sil = silicates (calculated chlorite + muscovite + albite), qtz = quartz, calc = calcite, py = pyrite, cp = chalcopyrite, fah = fahlore (tetrahedrite-tennantite solid solution), tot = calculated mineral total. n = number of samples used in the geomean.

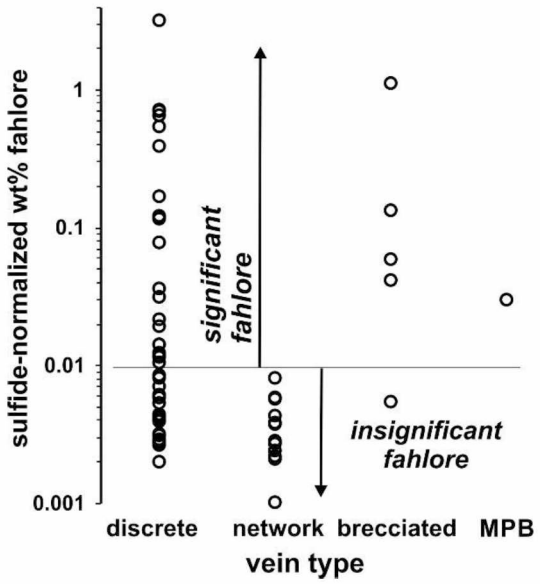

Figure 3.14. Sulfide-normalized fahlore abundances (wt %) vs. vein type for Kensington samples.

3.4 Ore-Associated Sulfide Textures

Sulfides (pyrite and chalcopyrite) primarily occur as 1) "massive sulfides" (aggregates > 20 cm in diameter) in veins, 2) "clots" (aggregates 1-20 cm in diameter) in veins, 3) "bands" in veins, 4) as disseminated grains in veins, and 5) as disseminated grains in altered diorite adjacent to quartz veins. Individual veins commonly contain multiple sulfide textures. I observed all of these sulfide textures in all zones and in both discrete and network veins. I categorized the majority of my samples into one of these textural types, but due to complete consumption of sample for XRF in some cases, I did not classify all.

3.4.1 Massive Sulfide (MS) in Veins

The most economically important sulfide texture is massive sulfide. Massive sulfide is different from MPB in that massive sulfide occurs within quartz veins, whereas MPBs are irregular masses of sulfide in altered diorite. I define "massive sulfide" as a vein-hosted, pyrite-rich aggregate > 20 cm in diameter. Massive sulfide (MS) occurs in both network and discrete veins; however, it is more common in discrete veins (e.g., Fig. 3.1b). I have found massive sulfide in all zones.

3.4.2 Sulfide Clots in Veins

I define sulfide "clots" as aggregates similar to, but smaller than (1-20 cm), massive sulfide (e.g., Fig. 3.15). They typically consist of coarse pyrite grains. Sulfide clots are present in network and discrete veins, with no obvious preference. Clots occur in all zones and appear to be common in the mine.

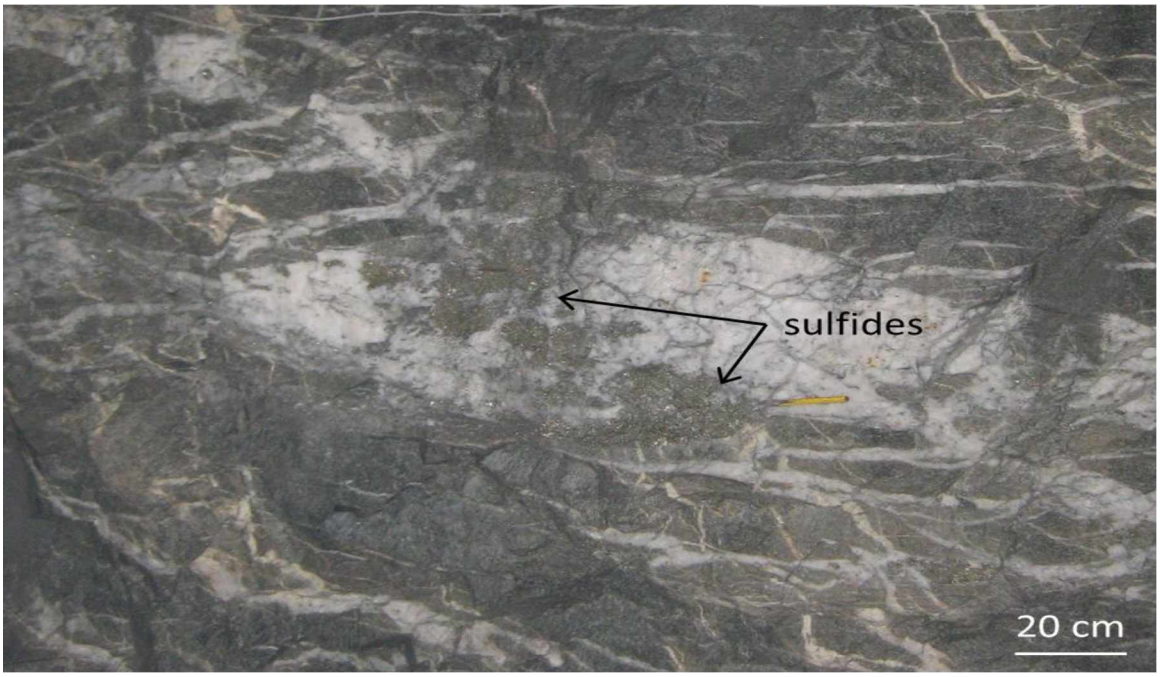

Figure 3.15. Underground photo of sulfide clots in a network vein, 1210-223 heading.

3.4.3 Sulfide Bands in Veins

Bands of sulfides occur in both discrete and network veins and in all zones. Bands are 1 – 10 cm wide and can be traced for several meters (e.g., Fig. 2.2). They commonly occur with clots and can form parallel to brecciated sections of veins. Approximately 15% of my samples for which I have identified a sulfide texture are sulfide bands, not including brecciated samples (which also form in bands).

3.4.4 Disseminated Sulfides in Veins

Disseminated sulfides represent the smallest sulfide aggregates I observed and are the least economic (volumetrically). I define disseminated sulfide as individual sulfide crystals and (or) mineral aggregates less than 1 cm in diameter. Disseminated sulfides occur within and adjacent to veins.

Both chalcopyrite and pyrite grains occur disseminated in veins (Fig. 3.16). Disseminated sulfides in veins are commonly present with other sulfide textures and are present in both discrete and network

veins. I do not have many samples of this sulfide texture because my objective was to collect sulfide-rich samples. These samples usually contain < 10% sulfides and probably account for < 10% of the total sulfide mined at Kensington.

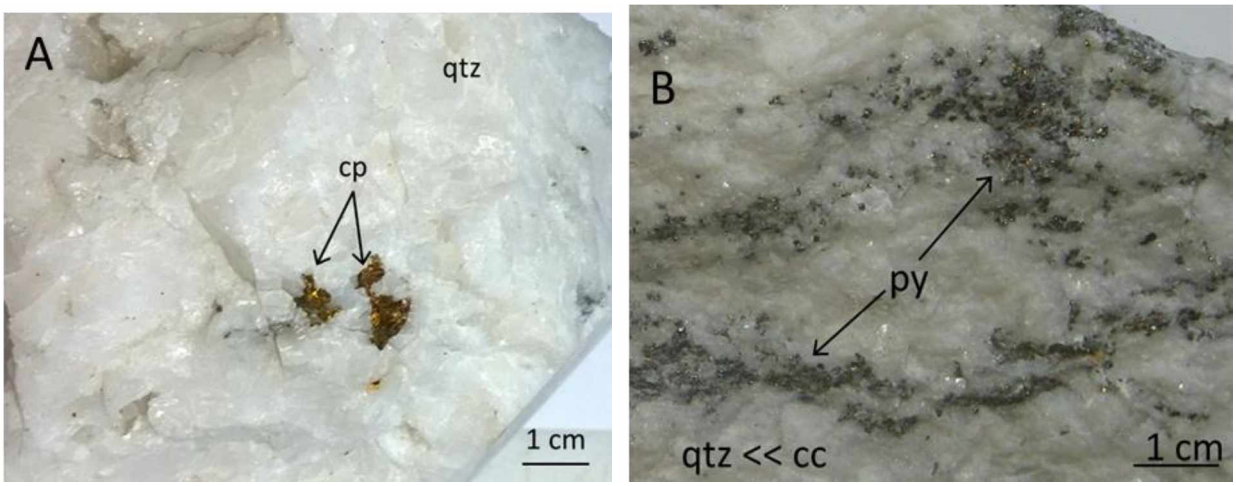

Figure 3.16. Disseminated chalcopyrite (cp) and pyrite (py) in vein quartz. A) Sample from 1355-210-13 B) sample from 705-184-2 heading.

3.4.5 Disseminated Sulfides in Altered Diorite

Disseminated sulfide grains occur adjacent to veins in altered diorite. Figure 3.17 is an example of disseminated pyrite in altered diorite adjacent to a quartz network vein (not shown). This texture is observed in all zones and is especially common adjacent to and between network veins. The sulfide abundance is rarely greater than about 10-15%. As with disseminated sulfides in veins, I do not have many samples of disseminated sulfides in altered diorite.

Figure 3.17. Close up of disseminated pyrite from 555S-3 (zone 10P)

3.4.6 Macroscale Sulfide Texture Summary and Distribution

Table 3.4 summarizes my macroscale observations of sulfide textural types at Kensington. Unfortunately, I was unable to classify all my samples, as many were entirely consumed by the XRF analysis. Of the samples I classified, the majority represent sulfide clots, i.e., aggregates 1-20 cm in diameter. I have equal numbers of massive sulfide (aggregates > 20 cm in diameter) and sulfide bands. These are found in all zones. I have only six samples of 'grains', i.e., disseminated sulfide with clusters of sulfide < 1 cm in diameter, with sufficient sulfide abundance for XRF analysis.

Table 3.5. Summary characteristics of Kensington vein types

Ore Type		Notes	Diameter (cm)	Number of Samples	Locations		
					Z41	Z10	Z10P
Sulfide texture	clots	Common w/ all veins	1-20	80	X	X	X
	massive	Mostly w/ discrete veins	> 20	28	X	X	X
	bands	Common w/ all veins	1-10	28	X	X	X
	grains	Mostly w/ network veins	< 1	6	X		X

Figure 3.18 shows the distribution of sulfide textural types on the long section, combined with the zones of higher Au and the areas of significant fahlore. A striking feature is that samples with sulfide bands are within or immediately adjacent to the higher-Au 'pipes' on the long section. Similarly, the areas of >.03% fahlore all possess sulfide bands (except 1 massive pyrite body sample). Finally, the vast majority of massive sulfide samples are located within the high-Au pipes, whereas sulfide clots show no such association. If anything, clot-textured sulfides are more common outside of the high-Au pipes.

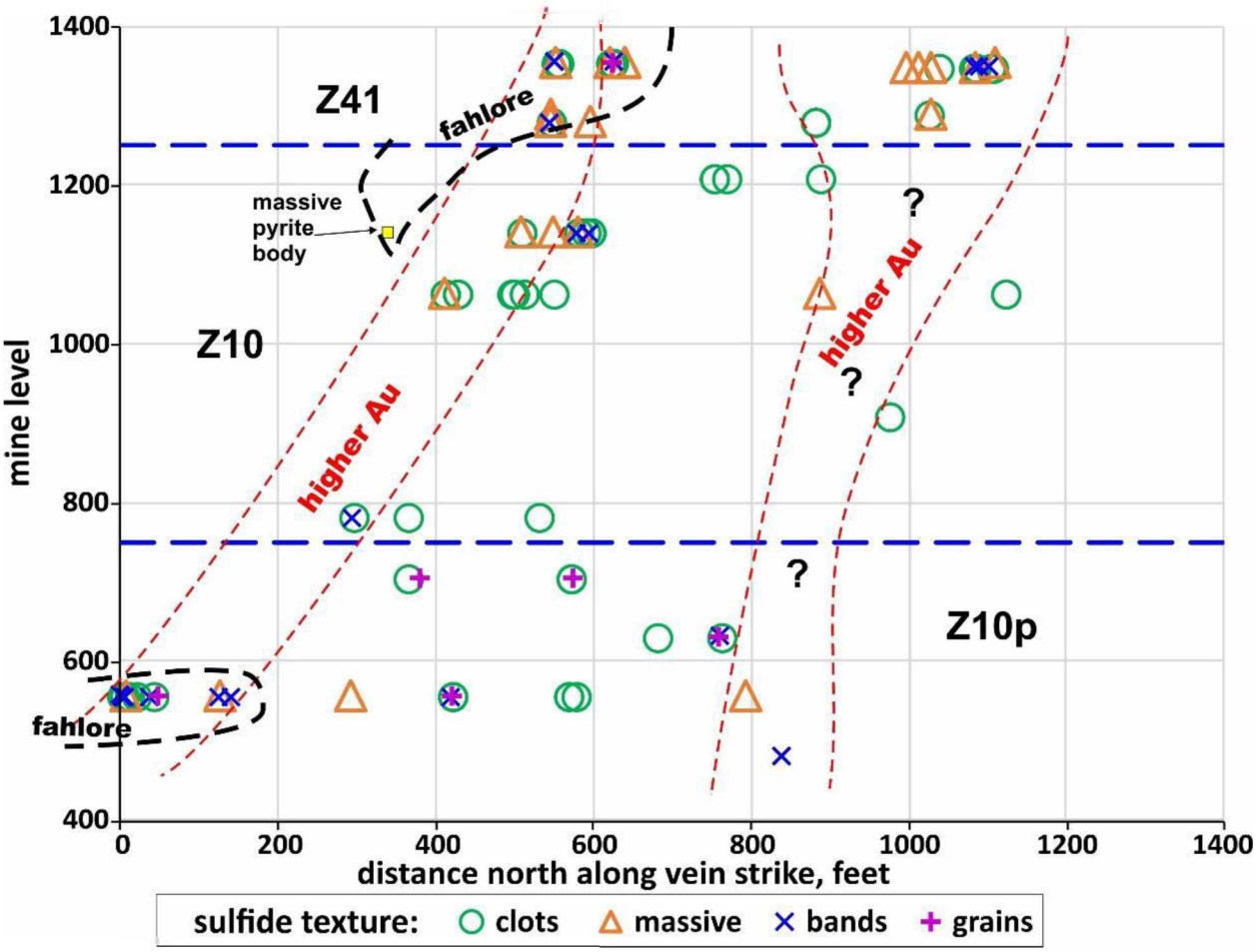

Figure 3.18. Long section showing distribution of my samples with known sulfide textural types with the zones of higher Au concentrations and >.03% fahlore from Figs. 2.8 and 2.18.

3.4.7 Sulfide Textural Types and Elemental Associations

Figure 3.19 shows ranges and geomean concentrations for the Te-associated elements, sorted by sulfide textural type. Samples from sulfide bands clearly possess the highest geometric mean (geomean) concentrations for all five elements: Au, Ag, Bi, Hg, and Pb. Unlike the situation with 'brecciated veins' (small number of analyses) the sulfide bands sample group represents a robust population, which for maximum and geomean concentrations are simply higher than the other textural types. Geomeans for sulfide clots and for massive sulfides are practically identical; Au is slightly higher for massive sulfides and Ag for sulfide clots. The 'sulfide grains' group is really too small to detect meaningful patterns.

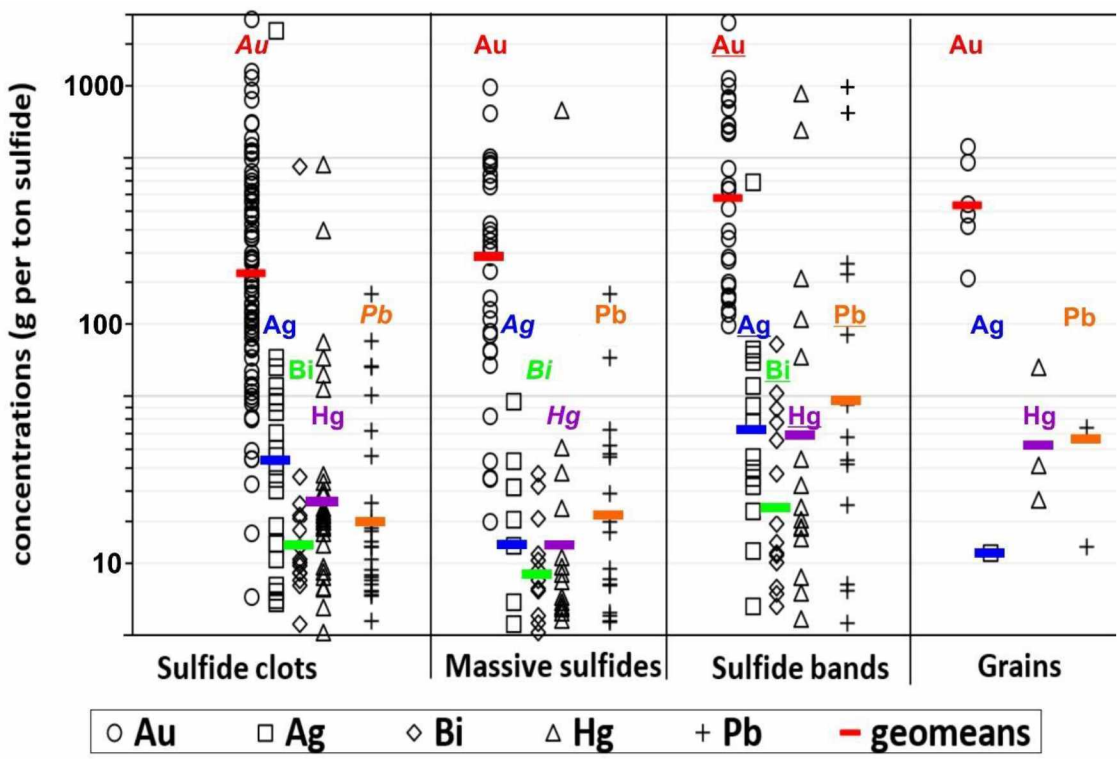

Figure 3.19. Concentration ranges and geometric means (geomeans) of telluride-associated elements by sulfide texture. Concentrations below detection limits are excluded. Underlined elements have the highest geomean concentrations (excluding 'grains' which are simply shown for comparison). Elements in italics are in the column with the lowest geomean concentration for that element.

Table 3.5 gives geomean concentrations for non-Te-associated elements and minerals sorted by the various sulfide textural types. Sulfide bands have Cu geomean concentrations nearly twice those of clots and massive sulfide, but there are few other distinguishing features in this compilation. Most surprisingly, the massive sulfide samples display the lowest geomean Co concentrations, although not tremendously less than the others. The geomean % fahlore is slightly higher for sulfide bands.

Table 3.6. Geometric mean data for non-Te associated elements and calculated minerals by texture

Sulfide Texture	n	Grams/Ton Sulfide					Calculated wt% in Original Sample*						
		Cu	Mo	Ni	Co	Se	sil*	qtz	calc	py	cp	fah	tot
clots	80	282	15	28	246	41	4	30	6	59	0.05	0.01	99
massive	28	390	10	33	195	42	2	13	3	80	0.07	0.01	97
bands	28	694	28	30	259	37	3	30	6	56	0.08	0.02	96
grains	6	814	28	27	295	35	24	20	22	33	0.10	0.002	99

Notes: elements/minerals underlined if especially high, non-bold if especially low; mineral abbreviations: sil = silicates (calculated chlorite + muscovite + albite), qtz = quartz, calc = calcite, py = pyrite, cp = chalcopyrite, fah = fahlore (tetrahedrite-tennantite solid solution), tot = calculated mineral total. n = number of samples used in the geomean.

3.5 Discussion and Conclusions

Most of my samples (>150) are pyrite-rich; perhaps 20-30 could be described as containing elevated Cu, but following my definition (>3 wt% Cu) only 14 are classified as Cu-rich. I collected about a dozen brecciated samples, but only 5 contained enough sulfide to be used for XRF analysis. All of the Cu-rich samples in zone 10 were taken from the 1065 level and the Cu-rich samples in zone 10P are restricted to the 555 level (Fig. 3.4). Because my sampling is not uniform through the mine (e.g., I did not even try to sample in the main haulage level) I cannot unambiguously explain the higher apparent abundance of Cu-rich samples in zone 41. It might be caused by vertical metal zoning or might instead be due to higher abundance of Cu-rich samples in discrete veins--which are proportionally more abundant in zone 41.

Table 3.6 summarizes relative abundances of different sample, vein, and textural types and their abundances in the three mine zones I sampled. My objective was to determine if elemental abundances in the Kensington mine could be related to the type of occurrence as well as the spatial location in the mine. Consequently, I attempted to break out potentially important differences. Some are probably less important than others, e.g., the distinction between 'massive sulfide' and 'sulfide clots'. Massive sulfide, for example, is more than twice as common in discrete veins as in network veins, which may be related to relative sizes. Massive sulfide consists of aggregates at least 20 cm in diameter and network veins are < 50 cm wide. It is much easier to accommodate large sulfide aggregates in wider than in narrower veins! Perhaps most important, Table 3.6 clearly indicates that some types and textures are more common than others, and the relative abundance is different in different zones of the mine. Perhaps most important is the contrast in relative abundance of discreet (larger, more continuous) vs. network veins in zone 41 (mostly discreet) and zone 10 (mostly network). Interestingly, sulfide bands are about equally common in discrete and network veins, but are most common in zone 10P.

Table 3.7. Sample type distribution (%) by vein type, sulfide texture, and location

		Sample Type*			Zone			Vein Type	
		Py	Cp	Bx	Z41	Z10	Z10P	Discrete	Network
Vein Type	Discrete	48	83	100	76	25	44		
	Network	52	17	0	24	75	56		
Sulfide Texture	Clots	61	22	0	50	76	58	56	69
	Massive	21	56	0	35	16	11	29	12
	Bands**	17	22	100	15	8	31	15	19

*py = pyrite-rich, cp = chalcopyrite-rich, bx = brecciated (grouped with 'bands')
**brecciated are treated as a type of band

Table 3.7 gives some statistics and elemental distribution patterns for the Te-associated elements at Kensington. The association of higher metal concentrations with brecciated veins is intriguing, but frustrating: brecciated veins are only present at the highest elevations in which I sampled (Fig. 3.12). I do not know whether they represent a localized phenomenon or if instead they are confined to a single mine level or whether they are common at higher elevations in the mine. Given their very restricted occurrence, I can't relate mine-wide elemental patterns to them.

The occurrence of higher metal values with banded veins and the presence of banded veins in or adjacent to the higher Au 'pipes' is more interesting because banded veins are present from the highest to the lowest levels from which I have samples. Of the various sulfide textures, banded sulfides have the highest concentrations and highest geomean concentrations of all the Te-associated metals. I do not know what makes them so special, but they are apparently related to regions of gold enrichment.

Table 3.8. Summary of telluride associated elemental behavior at Kensington

	Au	Ag	Bi	Pb	Hg
Geomean*	214	22	12	19	21
max	1907	1706	456	968	3307
3rd quart	489	38	16	32	26
% of samples > DL raw data	98	34	32	48	45
physical distribution	2 steep 'pipes'	S margin Z10; Z41+10P	Z41 and (less) Z10P	Similar to Ag	S margin of Z41 & 10; Z10P
distribution in vein types	Highest with brecciated veins				
distribution in sulfide textures	Highest with banded sulfides				

*concentrations in grams metal/ton of sulfide

I have shown that gold grade is essentially independent of chalcopyrite abundance for Cu-rich samples (Fig. 3.6). This is odd, because calaverite and gold are supposed to be largely associated with pyrite at Kensington. One would think that dilution of (Au-bearing) pyrite with (Au-barren) chalcopyrite would cause the gold abundance to decrease. However, such does not appear to be true. Clearly, microscopic evidence is required (does chalcopyrite actually host Au?) to solve this conundrum.

A final consideration is the connection between discrete veins and fahlore abundance (Fig. 3.14). It's clear that the vast bulk of fahlore is present in sulfides—with a variety of textures—but always hosted by discrete veins. I postulated that fahlore (that is, Sb+As) is added to the previously existing metals from the southern end of the long section, based on the spatial distribution of fahlore (Fig. 2.14). Following this line of reasoning, the components for fahlore were introduced via discrete veins, and the virtual absence of fahlore from zone 10 could be related to the virtual absence of discrete veins in that zone (Fig. 3.12).

I further postulated in chapter 2 that the Te-related elements were superimposed on metal values in a manner somehow associated with the fahlore. If this is true, then I postulate that these metals were similarly introduced via discrete veins, but spread out to the north through the network veins. If this is true, I expect to find evidence that fahlore and the Te-associated metals have a related textural paragenesis. I will pursue this and other micro-textural matters in chapter 4.

4 Mineralogy and Microscale Textures of Ore and Related Minerals

The ore at Kensington consists largely of pyrite grains with microscopic inclusions of ore and associated minerals. This chapter provides general descriptions of microscopic textures of gold, sulfide, and telluride minerals at Kensington including various inclusion textures. Polished section descriptions are located in Appendix I. The primary data used in this chapter is based on reflected light observations; however, EDS (Energy Dispersive Spectrometry) was used to identify non-Au telluride minerals due to their similar reflectivity and color. Non-Au tellurides observed are also usually small (< 30 µm), making reflected light identification difficult.

4.1 Constraints of Data Set

All of the ore and related minerals in the Kensington mine are opaque. This restricts microscopy to reflected light only. Samples analyzed by EDS were selected based on unidentifiable opaque minerals (optical) and (or) high metal concentrations from XRF data. XRF analyseis of samples with polished sections are located in Appendix I.

Not all polished sections have associated EDS data. I have 23 polished sections and moderate to extensive EDS data for about half. Of the remainder I have minimal EDS data for about a third, and no EDS data for about two thirds. I did not identify by reflected light microscopy accessory tellurides in samples with minimal to no EDS data. These slides may or may not have accessory tellurides.

Polished sections with minimal EDS data are not considered in the following sections unless the sample is low in accessory telluride metals (Ag, Bi, Pb, Hg, and Ni), as indicated by XRF data. Polished sections 07-1, 07-2, 1280-201-6, 1140-197-6, and 1065-206-3 have no EDS data, but also have low concentration of accessory metals. These samples most likely have very few accessory tellurides. The only drawback to lacking microprobe data is that very small (< 5 micron) inclusions of calaverite and gold could be overlooked. This may skew the observed average size of inclusions and their textures, however I am fairly confident that I was able to document the majority of inclusions.

I conducted a reflected light study of 20 polished sections, cataloguing the abundance, average size, and texture of gold and calaverite inclusions. I did not collect comprehensive reflected light data on non-Au tellurides, chalcopyrite, or fahlore. I used the estimated average size and abundance of each texture type of gold and calaverite grains to calculate the estimated total area of a given texture. The complete reflected light survey of gold and calaverite grains are located in Appendix J.

To check the quality of my observations, I plotted the calculated area of calaverite and gold in each slide and plotted it against the Au concentrations measured by XRF. It is important to note that the material used to make the XRF pellets and the polished section from that sample are essentially subsamples of the original sample, but are exactly the same material. I also may have missed some (if not most) of the very small grains (< 5µm). However, estimated total areas of calaverite + gold correlate reasonably well to the corresponding XRF Au concentrations (Fig. 4.1). Better agreement would likely be found through more refined treatment of the data, e.g., adjustment for the fact that different slides contained different surface areas of pyrite.

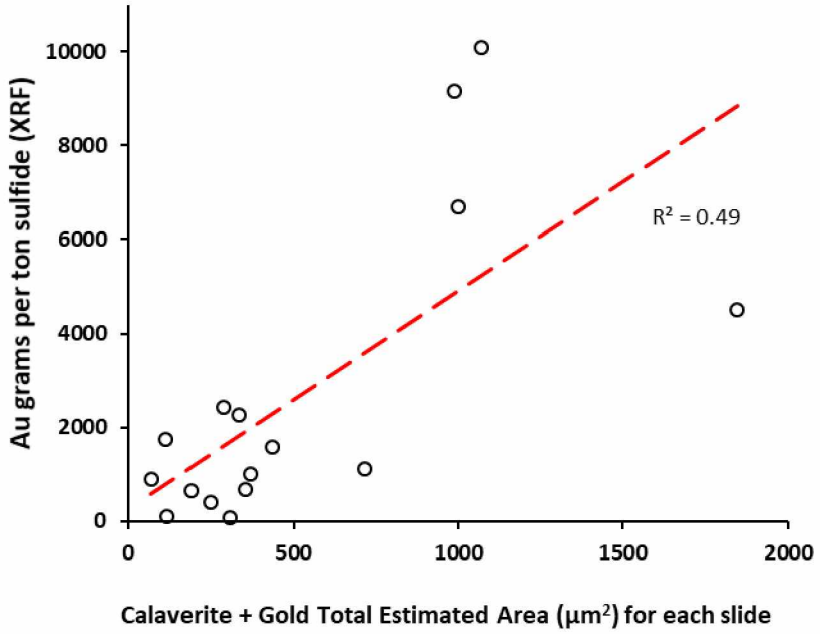

Figure 4.1. Comparison of XRF measured Au concentrations (grams per ton sulfide) and estimated total calaverite + gold grain area (µm2) from reflected light studies. A strong correlation confirms the validity of my mineral estimations.

In contrast, total number of observed calaverite + gold grains poorly correlates with Au concentrations (Fig. 4.2). This shows that the most meaningful way to present the contributions of different grain minerals to overall abundance is by accounting for number of grains and their sizes. (I observed calaverite grains in quartz in one polished section (555-188-3) and did not include these in the calculations due to their infrequency.)

Another complicating factor in comparing reflected light results to XRF data is that the XRF concentrations are normalized to 100% sulfide, but the surface areas of Au-bearing minerals were not. Most of my polished sections are competent pieces of ore, sulfides in situ with varying amounts of quartz, and other gangue minerals. Other polished sections are grain mounts of handpicked sulfide

grains with little or no quartz. Reflected light data is based on examination of 19 polished sections, of which 4 were grain mounts.

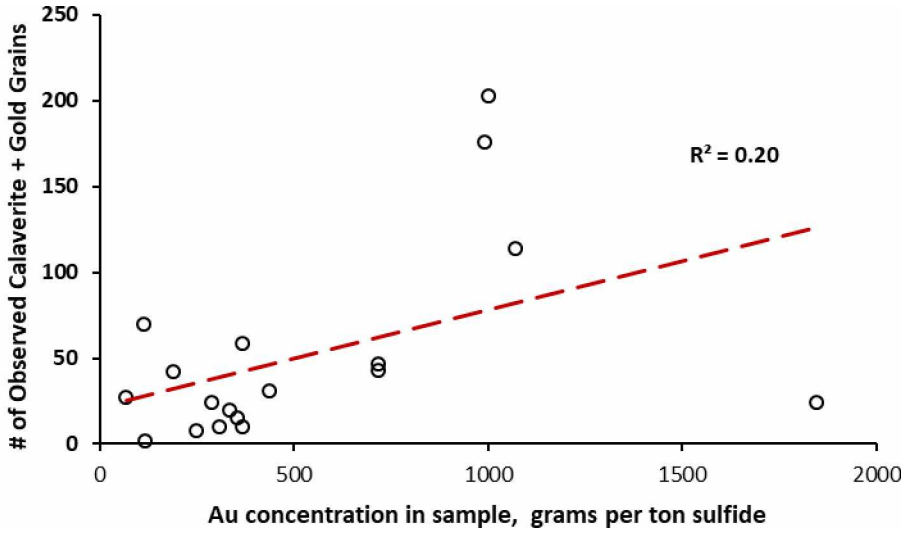

Figure 4.2. Total number of observed calaverite + gold grains in reflected light vs. concentrations of Au from the XRF sample. Relatively low correlation between the two suggests grain size is an important factor in assessing mineral abundance.

4.2 Microscopic Sulfide Textures

Pyrite is the primary ore hosting mineral; however previous workers (e.g., Casey, 2005) have not investigated the possibility that other sulfide minerals host Au. This section describes the common sulfide textures observed that gives insight in to relative timing of sulfide mineralization events. The ore hosting mineralization textures are subsequently used as a reference for timing of ore mineralization.

4.2.1 Microscopic Pyrite Textures

The most common microscopic pyrite texture is masses of pyrite aggregates. Pyrite grains that are distinguishable in these aggregates are typically polygonal and may display fractures (e.g., Fig. 4.3a). Another common texture consists of subhedral pyrite grains in a quartz > calcite >> ankerite matrix (Fig. 4.3b). Both of these textures are common in pyrite-rich samples. Pyrite, especially where it occurs in altered diorite, frequently contains quartz (and silicate) inclusions, giving it a spongy texture (Fig. 4.3c). Cubic pyrite grains are not common in my polished sections. Some samples have very fine grained (<5 µm) pyrite grains adhering to margins of larger more euhedral grains (Fig. 4.3d).

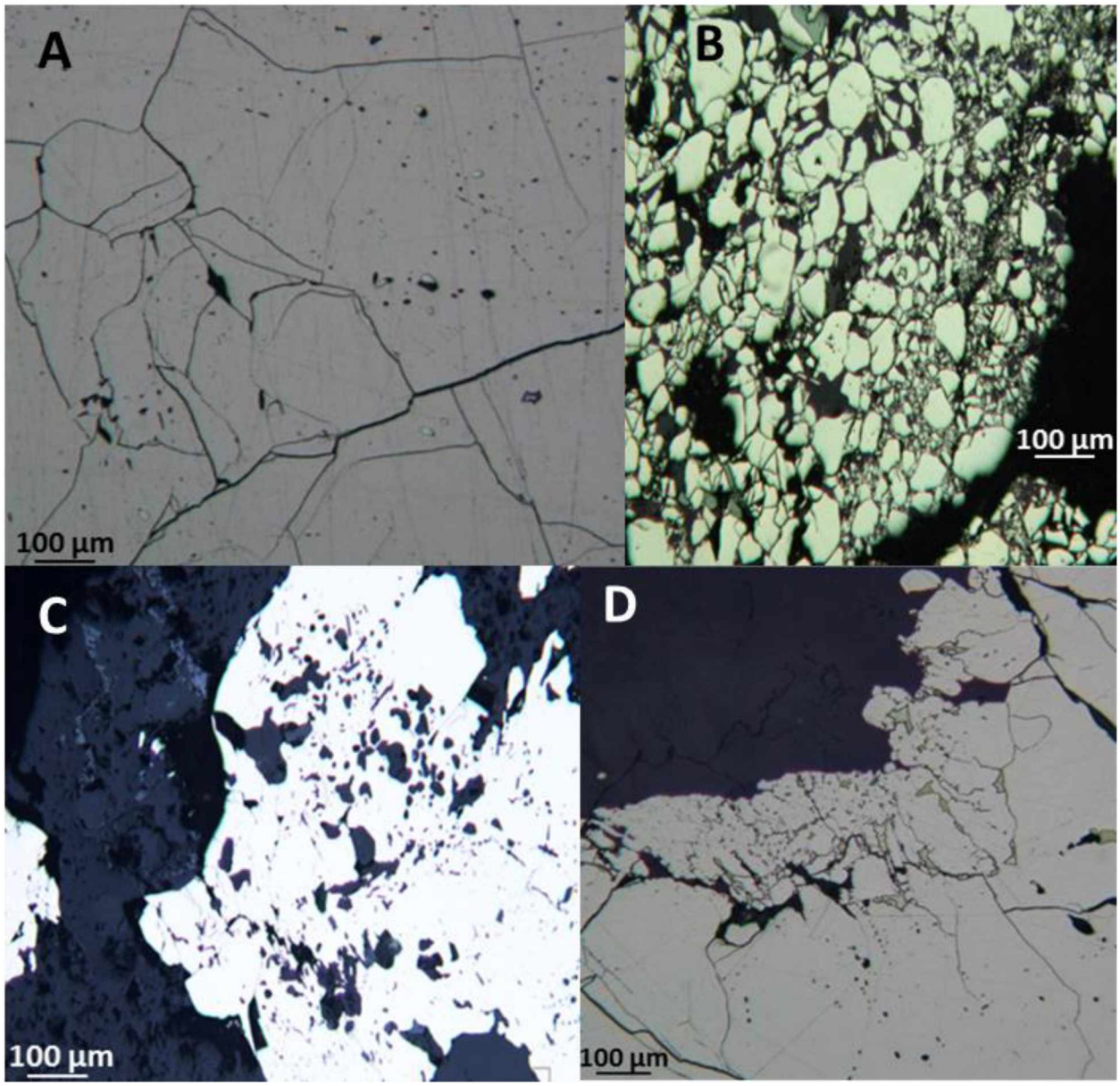

Figure 4.3. Photomicrographs showing typical pyrite textures. A) Sample 1065-189-1 showing typical 'massive' pyrite aggregate with few inclusions. B) Sample 555-160-2 showing typical fine grained subhedral to euhedral pyrite with interstitial quartz (black) and chalcopyrite (grey). This sample contains 0.2 % chalcopyrite and 0.4 % fahlore (sulfide-normalized). C) Sample 02-1 showing pyrite with quartz inclusions. D) Sample 555-188-3 showing complex chalcopyrite (yellow) inclusions in pyrite (light grey).

4.2.2 Chalcopyrite and Fahlore Textures

XRF analyses show that all my samples contain at least 50 grams Cu per ton sulfide. Chalcopyrite is the most abundant Cu bearing mineral, with lesser fahlore (tetrahedrite-tennantite solid solution). Anhedral chalcopyrite and fahlore commonly fill intercrystal spaces between pyrite grains. Pyrite grains that are highly fractured commonly have anhedral chalcopyrite, fahlore, and rare bornite filling fractures

(Fig. 4.4a and b). These pyrite and chalcopyrite textures are common in samples with elevated Cu concentrations (> 0.5 % sulfide-normalized chalcopyrite). Samples with low to moderate chalcopyrite and (or) fahlore abundances commonly display rounded inclusions of Cu bearing sulfides (Fig. 4.4c) in pyrite.

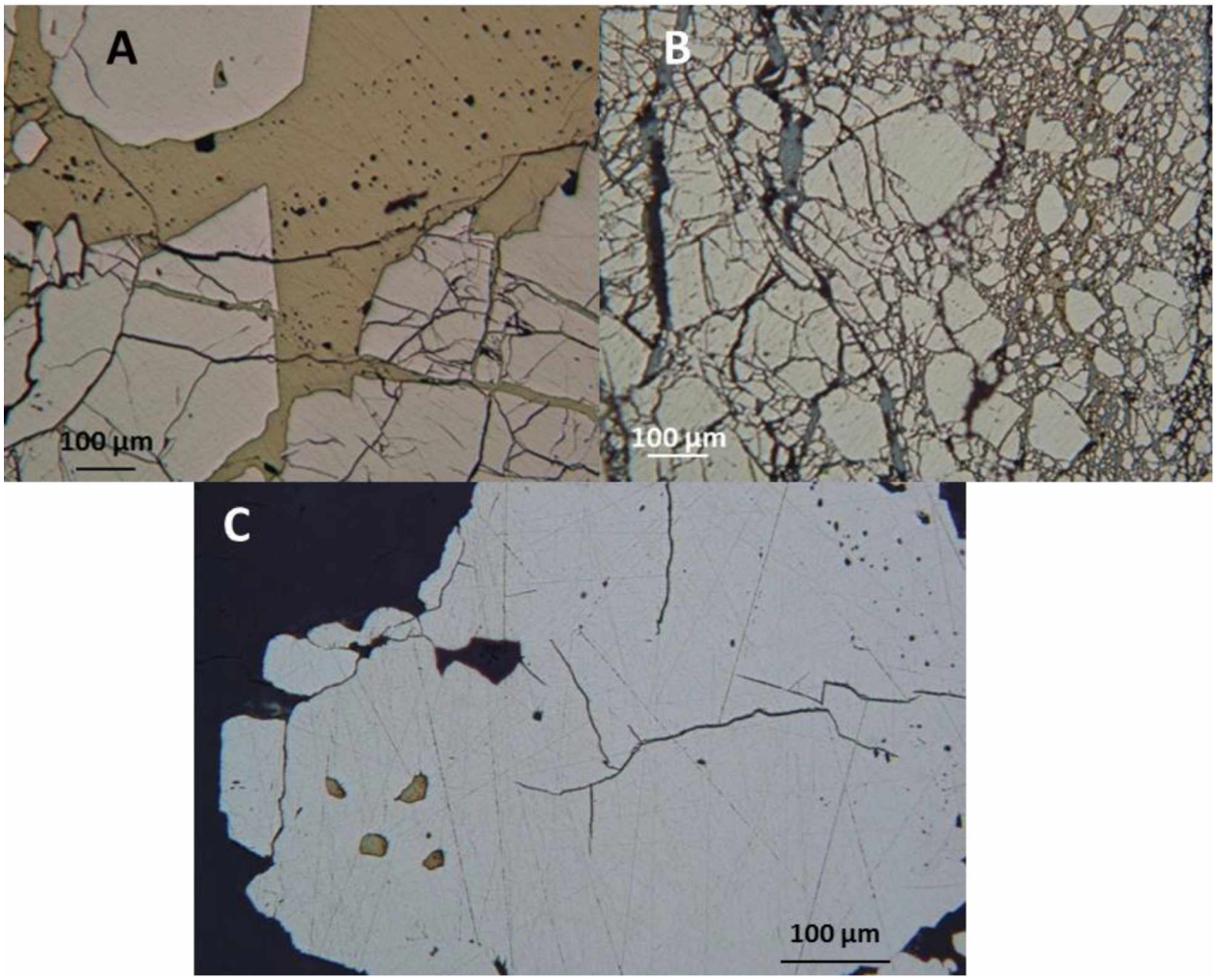

Figure 4.4. Intergrowths between pyrite and Cu-bearing sulfides A) Sample 1065-206-3, typical interstitial and fracture fill chalcopyrite (yellow) between pyrite grains. B) Sample 555-160-8 is similar to 1065-206-3, but with tetrahedrite (darker) and chalcopyrite fracture filling pyrite. C) Sample 630-224-4 with 4 rounded chalcopyrite inclusions in pyrite. This sample contains 140 grams Cu per ton sulfide.

Samples with very high chalcopyrite concentrations (> 25 relative %) commonly contain massive (> 500 µm) chalcopyrite grains with little to no associated pyrite (Fig. 4.5a). Similarly, samples with elevated fahlore concentrations contain large fahlore grains with chalcopyrite and minor pyrite (Fig. 4.5b). I did not observe any euhedral fahlore inclusions in pyrite. Rather, fahlore occurs as complex inclusions, grain boundary inclusions, and filling fractures in pyrite.

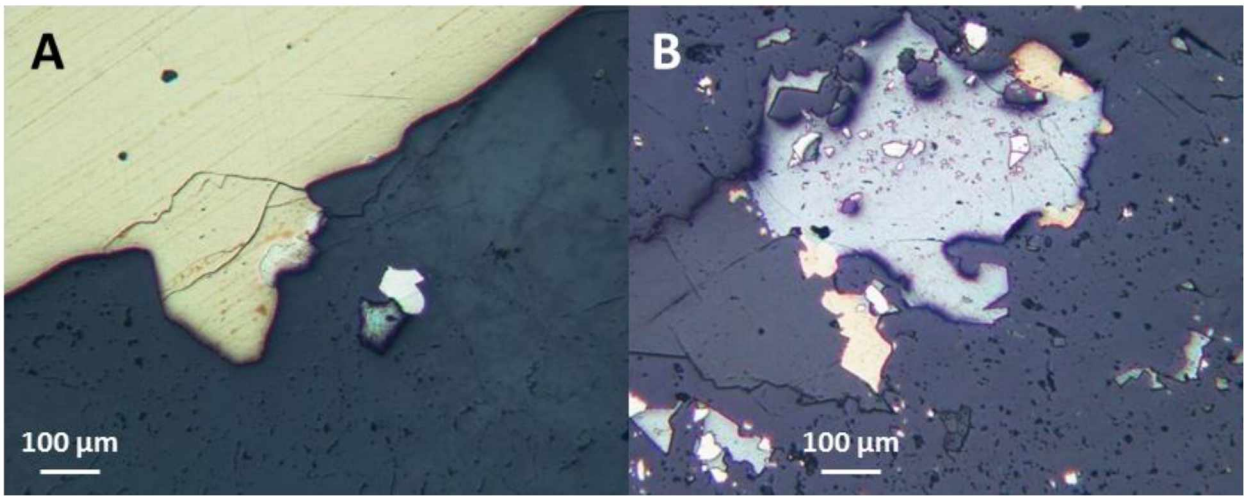

Figure 4.5. A) Photomicrograph from sample 555-188-5, which is 1/3 chalcopyrite. B) Photomicrograph from sample 1355-201-16b 1(1.1 relative % fahlore) with isolated fahlore grains (grey, rounded), some irregular pyrite (white) inclusions, and attached grains of chalcopyrite (yellow), all in a matrix of quartz + carbonate.

I did not observe any euhedral fahlore inclusions in pyrite. Fahlore occurs as complex inclusions, but mostly as grain boundary inclusions, and fracture filling in pyrite, hence, it appears to have formed later than the bulk of pyrite.

4.3 Microscopic Au Mineralogy and Textures

Here I begin by defining mineral intergrowth textures seen at Kensington, and discuss the mineralogy after doing so. I categorize the various ore textures into six types:

1) Rounded inclusions– rounded or rectangular inclusions in pyrite or chalcopyrite grains
2) Complex inclusions–complexly-shaped inclusions in pyrite grains
3) Apparent Grain Boundary inclusions– long and narrow, not associated with fracturing
4) Fracture Fills – gold and telluride minerals filling fractures in pyrite
5) Adjacent – ore minerals adjacent to grains of pyrite or chalcopyrite
6) Isolated grains in quartz and/or calcite, not directly associated with sulfides

4.3.1 Rounded Inclusions

I define rounded inclusions as those in pyrite or chalcopyrite displaying smoothly curved faces or else broadly rectangular shapes. Such inclusions are commonly asymmetrical and occur individually or in clusters of grains (located within .3 mm of each other, e.g., Fig. 4.6a). These are most common in pyrite grains, but I have seen 3 small inclusions in chalcopyrite grains of Cu-rich samples (Fig. 4.6b). Rounded and rectangular inclusions are < 5µm to almost 100µm in diameter. Such inclusions occasionally were

gouged out during the polishing process which left holes and partially 'filled' inclusions. Rounded inclusions typically contain only one mineral phase.

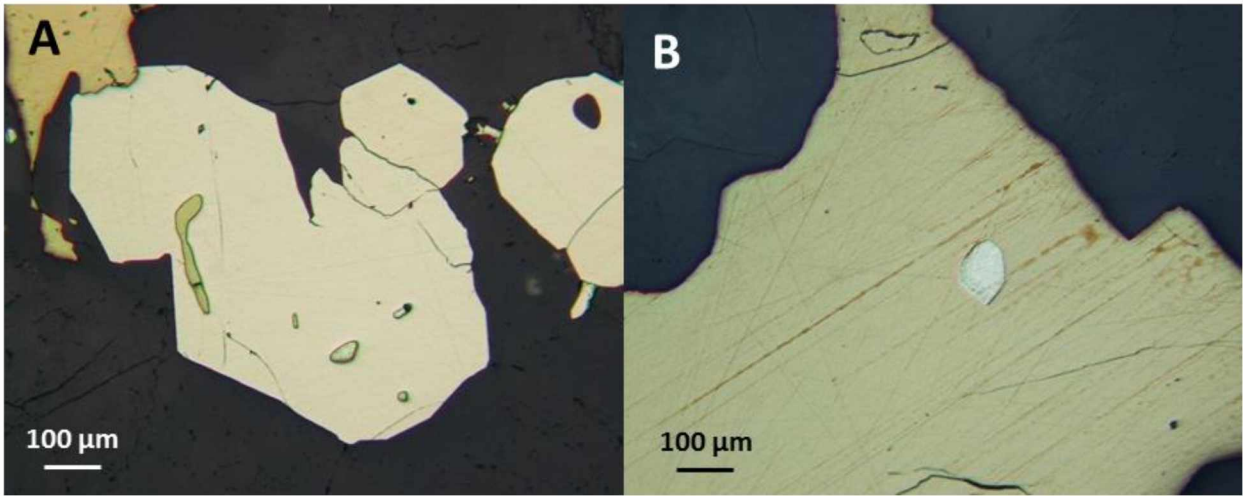

Figure 4.6. Photomicrographs depicting 'rounded' inclusions A) 1280-201-6e with irregular, but rounded chalcopyrite (yellow) in pyrite. B) Sample 555-188-5 Chalcopyrite grain in quartz with a sub-rectangular calaverite inclusion. This is an uncommon texture in that it is unusual to have such a large chalcopyrite grain without any associated pyrite. This sample is Cu-rich sulfide clot from a network vein in zone 10P.

4.3.2 Complex Inclusions

Complex inclusions have complex shapes with irregular or scalloped edges and typically contain multiple minerals (Fig. 4.7). They are <10 µm to >200 µm in diameter.

4.3.3 Grain Boundary Inclusions

Apparent grain boundary inclusions are mainly regularly shapes and (or) scalloped inclusions between two pyrite grains (Fig. 4.8a and b). It is not always clear that these inclusions formed along the edges of separate pyrite grains. These inclusions are 5 µm to > 500 µm long. In some cases they appear to have grown into a space between adjacent pyrite grains (Fig. 4.8a) and in others they appear to be partly replaced by or replacing the host pyrite (Fig. 4.8b).

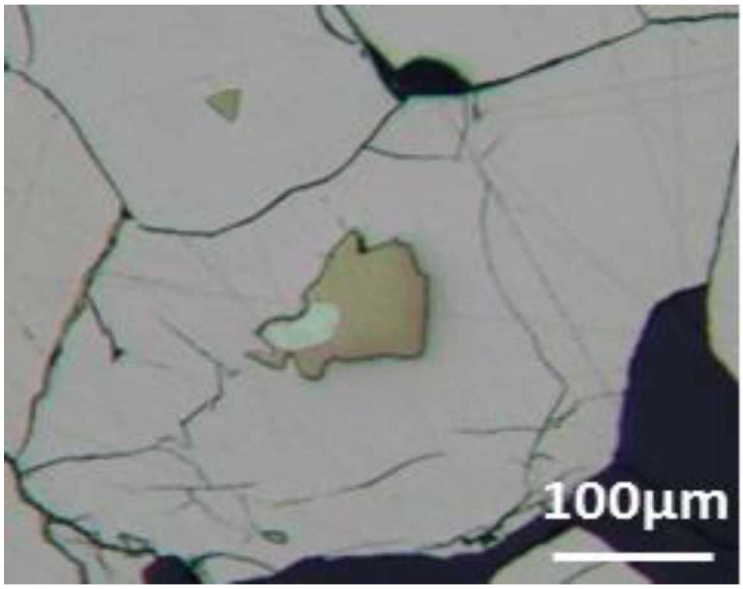

Figure 4.7. Photomicrograph illustrating a complex inclusion of chalcopyrite (yellow) and calaverite (bright) in pyrite. 555-188-3 site H.

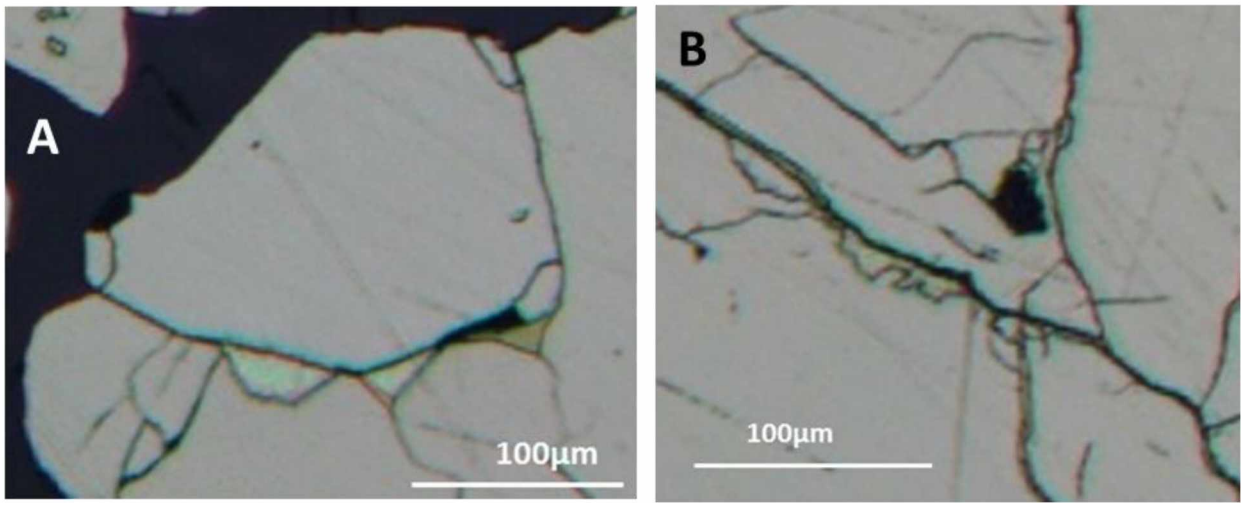

Figure 4.8. Photomicrographs illustrating 'grain boundary inclusions', from sample 555-188-3. A: euhedral-appearing grain boundary inclusions of AuTe2 and chalcopyrite between pyrite grains. B: complex intergrowth of pyrite and calaverite at a pyrite grain boundary.

4.3.4 Fracture Fills

Veinlets in pyrite are usually distinct from apparent grain boundary inclusions, particularly where there are matching vein walls. In some cases, the texture is less clear. For example, tiny veinlets of chalcopyrite clearly fill fractures in pyrite (Fig. 4.9), but the large, elongate body of chalcopyrite simply sits between adjacent pyrite grains. There is no clear evidence for a fracture that the large chalcopyrite grain filled. Gold, calaverite, and associated tellurides can appear as inclusions within chalcopyrite or

fahlore filling fractured pyrite as in Fig. 4.9. Gold and other ore minerals can also directly fill fractures. Such fracture-filling grains are < 5 µm to > 200 µm long.

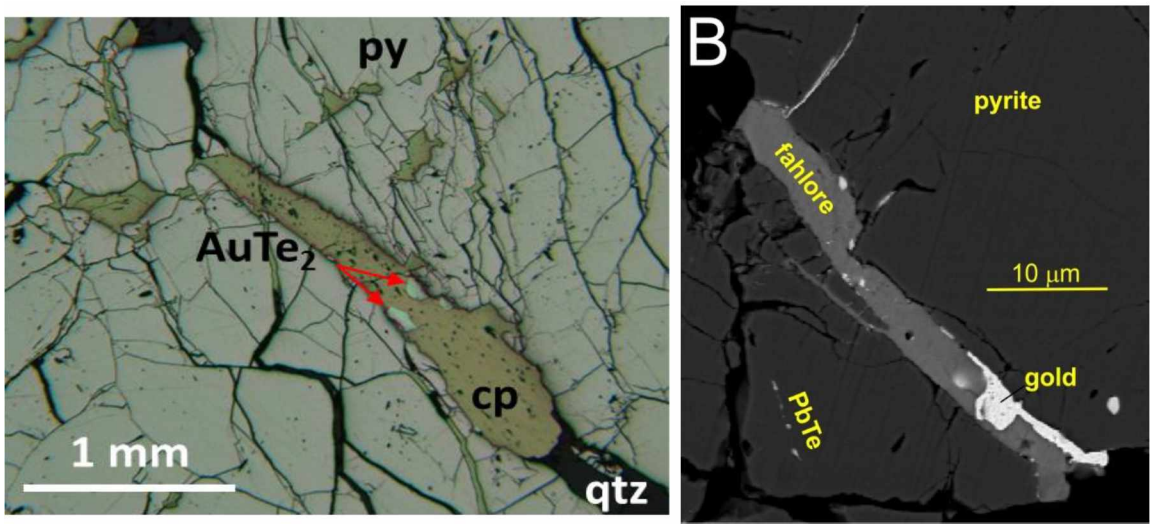

Figure 4.9. Photomicrograph (A) and BSE image (B) showing clear-cut and somewhat ambiguous 'fracture fill' textures in pyrite. A = interstitial grain boundary and 'fracture filling' chalcopyrite (cp) in pyrite. The large cp itself contains 3 irregularly-shaped inclusions of calaverite. Sample 1065-206-3. B = fracture fill of fahlore and gold in pyrite and a tiny string of elongate 'rounded' inclusions that may represent a headed fracture fill in pyrite.

4.3.5 Adjacent Grains

Calaverite and gold grains occur adjacent to pyrite (and less commonly chalcopyrite) in quartz and (or) calcite (Fig. 4.10). Adjacent grains tend to be larger than inclusion grains, 5 µm to > .5 mm long. They typically consist of only one mineral phase.

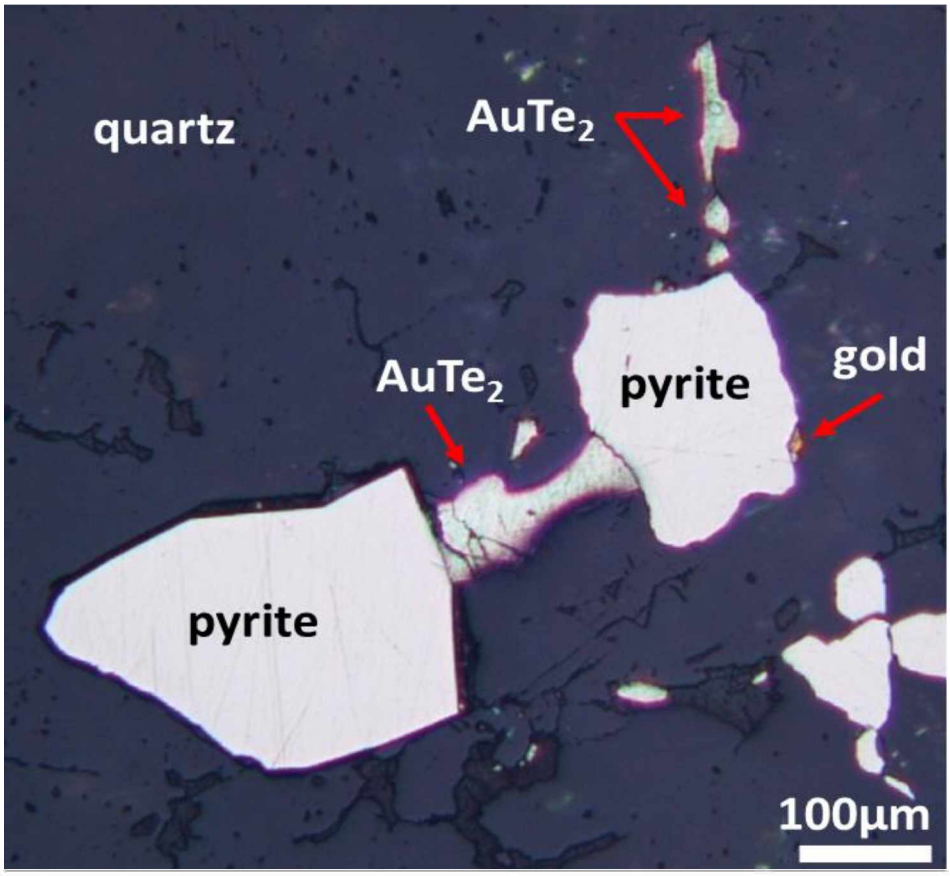

Figure 4.10. Photomicrograph illustrating 'adjacent grain' texture, with irregularly-shaped calaverite and gold grains are adjacent to subhedral pyrite grains in quartz. Sample 555-188-3.

4.3.6 Isolated Grains in Quartz and (or) Calcite

These are grains in quartz and (or) calcite that are not adjacent to any significant (> 10 µm diameter) sulfide grains; they are commonly much larger than inclusions. However, these 'isolated' grains are typically less than 1 mm from either pyrite, chalcopyrite, or fahlore. They occur in both pyrite-rich and Cu- rich samples. These grains tend to be anhedral and monomineralic (e.g., Fig. 4.11).

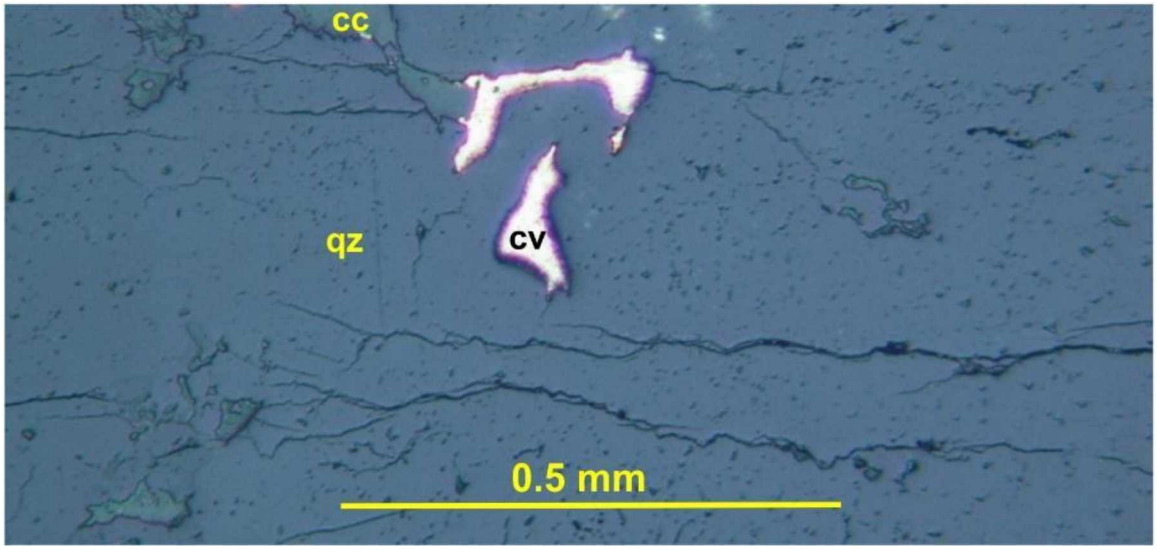

Figure 4.11. Photomicrograph illustrating 'isolated' mineral texture, with irregular calaverite (cv) grains in quartz (qz) and calcite (cc), at more than 0.5 mm from the nearest opaque minerals. Sample 555-188-5a.

4.3.7 Complex / Ambiguous Textures

I found three instances of fractures cutting across inclusions in pyrite grains (e.g., Fig. 4.12). It is difficult to distinguish between the fracture fill mineralogy and the original inclusion mineralogy. In this case, did the fahlore that fills fractures in pyrite also partly replace the complexly-intergrown gold grain? Or was there an original rounded inclusion of fahlore and gold that was cut by a fracture and filled with a later generation of fahlore? I did not include such ambiguous textures when I recorded my polished section examination. However, these appear to be comparatively rare.

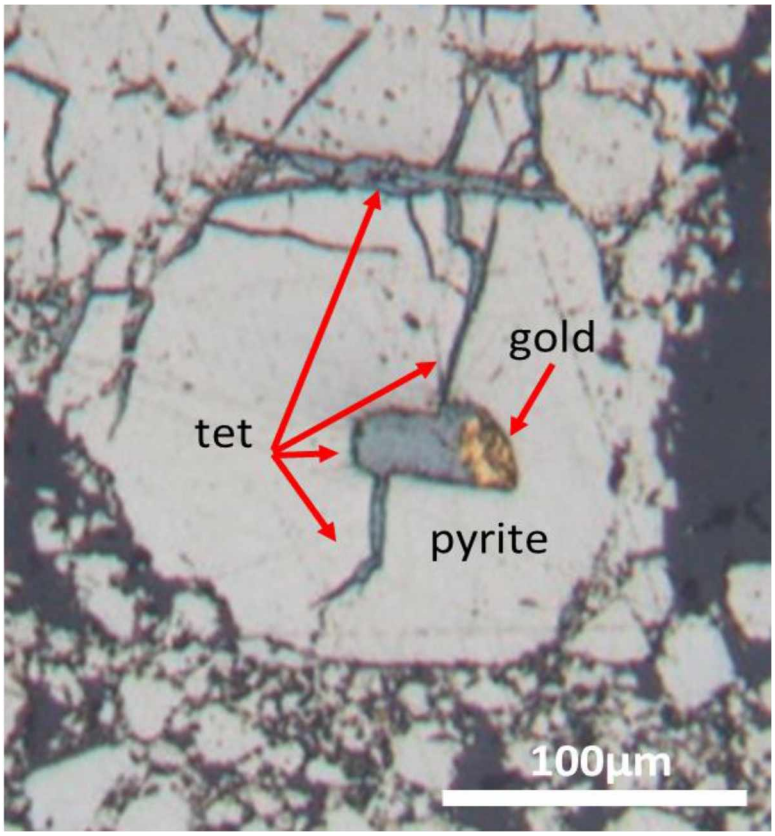

Figure 4.12. Photomicrograph illustrating a complex texture: a pyrite grain with a fahlore filled fracture cuts across a fahlore + gold filled rounded inclusion. Since rounded inclusions are typically mono-mineralic, the origin of this texture is unclear. Sample 1355-201-16a, with high fahlore content.

4.4 Variations in Calaverite and Gold Textures

Calaverite is the most common Au-bearing mineral I observed in polished sections, accounting for approximately 90% of the gold bearing minerals. I found calaverite in all polished sections with identifiable gold. Calaverite occurs with all 6 textures identified, as grains < 5 µm to > 400 µm long. Gold grains also occur as all texture types; however the largest gold grain I observed was 100 µm long.

Grain boundary inclusions and calaverite filling fractures in pyrite represent the largest fraction of calaverite (based on estimated areas, Fig. 4.13a). However, a single sample (1280-201-6) is responsible for 25% of the calaverite surface area and 2/3 of the calaverite in that sample is fracture fills. Neglecting that sample decreases the proportion of fracture fill calaverite to less than that of complex inclusions. Calaverite grains adjacent to pyrite and chalcopyrite represent the least common

texture, making up 9% by area. Gold, in contrast, predominantly (84%) occurs a fracture fill in pyrite (Fig. 4.13b).

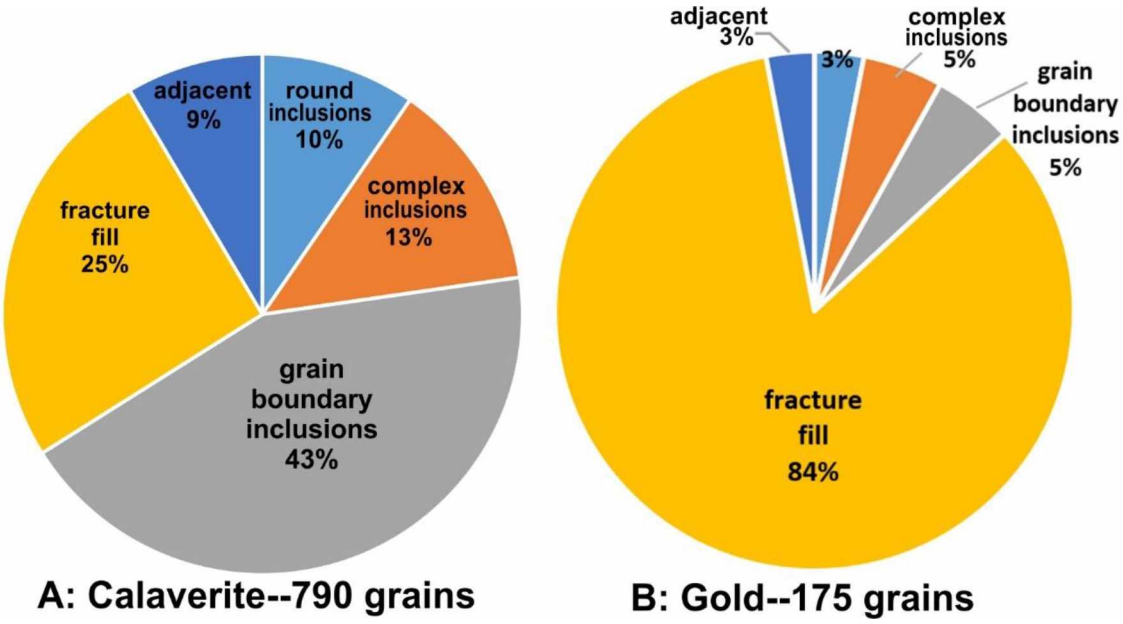

Figure 4.13. Pie graphs showing estimated percentages of ore mineral textures by area, as estimated from reflected light observations. A = calaverite, B = gold.

Table 4.1 gives the ratio of calaverite to calaverite + gold as estimated from reflected light examination, for 19 samples, representing all three zones of the mine (41, 10, and 10P). The average calaverite/ (gold + calaverite) is 84 area %. The three Cu-rich samples yield an essentially identical ratio (85%). For the three samples with measurable fahlore concentrations (from XRF) the ratio drops to an average of 43% (table 4.1). The Cu-rich and fahlore-bearing populations are small, but the huge difference in average % calaverite to gold + calaverite in fahlore- bearing polished sections is remarkable. Indeed, all the samples with low ratios (< 70%) are fahlore-bearing. Samples with fahlore do not have elevated Au concentrations (as grams per ton sulfide), however they have much more gold relative to calaverite. Cu- rich samples also are not especially enriched in Au, but they also have the same average % calaverite to gold as all of the samples. There is no correlation between elevated Au (grams per ton sulfide) and a high relative % native gold to calaverite ratio.

Table 4.2 gives details of relative calaverite areas broken down by textural types. Samples with high Au concentrations (> 700 grams per ton sulfide) measured by XRF generally contain over 10% of the total calculated area of calaverite. Samples 07-1 and 07-2, which are subsamples of the same sample do

not have a large calaverite area (2.7% and 3.6% respectively) relative to the XRF Au concentrations (716 grams per ton sulfide), but the amount of exposed pyrite on the section is relatively small.

Table 4.1. Relative calaverite and gold abundances, from reflected light, with additional XRF data

Sample #	% $AuTe_2/(Au^0+AuTe_2)$	Rel %cp**	re%fahlore**	Au (g/t sulf)**
07-1	100			716
07-2	100			716
1355-210-14	79	**26**		114
1355-201-16a	72	1.1	**1.1**	368
1355-201-16b	80			368
1280-201-6	100	0.1		1071
04-1	80			190
1140-197-6	100			68
08-1	73	0.4		437
1065-206-3	100	**9**		249
1065-189-1	99			991
780-176-2	100	0.2		1846
630-224-4	100			116
555-188-3	99	0.9		288
555-188-5	77	**37**		333
555-160-4*	100			
555-160-5*	18	0.1	**0.1**	353
555-160-8	40	0.8	**3.2**	309
555S-2	70	0.1		1001
Avg % $AuTe_2$/ ($AuTe_2$+ Au^o)	**84 (all)**	**85*** (Cu-rich)	43*(fahlore)	

*Calculated with only bolded values
**From XRF data Red = top 3rd quartile Blank = below detection

The four other elevated Au samples contain significantly more grain boundary inclusions and fracture fill (> 5%). In contrast, the abundance of 'early' rounded and complex inclusions of calaverite do not change appreciably with Au content of the sample. Grain boundary calaverite inclusions are responsible for the largest surface area, but unfortunately, they are of unclear origin. Are grain boundary inclusions early, but 'pushed away' from growing pyrites (instead of engulfed) or are grain boundary inclusions relatively late, filling in spaces between pyrites? The importance of fracture-filling calaverite is difficult to assess because a single sample (1280-201-6) is responsible for 2/3 of the fracture fill area (Table 4.2).

Table 4.2. Relative % calaverite area by slide and grain texture

zone	Slide	round	complex	GB	fracture fill	adjacent	total	Au	slide type
41	07-1	0.4	1.0	1.3			2.7	716	GM*
	07-2	1.1	0.8			1.7	3.6	716	GM
	1355-210-14		0.4	0.3	2.6		3.4	114	PS
	1355-201-16a	0.2	0.7		0.9		1.8	368	PS
	1355-201-16b		0.2				0.2	368	PS*
	1280-201-6	0.4	3.1	6.0	15.2		24.7	1071	PS
	04-1	0.1	0.8	0.3			1.3	190	GM
10	1140-197-6		0.9	1.3			2.2	68	PS
	08-1	1.0			1.8		2.8	437	PS
	1065-206-3				1.0		1.0	249	PS
	1065-189-1	1.9	1.6	17.9	0.2	0.7	22.2	991	PS
	780-176-2		0.5	9.8		0.7	11.1	1846	PS
10P	630-224-4		0.2				0.2	116	PS*
	555-188-3	0.1		0.4		5.4	5.9	288	PS
	555-188-5	4.3					4.3	333	PS
	555-160-4				0.8		0.8		GM*
	555-160-5				0.3		0.3	353	PS
	555-160-8	0.1					0.1	309	PS*
	555S-2		2.9	6.0	2.6		11.5	1001	PS

Slide type: GM = grain mount, PS = polished section Red = elevated Au; GB= grain boundary inclusion
* = slide has <20% sulfide; # = Au concentration in the associated XRF sample, grams Au/ton sulfide.

Table 4.3 gives areas attributed to native gold broken down by slide number and texture. The relationship between native gold and overall Au abundance in a given sample is not as clear. I observed gold in 11 (of 19) polished samples, or only slightly more than half. Samples from zone 10P have a much higher abundance of native gold (73%) than the other zones (table 4.3). However, this is partly due to a single sample (555S-2) which contains 40% of the gold area observed. That noted, nearly all of the zone 10P samples contain native gold; only half of the samples from the other zones do. The gold in sample 555S-2 is principally as fracture fill; further, fracture fill is the dominant style in all but two of the other slides. Notably, most of the higher Au samples contain little native gold.

Table 4.3. Relative % native gold area by slide and grain texture

Zone	Slide	Round	Complex	GB	Fracture Fill	Adjacent	Total	Au	Slide Type
41	07-1							716	GM
	07-2							716	GM
	1355-210-14		0.8		6.4		7.2	114	PS
	1355-201-16a	2.2	0.4		3.0		5.6	368	PS
	1355-201-16b	0.4					0.4	368	PS
	1280-201-6							1071	PS
	04-1		1.6	0.3	0.6		2.5	190	GM
10	1140-197-6							68	PS
	08-1				8.0	0.6	8.6	437	PS
	1065-206-3							249	PS
	1065-189-1		1.2			1.2	2.4	991	PS
	780-176-2							1846	PS
10P	630-224-4							116	PS
	555-188-3	0.3					0.3	288	PS
	555-188-5				10.4		10.4	333	PS
	555-160-4				10.4	0.5	10.9		GM
	555-160-5			3.6	7.2		10.8	353	PS
	555-160-8	0.4			0.5		0.9	309	PS
	555S-2		0.6	1.5	37.8		39.9	1001	PS

Note: abbreviations as for Table 4.2

4.5 Non-Au Telluride Mineralogy and Microscopic Textures

Kensington contains several non-Au species of telluride minerals. All tellurides present at Kensington have similar reflectivity and hardness, which makes distinguishing between them difficult in reflected light. Energy dispersive spectrometry (EDS) on the electron microprobe was used to identify the various non-Au telluride species. See Appendix J for textures of all non-Au telluride grains observed. Table 4.4 lists the minerals found and sample number. I did not exhaustively attempt to find all Te-minerals in a given section and a single sample (1355-210-14) yielded 40% of the identified Te minerals.

Hessite (Ag_2Te), petzite (Ag_3AuTe_2), and coloradoite (HgTe) are the most common non-Au tellurides I found (table 4.2). (Note that most petzite was from sample 1355-210-14, however.) I identified Ag_3AuTe_2 most commonly as inclusions in chalcopyrite veinlets between pyrite grains (Fig. 4.14). All $NiTe_2$ grains observed are filling fractures in pyrite. Coloradoite (HgTe) has the highest variation in texture types, and is the most common non-Au telluride in grain boundary inclusions. Only one polished section contained non-Au telluride (Ag_2Te) grains isolated from other sulfides.

Table 4.4. Observed native, telluride, and accessory sulfide minerals (EDS data)

Zone	Slide	Gold	Electrum	AuTe2	Ag3AuTe2	Ag2Te	AgTe	HgTe	NiTe2	PbTe	Bi2Te3	Fahlore	Galena	Bornite	Fahlore	Molybdenite	Sphalerite
41	1355-201-16a	x		x	x		x	x				x	x		X		
	1355-201-16b	x		x		x					x	x			X		x
	1355-210-14	x		x	x	x	x	x		x	x	x			x		
	1350-13	x		x	x	x	x			x	x	x	x		X	x	
	KEN-04-1	x		x	x												
	KEN-05-PS1*	x		x	x				x		x		x				
	KEN-07-1			x					x								
10	KEN-08-1	x		x				x				x			x		
	1065-189-1	x		x													
	780-176-2			x													
10P	705paste-3	x		x	x						x					x	
	630-224-4	x		x	x		x										
	555-160-2	x						x				x			X		
	555-160-5	x		x				x				x			x		
	555-160-8	x	x	x		x						x		x	X		
	555-188-3	x		x	x												
	555-188-5	x		x	x												
	555S-2	x		x	x	x		x		x		x			x		

*This sample also contains 1 grain of arsenopyrite.

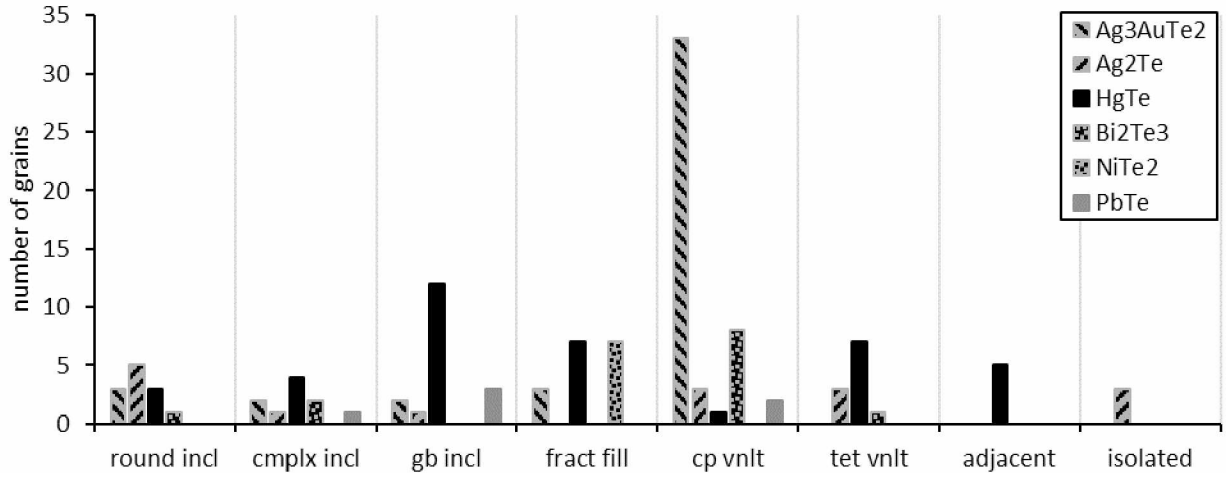

Figure 4.14. Textural distribution of non-Au tellurides. Abbreviations: cp = chalcopyrite, tet = fahlore, incl = inclusion, cmplx = complex, gb = grain boundary, vnlt = veinlet.

Non-Au telluride grains were characteristically seen within 100 µm of another Au bearing mineral or non-Au telluride (Fig. 4.15). One third of all non-Au telluride minerals are located in the vicinity of another non-Au telluride, compared to 40% located in the vicinity of Au-bearing minerals (gold and $AuTe_2$). The remaining one-third of non-Au telluride minerals are isolated.

Sample 1355-210-14 contains 40% of all observed non-Au telluride minerals in all of my polished sections, as counted by number, not surface area. Sample 1355-210-14 is one of the 3 Cu-rich polished sections and has 96% of observed non-Au tellurides occurring as inclusions in chalcopyrite veinlets (only 1 grain of gold is not in chalcopyrite veinlets, everything else is in those veinlets). It is also the only Cu-rich polished section from zone 41. The Cu-rich polished section from zone 10 (sample 1065-206-3) contains only $AuTe_2$ (no gold) and it occurs only in a chalcopyrite veinlet (as seen in reflected light, no EDS data). The only non-Au telluride in the Cu- rich polished section from zone 10P (sample 555-188-5) is Ag_3AuTe_2. Sample 555-188-3 is the only polished section with isolated non-Au tellurides (Ag_2Te). This sample also has an unusual calaverite texture, mostly large (approx. 100 µm) grains isolated in quartz. In other words, telluride mineral textures in Cu-rich samples might not be representative of those minerals in other (pyrite-rich) samples.

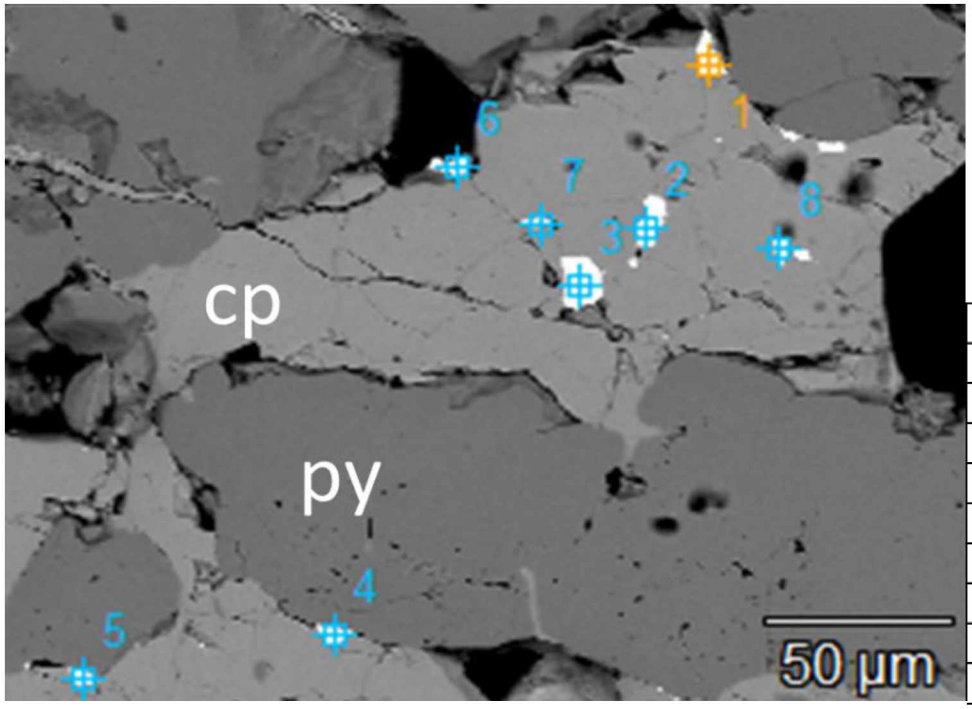

1355-210-14a	
point	mineral
1	Ag3AuTe2
2	Bi2Te3
3	Ag3AuTe2
4	Ag3AuTe2
5	Ag3AuTe2
6	Ag3AuTe2
7	Ag2Te
8	Ag3AuTe2

Figure 4.15. Photomicrograph of a Cu-rich sample showing a typical texture of telluride grains in a chalcopyrite veinlet. Sample 1355-210-14 site A.

4.6 Other Sulfide Minerals

4.6.1 Bornite

I observed bornite in 1 polished section: 555-160-8. It occurs as inclusions in fahlore and chalcopyrite that in turn fill fractures in pyrite (Fig. 4.16). 555-160-8 has 'moderate' concentration of chalcopyrite (0.85 relative % chalcopyrite); higher than average but not Cu-rich.

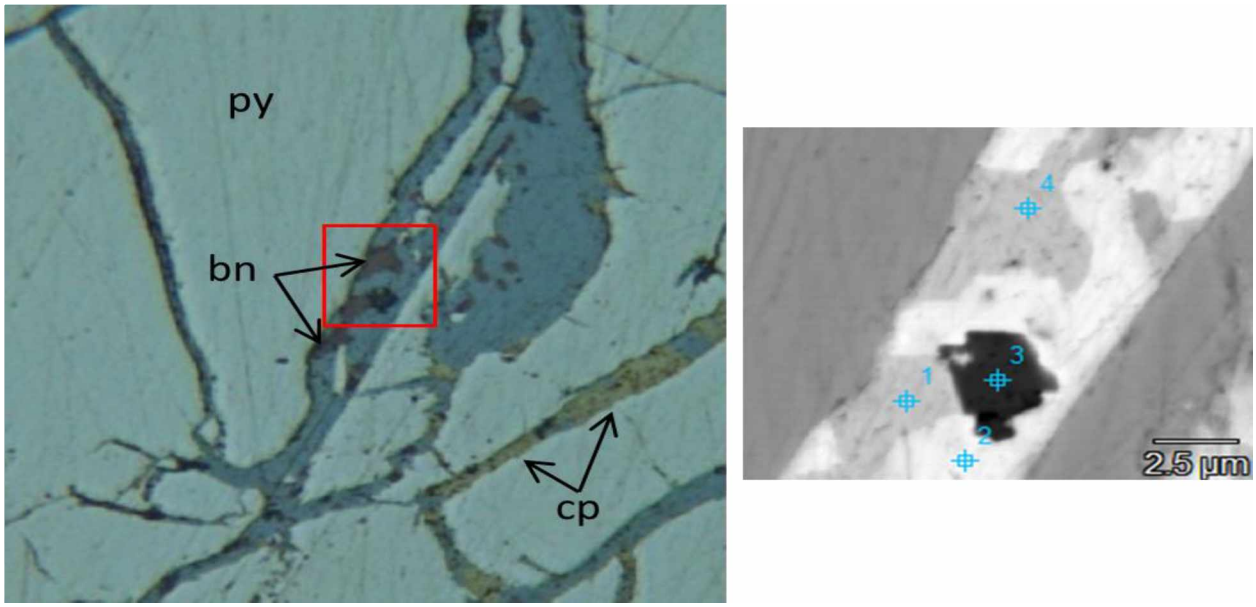

Figure 4.16. . Polished section 555-160-8, showing (left, photomicrograph) bornite as inclusions in fahlore (darker blue) and (right, BSE image) bornite in chalcopyrite veinlets filling fractured pyrite. The black mineral in the BSE image is ankerite.

4.6.2 Molybdenite

Despite extensive searching, I found Molybdenite in only 2 polished sections--via EDS (Table 4.4, Fig. 4.17). Sample 705paste-3 (zone 10P) contains tiny molybdenite grains intergrown with muscovite (Fig. 4.17A) and not with pyrite. This sample also yielded hand-held XRF data showing an increase in Mo with increase in muscovite and decrease in pyrite (Fig. 2.20B.) In this sample most of the MoS_2 occurs as flakes 5-10 x 1-3 microns, making them virtually invisible in reflected light. Although present in the general vicinity of pyrite, they are clearly outside of—and unrelated to—the pyrite. The timing of MoS_2 deposition in this sample relative to pyrite is unknown.

The other sample with identified MoS_2 is from zone 41 (sample 1350-13), more than 600 feet (200 m) above the first. In this sample I observered MoS_2 as clots approximately 10-15 microns in diameter, surrounded by pyrite (Fig. 4.17B). Hand-held XRF data from this sample (Fig. 2.20A) showed

increasing concenration of Mo with increasing sulfide. In this case MoS_2 precipitation took place during or before pyrite. Unfortunately, I do not know which style of MoS_2 deposition is typical of the higher-Mo samples.

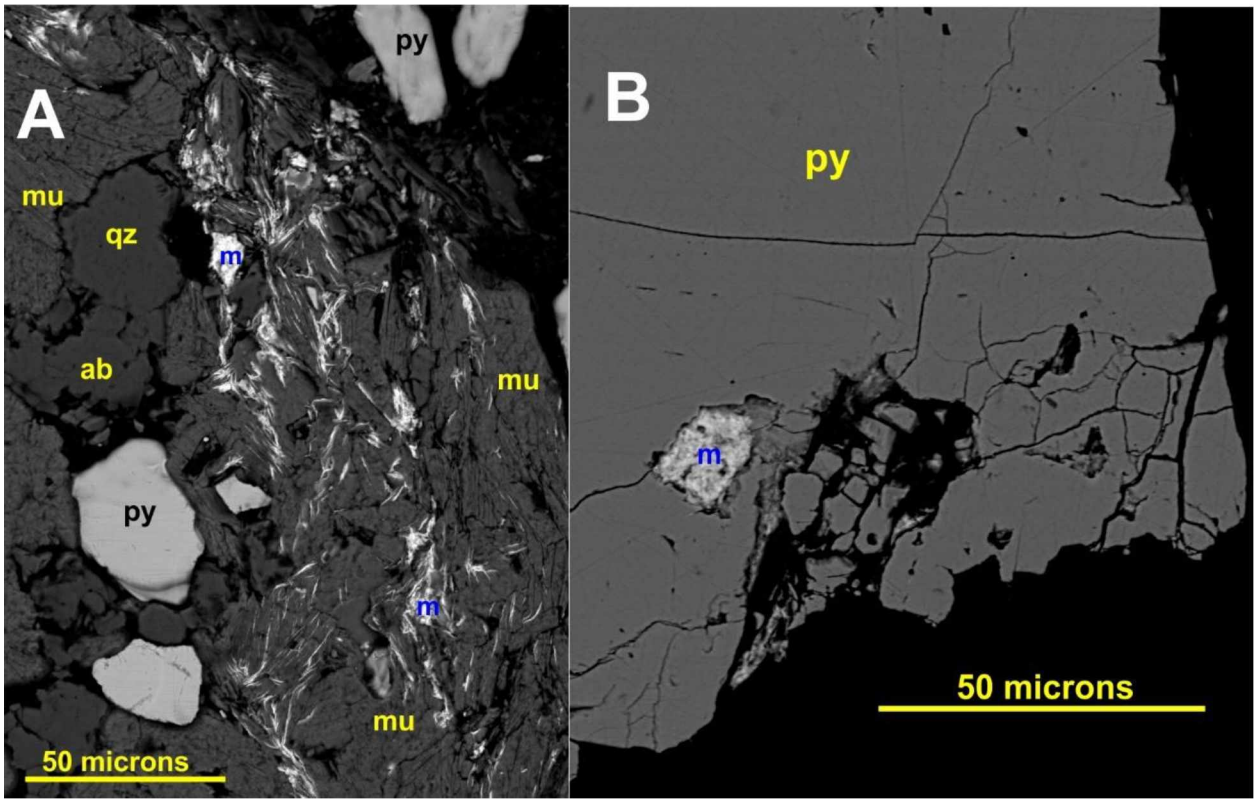

Figure 4.17. BSE images showing two contrasting styles of MoS2 occurrences. A) MoS2 with muscovite, outside of pyrite (sample 705Paste3). B) MoS2 clump as an inclusion in pyrite (sample 1350-13).

4.6.3 Galena

I found Pb minerals in 5 polished sections (all from samples with high Pb), and galena in 3 of them (Table 4.4). Galena occurs as sub-micron grains along pyrite margins, as small (< 5 µm) inclusions in fahlore- filled fractures between pyrite grains (Fig. 4.18), and as tiny grains outside of, but near, pyrite. That is, all occurrences of galena texturally post-date pyrite formation. They are also all from zone 41. I found 1 tiny (0.3 micron diameter) grain of PbTe in sample 1350-13, which makes it the only sample to contain both Pb minerals (Table 4.4). Sample 555S-2--the other high Pb sample, from zone 10P, appears to contain altaite (PbTe) but not galena (Table 4.4). Unfortunately, this is the only high-Pb sample outside of zone 41 for which I have a polished section. Consequently, it appears that galena is restricted to zone 41, but this may be simply an artifact from limited samples.

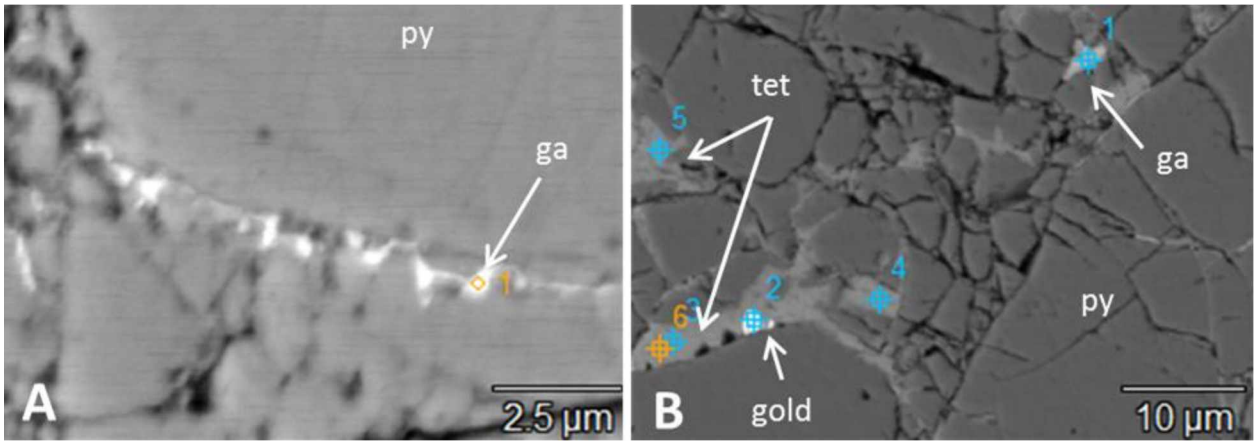

Figure 4.18. BSE images from polished section 1355-201-16a illustrating textural occurrences of galena

4.6.4 Arsenopyrite

I found a single 3 x 1 micron grain of arsenopyrite, isolated from other sulfide minerals, in a breccia zone in sample KEN-05-PS1 (Table 4.4). The sample contains very little chalcopyrite, and none within a centimeter of the arsenopyrite. I believe that this is the first confirmed arsenopyrite found at Kensington.

4.6.5 Sphalerite

I found Sphalerite in 1 polished section (1355-201-16b) which has the second highest Zn concentration (XRF). Sample 555-160-8 has over twice as much Zn; however, I could not find sphalerite in it. This sample also contains abundant fahlore, and based on XRF data (Chapter 2), the fahlore contains abundant Zn. The sphalerite grain in 1355-201-16b is very small (approximately 5 microns, Fig. 4.19) and such grains could be easily overlooked.

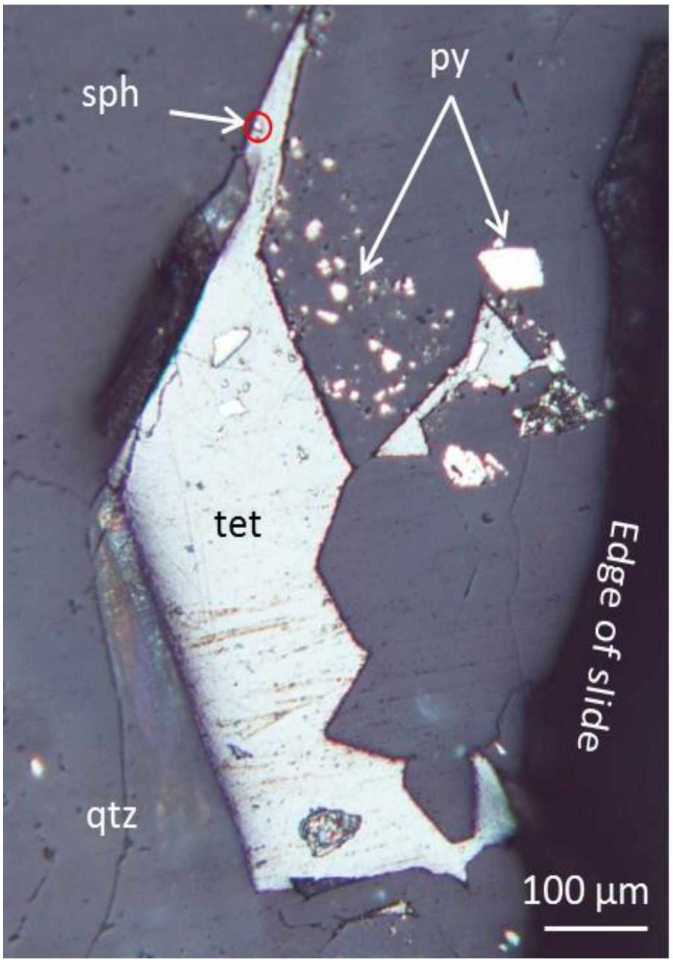

Figure 4.19. Photomicrograph showing tiny sphalerite grain in fahlore from polished section 1355-201-16b. The sphalerite grain is in the red circle.

4.7 Discussion and Conclusions

There is a strong correlation (R2 = 0.49) between Au concentrations measured by XRF and the total calaverite + gold area observed in reflected light surveys. This is especially impressive considering the XRF data is normalized to 100% sulfide, but the reflected light areas are not. Further, the sample for reflected light examination is not identical to that analyzed by XRF. There is a significant range in total sulfide surface area between polished sections. Ultimately, this indicates that what I observed by reflected light microscopy matches reasonably well with the XRF chemical analyses.

I categorized six types of microscopic textures; but these can be broadly broken into two types: pre- or syn-pyrite and post-pyrite. Simple rounded and complex inclusions must have formed before or during pyrite growth in order to have been engulfed by pyrite. (But note that elongate trails of simple inclusions might represent healed fractures in pyrite, e.g., Fig. 4.9b). Grain boundary inclusions probably formed during or before pyrite and were trapped between pyrite grains, instead of being surrounded by

pyrite grains. On the other hand, minerals that occur (directly or indirectly) in fractured pyrite are post-pyrite. Minerals adhering to pyrite ('adjacent') likely formed after pyrite, but initial growth might have been syn-pyrite. I suspect that isolated grains in quartz or calcite formed relatively late; if they had predated pyrite they would have likely been engulfed by it.

Two-thirds (by surface area) of the calaverite I identified is present as inclusions of one sort or another, i.e. pre- to syn-pyrite (Fig. 4.13A). Furthermore, 2/3 of the fracture fill calaverite grains came from a single sample (out of 19). I think it is fair to conclude that most of the calaverite deposition took place before or during pyrite formation. Interestingly, the abundance of rounded and complex calaverite inclusions is essentially independent of calaverite abundance in a sample, but grain boundary inclusions are much more abundant in samples with greater calaverite concentrations (Table 4.2). In other words, whatever conditions caused grain boundary calaverite to form varied more than the conditions required for rounded and complex inclusions. Samples with higher gold grades generally contain a greater abundance of 'grain boundary' calaverite inclusions. From a metallurgical perspective, such grains would more readily yield calaverite during crushing, as they would tend to break along such boundaries. Lower grade (measured as grams Au/ton sulfide) materials seemingly possess a larger proportion of calaverite 'encapsulated' by pyrite.

Native gold is overwhelmingly observed as fracture fills in pyrite, although many instances are complex fractures with gold as merely one of several minerals in the fracture (e.g., Fig. 4.9 b). In sample Ken-05-PS1, for example, most of the gold is present with $NiTe_2$ fracture fills. With the exception of one sample (780-176-2) gold always occurs with non-Au telluride minerals +/- fahlore. The converse is also true: all samples with non-Au telluride minerals (+/- fahlore) contain identified native gold. It is fair to conclude that the bulk of native gold was deposited after pyrite and after the bulk of calaverite.

My survey of non-Au telluride minerals and their textures was less extensive than that for Au minerals and based exclusively on identifications made with the electron microprobe. (As many of these minerals are present as 1-3 micron grains, exhaustively examining a single section would have taken a day or more). The non-Au telluride minerals always occur in samples with native gold; the one sample I examined by microprobe that contained calaverite without gold also lacked other telluride minerals (Table 4.4). Nevertheless, most of these minerals occur with textures suggesting or indicating deposition after pyrite (e.g., Fig. 4.14). Where textures are unambiguous, they indicate fahlore deposition entirely post-dated pyrite. Furthermore, all fahlore occurrences are present in slides with native gold and with non-Au telluride minerals (Table 4.4).

Galena, bornite, and sphalerite are extremely rare and present largely as inclusions in post-pyrite fahlore veinlets filling pyrite fractures. In fahlore-absent sample KEN-05-PS1 galena instead occurs with $NiTe_2$. My two identifications of molybdenite (Fig. 4.17) are (a) associated with muscovite, well away from pyrite and (b) as an inclusion near the edge of a pyrite grain. The former is of unknown timing relative to pyrite. Based on the common occurrence both as rounded or complex inclusions and as fracture fills in pyrite, chalcopyrite deposition both pre-dated and post-dated pyrite.

These mineralogical observations clarify the elemental correlations seen (and not seen) in the XRF data. Even though the non-Au telluride minerals (and fahlore) occur predominantly with native gold, the bulk of Au at Kensington is as calaverite. Consequently there's no correlation between these elements (Pb, Hg, Ag, Bi, Ni, Sb, As, Zn) and Au. Furthermore, the various non-Au Te elements and fahlore are not consistently associated. For example, fahlore always occurs with non-Au Te minerals, but not always with the same ones, hence the poor correlations between Sb-As-Zn and other elements.

Based on textural observations, I infer that the bulk of calaverite deposition took place before or during the deposition of pyrite and that the bulk of gold, of non-Au telluride minerals, tetrahedrite, and galena were deposited after pyrite. To the extent that all pyrite was deposited at about the same time, this requires calaverite deposition before Au + non-Au Te minerals. I attempt to test this hypothesis through identification of pyrite (and other mineral) 'generations' based on their chemical compositions in Chapter 5.

5 Mineral Compositions and Mineral Zonation

In chapter 4 I discussed the potential timing implications of different ore inclusion textures (e.g., rounded inclusions vs. fracture fill) in pyrite. This chapter will focus on differentiating the various ore mineral inclusion populations based on composition as well as mineral zonation. The compositional data used in this chapter will primarily be EDS with comparisons to the corresponding XRF data.

Four minerals will be discussed in this chapter: native gold, calaverite, pyrite, and fahlore. Both native gold and calaverite contain at least trace amounts of Ag, which can be used as a population marker. Non-Au tellurides similarly can contain other trace metals, however the grains are usually small (< 30 μm) and insufficiently abundant to collect a meaningful data set.

Pyrite is the primary ore hosting sulfide and as such I have focused on looking for evidence of multiple Au-bearing pyrite generations through variations in cobalt concentrations. Fahlore is commonly zoned and there are two spatially separate locations for fahlore-bearing specimens (Southern zones 41 and 10P, Fig. 2.18). In this chapter I will examine the compositions of the two populations.

5.1 Calaverite Composition Variability

Calaverite usually contains trace Ag, and can contain up to 3.5 wt % Ag (Nekrasov, 1996). Given the relatively high error ($\pm$ 0.15 wt % Ag) associated with my EDS technique and the limited number of calaverite grains analyzed with multiple points, it is difficult to determine the extent to which larger grains have homogeneous Ag concentrations. However, with these limits on my data I can state that there are no gross changes in Ag concentration within a given grain (e.g., Fig. 5.1).

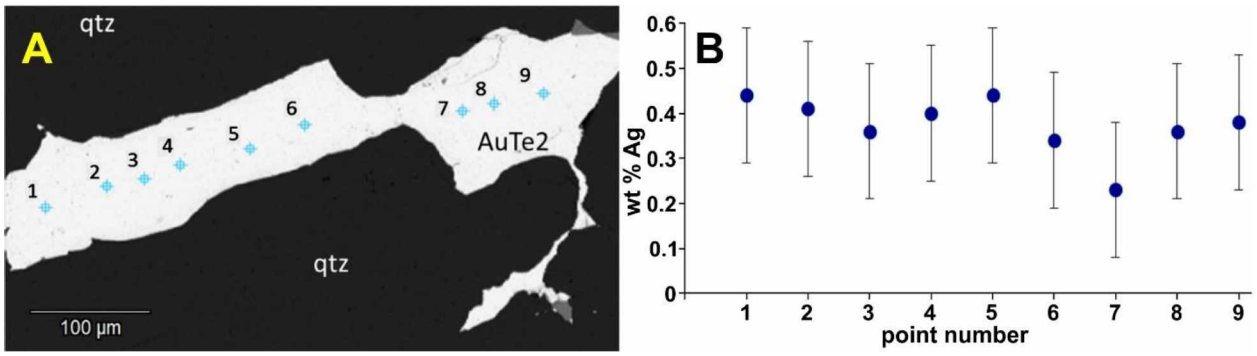

Figure 5.1. Calaverite compositional variations in a large grain aggregate. A) (Left) BSE image showing analysis locations. B) (Right) compositions plotted with estimated uncertainties. Average composition = 0.37 + 0.06 wt% Ag which is well within the estimated analytical error of ±0.15 wt%.

An obvious possible reason for changes in calaverite composition is timing, as suggested by calaverite textural type (Chapter 4), e.g., rounded inclusion vs. fracture filling pyrite. I originally was not collecting Ag compositions from calaverite grains, so I don't have abundant or even representative data points for each type of calaverite inclusion from multiple polished sections. Given that proviso, figure 5.2 provides a summary of Ag concentrations (EDS data) in calaverite by grain type. Almost a third (28%) of the analyses yielded Ag concentrations below detection limits (0.05 wt% Ag).

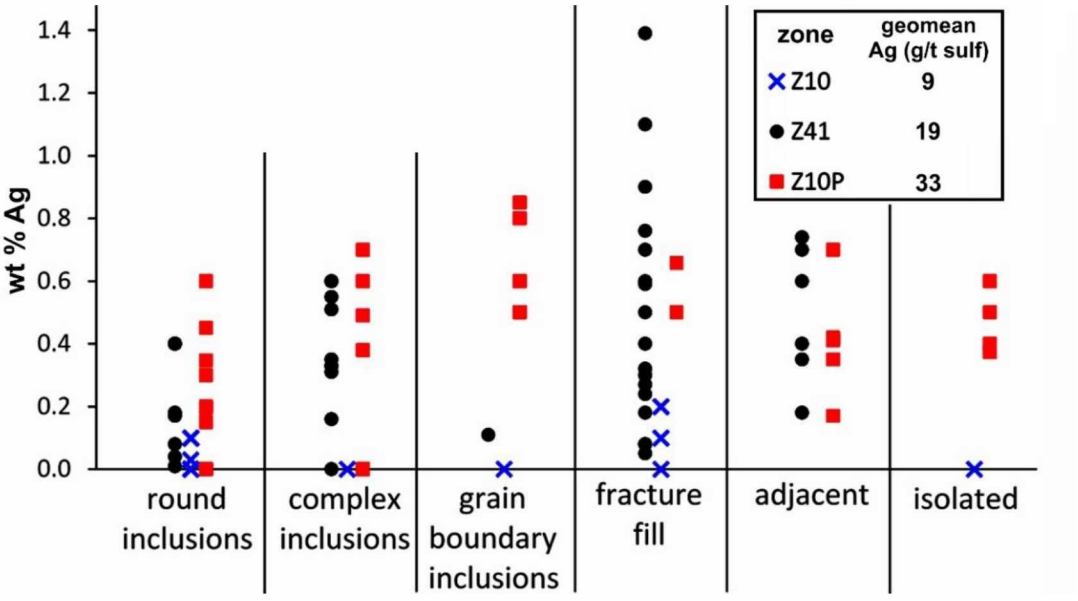

Figure 5.2. Ag wt% in calaverite grains from EDS data. All grains with multiple points have been averaged to eliminate duplicates. This data represents 14 polished slides from 13 individual samples. Geometric mean Ag concentrations for each zone are shown for comparison.

All calaverite grains analyzed from the 3 zone 10 samples contain little (< 0.10 to 0.25 wt %) Ag. In contrast calaverites from zones 41 (6 samples) and zone 10P (8 samples) have a much larger range in Ag concentrations (up to 1.4 wt %). This variation parallels the geomean Ag concentrations from each zone, with Ag in zone 10 samples much lower than the others (Fig. 5.2).

Compositional data for calaverite and gold combined with XRF data (Table 5.1) appears to show some patterns. There is a modest correlation between total Ag concentrations of a sample (XRF) and average Ag concentrations in calaverite (table 5.1) from that sample (Fig. 5.3). Similarly, higher wt% Ag in calaverite is generally associated with the presence of either petzite or hessite (Table 5.1). These data are too imprecise to determine whether sample type or vein type is an indicator for Ag in calaverite. Given the uncertainties in the calaverite compositions, it is fair to say that generally higher XRF Ag is associated with presence of Ag tellurides and higher wt% Ag in calaverite.

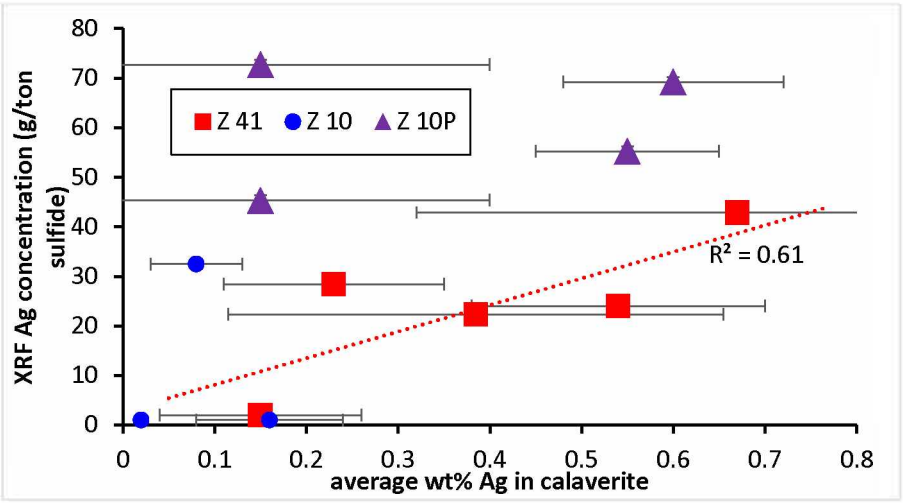

Figure 5.3. Average wt% Ag in calaverite vs. XRF Ag concentration in the sample, by zone. Regression line is for the zone 41 data only. Error bars represent 1 standard deviation.

Table 5.1. Measured Ag Concentrations (wt %) in Calaverite and Gold Grains (EDS) with sample data

zone	Sample name	sample type	vein type	sulfide texture	Ag/ (Ag+Au) (XRF)	Ag in calaverite			Ag in gold		
						avg wt%	stdv	# grains analyzed	avg fineness	stdv	# grains analyzed
41	1355-201-16	bx	bx	bands	0.25	0.68	0.3	7	937	3	9
						0.09	0.1	2	913	3	2
	1350-13avg	bx	bx	bands	0.46	no data			837	86	4
	1355-210-14	Cu	disc	clots	0.39	0.67	0.4	3	937	2	7
	1355-201-13	py	disc	clots	0.04	no data			no data		
	KEN-04avg	py	disc		0.16	0.54	0.2	13	no data		
	KEN-05avg	py	disc		0.08	0.23	0.1	5	897	27	9
	KEN-07	py	disc		0	0.15	0.1	12	no data		
10	KEN-08avg	py	MPB	MPB	0.11	0.03	0.0	8	907	4	3
	1065-189-1	py	net		0	0.16	0.1	12	955		1
	780-176-2	py	disc	bands	0	0.02	0.0	5	no data		
10P	705-PASTE-3	py	disc	clots	0.20	0.15	0.3	3	no data		
	630-224-4	py	disc	bands	0.40	0.15	0.3	4	no data		
	555-160-2	py	disc	bands	0.13	no data			870		1
	555-160-5	py	disc		0.13	no data			912	5	7
	555-160-8	py	disc	bands	0.68	0.21	0.1	4	841	15	15
	555-188-3	py	disc	clots	0.01	0.40	0.1	8	no data		
	555-188-5	Cu	net	clots	0.22	0.55	0.1	4	no data		
	555S-2	py	disc	bands	0.10	0.60	0.1	10	937	4	4

Notes: Cells highlighted in yellow indicate samples with Ag-bearing tellurides. Abbreviations: bx = breccia, py = pyrite, cp = chalcopyrite, MPB = massive pyrite body, disc = discreet, net = network, stdv = standard deviation.

5.2 Variations in Gold Composition

Gold compositions are historically presented as fineness = 1000* Au/(Au + Ag) by weight. All gold grains that I analyzed several times by EDS yielded fineness values with standard deviations within the analytical error for Ag (±0.2 wt %, Fig. 5.4). As best I can tell (with limited data) there is no significant compositional zoning in the gold grains I analyzed. Given the major differences in atomic number between gold and silver, I would expect to see some variations in BSE brightness if significant zoning was present. I did not see such.

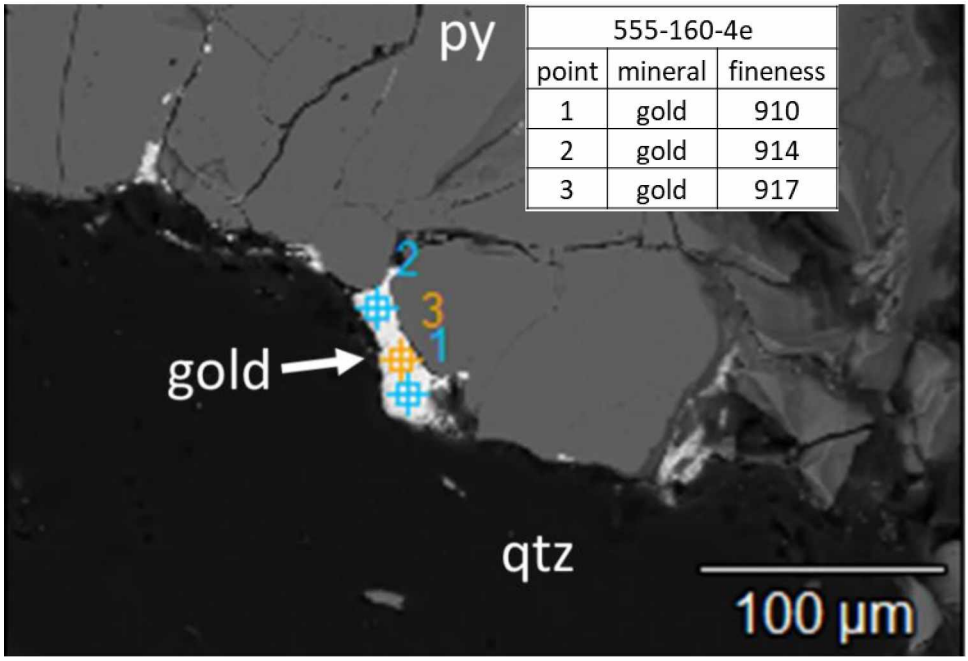

555-160-4e		
point	mineral	fineness
1	gold	910
2	gold	914
3	gold	917

Figure 5.4. BSE image of sample 555-160-4 site E, showing an anhedral gold grain adjacent to a pyrite mass in quartz. This grain has an average fineness of 914 + 4.

Gold fineness in my polished sections ranges from 720 to 955 with an overall average of 892 (Fig. 5.5). Some sections yielded a large range in gold compositions; others apparently did not. (Complete mineral compositional data are given in Appendix L). Variability in composition (as measured by standard deviation) generally increases as fineness decreases (Table 5.1). The data set suffers from limited number of analyses; in three cases I only have 1-2 analyses per slide. I suspect that the variation in fineness is greater than that shown on Table 5.1 and Fig. 5.5, as illustrated by sample 1355-201-16. For this sample I prepared two different sets of pyrite grain mounts. One (Table 5.1) yielded average fineness of 937 $\pm$ 3 (9 grains) and the other 913 $\pm$ 3 (2 grains). Clearly, these do not overlap.

Fineness is the most heterogeneous for gold filling fractures in pyrite, especially for samples from zones 41 and 10P (Fig. 5.5). The considerable variability in fracture fill gold fineness is based on two samples, 555-160-8 and 05-PS1. I shudder to think what additional data might generate. All other samples have relatively homogeneous gold fineness independent of texture.

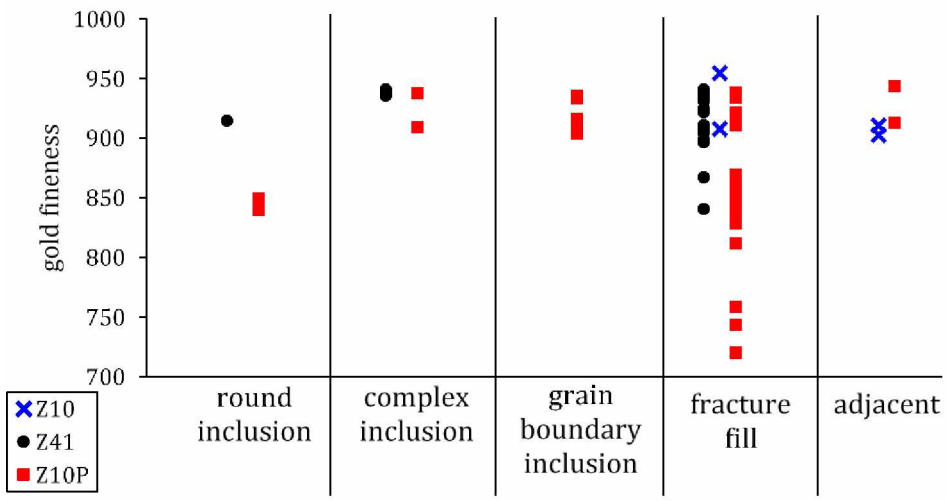

Figure 5.5. Fineness (=Au/Au+Ag) for gold grains from EDS data. All duplicates have been averaged. This data represents 11 polished slides from 10 individual samples the only gold grain texture type with seriously heterogeneous fineness is fracture fill. Zone 10P fracture fill gold grains have the largest range in fineness (720 – 950).

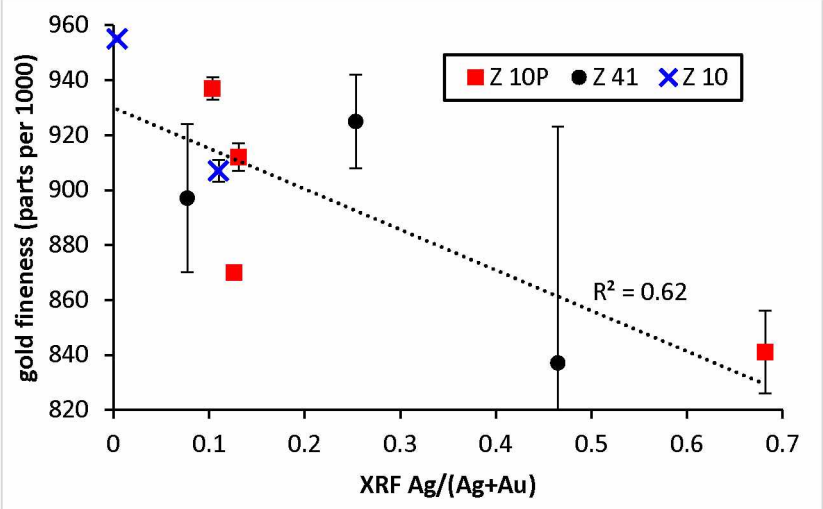

Figure 5.6. Gold fineness vs. sample Ag/(Ag+Au) from XRF analysis for points distinguished by zone. The regression line is for all the points. Error bars represent 1 standard deviation for compositions of all gold grains in the sample; samples lacking error bars represent single grain analyses.

Figure 5.6 shows that the fineness data display a modest correlation with sample Ag/Au+Ag (XRF). That is, higher relative silver concentrations in a sample are reflected in gold with higher Ag contents. Given the commonly large uncertainties in sample average gold fineness, and the large number of samples with fineness for just 1-2 grains, one can only speculate that better data would show

a better trend. Given the serious uncertainties in calaverite and gold compositions, plotting them against each other to look for a trend is pointless.

Sample 555-160-8 is from zone 10P and has the second highest Ag concentration of all the samples (~ 400 g Ag/ton sulfide). Based on the compositions of gold filling fractures, this sample yielded two populations of gold fineness with averages of about 845 and 760 (Fig. 5.7). This sample also contained two rounded inclusions of gold with fineness of 840-850. These two grain compositions fall within the 'high' fineness group that is also present in the fracture fill gold grains (Fig. 5.7).

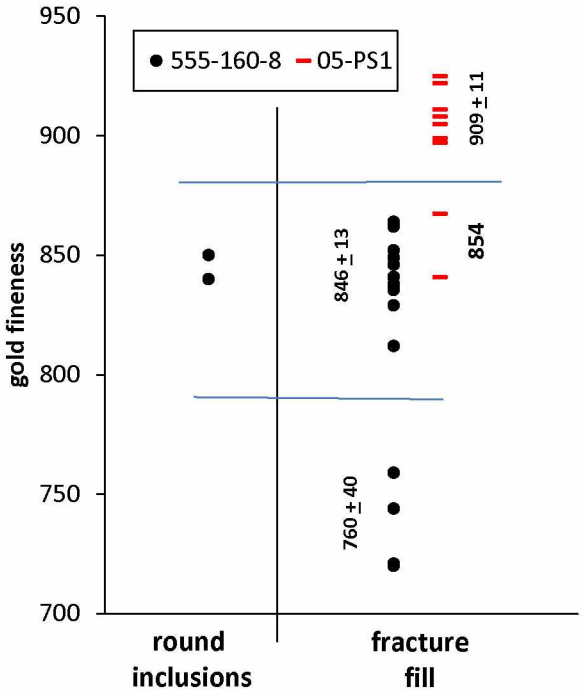

Figure 5.7. Gold fineness from samples 555-160-8 and 05-PS18. All grains with multiple analyses have been averaged to eliminate duplicates. Sample 555-160-8 is from zone 10P and 05-PS1 is from zone 41.

Sample 05-PS1, from zone 41, has a lower but measurable XRF Ag concentration of 28 grams per ton sulfide. The range in gold fineness for this sample is much smaller than that of sample 555-160-8; however it also has much less Ag overall. Sample 05-PS1 contains fracture fill gold grains with two possible gold populations. The 'low' fineness group consists of two grains with an average fineness of 854 and a 'high' fineness group with an average of 909.

5.3 Fahlore Compositions

Tetrahedrite-tennantite solid solution (fahlore) has a complicated composition, commonly given as $(Cu,Ag)_{10}(Zn,Fe)_2(Sb,As)_4S_{13}$. Back-scattered electron imaging (BSE) shows that at least some Kensington fahlore is compositionally zoned (e.g., Fig. 5.8B, 5.9B), which complicates determining fahlore compositional variations. Sample 1355-201-16 has the second highest relative % tetrahedrite (1.13 wt%, from XRF). Larger fahlore grains show complex compositional bands (e.g., Fig. 5.8, 5.9), while smaller fracture filling fahlore grains display more obscure compositional zoning.

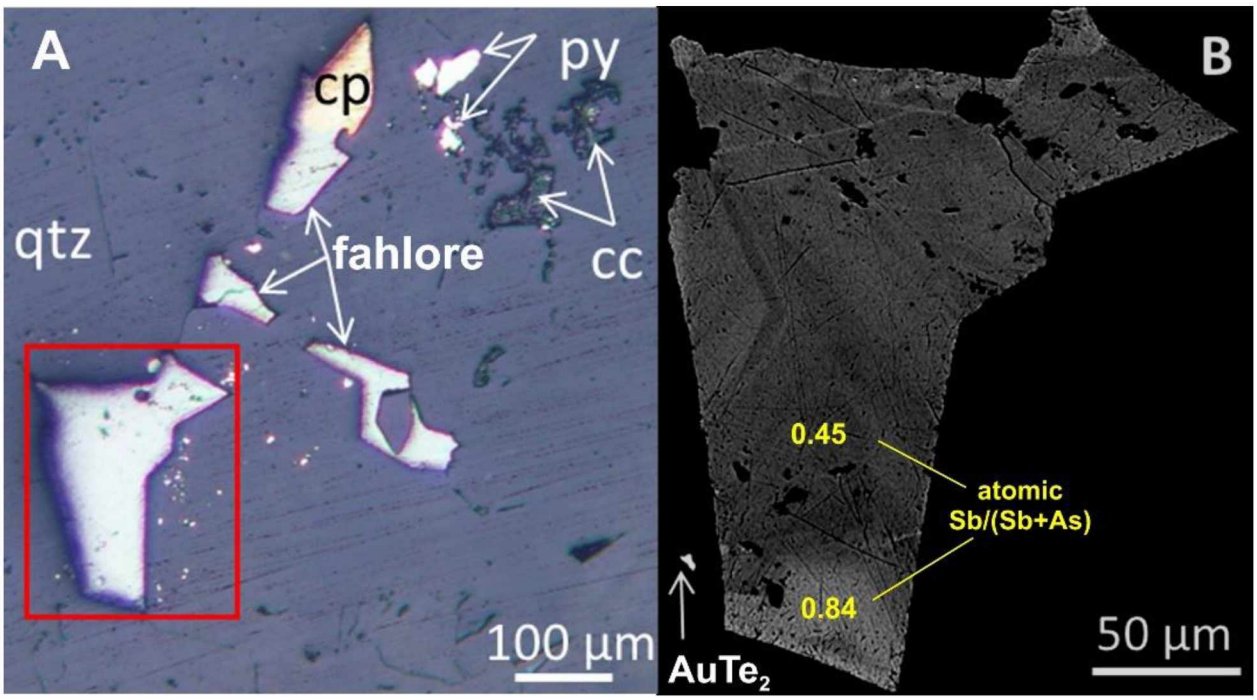

Figure 5.8. Photomicrograph A) and BSE image B) showing a compositionally zoned fahlore and surroundings. Brighter BSE = higher Sb. Sample 1355-201-16B. py = pyrite, cc = calcite, qtz = quartz.

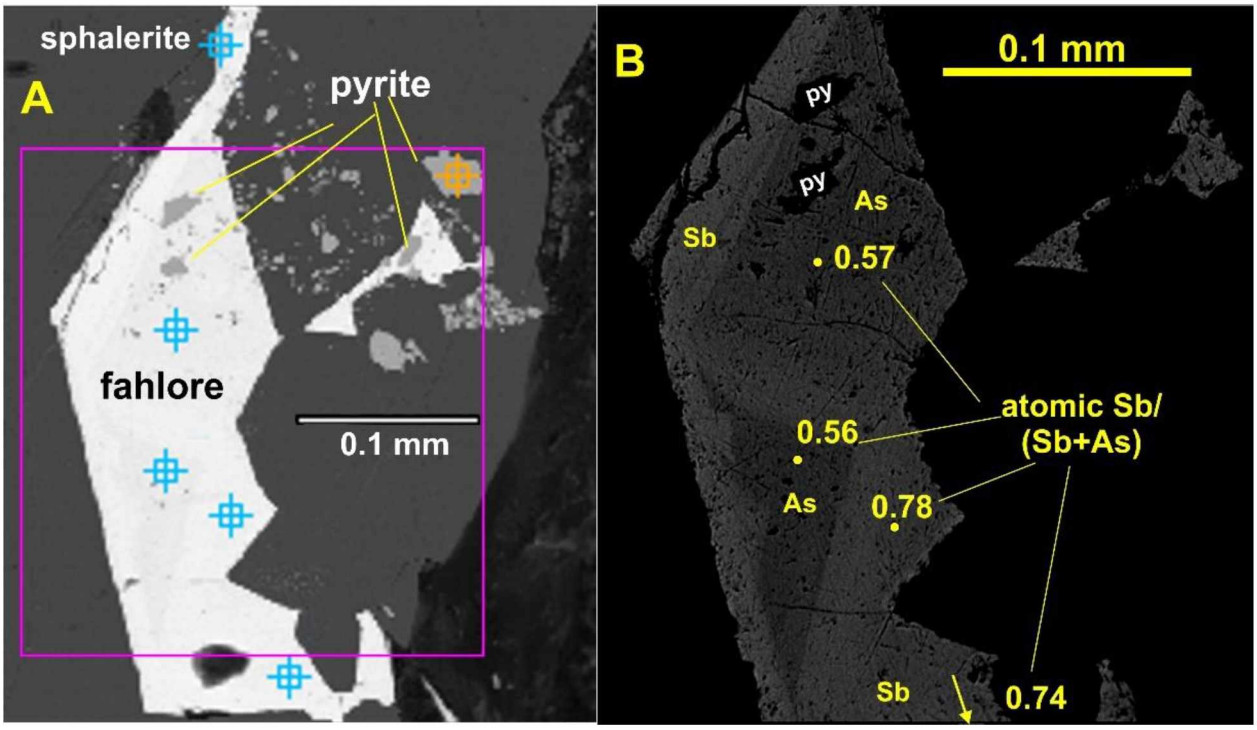

Figure 5.9. BSE images of zoned fahlore with pyrite inclusions and analyses. A) 'Normal' BSE w/ magenta box showing area of B) maximum contrast, pyrite now black. Sample 1355-201-16b.

Based on the XRF data, fahlore is present at calculated abundance of up to about 3% (sulfide normalized). Based on the assumption that all As and Sb at Kensington are present in fahlore (and not other minerals) the calculated average fahlore has atomic Sb/Sb+As of 68 ± 13%. Most calculated compositions yield (Sb/As+Sb) between 64 and 77%. That is, the mineral is technically 'tetrahedrite' (>50% of that component) but it has sufficient As to be considered the intermediate mineral, and not the end-member.

Table 5.2 gives representative EDS fahlore analyses, both as wt% and cations calculated for 13 S, based on analyses from 6 different polished sections (3 each from zones 41 and 10P). Note that the sum of Cu+Ag is always low (should be 10, is actually 8.7-9.8), Zn+Fe is generally high (should be 2, is actually 1.9-2.5), and Sb+As is generally high (should be 4, is actually 3.9-4.4). Nevertheless, the cation abundances are close enough to theoretical values for qualitative purposes. Clearly, major variations in relative Sb and As concentrations bear out the zoning seen in BSE images. Zn is always present at a concentration of 7-9 wt%. Silver is generally above detection, but invariably low. Table 5.2 includes fahlore with the highest (1.7%) and one of the higher (0.6%) silver contents.

Table 5.2. Representative EDS fahlore analyses from the Kensington deposit

Weight %							Cations Based on 13 S									
Cu	Ag	Zn	Fe	Sb	As	S	Cu	Ag	Cu+ Ag	Zn	Fe	Zn+ Fe	Sb	As	As+ Sb	%Sb/ (As+Sb)
39	0.2	6.8	1.4	10	14.0	28	9.3	0.03	9.3	1.6	0.4	2.0	1.2	2.9	4.1	29
36	0.2	9.1	1.2	20	7.2	26	8.9	0.03	8.9	2.2	0.3	2.5	2.6	1.5	4.1	63
35	1.7	8.7	0.9	22	5.9	25	9.1	0.27	9.4	2.2	0.3	2.5	3	1.3	4.3	70
38	0.3	6.3	1.1	23	5.1	26	9.7	0.05	9.8	1.6	0.3	1.9	3.1	1.1	4.2	74
37	0.3	7.7	1.2	24	4.7	25	9.5	0.04	9.5	2.0	0.3	2.3	3.3	1.0	4.3	77
36	0.6	7.0	1.3	25	4.4	25	9.3	0.09	9.4	1.8	0.4	2.2	3.4	1	4.4	77
38	0.2	6.9	1.3	24	3.4	26	9.6	0.03	9.6	1.7	0.4	2.1	3.2	0.7	3.9	82
34	0.1	7.1	1.5	29	2.4	26	8.7	0.02	8.7	1.8	0.4	2.2	3.9	0.5	4.4	89

A histogram of wt % Ag in Kensington fahlore (Fig. 5.10A) shows that most concentrations are < 0.2 wt% Ag, that is, barely above detection limits. Very rare higher Ag concentrations were encountered, but at least one of these may have been enhanced by nearby grains of Ag telluride. In comparison, a histogram of calculated XRF-derived wt% Ag in fahlore (assuming all Ag is there) requires much more silver than is actually present. Thus, the correlations between Ag and Sb-As-Zn (Table 2.4) seen in the XRF data, must be due to mineralogical association, not solid solution.

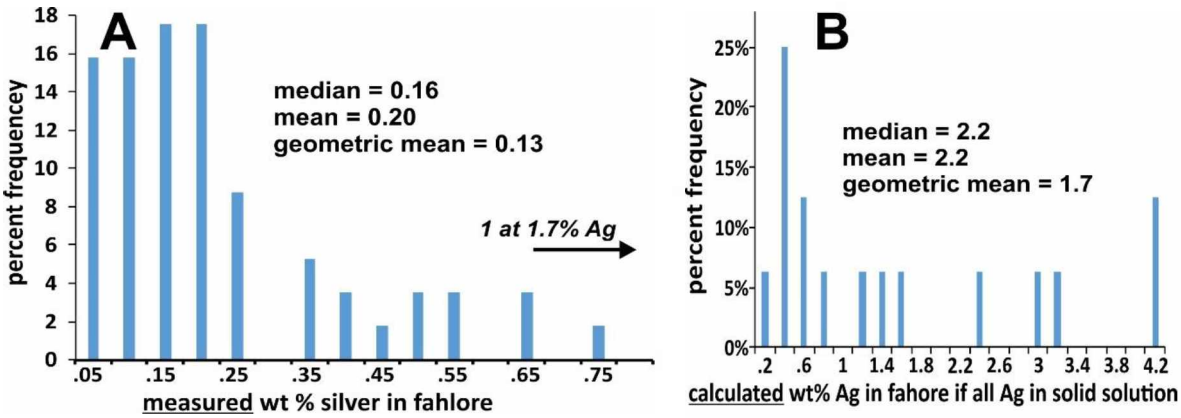

Figure 5.10. Histograms of EDS Ag concentrations in fahlore. A) Based on measured microprobe-based EDS data. B) Calculated from XRF data, assuming all Ag is present in solid solution in fahlore. The calculated Ag concentrations are not unreasonable for Ag-rich fahlore, but based on microprobe data, Kensington fahlore is not Ag-rich.

I did not conduct a systematic survey of all fahlore grains in all six polished sections, but rather focused on fahlore where other ore minerals were present. That is: the EDS data is limited to random fahlore grains. That said, the mean compositions as atomic Sb/(Sb+As) from EDS points (Fig. 5.11)

matches quite well with the calculated compositions from XRF data for samples 1355-201-16 (A and B are splits from the same sample) and 555-160-8. That is, within analytical uncertainties and despite the tremendous compositional variability even on the scale of a single grain (Figs. 5.8, 5.9), compositions calculated from XRF data match those determined by semi-quantitative microprobing.

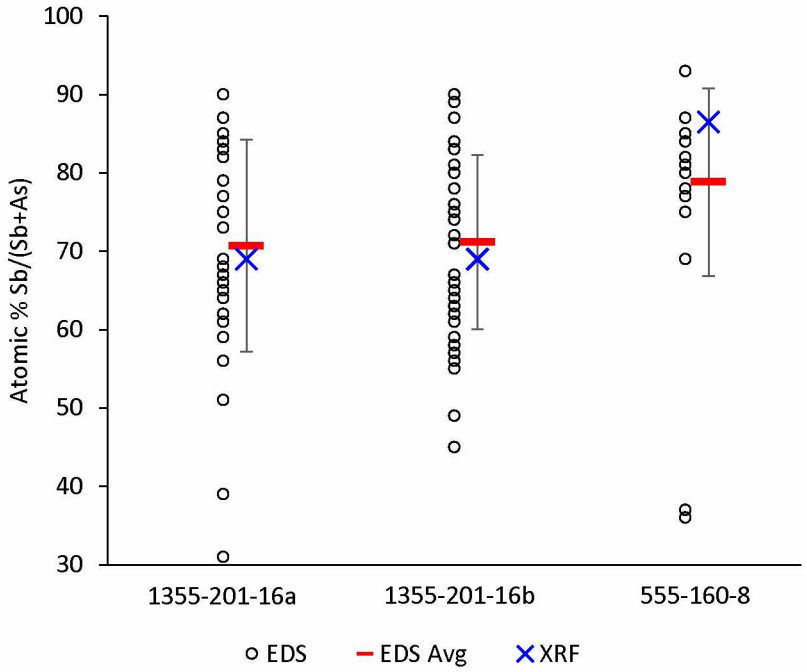

Figure 5.11. Fahlore compositions presented as atomic % Sb/(Sb+As) from EDS microprobe compared to that those determined from XRF data for 3 samples. Error bars represent 1 standard deviation.

I measured far fewer fahlore compositions from slides 55-160-4, 55-160-2, and 1350-13; certainly not enough to compare to XRF compositions. However, I combined these compositions with the others to create 'average' fahlore composition for zones 41 and 10P and compare those to XRF-derived average compositions (Fig. 5.12).

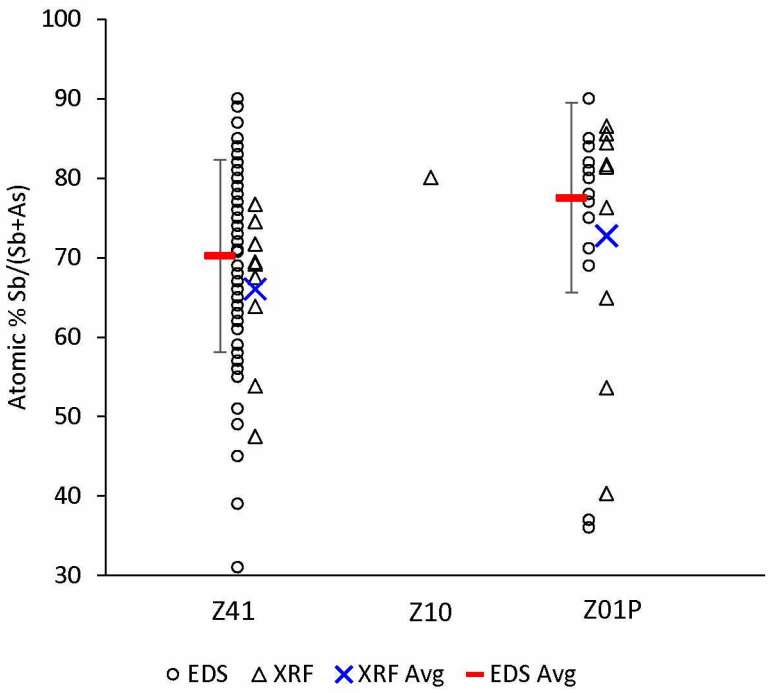

Figure 5.12. Calculated atomic % Sb/(Sb+As) for fahlore from different Kensington mine zones, using both microprobe EDS and XRF data. Only one sample from Z10 (a massive pyrite body) yielded sufficient Sb and As to calculate a fahlore composition. Error bars represent 1 standard deviation.

Fahlore from both zones (41 and 10P) have compositional (atomic Sb/As+Sb)) means (Fig. 5.12) using microprobe EDS data that are essentially indistinguishable from those calculated from the XRF data. Compositions calculated from XRF data assume that all Sb and As in the analysis are present in the mineral fahlore; the compositions become more uncertain as the absolute concentrations of As and Sb falls. Although mean atomic Sb/(As+Sb) is slightly different for the two zones and for microprobe vs. XRF data, the mean values are statistically indistinguishable. There is only 1 sample from zone 10 that had sufficient As and Sb to reliably calculate the tetrahedrite composition. The good agreement between these data sets implies that both are of relatively high quality.

5.4 Sphalerite Composition

Despite careful searching, and sulfide-normalized Zn concentrations of up to 0.25%, I found only 1 tiny grain of sphalerite in my polished sections. As I inferred from the strong As-Sb-Zn correlations in the XRF data, the bulk of Zn at Kensington must be present in fahlore. Consistently high (8-10 wt %) Zn in Kensington fahlore (Table 5. 2) bears this out. Sphalerite is a solid solution mineral that contains

variable Fe, up to 20 mole percent FeS. The one sphalerite grain I found is quite Fe-poor, with a composition of $(Fe_1Zn_{99})S$

5.5 Trace Metals in Pyrite (Mo, Ni, Se, and Co)

Concentrations of Mo, Ni, and Se in pyrite inferred from XRF data are too low (< .01%) to accurately detect by microprobe. Only Co, with maximum inferred concentrations > 0.1%, is sufficiently abundant for microprobe analysis. Because average sulfide-normalized Co concentrations vary considerably at Kensington (Fig. 2.23), it seemed a likely target for potentially identifying different generations of pyrite. My investigations primarily employed microprobe-based compositional maps. (See Appendix M for Co map routine).

5.5.1 Cobalt Variations in Pyrite

Boundaries between individual grains in aggregates of pyrite are not always visible in reflected light. As discussed in chapter 4, long and narrow inclusions appear to have grown between euhedral pyrite grains, with inclusions 'filling' the spaces between coalescing euhedral pyrite grains. It is impossible to determine by reflected light examination the relative timing of pyrite and the 'grain boundary' inclusions. Consequently, I sought to find some compositional differences between pyrite grains to better understand such textures.

Based on its relatively high concentrations at Kensington, I considered Co to be the marker element to distinguish between pyrite generations. Making microprobe maps of Co distribution in pyrite seemed like the best way to see the details of Co distributions in pyrite, but making these requires a large investment of time and funding. Consequently, I needed to limit the number of microprobe maps made. My four criteria for sample selection for Co mapping were (1) high concentrations of Co, (2) high concentrations of Au, (both as indicated by XRF analysis), (3) availability of polished sample material and (4) a distribution of samples in the various zones and of the various types previously identified. Some of the sections I initially used, while working out the method had lower Co values, but these were generally adequate. Based on these criteria I selected 12 samples for Co mapping (Table 5.3).

Table 5.3. Descriptions of samples used to create cobalt maps

Sample name	Au	Co	zone	sulf type	vein type	sulf text	rel% cp	rel% tet	rel% py
KEN-07	**716**	225	41	pyrite	discrete	massive	0.0	0.0	100
1355-201-16	368	**635**		brecciated	brecciated	brecciated	1.1	**1.1**	98
KEN-04avg	190	333		pyrite	discrete	massive	0.0	0.0	100
KEN-08avg	437	191	10	pyrite	msb	grains	0.4	0.0	100
1140-197-6	68	**1271**		pyrite	network	massive	0.0	0.0	100
780-176-2	**1846**	**419**		pyrite	network	clots	0.2	0.0	100
630-224-4	116	**1370**	10P	pyrite	network	bands	0.0	0.0	100
555-160-5avg	353	**476**		pyrite	discrete	clots	0.1	**0.1**	100
555-160-8	309	343		pyrite	discrete	bands	0.8	**3.2**	96
555-188-3	288	**609**		pyrite	discrete	grains	1.4	0.0	99
555S-2	**1001**	**813**		pyrite	discrete	bands	0.1	0.0	100

Concentrations above the 3rd quartile are indicated by red; Au and Co are in grams per ton sulfide

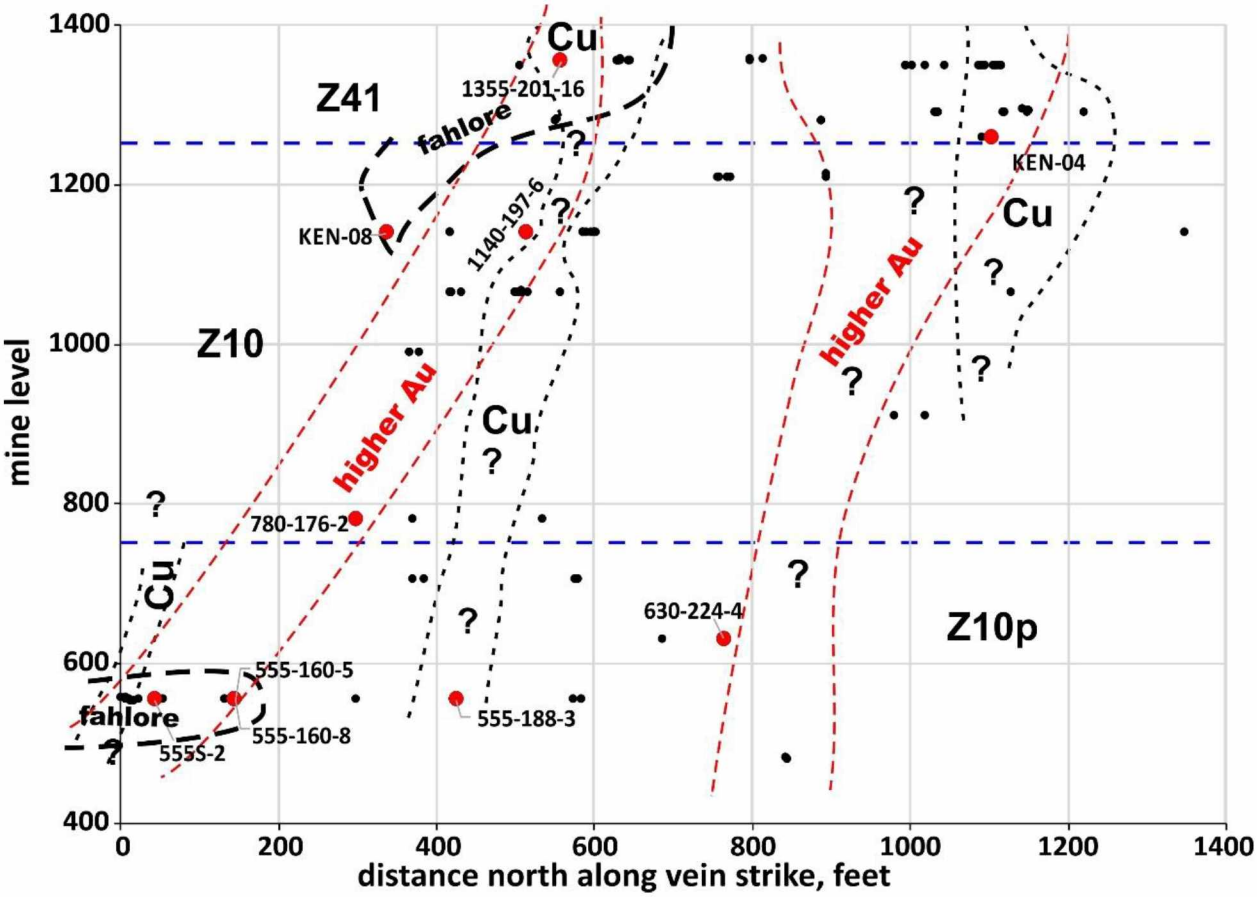

Figure 5.13. Kensington vein long section, showing locations of samples (red dots) for which Co maps were created. The zones of higher Au, of Cu-rich samples, and of fahlore occurrences are taken from chapter 2.

I did not always select the samples with the highest Co because they did not have high enough Au concentrations or because I used the entire sample in making the XRF pellet. The majority of the samples mapped are from zone 10P, although samples are from all zones (Table 5.3, Fig. 5.13). Most of the samples are in or immediately adjacent to the two higher-Au pipes and (or) in the zones of Cu-rich samples (Fig. 5.13). Four of the samples are also located in the two fahlore zones.

Native gold occurs predominantly as fracture fills in pyrite (79% of the total volume based on reflected light, chapter 4). All inclusion textures (round, complex, and grain boundary) only account for 12% of the total volume of native gold (as seen in reflected light). The fracture fill native gold occurred after pyrite deposition, hence is presumably unrelated to Co zoning in pyrite.

Calaverite inclusions (round, complex, and grain boundary) account for 66% of the total volume of calaverite observed in reflected light. This indicates that there is a complex relationship between pyrite and calaverite precipitation. The XRF data does not show any significant correlations between Au and Co, which implies that any spatial relations will be complicated.

All Co maps are shown (Figs. 5.14-5.20) with their associated BSE image to the right. Gold and other high atomic mass elements cause high background counts, and to save time, each point on a Co map is simply a record of counts per second at the Co K□ peak position. Hence, high atomic mass minerals produce high counts at the Co peak position, thus 'false positive values'. I have used the BSE image to help identify such minerals, as they are bright spots on BSE. All Co maps are located in Appendix M.

I made 31 Co maps from 11 samples (1355-201-16a and 1355-201-16b are from the same sample). I have reflected light data for all samples with Co maps. My EDS data is not as extensive as my reflected light data due to analytical costs. I also have no EDS data for sample 1140-197-6, but it is representative of samples with high Co and little Au. When comparing different calaverite inclusion textures I predominantly use the reflected light data.

The scope of this data set is not sufficiently extensive to draw conclusions relating Co enriched pyrite to calaverite deposition. This is in part because most of the Co maps show pyrite grains with complex or irregular zoning patterns. I also lack sufficient data to draw conclusions regarding Co enriched pyrite and accessory telluride minerals. Nevertheless, the images provide some clues concerning pyrite generations and indicate patterns of Co enrichment that commonly accompany grain boundary inclusions.

Zones of Co-enrichment in pyrite display a wide variety of often puzzling textures. However, based on my examination of the 31 maps, I define six categories of Co enrichment textures: (1) rim enriched, (2) core enriched, (3) oscillatory, (4) complex multi-generational, (5) veined and (6) irregular. All the samples I mapped contained multiple types and some are more common than others.

5.5.1.1 Rim Enriched Pyrite

The least complicated (and most common) zoning is rim-enriched pyrite, with Co-poor cores and abrupt Co-rich rims (e.g., Fig. 5.14). Four separate stages of pyrite growth are evident on Figure 5.14A: (1) a homogeneous Co-poor core (200 µm) with (2) thin (5 µm) discontinuous Co-rich rim. This was followed by (3) another low-Co crystallization event with another very abrupt (4) discontinuous Co-rich rim. All Co maps from sample 555-188-3 display rim-enriched textures and all but one of the samples processed show rim-enriched textures. Grain boundary calaverite grains are commonly associated with rim-enriched pyrite (Fig. 5.14a,b). The rare grain boundary native gold inclusions observed are also associated with rim enriched pyrite (2 samples, 5 gold grains). Chalcopyrite inclusions in pyrite (Fig. 5.14a) are clearly syn-pyrite, as they grew after the inner pyrite and before the outer pyrite. Co concentrations in the rims seems inversely related to thickness: thinner rims have higher % Co.

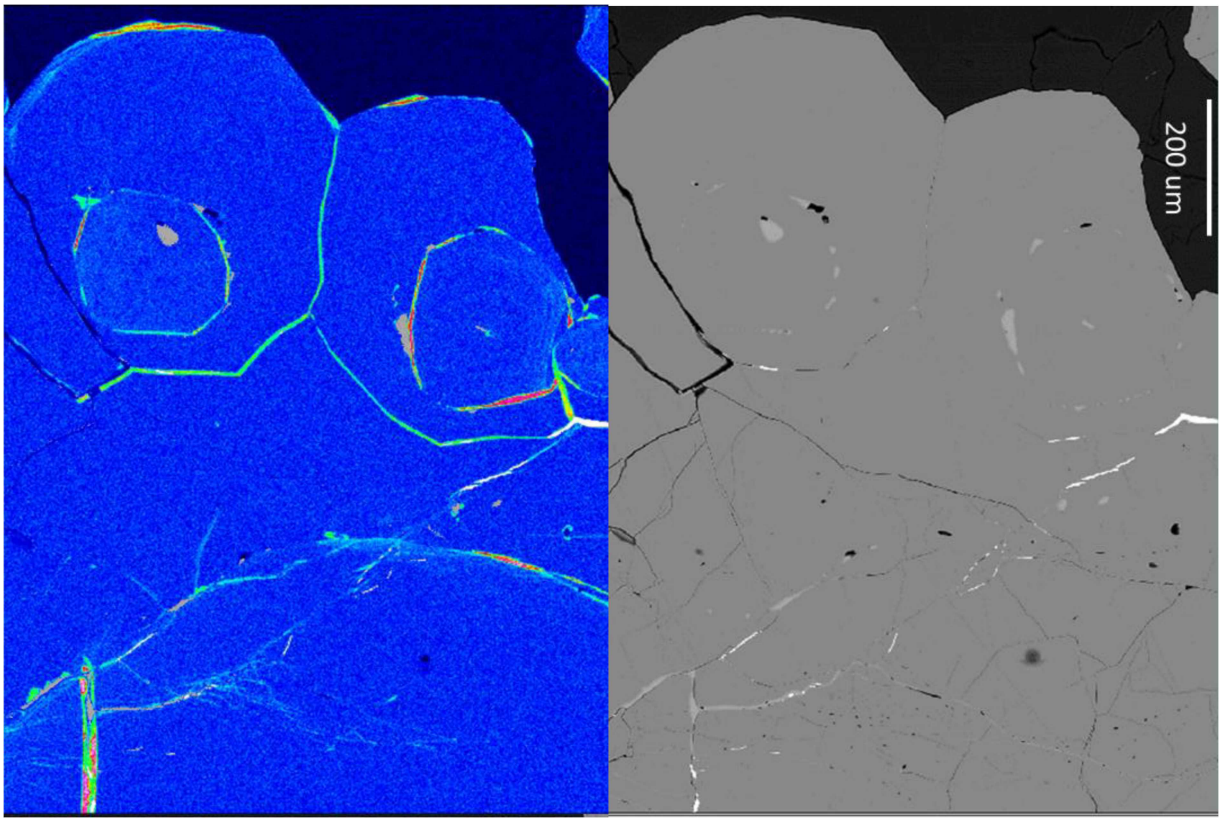

Figure 5.14. Two examples of pyrite with Co-rich rims, sample 555-188-3. A= pyrite grains with 1-2 high Co rims, commonly associated with AuTe2 grain boundary inclusions. Maximum Co = 1.5 wt%. B= low Co pyrite with complex inclusion of chalcopyrite and calaverite; higher Co-rims 10-30 ?m wide contain rounded and (or) grain boundary inclusions of Au2Te. A high-Co (barren?) core lies on the left center.

5.5.1.2 Multi-Generational

I refer to another common texture as complex multi-generational. Pyrite with this texture has a low Co pyrite core with a relatively wide, heterogeneously Co-enriched rim (e.g., Fig. 5.15). One-third of the samples yielded at least one Co map showing such irregular multiple generations of pyrite. Multi-generational pyrite is associated with an increase in grain boundary inclusions (observed in both reflected light and by EDS). As seen in Figure 5.15, early, Co-poor pyrite contains chalcopyrite, but not calaverite, inclusions. The later, variably Co-enriched pyrite contains abundant grain boundary calaverite.

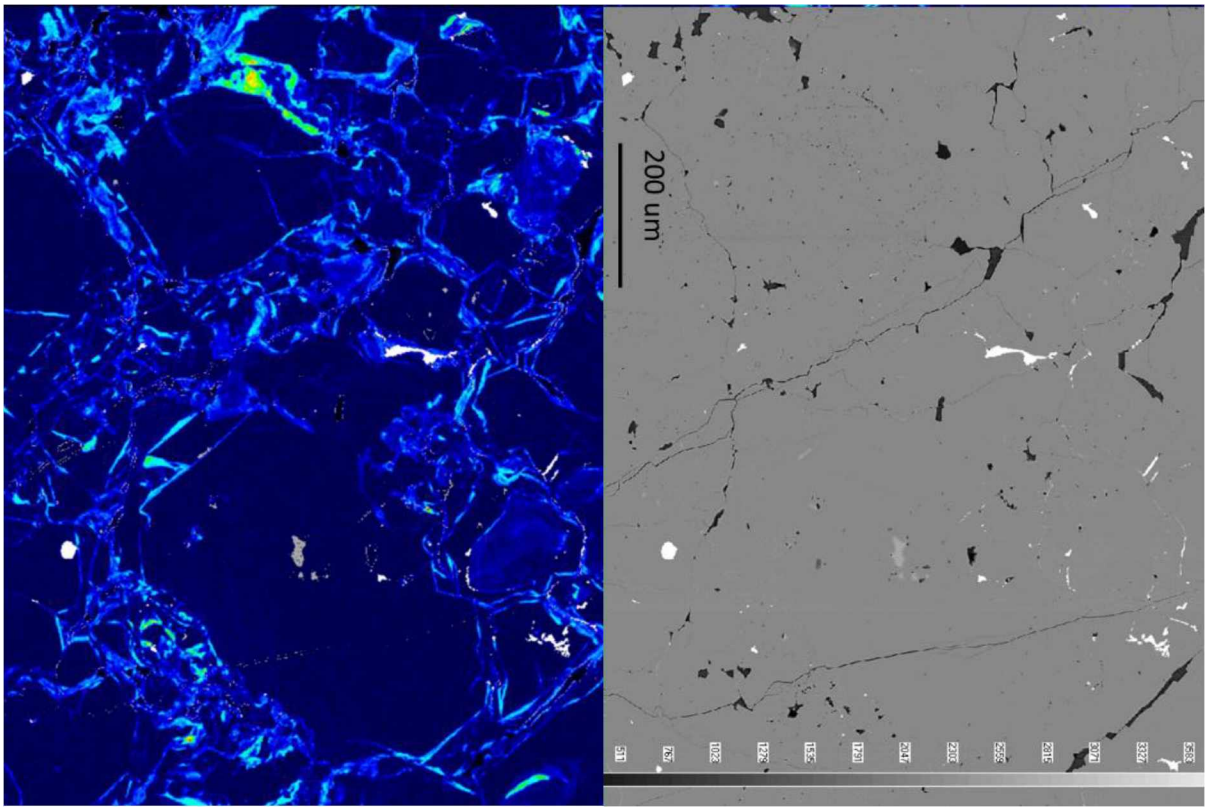

Figure 5.15. Multi-generational rim enrichment in pyrite, as seen in sample 555S-2e. Early, Co-poor pyrite contains only chalcopyrite inclusions; later, variably Co-enriched pyrite contains abundant grain boundary calaverite.

5.5.1.3 Oscillatory

Oscillatory Co zoning, illustrated by Figure 5.16, is uncommon. Oscillatory zoning is different from repeated Co zone enrichment (e.g., Fig. 5.14) as the latter typically consists of only 1-2 such repeats. Discontinuous oscillatory zones form both along euhedral pyrite rims and in pyrite cores (Fig. 5.16a). The oscillatory core could almost be described as a Co-rich core.

In some cases (Fig. 5.16 b) it's unclear whether the bands are better described as oscillations or as veinlets. Oscillatory zoning is variably associated with rounded and grain boundary inclusions, and can be cut by fractures and filled with gold and (or) non-Au telluride minerals (Fig. 5.16).

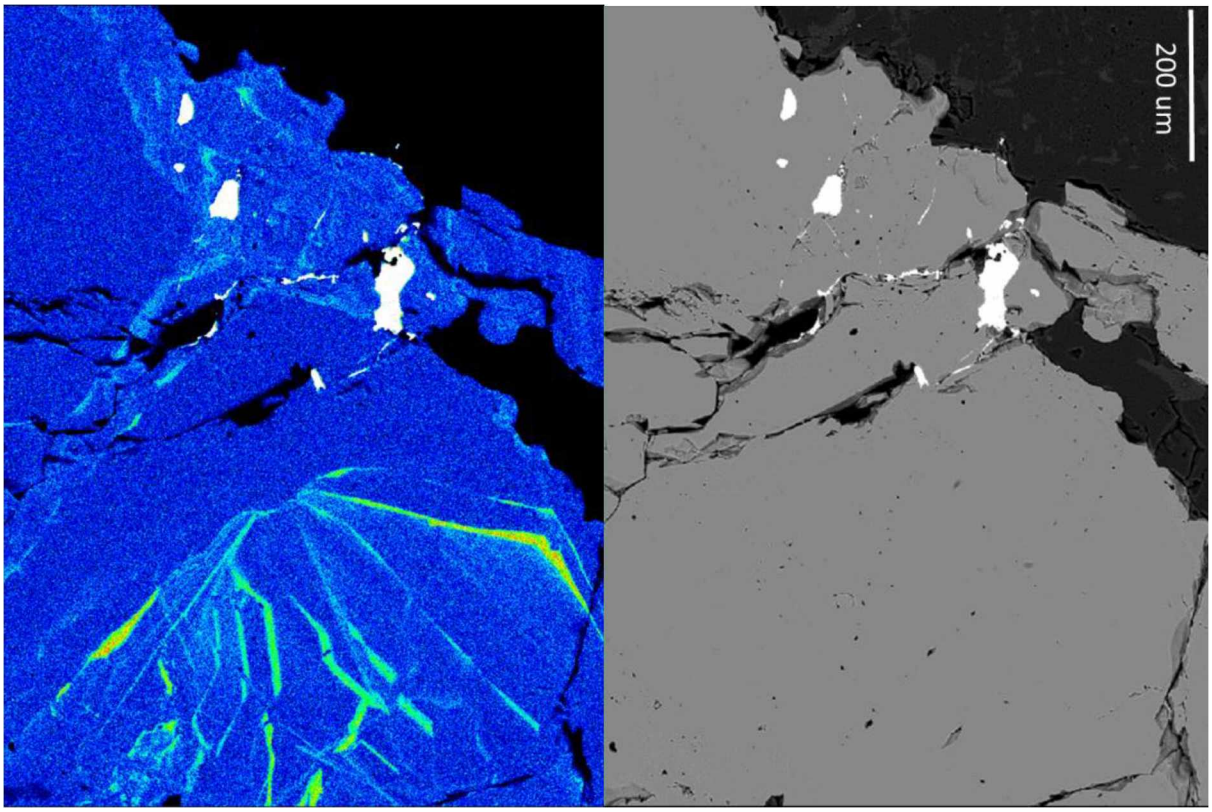

Figure 5.16. Pyrite displaying oscillatory zoning A = 555-160-8, complex oscillatory Co enriched pyrite grain with round Ag2Te and AuTe2 inclusions near the outer rim. All bright fracture filling grains are native gold. B= KEN-08-1d, irregular oscillatory (?) zoning. The larger inclusions are coloradoite (HgTe); the largest one may represent a complex fracture filling, as it appears to truncate Co-enriched zones. The strange oscillatory pattern in the lower half is inclusion-free. Red=0.7 wt% Co.

5.5.1.4 Veined

Co maps in a several cases show narrow linear Co-rich zones that appear to cut across pyrite grains as outlined by Co-enriched zones (e.g., Fig. 5.17, upper right). I hypothesize that these narrow, sub-linear, apparently cross-cutting zones represent fractures healed with Co-enriched pyrite. These fractures (if that's what they are) are not visible in either reflected light or BSE images: they are essentially invisible except on Co maps. It is not always clear whether a narrow linear zone is a rim enrichment or a veinlet, and clear-cut veinlets are uncommon. (Some of the linear Co-enriched zones in Figure 5.16, for example, may represent pyrite veinlets truncated by the edge of a grain.) I know of no cases where calaverite is precipitated with the Co-enriched pyrite veinlets, but some pyrite veinlets contain non-Au telluride minerals and (or) gold.

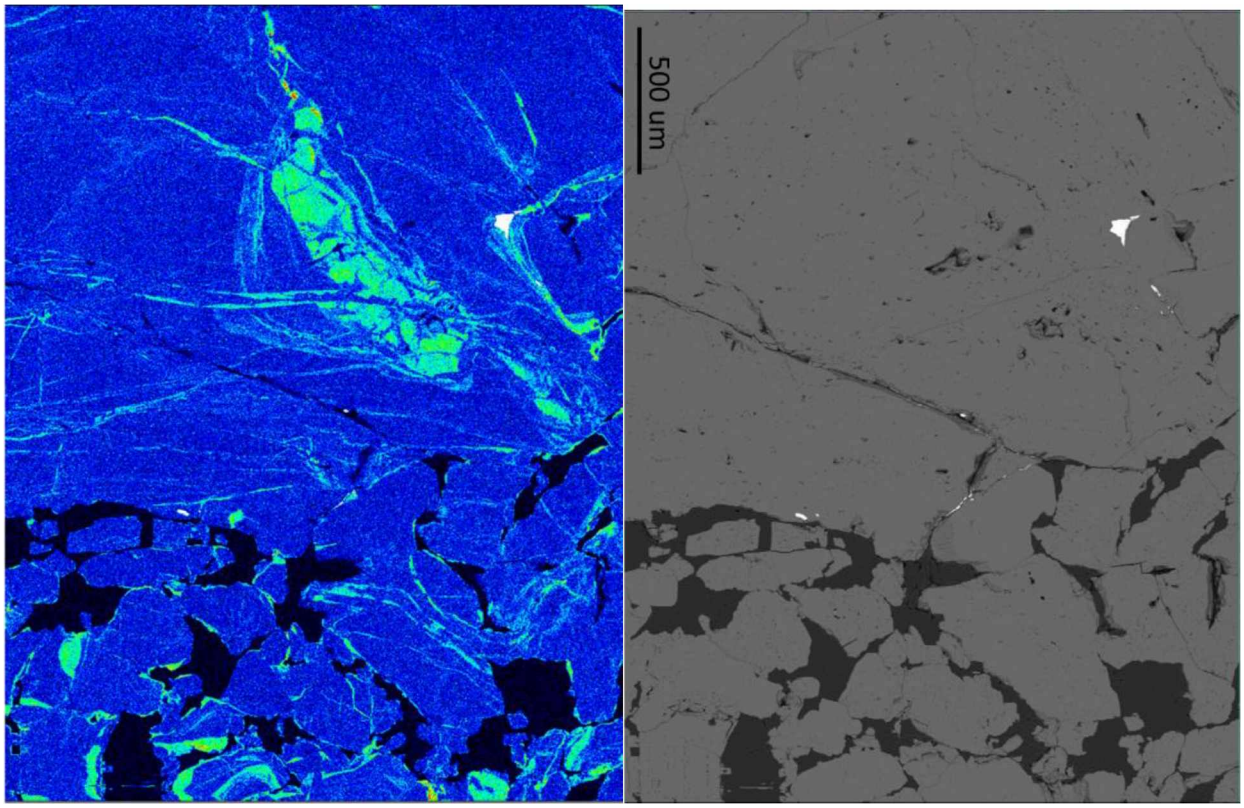

Figure 5.17. An example of 'invisible' pyrite veinlets in pyrite that are seen due to their higher Co contents. Pyrite in the upper center also appears to possess a Co-enriched core. Some of the nearby pyrite grains appear to show Co rim-enrichment, including one with a calaverite inclusion along the former rim. Sample 1140-197-6a.An example of 'invisible' pyrite veinlets in pyrite that are seen due to their higher Co contents. Some of the nearby pyrite grains appear to show Co rim-enrichment, including one with a calaverite inclusion along the former rim. Sample 1140-197-6a.

5.5.1.5 Core Enriched

Core enriched pyrites are distinctive, and moderately common. Figure 5.18 shows the best examples of such, and several less dramatic examples were encountered (e.g., Fig. 5.17, 5.16a). Core-enriched pyrite is not homogeneously Co-enriched and is variably surrounded by Co poor pyrite. No calaverite or gold inclusion are associated with these Co enriched cores; however, nearby pyrites with Co-enriched rims can contain abundant calaverite inclusions. It is tempting to conclude that the Co-rich pyrites represent early pyrite deposition before significant calaverite crystallization.

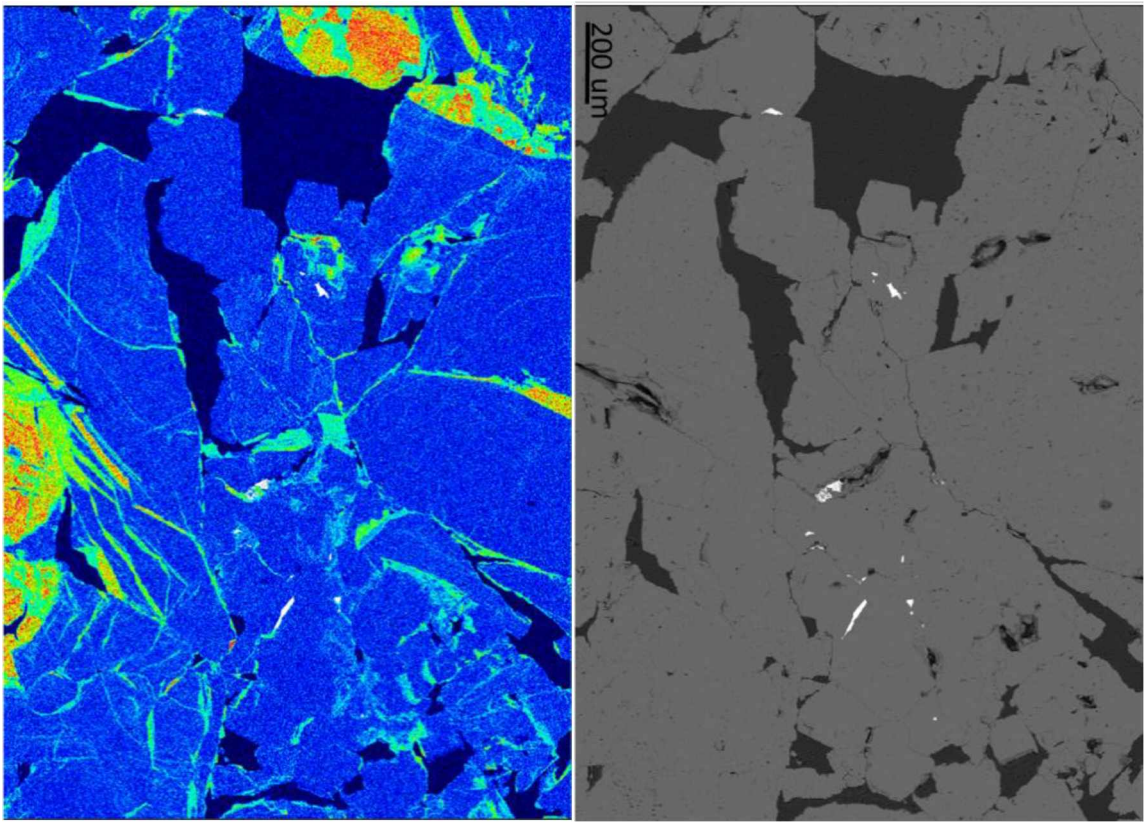

Figure 5.18. An example of pyrite with Co-enriched cores that apparently lack calaverite inclusions. The nearby Co-rimed pyrite grains do contain significant calaverite inclusions. Sample 1140-197-6X.

5.6 Discussion

Although a few grains I analyzed displayed uniformly low (<.01%) Co, most displayed simple to complex Co zoning patterns, with maximum spot Co concentration of nearly 2 wt%. Based on my analysis of the data, Co-bearing pyrite grew before, during and after gold deposition and both low- and high Co-pyrite is present in all vein types. That said, pyrite with Co-enriched rims commonly contains rounded and (or) grain boundary calaverite. Table 5.4 presents a summary of the features seen in the Co maps for each sample.

Most samples with rim-enriched pyrite also contain irregular or complex multi-generational pyrite aggregates. In all but one case (1355-201-16b, only one map created) Co-enriched rims (whether regular or irregular) are spatially associated with calaverite inclusions (Table 5.4). I hypothesize that some abrupt change in fluid conditions resulted in the precipitation of higher-Co pyrite and that this abrupt change also caused precipitation of calaverite. In some cases the calaverite is seen as rounded inclusions within the outer, Co-enriched pyrite (Figs. 5.14b, 5.16a, 5.17, 5.18) and in other cases the calaverite is present as grain boundary inclusions immediately adjacent to Co-enriched pyrite (Figs. 5.14,

5.15). In many cases, both are present. I noted in chapter 4 that samples with higher Au concentrations displayed an unusually high abundance of grain boundary calaverite inclusions; I now have a possible explanation for such.

Because the Co-enriched rims typically represent a small volume of the pyrite present, the presence of Co-enriched rims does not lead to higher Co concentrations (as grams Co/ton sulfide) in the XRF data. Instead, the two samples with extraordinarily high Co concentrations (> 1000 grams per ton sulfide) contain Co-enriched pyrite cores. These represent a much larger volume of Co enrichment and thus give rise to the higher Co concentrations. Of course, it's puzzling why the high Co-pyrite cores formed in the first place.

Table 5.4. Co enrichment textures by slide

Zone	Sample	Rim Enriched	Oscillatory	Veined	Multi Generational	Core Enriched	Irregular	Co*	Au*
41	1355-201-16a			X				635	368
	1355-201-16b						X	635	368
	KEN-04-1	X		X				333	190
10	1140-197-6	X			X	X		1271	68
	KEN-08-1		I					191	437
	780-176-2	X			C			419	1846
10P	630-224-4	X			C			1370	116
	555-188-3	X						609	288
	555-160-5	I						476	353
	555-160-8		X					416	309
	555S-2	I			X			813	1000

Notes: I = irregular, C = complex, *grams per ton sulfide (XRF)

In a similar manner, fahlore grains commonly display extensive compositional zoning, commonly with As-rich cores and Sb-rich rims, but commonly displaying oscillatory zoning (Figs. 5.8, 5.9). Such zoning suggests that fluid conditions during fahlore deposition were not static, but were characterized by rapid, dis-equilibrium growth.

Most non-Au tellurides occur texturally later than pyrite. Ag_2Te is the most abundant non-Au telluride that occurs as an 'early' round inclusion in pyrite. The Co map from 555-160-8 (Fig. 5.15) shows one of the Ag_2Te round inclusions within a Co poor pyrite growth ring in an oscillatory zoned pyrite grain. So, even though this is a round inclusion ('early'), it formed late in the pyrite crystallization history.

Based on an admittedly small sample size, I hypothesize that most Kensington pyrite grew under relatively constant conditions that yielded low-Co pyrite with a relatively low density of calaverite inclusions. A sudden change in conditions resulted in higher Co pyrite deposition, commonly with associated calaverite. Furthermore, whatever happened at one spot was not clearly connected to what happened elsewhere. Perhaps the higher Au 'pipes' identified in the long section (Fig. 5.13) represented zones that experienced greater changes in fluid conditions.

6 Summary and Conclusions

6.1 Limitations of Interpreting Mineralogical Correlations with XRF Data

The bulk of my interpretations and direction of further analysis is dependent on metal concentrations measured by XRF. There are several strong correlations within the XRF data that were easily explained due to known mineralogy. Au and Te (Fig. 2.5) and As and Sb (Fig. 2.16) are expected to have high correlations due to high concentrations of calaverite ($AuTe_2$) and the presence of fahlore ($Cu_{10}(Fe, Zn)_2(As,Sb)_4S_{13}$). However, the additional correlation of Sb-As with Zn (Table 2.4) is apparently due to (a) consistently high Zn in Kensington fahlore (Table 5.2) and (b) very low sphalerite (ZnS) abundance.

Other metal correlations are more subtle and require breaking out sample subcategories to uncover correlations that are obscured in the general XRF data set. This is especially true for metals that commonly occur in solid solution and multiple minerals. For example, Ag displays a moderate correlation with As-Sb-Zn (R^2 = .39-.64). This is possibly due to solid solution, as Ag is known to substitute for Cu in Sb-rich tetrahedrite (e.g., Repstock et al., 2016).

However, this is not the entire story of the relationship between Ag and fahlore. Ag can occur in at least four other minerals besides fahlore that occur at Kensington. Ag forms a solid solution with native gold, it can substitute into calaverite, and is present in hessite and petzite. Based on EDS data, I concluded that most fahlore lacked sufficient Ag to account for the XRF Ag concentrations (section 5.3). Instead, the primary relationship between Ag and fahlore is apparently that Ag telluride minerals (and gold) commonly occur as inclusions in fahlore (Fig. 4.14). I could not have discovered this relationship based on XRF data. In other words, the XRF data can be interpreted in terms of mineral and (or) solid solution-relations (as in the case of Zn), but cannot alone demonstrate such.

A weak XRF-based correlation that I can explain is that of Te and Hg, with an R^2 of 0.25 (Table 2.4). Hg is the only element that significantly correlates with Te outside of Au. I interpret this as due to five samples with very high (> 600 grams/ton sulfide) Hg that also contain high Te, and for which I have observed abundant HgTe inclusions (Fig. 4.14, Table 4.4).

On the other hand, I find the Bi-Ag (R^2 = .61) and Mo-Bi (R^2 = .36) correlations mineralogically baffling. I presume that these are artifacts of the fact that all three elements are commonly present below detection, and only a few samples contain both elements above detection. All of the polished

sections for which I identified Bi telluride also contained one or more Ag telluride minerals (Table 4.4), indicating that the two can occur at least in the same sample. Similarly, the two samples in which I found MoS_2 also contained Ag telluride minerals, even though they never seemed to occur in spatial proximity.

6.2 Evidence for Au and Te 'Recycling' at Kensington

One of the oddest features shown by the XRF data is that outside of the five samples with very high Hg, almost all yield an atomic Au/Te ratio of about 0.5 (Table 2.7), despite a range in concentrations from 50 to nearly 2000 grams Au/ton sulfide. This is true for samples with optically identified gold/calaverite ratios of 0-1.5, that is, for samples in which all the Au is present as calaverite to those with 1.5 times as much gold as calverite (Table 4.1). It is also true for ratios of atomic Au/ (atomic Ag+Bi+Pb+Ni+Hg) from 0.15 to 200 (Fig. 6.1). That is, the atomic Au/Te ratio of about 0.5 is present even where the concentration of non-Au Telluride forming elements is much greater than the concentration of Au (i.e., the abundance of non Au-telluride minerals MUST be much greater than that of calaverite), as well as where the only telluride mineral is calaverite (Fig. 6.1).

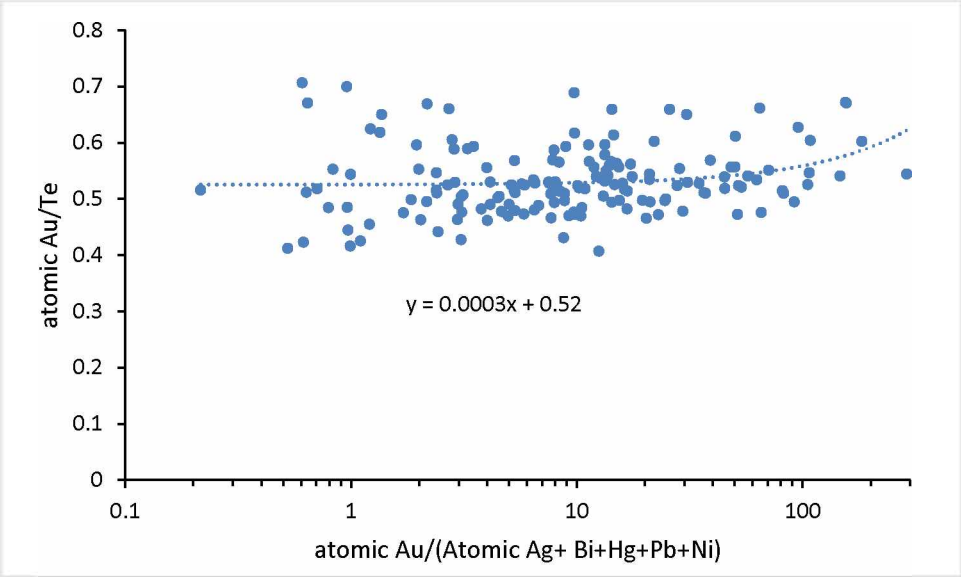

Figure 6.1. Atomic Au/ atomic Ag+Bi+Hg+Pb+Ni) versus atomic Au/Te for most of the Kensington XRF data. The graphic excludes analyses with Pb or Hg > 600 grams/ton sulfide and with Au or Te < 50 grams/ton sulfide. The best fit line shows that the ratio (which is 0.5 for pure calaverite) is essentially independent of the proportion of calaverite present. Even for analyses for which an appreciable amount of the Au is gold and the Te is non-Au related exhibit an atomic Au/Te ratio close to that for calaverite. Note the linear trend line is curved due to the log scale used.

The best explanation I can offer is related to the textural evidence (Chapter 4) that the bulk of calaverite was deposited during pyrite precipitation, whereas the bulk of gold was deposited after the pyrite was deposited and fractured (Fig. 4.13). I also showed (Table 4.1) that the Au concentration in a sample is unrelated to the amount of native gold in that sample. I interpret these observations to indicate that the bulk of Au at Kensington was deposited during pyrite growth as calaverite ($AuTe_2$). Elemental gold was deposited later by remobilization of the Au in calaverite. I envision a reaction like:

$$AuTe_2 + 2Hg = Au + 2HgTe$$

That is, both the Au and Te were derived from the previously-deposited calaverite. The reaction in general would be more complicated, as the majority of elements forming telluride minerals are present as ions (Bi^{3+}, Ag^{+}, Pb^{2+}, Ni^{2+}) and not native elements, so the reaction would also require some electron transfers. Nevertheless, I see no obvious way to maintain the early deposited calaverite atomic Au:Te ratio (0.5) during precipitation of gold and non-Au telluride minerals unless both Au and Te were scavenged from earlier-deposited calaverite.

The early calaverite is itself commonly accompanied by bands or zones of Co-enriched pyrite, e.g., Table 5.4, Appendix M. Rare zones of early, Co-enriched pyrite (seen as cores to Co-poor pyrite) lack such inclusions, but potentially represent relatively stable growth conditions. In contrast, the outer, generally narrow or irregular zones of Co enrichment seemingly represent abrupt changes in pyrite growth conditions. Whatever these changes were, if they truly are related to increased grain-boundary calaverite growth, they appear to have been more common in the two gold 'pipes' identified by abnormally high gold (grams/ton sulfide) concentrations (e.g., Fig. 2.8).

6.3 Spatially Zoned, Late Cu-Fahlore-Non Au Telluride-Galena Post Pyrite Event

In chapter 2 I documented that the majority of Cu at Kensington is present as chalcopyrite. Chalcopyrite-rich samples are uncommon (12 samples with > 8% (sulfide normalized) chalcopyrite), and small samples can contain up to 100% (sulfide normalized) chalcopyrite. All the XRF samples contained at least 51 grams Cu per ton sulfide (Appendix F). Elevated Cu concentrations occur throughout zones 41, 10, and 10P as near vertical pipes that partially intersect the high Au pipes (Fig. 2.15).

Multiple inclusion types indicate multiple generations of chalcopyrite. Round, complex, and grain boundary inclusions are present in all polished sections and are generally infrequent. This early

syn-pyrite chalcopyrite is volumetrically minor compared to late (post pyrite) chalcopyrite. Late chalcopyrite occurs as veinlets in fractured pyrite as well as 'massive' (< 5 cm) globules independent of pyrite grains.

In contrast, the vast majority of fahlore occurs as veinlets in fractured pyrite. Significant fahlore (> 500 grams per ton sulfide) is present exclusively in the southern ends of zones 41 and 10P (Fig. 2.27). The elevated fahlore area of zone 41 does dip down into the upper section of zone 10, but is generally restricted to zones 41 and 10P. Fahlore never occurs in Cu-rich samples, and if anything, the abundances of fahlore and chalcopyrite are antithetic (Fig. 2.17). Based on this relationship, it's possible that fahlore was cannibalized from earlier-deposited chalcopyrite (by addition of As, Sb, and Zn). Because the non-Au tellurite minerals are so commonly inclusions in fahlore, I speculate that the elements Sb, As, and Zn were added along with Hg, Bi, Pb, and Ag, from the south, and spread out to the north, particularly in zones 41 and 10P (Fig. 2.27). I exclusively observed elevated fahlore (>100 grams/ton sulfide) in samples from discrete and brecciated veins (Fig. 3.14). Consequently, I speculate that discrete veins along the southern margin served as conduits for fluids that created the later fahlore-rich assemblage.

A log f_{S2}-logf_{Te2} diagram (Fig. 6.2) expresses the proposed changes from the early to the late assemblage and explains the observed telluride (and non-telluride) minerals. The logf_{S2} conditions must have been higher than that required for pyrrhotite stability and below the stability of enargite. In addition, Sb present as the tetrahedite component + pyrite (rather than as $FeSb_2S_4$) further restricts minimum logf_{S2}. Although bornite is very occasionally present, it is not present with pyrite, and only the assemblage of bornite + pyrite demands a very high logf_{S2}.

The absence of Mo, Cu, Fe, Co, Zn, and Sb telluride minerals at Kensington is caused by the fact that logf_{Te2} was never high enough to stabilize them. Further, the presence of both $AuTe_2$ and Au and of both PbS and PbTe seemingly restricts the formation conditions at Kensington to a small region of possible fS2-fTe2 (Fig. 6.2). These same conditions require the presence of Bi, Hg, and Ag telluride minerals. Because the concentrations of Ni in pyrite are extremely low (usually < 40 grams/ton sulfide; Fig. 2.10) the activity of the NiS_2 component in pyrite was very low, greatly extending the stability of Ni-pyrite relative to other phases.

Finally, I propose that the change from the early calaverite-dominated assemblage to the later gold+ tellurides assemblage was due to a small drop in f_{Te2} (Fig. 6.2). That conditions didn't change

much is suggested by the continuing presence of early calaverite and the presence of both PbS and PbTe.

At the heading scale, the non-Au telluride elements (Hg, Ag, Bi, Ni, and Pb) are broadly associated (Fig. 2.27) with each other and with fahlore. Coloradoite (HgTe) is the most abundant non-Au telluride and is restricted to the southern edges of zones 41 and 10, but extends through the north end of zone 10P. Ag is strongly associated with Pb and they are both more broadly distributed than Ni and Bi (Fig. 2.27).

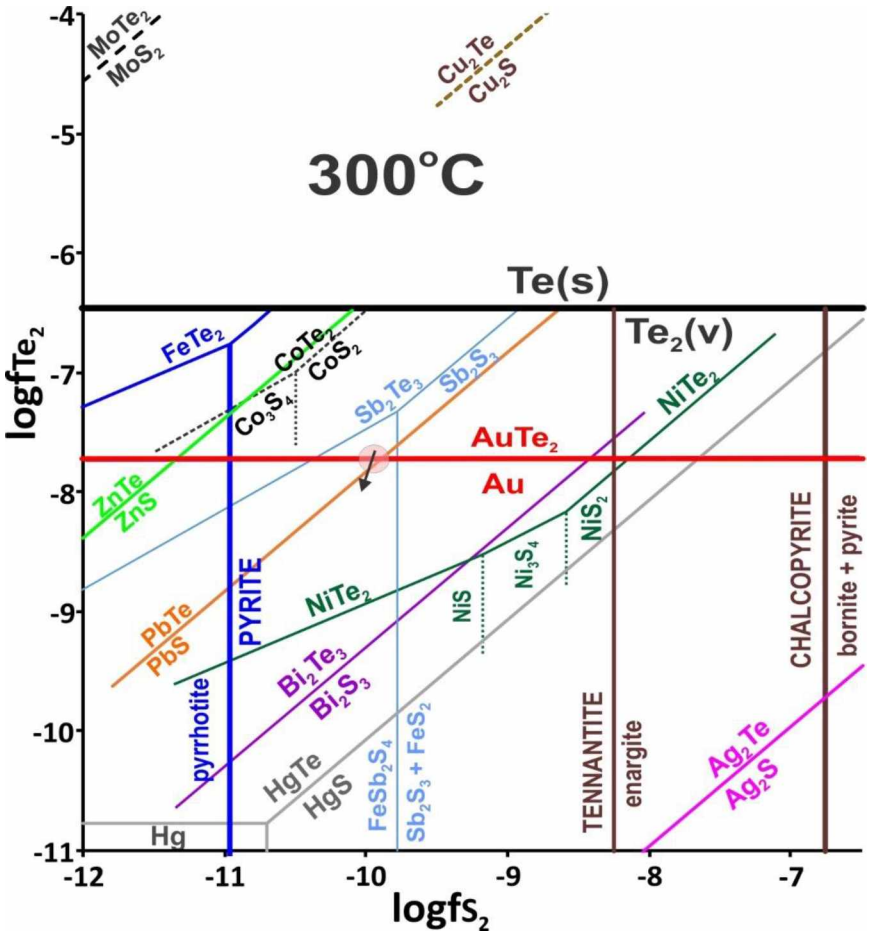

Figure 6.2. Log f_{S2}-logf_{Te2} diagram for telluride and sulfide equilibria relevant to the Kensington deposit at T = 300oC. Lines are color-coded for the different metallic elements. Dashed lines above tellurium saturation are shown to emphasize the instability of the Mo and Cu tellurides, as fTe_2 cannot exceed Te saturation. Estimated overall conditions are shown by the pink circle; the black arrow shows inferred change in conditions during metal deposition, from early to late. Lines are plotted based on thermodynamic data in Barton and Skinner (1979) and Nekrasov (1996).

Galena is present as fracture fills and inclusions in fahlore, exclusively from the south end of zone 41 (Table 4.4). All but one of the PbTe occurrences is also in zone 41, the other is in lower, south, zone 10p. The fahlore 'rich' southern ends of zones 41 and 10P also correlate to elevated concentrations of non-Au tellurides. The Cu-fahlore-non Au telluride event was not as extensive in zone 10, perhaps due to the lower abundance of discrete veins in this zone (Fig. 3.12).

The non-Au telluride forming elements associated with the Cu-fahlore event would have consumed Te from calaverite to form non-Au tellurides. This would explain the abundance of native gold spatially associated with non-Au tellurides, while not affecting the overall Au to Te ratios. This effectively means that the late Cu-fahlore-non Au telluride event did not contribute measurable amounts of Au to the system.

Pyrite is present in all stages of mineralization; pre, syn, and post main stage mineralization (Au). Based on all of my available data there are two metal enrichment events of ore at Kensington relative to pyrite mineralization:

1) Earlier syn pyrite Au – Te event
2) Later post pyrite Cu event: = non-Au tellurides + fahlore + bornite + galena + gold, but with no significant additional Au or Te deposited.

6.4 Comparison of Metal Enrichment at Kensington to the Juneau Gold Belt

Kensington is hosted in the Jualin pluton, which experienced a weak Cu porphyry event that enriched the pluton in Au, Cu, Te, and Mo (Fig. 1.7; Leveille, 1991; Newberry et al., 1995). The most obvious difference between Kensington and all other Juneau Gold Belt (JGB) deposits is that the primary gold mineral is calaverite, not native gold. Kensington (and other Jualin pluton-hosted deposits of the JGB) also contains significantly more Cu and much less As, Pb, and Zn than deposits outside of the Berners Bay area (Fig. 6.3). Several deposits contain elevated Cu; however, Kensington (along with other deposits of Berners Bay) is remarkable because there is no significant increase in As associated with increase in Pb+Zn. That is, the increase in Zn and As caused by the Zn-rich tennantite component is quite small relative to deposits outside of Berners Bay, with abundant arsenopyrite, sphalerite, and galena. These relations suggest local sources for at least many of the metals at Kensington, with later enrichment in As, Sb, Hg, Bi, Ag (at Kensington) possibly due to later appearance of fluids carrying more regionally-derived chemical components.

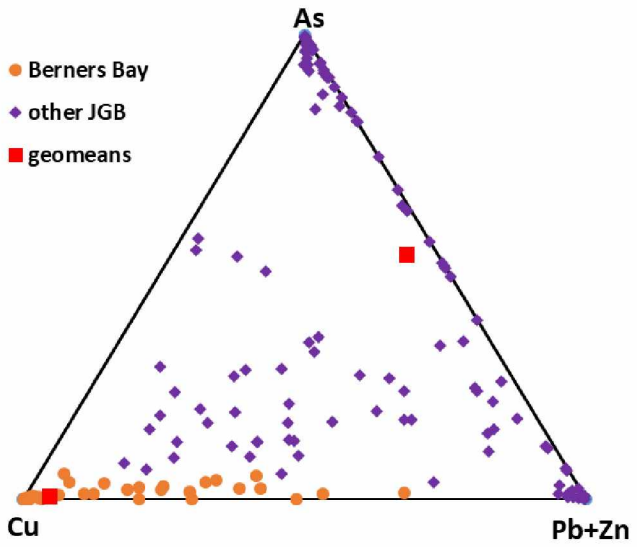

Figure 6.3. Compositional contrasts between deposits of the Berners Bay area (including Kensington) and other deposits of the Juneau gold belt. Relative Cu-As-Pb+Zn., showing much higher As characteristic of Juneau gold belt deposits outside of the Berners Bay area. Data from Redman et al. (1991), Newberry et al. (1995), this study, and Newberry, writ. Comm.

6.5 Future Work

Research is rarely 'finished'; rather, enough has been completed to tell a coherent story. Such is the case for this thesis. Some obvious questions to pursue involve (a) further documentation of the patterns presented for Kensington and (b) tying Kensington into other, nearby, deposits.

With regards to topic (a), it would be wonderful to have additional samples taken and analyzed as the mining continues, to see if the 'fahlore-gold-telluride event' can be extended to other parts of the vein system. As all the microprobe analyses presented are lower-quality EDS analyses, re-analysis using WDS methods would potentially show additional patterns, e.g., relations between Ag concentrations in gold and in calaverite. Most of my mineral searches using BSE techniques were of limited scope and extent on a given sample; these could be extended to include the entire polished sample.

The Jualin vein system is only a few kilometers from Kensington (Fig. 1.3). It's know to contain gold and a small proportion of calaverite. Can the mineral patterns I documented at Kensington be also seen there? That is, does the gold represent a more extensive redistribution of original calaverite or does it possess a completely different sequence of events? There is so much still to learn about these fascinating deposits.

References

Abraitis, P.K., Pattrick, R.A.D., and Vaughan, D.J. (2004). Variations in the compositional, textural and electrical properties of natural pyrite: a review, International Journal of Mineral Processing, V. 74, p. 41-59.

Barton, P.B. and Skinner, B.J. (1979). Sulfide Mineral Stabilities, in H.L. Barnes, ed., Geochemistry of Hydrothermal Ore Deposits, 2nd Ed. Wiley-Interscience, New York p. 278-403.

Beebe, K., Oduro, I., and Mondragon, R. (2018). Technical Report for the Kensington gold mine, Juneau, NI 43-101 TECHNICAL REPORT, p. 254.

Brew, D.A., and Ford, A.B., 1978, Megalineament in Southeastern Alaska Marks Southwest Edge of Coast Range Batholith Complex: Canadian Journal of Earth Science, v. 15, no. 11, p. 1763 – 1772.

Caddey, S.W., Harvey, D., Buxton, C., and Cato, K., 1994, Structural Analysis of the Kensington Gold Deposit: Deformation History, Deposit Formation, Ore Controls, and Exploration Guides, Juneau, Southeast Alaska. Internal Report prepared for Coeur Alaska, Inc., p. 18.

Casey, S.D. (2000). Mineralogy and stable isotope geochemistry of gold-silver telluride mineralization in the Berners Bay district, Alaska (Unpublished master's thesis). Iowa State University, Ames, IA.

Klemm, D.D. (1965). Synthesis and analysis of minerals in the systems FeAsS-CoAsS-NiAsS and FeS2-CoS2-NiS2. Neues Jahrbuch für Mineralogie - Abhandlungen, v. 103, p. 205-255.

Leveille, R.A. (1991). Geology and gold deposits of the Jualin mine area Berners Bay district, southeastern Alaska (Unpublished master's thesis). University of Alaska Fairbanks, Fairbanks, AK, p. 215.

Miller, L. D., Goldfarb, R. J., Snee, L. W., Gent, C. A., & Kirkham, R. A. (1995). Structural geology, age, and mechanisms of gold vein formation at the Kensington and Jualin deposits, Berners Bay district, southeast Alaska. Economic Geology, v. 90, p. 343-368.

Nekrasov, I. Ya. (1996). Geochemistry, Mineralogy and Genesis of Gold Deposits. A.A. Balkema, Rotterdam, p. 329.

Newberry, R. J., McCoy, D. T., & Brew, D. A. (1995). Plutonic-hosted gold ores in Alaska: igneous vs. metamorphic origins. Resource Geology Special Issue, v. 18, p. 57-100.

Redman, E.C., Maas, K.M., Kurtak, J.M., and Miller, L.D. (1991). Section D: Juneau Gold Belt subarea, in U.S. Bureau of Mines, Mineral investigations in the Juneau Mining District, Alaska, 1984-1988: Volume 2 - Detailed mine, prospect, and mineral occurrence descriptions: U.S. Bureau of Mines Special Publication VOL. 2D, p. 424.

Repstock, A., Voudouris, P., Zeug, M., Melfos, V., Zhai, M., Li, H., Kartal, T, and Matuszczak, J. (2016). Chemical composition and varieties of fahlore-group minerals from Oligocene mineralization in the Rhodope area, S. Bulgaria and N. Greece. Mineralogy and Petrology, v. 110, p. 103-123.

Saunders, J.A., Hofstra, A.H., Goldfarb, R.J. and Reed, M.H. (2014). Geochemistry of Hydrothermal Gold Deposits. In: Holland H.D. and Turekian K.K. (eds.) Treatise on Geochemistry, Second Edition, vol. 13, p. 383-424. Oxford: Elsevier.

Shackleton, J.M., Spry, P.G., and Bateman, R. (2003). Telluride Mineralogy of the Golden Mile Deposit, Kalgoorlie, Western Australia. The Canadian Mineralogist; 41 (6): p. 1503 – 1524.

Vaughan, D.J. and Craig, J.R. (1978). Mineral Chemistry of Metal Sulfides Cambridge Univ. Press, Cambridge, p. 284.

Appendix A. Fundamental Sampling and Analyses Procedures

1. Sulfide rich hand samples are directly chiseled out from either the drift ribs or faces. This method allows for collection of different sulfide textures within a single vein and an opportunity to better document and define textures of the vein and sulfides sampled. In cases of sulfide rich bands and continuous massive sulfide it is important to sample along strike of the vein (or sulfide feature). Note sample location, vein type, sulfide texture, and other descriptive data.
2. Hand samples and in situ sulfides can be analyzed with a hand held XRF for immediate preliminary results.
3. Hand samples should be cut or broken with a hammer to separate the sulfides from waste minerals (quartz and calcite). 12.5 grams of sulfide rich material should be handpicked from the hand sample to be processing into XRF pellets. Hand samples with significant sulfide components and enough material should be sub sampled (XRF pellets).
4. Handpick 12.5 grams of sulfide rich material from the hand sample for XRF pellet processing. See Appendix C for sulfide rich pelletization process.
5. All samples undergo XRF analyses with a XRF routine specifically calibrated for sulfide rich material with heavy metals. See Appendix D for XRF routine calibrations. Post processing of XRF data is described in Appendix E.
6. Samples with anomalous XRF results (elevated metal concentrations) should have polished section made out of the remaining sulfide rich material from the corresponding hand sample. Polished section preparation procedures in Appendix H.
7. Reflected light microcopy is used to identify gold and calaverite. Locations and textures of gold, calaverite, and non-Au tellurides should be noted. The coordinates from the microscope will then be converted to coordinates in the microprobe.
8. Polished sections are then carbon coated for EDS (microprobe) analyses.
9. Qualitative mineral compositions collected with EDS. Textures of non-Au tellurides and other small opaque minerals are documented with their compositions. Ag concentrations in calaverite and gold are of particular interest.
10. Polished sections of samples with elevated Co concentrations should have Co maps made of areas with several different gold, telluride, or sulfide textures visible. The gold and telluride grains in these Co map areas should have corresponding EDS compositions. See Appendix M for Co map routine.

Appendix B. Sample Locations, Descriptive Data, and Analyses Used

Table B-1. Sample Locations, Descriptive Data, and Analyses Used

Sample name	Location (ft.)			Descriptive Data			Analyses Used			
	Relative Easting	Relative Northing	Elevation Above Sea Level	Sample Type	Vein Type	Sulfide Texture	XRF	Reflected Light	EDS	Co Maps
1065-189-1	287	417	1065	pyrite-rich	network	massive	X	X	X	
1065-189-2	288	431	1065	pyrite-rich	network	clots	X			
1065-189-3	267	431	1065	pyrite-rich	network	clots	X			
1065-189-5	247	418	1065	pyrite-rich	network	clots	X			
1065-189-6	244	418	1065	pyrite-rich	network	clots	X	X		
1065-189-8	234	419	1065	pyrite-rich	network		X			
1065-197-4	226	509	1065	pyrite-rich			X			
1065-197-6	252	500	1065	pyrite-rich	network	clots	X			
1065-197-7	197	504	1065	pyrite-rich	discrete	clots	X			
1065-197-8	279	516	1065	pyrite-rich	network	clots	X			
1065-206-1	227	556	1065	pyrite-rich	network		X			
1065-206-2	244	556	1065	pyrite-rich	discrete	clots	X			
1065-206-3	246	556	1065	Cu-rich	discrete	massive	X	X		
1065-206-4			1065		network	clots	X			
1065-206-5	140	1127	1065	Cu-rich	discrete	clots	X			
1065-5	150	417	1065	pyrite-rich	network	clots	X			
1140-189-1	265	417	1140	pyrite-rich	network		X			
1140-189-2			1140		discrete	clots	X			
1140-189-3	276	417	1140	pyrite-rich	network		X			
1140-189-4	276	417	1140	pyrite-rich	network		X			
1140-189-5	274	417	1140	pyrite-rich	network		X			
1140-197-12	219	514	1140	pyrite-rich	network	clots	X			
1140-197-13	219	514	1140	pyrite-rich	network		X			
1140-197-2	283	514	1140	pyrite-rich	network	massive	X			
1140-197-4	277	514	1140	pyrite-rich	network	clots	X			
1140-197-5	275	514	1140	pyrite-rich	network		X			
1140-197-6	272	514	1140	pyrite-rich	network	massive	X	X	X	X
1140-197-8	219	514	1140	pyrite-rich	network	massive	X			
1140-197-9			1140		network	disseminated	X			
1140-197-X			1140	pyrite-rich	network		X			
1140-206-1	166	601	1140	pyrite-rich	discrete	clots	X			
1140-206-10	226	589	1140	pyrite-rich	network		X			
1140-206-11	198	585	1140	pyrite-rich	discrete	clots	X			
1140-206-12	192	585	1140	pyrite-rich	network	bands	X			
1140-206-13	184	585	1140	pyrite-rich	discrete	massive	X			
1140-206-14	178	585	1140	pyrite-rich	discrete	clots	X			
1140-206-2	182	601	1140	pyrite-rich	network	clots	X			
1140-206-3	221	601	1140	pyrite-rich	network	clots	X			
1140-206-4	223	601	1140	pyrite-rich	network	clots	X			
1140-206-5	287	601	1140	pyrite-rich	discrete	bands	X			
1140-206-6	305	601	1140	pyrite-rich	network	clots	X			
1140-206-7	311	601	1140	pyrite-rich	MSB	massive	X			
1140-206-8	311	595	1140	pyrite-rich	network	clots	X			
1210-223-4			1210		network	disseminated	X			
1210-223-5	210	757	1210	pyrite-rich	discrete	clots	X			
1210-223-6	188	769	1210	pyrite-rich	network	disseminated	X			
1210-223-7			1210		network		X			
1210-233-1	232	772	1210	pyrite-rich	network	clots	X			
1210-233-3	132	758	1210	pyrite-rich	network	clots	X			
1280-201-1	247	551	1280	pyrite-rich	discrete	bands	X			
1280-201-10	198	551	1280	pyrite-rich	discrete	clots	X			
1280-201-2	241	551	1280	pyrite-rich	discrete	clots	X			
1280-201-3	241	551	1280	pyrite-rich	network	clots	X			
1280-201-4	236	551	1280	pyrite-rich	network	massive	X			
1280-201-5	235	551	1280	pyrite-rich	network	massive	X			
1280-201-6	221	551	1280	pyrite-rich	discrete	bands	X	X		
1280-201-7	225	551	1280	pyrite-rich	discrete	clots	X			
1280-201-8	213	551	1280	pyrite-rich	network	bands	X			
1280-201-9	201	551	1280	pyrite-rich	network	clots	X			
1280-235-10	123	888	1280	pyrite-rich	discrete	clots	X			
1280-235-11	124	888	1280	pyrite-rich	discrete	clots	X			

Table B-1 cont. Sample Locations, Descriptive Data, and Analyses Used

Sample name	Location (ft.)			Descriptive Data			Analyses Used			
	Relative Easting	Relative Northing	Elevation Above Sea Level	Sample Type	Vein Type	Sulfide Texture	XRF	Reflected Light	EDS	Co Maps
1280-235-2	126	888	1280	pyrite-rich	discrete		X			
1280-235-4	128	888	1280	pyrite-rich			X			
1280-235-5	130	888	1280	pyrite-rich	network	clots	X			
1280-235-6	132	888	1280	pyrite-rich	network	clots	X			
1280-235-8	134	888	1280	pyrite-rich	network	clots	X			
1280-235-9	136	888	1280	pyrite-rich	network		X			
1290-1	85	1032	1290	pyrite-rich	discrete	clots	X			
1290-2	89	1033	1290	pyrite-rich	discrete	massive	X			
1290-3	93	1035	1290	pyrite-rich	discrete	massive	X			
1290-4	99	1034	1290	pyrite-rich			X			
1290-5	101	1036	1290	pyrite-rich			X			
1350-1	59	994	1350	pyrite-rich			X			
1350-10	120	1044	1350	pyrite-rich	discrete	clots	X			
1350-11	94	1019	1350	pyrite-rich	discrete	massive	X			
1350-12	62	1003	1350	pyrite-rich	discrete	massive	X			
1350-13	26	1108	1350	brecciated	brecciated	bands	X	X	X	
1350-14			1350	brecciated	brecciated	bands	X			
1350-15			1350	brecciated	brecciated	bands	X			
1350-16			1350	brecciated	brecciated	bands	X			
1350-17	188	1088	1350	pyrite-rich	discrete	bands	X			
1350-18			1350	brecciated	brecciated	bands	X			
1350-19	5	1091	1350	pyrite-rich	discrete	clots	X			
1350-2	60	995	1350	pyrite-rich			X			
1350-20			1350	brecciated	brecciated	bands	X			
1350-21	1	1094	1350	pyrite-rich	discrete	bands	X			
1350-22			1350	brecciated	brecciated	bands	X			
1350-23	0	1096	1350	pyrite-rich			X			
1350-3	96	1086	1350	pyrite-rich	discrete	clots	X			
1350-4	94	1089	1350	pyrite-rich	discrete	massive	X			
1350-5	87	1115	1350	pyrite-rich	network	massive	X			
1350-6	118	1113	1350	pyrite-rich	network	clots	X			
1350-7	116	1110	1350	pyrite-rich			X			
1350-8	118	1108	1350	pyrite-rich	discrete	clots	X			
1350-9	118	1106	1350	pyrite-rich	network	bands	X			
1355-193-2			1355	pyrite-rich			X			
1355-193-3	16	505	1350	pyrite-rich			X			
1355-201-1	140	560	1355	pyrite-rich	network	clots	X			
1355-201-10	75	557	1355	pyrite-rich	discrete	massive	X			
1355-201-11	74	557	1355	brecciated	brecciated	bands	X			
1355-201-12	73	557	1355	pyrite-rich	discrete	massive	X			
1355-201-13	72	557	1355	pyrite-rich	discrete	clots	X			
1355-201-14	71	557	1355	brecciated	brecciated	bands	X			
1355-201-16	70	557	1355	brecciated	brecciated	bands	X	X	X	X
1355-201-2	104	558	1355	pyrite-rich	discrete	clots	X			
1355-201-7	96	557	1355	pyrite-rich	discrete	bands	X			
1355-210-1	121	638	1355	pyrite-rich	discrete	massive	X			
1355-210-10	86	623	1355	pyrite-rich	discrete	clots	X			
1355-210-11	112	638	1355	pyrite-rich	discrete	massive	X			
1355-210-12			1358	pyrite-rich	discrete	clots	X			
1355-210-13	116	624	1355	Cu-rich	discrete	disseminated	X			
1355-210-14	115	624	1355	Cu-rich	discrete	clots	X	X	X	
1355-210-15			1355		discrete	clots	X			
1355-210-16	116	624	1355	pyrite-rich	discrete	clots	X			
1355-210-2	117	639	1355	pyrite-rich	discrete	massive	X			
1355-210-3	113	639	1355	Cu-rich	discrete	massive	X			
1355-210-4	103	638	1355	pyrite-rich	discrete	massive	X			
1355-210-5	120	624	1355	Cu-rich	discrete	clots	X			
1355-210-6	121	624	1355	Cu-rich	discrete	bands	X			
1355-210-7	102	622	1355	pyrite-rich	network	clots	X			
1355-210-8	97	622	1355	brecciated	brecciated	massive	X			
1355-210-9	96	622	1355	pyrite-rich	discrete	massive	X			
1355-227-1	75	798	1355	pyrite-rich	discrete	massive	X			
1355-227-2	74	798	1358	pyrite-rich	discrete	clots	X			
1355-227-3	74	813	1358	pyrite-rich	discrete		X			
480ACESS-1	702	843	483	pyrite-rich	network	clots	X	X		
480N-1	692	844	480	pyrite-rich	discrete	bands	X			
480N-3	693	844	480	pyrite-rich	discrete	bands	X			
555-152-1	479	54	555	pyrite-rich			X			

Table B-1 cont. Sample Locations, Descriptive Data, and Analyses Used

Sample name	Location (ft.)			Descriptive Data			Analyses Used			
	Relative Easting	Relative Northing	Elevation Above Sea Level	Sample Type	Vein Type	Sulfide Texture	XRF	Reflected Light	EDS	Co Maps
555-152-2	474	54	555	pyrite-rich	network	disseminated	X			
555-160-1	490	131	555	pyrite-rich	discrete	bands	X			
555-160-2	475	131	555	pyrite-rich	discrete	bands	X	X	X	
555-160-3	470	131	555	pyrite-rich	discrete	massive	X			
555-160-4			555	pyrite-rich	discrete	massive		X		
555-160-5	460	145	555	pyrite-rich	discrete		X	X	X	X
555-160-6	470	145	558	pyrite-rich	discrete	clots	X			
555-160-7	474	145	555	pyrite-rich	discrete		X			
555-160-8	515	145	555	pyrite-rich	discrete	bands	X	X	X	X
555-176-1	507	298	555	pyrite-rich	discrete	massive	X			
555-188-3	538	425	555	pyrite-rich	discrete	disseminated	X	X	X	X
555-188-4	532	425	555	pyrite-rich	network	bands	X			
555-188-5	511	425	555	Cu-rich	network	clots	X	X	X	
555-188-6	525	426	555	pyrite-rich	network	clots	X			
555-188-7	529	426	555	pyrite-rich	network	clots	X			
555-188-8	534	426	555	Cu-rich	network	clots	X			
555-188-9	561	426	555	pyrite-rich	network	clots	X			
555-204-1	627	573	555	pyrite-rich	network	clots	X			
555-204-2	620	584	555	pyrite-rich	network	clots	X			
555-204-3	640	574	555	pyrite-rich	network	clots	X			
555-204-5	650	584	555	pyrite-rich	network	clots	X			
555S-1	548	46	555	pyrite-rich	discrete	clots	X			
555S-10	518	6	555	pyrite-rich	network	clots	X			
555S-11	519	10	555	pyrite-rich	network	clots	X			
555S-13	529	0	558	pyrite-rich	network	clots	X			
555S-14	534	6	558	Cu-rich	network	bands	X			
555S-15	537	9	555	pyrite-rich	network	bands	X			
555S-16	537	10	555	pyrite-rich	network	bands	X			
555S-17	549	24	555	pyrite-rich	network	clots	X			
555S-2	546	43	555	pyrite-rich	discrete	bands	X	X	X	X
555S-3			555		network	disseminated	X	X	X	
555S-4	525	17	554	pyrite-rich	discrete	clots	X			
555S-5	523	12	554	pyrite-rich	discrete	massive	X			
555S-6	522	10	555	pyrite-rich	network	massive	X			
555S-7	520	8	555	pyrite-rich	network	clots	X			
555S-8	520	7	555	pyrite-rich	discrete	bands	X			
555S-9	519	7	555	pyrite-rich	discrete	clots	X			
630-1	602	687	630	pyrite-rich	network	clots	X			
630-224-1	591	767	630	pyrite-rich	network	clots	X			
630-224-2			630				X			
630-224-3	589	766	630	pyrite-rich	network	disseminated	X			
630-224-4	589	765	630	pyrite-rich	network	bands	X	X	X	X
705-184-1	421	371	705	pyrite-rich	network	clots	X			
705-184-2	426	385	705	pyrite-rich	network	disseminated	X			
705-PASTE-2	507	576	705	pyrite-rich	network	clots	X			
705-PASTE-3	508	577	705	pyrite-rich	network	clots	X			
705-PASTE-4	508	579	705	pyrite-rich	network	disseminated	X			
780-176-1	362	301	780	pyrite-rich	network	clots	X			
780-176-2	338	299	780	pyrite-rich	network	bands	X	X	X	X
780-184-1	346	371	780	pyrite-rich	discrete	clots	X			
780-200-1	410	535	780	pyrite-rich	network	clots	X			
910N-2	263	1020	910	pyrite-rich	network		X			
910N-4	285	980	910	pyrite-rich	network	clots	X			
K12-10	239	602	1140	pyrite-rich	discrete	clots	X			
K12-12			1350				X			
K12-13	44	995	1350	pyrite-rich			X			
K12-14			1280				X			
K12-19			1210				X			
K12-20	146	894	1213	pyrite-rich	discrete	clots	X			
K12-21	140	894	1210	pyrite-rich	discrete	clots	X			
K12-4	81	1117	1290	pyrite-rich			X			
K12-5	83	1119	1290	pyrite-rich			X			
K12-7	189	1347	1140	pyrite-rich	network		X			
K12-8			1140				X			
K12-9			1140				X			
K13-10			1290				X			
K13-11	76	1220	1290	Cu-rich	discrete		X			
K13-12	68	1142	1295	pyrite-rich	discrete		X			

Table B-1 cont. Sample Locations, Descriptive Data, and Analyses Used

Sample name	Location (ft.)			Descriptive Data			Analyses Used			
	Relative Easting	Relative Northing	Elevation Above Sea Level	Sample Type	Vein Type	Sulfide Texture	XRF	Reflected Light	EDS	Co Maps
K13-14	68	1148	1293	pyrite-rich	discrete		X			
K13-15	68	1151	1292	Cu-rich	discrete		X			
K13-16	68	1148	1290	Cu-rich	discrete		X			
K13-17	232	508	1065	Cu-rich	discrete		X			
K13-18	230	508	1068	pyrite-rich			X			
K13-19	228	508	1065	pyrite-rich			X			
K13-21							X			
K13-22							X			
K13-24							X			
K13-25							X			
K13-4	145	552	1283	pyrite-rich			X			
KEN-01			1140	pyrite-rich	network			X		
KEN-02	179	337	1143	pyrite-rich	network		X			
KEN-03			1140	pyrite-rich	network			X		
KEN-04	170	1104	1260	pyrite-rich	discrete		X	X	X	X
KEN-05	169	1091	1260	pyrite-rich	discrete		X	X		
KEN-06			1260	pyrite-rich	discrete			X		
KEN-07				pyrite-rich	discrete		X	X	X	X
KEN-08	180	337	1140	pyrite-rich	MSB		X	X	X	X
XCUT4-2	310	366	990	pyrite-rich			X			
XCUT4-3	306	378	990	pyrite-rich			X			
XCUT4-4	304	366	990	pyrite-rich			X			

Appendix C. Optimized Sulfide-Rich Pelletization Recipe

Materials and Equipment:

PXR-225 (binding agent)	37 mm XRF sample cup
Vertrel XF (lubricating agent)	Sample material
Watch glass	Fume hood
Rubbing alcohol	Steel ball mill
Quartz rich sand	Hydraulic press
Latex free gloves	

Procedure:

- Measure 12.50 grams of sulfide rich sample and put in a steel ball mill vial
- Add 1.25 grams PXR-225 to the vial
- Add ~ 7 mL of vertrel XF to the vial. This should be done under a fume hood (read the MSDS for vertrel XF). Excess vertrel XF will not spoil the sample, it will just take your sample a little longer to dry.
- Close vial and mix in ball mill for 4 minutes.
- Remove sample from mill and open steel vials under a fume hood. Scrape all material onto the watch glass and let dry (under the fume hood). This should only take a few minutes.
- Once vials are empty and dry they can be removed from the fume hood.
- Clean the steel ball vials by getting most of the sulfide powder out with a dry paper towel. Then add quartz sand to the vials (about the same amount in each vial), put them back and mill for 2-3 minutes. Once done milling, remove steel balls and dump powder into trash. Clean out with rubbing alcohol OR water. You will also need to take off the rubber gaskets and clean under them too.
- If you use water to clean out the vials, make sure they are completely dry. They rust easily.
- Make sure there are no pieces of rock left in your sample. If there are, just take them out and note their weight. If you skip this step you run the risk of denting the pressing part of the die. It is very difficult to remove dents on the surface of the die.
- Put cup in the 40 mm XRF press and transfer pulverized sample mixture into it.

- Center the die in the press and press @ 22,000 lb. for 30 seconds. Your sample may de-gas and cause the pressure to drop as you're trying to pressurize it. This is ok, just keep adding pressure until its done de-gassing. Try to release the press gradually.
- Remove the die from the press and flip it upside down. Take the bottom off the press.
- Label your sample and store appropriately. They are ready to be analyzed immediately.
- Clean the die with rubbing alcohol and store properly to protect the surface of the die.

*Note: This recipe is designed for ~50 to 100% pyrite samples.

**Your sample will be diluted by 9%

Appendix D. XRF Routine Setup Details

Table D-1. KEN2 XRF Routine Setup (no tube filter used)

Channel	Line	X-tal	Collimator	Detector	kV	mA	Angle	Offset Bg1	Offset Bg2	PHD1	PHD1	PHD2	PHD2
Cu5	KA	LiF 220	150 µm	Flow	60	66	65.533	-0.8312	1.2458	26	36	42	57
Ag7	KA	LiF 220	150 µm	Scint.	60	66	22.6436	-1.66	1.7906	35	63		
Te4	KA	LiF 220	150 µm	Scint.	60	66	18.217	-0.4214	2.1588	37	61		
Bi5	LA	LiF 220	150 µm	Scint.	60	66	47.353	-1.1068	2.3086	30	70		
Au6	LA	LiF 220	150 µm	Scint.	60	66	53.2418			33	69		
Rh8	KA-C	LiF 220	150 µm	Scint.	60	66	26.1924	-1.7078	3.7846	33	66		
W3	LA	LiF 220	150 µm	Flow	60	66	62.4504	-0.617	1.938	29	38	43	60
Mo3	KA	LiF 220	150 µm	Scint.	60	66	28.8306	-0.5536	0.6618	33	65		
Pb5	LB2	LiF 220	150 µm	Scint.	60	66	40.3506	-0.7868	0.7472	36	63		
Zn7	KA	LiF 220	150 µm	Scint.	60	66	60.5216	-0.7232	0.7768	35	64		
Sb3	KA	LiF 220	150 µm	Scint.	60	66	18.989	-0.4148	0.4946	36	56		
Ni3	KA	LiF 220	150 µm	Flow	60	66	71.2908	-0.8632	0.9764	26	35	44	59
As5	KA	LiF 220	150 µm	Scint.	60	66	48.7516	-0.5142	1.1276	35	64		
Co2	KA	LiF 220	150 µm	Flow	60	66	77.9158	-3.49	1.2836	25	33	44	60
Hg1	LA	LiF 220	150 µm	Scint.	60	66	51.6636	-1.4734	2.6058	34	67		
Fe8	KA	LiF 220	150 µm	Flow	60	66	85.7462	-2.6724	3.7012	21	30	41	58
S1	KA	Ge 111	300 µm	Flow	32	125	110.6868	-4.059	5.2596	27	73		
Al4	KA	PE 002	300 µm	Flow	32	125	144.9218	-6.9556		30	70		
Ca3	KA	LiF 200	150 µm	Flow	32	125	113.1264	-4.6128	6.3396	8	17	30	70
K3	KA	LiF 200	300 µm	Flow	32	125	136.6994	-5.5832	5.2828	32	67		
Mg3	KA	PX1	700 µm	Flow	32	125	22.4328	-2.2154	2.479	30	71		
Na3	KA	PX1	700 µm	Flow	32	125	27.088	-2.16	1.9896	30	70		
Si4	KA	PE 002	300 µm	Flow	32	125	109.1346	-12.1156	7.3074	30	70		
Rh7	KB-C	LiF 220	150 µm	Scint.	60	66	23.2686			27	78		
Se1	KA	LiF 220	150 µm	Scint.	60	66	45.6588	-0.6068	0.6698	36	67		
Mn2	KA	LiF 200	300 µm	Flow	57	70	62.9764	-1.1202	1.2684	18	29	40	59
Ti3	KA	LiF 200	300 µm	Flow	42	95	86.1712	-1.3548	2.1364	10	20	38	62
P2	KA	Ge 111	300 µm	Flow	32	125	140.9206	-3.5284	1.8564	33	67		

Table D-2. KEN2 XRF Routine Count Times

Minimum tine (s) = 154, Maximum time (s) = 4078

Ch.	Time (s)	CSE (%)	Drift Corrected	Background Factor
Cu5	60	0.5	Yes	
Cu5Bg1	60	0.5		0.5998083
Cu5Bg2	60	0.5		0.4001918
Ag7	60	0.5	Yes	
Ag7Bg1	60	0.5		0.5189242
Ag7Bg2	60	0.5		0.4810758
Te4	90	0.5	Yes	
Te4Bg1	60	0.5		0.7503565
Sb3Bg2	60	0.5		0.2496435
Bi5	60	0.5	Yes	
Bi5Bg1	60	0.5		0.6759381
Bi5Bg2	60	0.5		0.3240618
Au6	238	0.5	Yes	
Hg1Bg1	120	0.5		0.2519129
Hg1Bg2	120	0.5		0.7480871
Rh8	30	0.5	Yes	
Rh8Bg1	60	0.5		0.6890612
Rh8Bg2	60	0.5		0.3109388
W3	60	0.5	Yes	
W3Bg1	60	0.5		0.7585125
W3Bg2	60	0.5		0.2414875
Mo3	60	0.5	Yes	
Mo3Bg1	60	0.5		0.5445114
Mo3Bg2	60	0.5		0.4554886
Pb5	60	0.5	Yes	
Pb5Bg1	60	0.5		0.4870925
Pb5Bg2	60	0.5		0.5129076
Zn7	60	0.5	Yes	
Zn7Bg1	60	0.5		0.517868
Zn7Bg2	60	0.5		0.482132
Sb3	60	0.5	Yes	
Te4Bg1	60	0.5		0.2930097
Sb3Bg2	60	0.5		0.7069903
Ni3	60	0.5	Yes	
Ni3Bg1	60	0.5		0.5307648
Ni3Bg2	60	0.5		0.4692352
As5	60	0.5	Yes	
As5Bg1	60	0.5		0.6868082
As5Bg2	60	0.5		0.3131918
Co2	60	0.5	Yes	
Co2Bg1	60	0.5		0.2688957

Table D-2 cont. KEN2 XRF Routine Count Times

Ch.	Time (s)	CSE (%)	Drift Corrected	Background Factor
Co2Bg2	60	0.5		0.7311043
Hg1	120	0.5	Yes	
Hg1Bg1	120	0.5		0.6388018
Hg1Bg2	120	0.5		0.3611982
Fe8	60	0.5	Yes	
Fe8Bg1	60	0.5		0.5807086
Fe8Bg2	60	0.5		0.4192913
S1	30	0.5	Yes	
S1Bg1	30	0.5		0.5644191
S1Bg2	30	0.5		0.4355809
Al4	30	0.5	Yes	
Al4Bg1	30	0.5		1
Ca3	30	0.5	Yes	
Ca3Bg1	30	0.5		0.578832
Ca3Bg2	30	0.5		0.421168
K3	30	0.5	Yes	
K3Bg1	30	0.5		0.4861778
K3Bg2	30	0.5		0.5138222
Mg3	30	0.5	Yes	
Mg3Bg1	30	0.5		0.5280759
Mg3Bg2	30	0.5		0.4719241
Na3	30	0.5	Yes	
Na3Bg1	30	0.5		0.4794678
Na3Bg2	30	0.5		0.5205322
Si4	30	0.5	Yes	
Si4Bg1	30	0.5		0.3762242
Si4Bg2	30	0.5		0.6237758
Rh7	30	0.5	Yes	
Ag7Bg1	60	0.5		0.3377963
Ag7Bg2	60	0.5		0.6622037
Se1	60	0.5	Yes	
Se1Bg1	60	0.5		0.5246762
Se1Bg2	60	0.5		0.4753238
Mn2	30	0.5	Yes	
Mn2Bg1	30	0.5		0.5310218
Mn2Bg2	30	0.5		0.4689782
Ti3	30	0.5	Yes	
Ti3Bg1	30	0.5		0.6119375
Ti3Bg2	30	0.5		0.3880625
P2	30	0.5	Yes	
P2Bg1	30	0.5		0.3447483
P2Bg2	30	0.5		0.6552517

Table D-3. Compositions of Artificial Standards

	Au					Ag					Te					Hg				
Blank	2.25	8			**4.8**	0	8	27	19	**26**	0	7		9	**9**	0			-47	**-7**
Low	200	276	191		**239.4**	10	276	39	24	**28**	100	92	116	128	**120**	30		35	61	**36**
Medium	500	675	479		**585.2**	40	675	65	56	**56**	300	276	299	393	**360**	60		25	68	**64**
High	900	717	559		**618.4**	150	717	168	166	**163**	900	856	913	1184	**1113**	100		79	184	**105.1**

Key

	Theoretical
	Buck3
	IQ+
	ProTrace
	KEN2

Table D-4. Calculations of Lower Limits of Detection of Metals for KEN2 XRF Routine

Standard	Sum	Au	Cu	As	Ag	Te	Bi	W	Mo	Pb	Zn	Sb	Ni	Hg	Co	Se
CaCO3-BLANK	59.5	10	14	0	20	1	2	1	1	-1	9	6	-12	9	4	0
CaCO3-BLANK	59.5	9	13	0	14	-1	1	3	2	0	9	7	-14	10	2	0
CaCO3-BLANK	59.5	9	13	0	14	2	1	2	2	-1	9	5	-12	9	-1	-1
stdev CaCO3-BLANK		0.58	0.44	0.21	3.39	1.36	0.55	0.72	0.35	0.58	0.36	1.27	0.93	0.53	2.25	0.58
SiO2-BLANK	107.0	-11	12	0	-6	-1	2	7	1	1	13	8	-19	1	2	0
SiO2-BLANK	106.9	-12	12	-1	-2	-6	1	8	1	1	13	10	-18	1	2	0
SiO2-BLANK	107.2	-11	12	1	-5	0	1	7	1	-2	13	5	-20	1	2	0
stdev SiO2-BLANK		0.40	0.23	0.80	2.48	2.85	0.65	0.75	0.00	1.65	0.21	2.32	1.00	0.30	0.20	0.19
LLD SiO2-BLANK		1	1	2	7	9	2	2	0	5	1	7	3	1	1	1
LLD CaCo3-BLANK		2	1	1	10	4	2	2	1	2	1	4	3	2	7	2
LLD		**2**	**1**	**2**	**10**	**9**	**2**	**2**	**1**	**5**	**1**	**7**	**3**	**2**	**7**	**2**

Table D-5. Calculations of Lower Limits of Detection of Oxides for KEN2 XRF Routine

Standard	Sum	S	Al2O3	CaO	K2O	MgO	Na2O	SiO2	MnO	TiO2	P2O5	Fe2O3
CaCO3-BLANK	59.5	0.06	-0.08	59.38	0.01	0.03	0.11	0.04	0.00	0.00	0.00	-0.04
CaCO3-BLANK	59.5	0.06	-0.08	59.33	0.01	0.03	0.11	0.04	0.00	0.00	0.00	-0.04
CaCO3-BLANK	59.5	0.06	-0.08	59.37	0.01	0.03	0.11	0.05	0.00	0.00	0.00	-0.04
stdev CaCO3-BLANK		0.00	0.00	0.03	0.00	0.00	0.00	0.00	0.00	0.00	0.00	0.00
SiO2-BLANK	107.0	0.0	0.3	-0.1	0.0	-0.1	0.1	106.6	0.0	0.0	0.0	0.0
SiO2-BLANK	106.9	0.0	0.4	-0.1	0.0	-0.1	0.1	106.6	0.0	0.0	0.0	0.0
SiO2-BLANK	107.2	0.0	0.3	-0.1	0.0	-0.1	0.1	106.8	0.0	0.0	0.0	0.0
stdev SiO2-BLANK		0.00	0.00	0.00	0.00	0.00	0.00	0.14	0.00	0.00	0.00	0.00
LLD SiO2-BLANK		0.00	0.01	0.00	0.00	0.00	0.00	0.42	0.00	0.00	0.00	0.00
LLD CaCo3-BLANK		0.01	0.00	0.08	0.00	0.00	0.00	0.00	0.00	0.00	0.00	0.00
LLD		**0.01**	**0.01**	**0.80**	**0.00**	**0.00**	**0.00**	**0.42**	**0.00**	**0.00**	**0.00**	**0.00**

Table D-6. Comparison of Results of KEN2 Routine and Known* Kensington Concentrates

	ppm														wt%											
	As	**Ag**	**Te**	**Bi**	**Au**	**W**	**Mo**	**Pb**	**Zn**	**Sb**	**Ni**	**Hg**	**Co**	**Se**	**%Cu**	**Al2O3**	**CaO**	**K2O**	**MgO**	**Na2O**	**MnO**	**TiO2**	**P2O5**	**SiO2**	**%Fe**	**%S**
PY Conc1	7	43	269	3	254	68	66	10	71	24	42	13	256	24	1.00	7.03	5.85	1.10	2.46	0.36	0.13	0.33	0.13	19.55	27.88	22.23
PY Conc2	7	46	271	1	252	69	66	12	68	20	45	12	256	23	1.03	6.85	5.75	1.08	2.42	0.34	0.13	0.33	0.13	19.11	28.41	22.75
PY Conc avg	7	44	270	2	253	69	66	11	70	22	44	12	256	23	1.02	6.94	5.80	1.09	2.44	0.35	0.13	0.33	0.13	19.33	28.14	22.49
real*	9	13	276	2	235	49	71	10	49	24	19	--	272	22	0.93	4.30	3.80	0.73	1.00	1.00	0.10	0.13	--	--	34.00	37.00
stdev	2	22	4	0	13	14	3	0	14	1	17		11	1	0.06	1.87	1.41	0.25	1.02	0.46	0.02	0.14			4.14	10.26

* Au, Te, Fe, and S from Kensington mill (fire assay); all others from American Analytical Services Inc. (ICPMS)

Appendix E. XRF Data Post Processing Procedure

1. Any sample analyzed with KEN2 that had a measurement of W ≥ 50 ppm was re-analyzed with a separate Ag-Te-Au-W routine that only measured those metals. Those values then replaced the KEN2 values.
2. Manual background corrections for several metals listed below were performed by subtracting a calculated value from the original corresponding metal value.

metal	As	Ag	Te	Bi	W	Mo	Zn	Sb	Hg
Subtract	2	20	2	3	10	2	3	5	5

3. A separate Ag correction is needed after the background correction. Ag values are multiplied by 0.6.
4. Sulfide species are calculated from XRF values to be used in normalizing the data in a later step. Atomic weights are used and will be notated as A_r(X) where X = atomic symbol. The measured values are notated as X where X = atomic symbol. Equations are listed in order of application on data.

Convert Fe_2O_3 into Fe for sulfide calculations:

$$Fe_{calc} = \frac{Fe_2O_3 * A_r\,(Fe)}{A_r\,(Fe) + 1.5 *\ A_r\,(O)}$$

% tetrahedrite if all of the Sb is in tetrahedrite:

$$\%\ tetSb = \frac{A_r\,(Cu) * 10 + A_r\,(Zn) * 2 + A_r\,(Sb) * 4 + A_r\,(S) * 13}{(A_r\,(Sb) * 4) * \left(\frac{Sb}{10000}\right)}$$

% tennantite if all of the As is in tennantite:

$$\%\ tennAs = \frac{A_r\,(Cu) * 10 + A_r\,(Zn) * 2 + A_r\,(Sb) * 4 + A_r\,(S) * 13}{(A_r\,(As) * 4) * \left(\frac{As}{10000}\right)}$$

Total % fahlore:

$$tot\%fah = \%tetSb + \%tennAs$$

% chalcopyrite assuming all of the Cu is in chalcopyrite, tetrahedrite, and tennantite:

$$\%cp = \frac{A_r\,(Cu) + A_r\,(Fe) + A_r\,(S) * 2}{A_r\,(Cu)} * \left[\frac{Cu}{10000} - \frac{A_r\,(Cu) * 10}{A_r\,(Cu) * 10 + A_r\,(Zn) * 2 + A_r\,(Sb) * 4 + A_r\,(S) * 13} * \%tetSb - \frac{A_r\,(Cu) * 10}{A_r\,(Cu) * 10 + A_r\,(Zn) * 2 + A_r\,(As) * 4 + A_r\,(S) * 13} * \%tennAs\right]$$

% chalcopyrite assuming all of the S is in chalcopyrite, tetrahedrite, and tennantite

$$\%cpS = \frac{2 * A_r\,(S)}{A_r\,(Cu) + 2 * A_r\,(S) + A_r\,(Fe)} * \%cp$$

% pyrite assuming all of the S is in chalcopyrite, tetrahedrite, tennantite, and pyrite:

$$\%pyS = \left[S - \%cpS - \frac{A_r\,(S) * 13}{A_r\,(Cu) * 10 + A_r\,(Zn) * 2 + A_r\,(Sb) * 4 + A_r\,(S) * 13} * \%tetSb - \frac{A_r\,(S) * 13}{A_r\,(Cu) * 10 + A_r\,(Zn) * 2 + A_r\,(As) * 4 + A_r\,(S) * 13} * \%tennAs\right] * \frac{A_r\,(S) * 2 + A_r\,(Fe)}{A_r\,(S) * 2}$$

5. Samples with duplicates are compared. The method for choosing the value for duplicate samples are as follows:
   - Any duplicate with < 20 total wt% sulfide is automatically discounted.
   - Subsamples are then normalized to 100% sulfide.
   - If the metal concentrations in the duplicates are significantly different after normalizing (> 100% standard deviation), the duplicate with higher Au value is used.
   - If the % standard deviation in the metal concentrations of the duplicates are small (< 100%) then the average of the duplicates is used for that sample.

6. Remove samples with low total sulfide (< 20%) from the data set.
7. Normalize all resulting samples to 100% sulfide.

Appendix F. Processed XRF Data

Table F-1. Calculated Sulfide Concentrations

Sample name	%pyS	%cp	%tetSb	%tenAs	tot%tet	totSulf	rel%cp	rel%py	rel%tet
1065-189-1	74.3	0.0	0.0	0.0	0.0	74.3	0.0	100.0	0.0
1065-189-2A	78.8	0.0	0.0	0.0	0.0	78.8	0.0	100.0	0.0
1065-189-2B	70.2	0.0	0.0	0.0	0.0	70.2	0.0	100.0	0.0
1065-189-2C	84.3	0.0	0.0	0.0	0.0	84.3	0.0	100.0	0.0
1065-189-3	54.1	0.0	0.0	0.0	0.0	54.1	0.0	100.0	0.0
1065-189-5	76.3	0.0	0.0	0.0	0.0	76.3	0.0	100.0	0.0
1065-189-6	75.9	0.0	0.0	0.0	0.0	75.9	0.0	100.0	0.0
1065-189-8A	74.9	0.2	0.0	0.0	0.0	75.0	0.2	99.8	0.0
1065-189-8B	86.8	0.2	0.0	0.0	0.0	86.9	0.2	99.8	0.0
1065-197-4	80.8	0.0	0.0	0.0	0.0	80.8	0.0	100.0	0.0
1065-197-6	50.0	0.3	0.0	0.0	0.0	50.3	0.7	99.3	0.0
1065-197-7	84.9	0.0	0.0	0.0	0.0	84.9	0.0	100.0	0.0
1065-197-8	82.2	0.0	0.0	0.0	0.0	82.2	0.0	100.0	0.0
1065-206-1	45.3	0.2	0.0	0.0	0.0	45.4	0.4	99.6	0.0
1065-206-2	65.3	0.0	0.0	0.0	0.0	65.3	0.0	100.0	0.0
1065-206-3	67.4	8.8	0.0	0.0	0.0	76.2	11.5	88.5	0.0
1065-206-4	17.9	0.1	0.0	0.0	0.0	18.0	0.6	99.4	0.0
1065-206-5	77.5	10.8	0.0	0.0	0.0	88.3	12.2	87.8	0.0
1065-5	70.6	0.0	0.0	0.0	0.0	70.6	0.0	100.0	0.0
1140-189-1	40.4	0.0	0.0	0.0	0.0	40.4	0.0	100.0	0.0
1140-189-2	17.9	0.0	0.0	0.0	0.0	17.9	0.1	99.9	0.0
1140-189-3	70.6	0.1	0.0	0.0	0.0	70.6	0.1	99.9	0.0
1140-189-4B	57.3	0.0	0.0	0.0	0.0	57.3	0.0	100.0	0.0
1140-189-4C	67.2	0.0	0.0	0.0	0.0	67.2	0.1	99.9	0.0
1140-189-5	24.3	0.0	0.0	0.0	0.0	24.3	0.1	99.9	0.0
1140-197-12	66.3	0.0	0.0	0.0	0.0	66.3	0.0	100.0	0.0
1140-197-13	55.0	0.0	0.0	0.0	0.0	55.0	0.0	100.0	0.0
1140-197-2	66.1	0.1	0.0	0.0	0.0	66.2	0.1	99.9	0.0
1140-197-4	51.5	0.0	0.0	0.0	0.0	51.5	0.0	100.0	0.0
1140-197-5	64.1	0.1	0.0	0.0	0.0	64.2	0.2	99.8	0.0
1140-197-6	92.3	0.0	0.0	0.0	0.0	92.3	0.0	100.0	0.0
1140-197-6A	94.3	0.0	0.0	0.0	0.0	94.3	0.0	100.0	0.0
1140-197-8	79.5	0.0	0.0	0.0	0.0	79.5	0.0	100.0	0.0
1140-197-9	3.8	0.0	0.0	0.0	0.0	3.8	0.2	99.8	0.0
1140-197-X	90.0	0.0	0.0	0.0	0.0	90.0	0.0	100.0	0.0
1140-206-1	69.7	0.0	0.0	0.0	0.0	69.8	0.1	99.9	0.0
1140-206-10	66.4	0.0	0.0	0.0	0.0	66.4	0.0	100.0	0.0
1140-206-11	56.4	0.1	0.0	0.0	0.0	56.5	0.1	99.9	0.0
1140-206-12	66.3	0.0	0.0	0.0	0.0	66.4	0.0	100.0	0.0
1140-206-13	86.1	0.0	0.0	0.0	0.0	86.1	0.0	100.0	0.0
1140-206-14	54.1	0.1	0.0	0.0	0.0	54.2	0.1	99.9	0.0
1140-206-2	64.2	0.0	0.0	0.0	0.0	64.2	0.0	100.0	0.0
1140-206-3	32.3	0.0	0.0	0.0	0.0	32.3	0.0	100.0	0.0
1140-206-4	66.0	0.1	0.0	0.0	0.0	66.1	0.1	99.9	0.0
1140-206-5	88.2	0.0	0.0	0.0	0.0	88.2	0.0	100.0	0.0
1140-206-6	71.3	0.0	0.0	0.0	0.0	71.4	0.0	100.0	0.0
1140-206-7	76.8	0.0	0.0	0.0	0.0	76.8	0.0	100.0	0.0
1140-206-8	59.0	0.0	0.0	0.0	0.0	59.1	0.0	100.0	0.0
1210-223-4	9.6	0.0	0.0	0.0	0.0	9.6	0.1	99.9	0.0
1210-223-5	68.5	0.0	0.0	0.0	0.0	68.6	0.0	100.0	0.0
1210-223-6	37.2	0.0	0.0	0.0	0.0	37.3	0.0	100.0	0.0
1210-223-7	8.9	0.0	0.0	0.0	0.0	8.9	0.1	99.9	0.0
1210-233-1	80.1	0.0	0.0	0.0	0.0	80.2	0.0	100.0	0.0
1210-233-3	20.7	0.0	0.0	0.0	0.0	20.7	0.0	100.0	0.0
1280-201-1	80.7	0.1	0.0	0.0	0.0	80.8	0.1	99.9	0.0
1280-201-10	71.7	0.0	0.0	0.0	0.0	71.8	0.0	100.0	0.0
1280-201-2	58.8	0.0	0.0	0.0	0.0	58.9	0.1	99.9	0.0
1280-201-3	68.4	0.0	0.0	0.0	0.0	68.4	0.0	100.0	0.0
1280-201-4	88.9	0.0	0.0	0.0	0.0	88.9	0.0	99.9	0.0
1280-201-5	73.3	0.0	0.0	0.0	0.0	73.3	0.0	100.0	0.0
1280-201-6	46.9	0.1	0.0	0.0	0.0	47.0	0.2	99.8	0.0
1280-201-7	57.1	0.0	0.0	0.0	0.0	57.1	0.1	99.9	0.0
1280-201-8	62.7	0.0	0.0	0.0	0.0	62.7	0.0	100.0	0.0
1280-201-9	42.4	0.0	0.0	0.0	0.0	42.4	0.0	100.0	0.0
1280-235-10A	62.3	0.0	0.0	0.0	0.0	62.3	0.0	100.0	0.0
1280-235-10B	66.4	0.0	0.0	0.0	0.0	66.4	0.0	100.0	0.0
1280-235-11A	88.0	0.0	0.0	0.0	0.0	88.0	0.0	100.0	0.0
1280-235-11B	86.2	0.0	0.0	0.0	0.0	86.2	0.0	100.0	0.0

Table F-1 cont. Calculated Sulfide Concentrations

Sample name	%pyS	%cp	%tetSb	%tenAs	tot%tet	totSulf	rel%cp	rel%py	rel%tet
1280-235-11C	80.8	0.0	0.0	0.0	0.0	80.9	0.0	100.0	0.0
1280-235-2	45.2	0.0	0.0	0.0	0.0	45.3	0.0	100.0	0.0
1280-235-4	80.6	0.0	0.0	0.0	0.0	80.7	0.0	99.9	0.0
1280-235-5	68.7	0.0	0.0	0.0	0.0	68.7	0.0	100.0	0.0
1280-235-6	47.6	0.1	0.0	0.0	0.0	47.7	0.3	99.7	0.0
1280-235-8	51.4	0.0	0.0	0.0	0.0	51.5	0.1	99.9	0.0
1280-235-9	3.7	0.0	0.0	0.0	0.0	3.7	0.8	99.2	0.0
1290-1	77.0	0.5	0.0	0.0	0.0	77.5	0.7	99.3	0.0
1290-2	77.9	0.0	0.0	0.0	0.0	78.0	0.0	100.0	0.0
1290-3	92.5	0.3	0.0	0.0	0.0	92.9	0.4	99.6	0.0
1290-4	59.4	0.3	0.0	0.0	0.0	59.7	0.5	99.5	0.0
1290-5	49.1	0.3	0.0	0.0	0.0	49.4	0.5	99.5	0.0
1350-1	81.1	0.0	0.0	0.0	0.0	81.2	0.0	100.0	0.0
1350-10	91.8	0.0	0.0	0.0	0.0	91.9	0.0	100.0	0.0
1350-11	80.8	0.0	0.0	0.0	0.0	80.8	0.0	100.0	0.0
1350-12A	85.1	0.4	0.0	0.0	0.0	85.5	0.5	99.5	0.0
1350-12B	76.1	0.2	0.0	0.0	0.0	76.4	0.3	99.7	0.0
1350-12C	84.0	0.0	0.0	0.0	0.0	84.0	0.1	99.9	0.0
1350-13	21.7	0.0	0.0	0.0	0.0	21.7	0.0	99.9	0.0
1350-13A	25.4	0.0	0.0	0.0	0.0	25.4	0.0	100.0	0.0
1350-13B	22.0	0.0	0.0	0.0	0.0	22.1	0.0	100.0	0.0
1350-14	10.8	0.0	0.0	0.0	0.0	10.8	-0.1	99.9	0.2
1350-15A	2.5	0.0	0.0	0.0	0.0	2.5	-0.3	99.8	0.5
1350-15B	5.9	0.0	0.0	0.0	0.0	5.9	-0.3	99.9	0.4
1350-15C	1.4	0.0	0.0	0.0	0.0	1.4	0.4	99.6	0.0
1350-16FG-A	3.1	0.0	0.0	0.0	0.0	3.1	-0.4	99.6	0.8
1350-16FG-B	3.0	0.0	0.0	0.0	0.0	3.0	-0.1	99.3	0.8
1350-16MG	10.1	0.0	0.0	0.0	0.0	10.1	0.1	99.9	0.0
1350-17	44.6	0.0	0.0	0.0	0.0	44.6	0.0	100.0	0.0
1350-18	1.8	0.0	0.0	0.0	0.0	1.9	1.6	98.0	0.3
1350-19	61.0	0.0	0.0	0.0	0.0	61.0	0.0	100.0	0.0
1350-20	12.0	0.0	0.0	0.0	0.0	12.0	0.0	99.9	0.1
1350-21	80.2	0.0	0.0	0.0	0.0	80.2	0.0	100.0	0.0
1350-21B	57.1	0.0	0.0	0.0	0.0	57.1	0.0	100.0	0.0
1350-22	15.9	0.0	0.0	0.0	0.0	15.9	0.2	99.8	0.1
1350-23	46.7	0.0	0.0	0.0	0.0	46.7	0.0	100.0	0.0
1350-2A	67.4	0.0	0.0	0.0	0.0	67.5	0.0	100.0	0.0
1350-2B	87.7	0.0	0.0	0.0	0.0	87.7	0.0	100.0	0.0
1350-3	80.3	0.1	0.0	0.0	0.0	80.4	0.1	99.9	0.0
1350-3A	92.3	0.5	0.0	0.0	0.0	92.8	0.5	99.5	0.0
1350-4A	81.2	0.1	0.0	0.0	0.0	81.3	0.1	99.9	0.0
1350-4B	83.5	0.1	0.0	0.0	0.0	83.6	0.1	99.9	0.0
1350-4C	75.9	0.1	0.0	0.0	0.0	76.1	0.2	99.8	0.0
1350-5A	18.2	0.2	0.0	0.0	0.0	18.3	0.8	99.2	0.0
1350-5A	18.9	0.2	0.0	0.0	0.0	19.0	0.8	99.2	0.0
1350-5B	69.7	0.0	0.0	0.0	0.0	69.7	0.1	99.9	0.0
1350-6	84.5	0.0	0.0	0.0	0.0	84.5	0.0	100.0	0.0
1350-7	64.9	0.0	0.0	0.0	0.0	64.9	0.0	100.0	0.0
1350-8	76.8	0.0	0.0	0.0	0.0	76.8	0.0	100.0	0.0
1350-9	45.9	1.0	0.0	0.0	0.0	46.9	2.2	97.8	0.0
1355-193-2	52.5	0.0	0.0	0.0	0.0	52.6	0.0	100.0	0.0
1355-193-3	25.3	0.0	0.0	0.0	0.0	25.3	0.1	99.9	0.0
1355-201-1	53.4	0.2	0.0	0.0	0.0	53.6	0.4	99.6	0.0
1355-201-10	76.6	0.0	0.0	0.0	0.0	76.6	0.0	100.0	0.0
1355-201-11	78.6	0.0	0.0	0.0	0.1	78.6	0.0	99.9	0.1
1355-201-12	69.8	0.2	0.0	0.0	0.0	70.1	0.3	99.6	0.0
1355-201-12B	68.1	0.2	0.0	0.0	0.0	68.4	0.3	99.6	0.0
1355-201-12C	69.8	0.2	0.0	0.0	0.0	70.0	0.3	99.7	0.0
1355-201-13	74.4	0.1	0.4	0.1	0.6	75.1	0.1	99.1	0.8
1355-201-14 FG	54.7	0.2	0.1	0.1	0.1	55.1	0.4	99.4	0.2
1355-201-14 MG-F	72.6	0.1	0.0	0.0	0.1	72.8	0.1	99.7	0.1
1355-201-14MGA	81.7	0.6	0.0	0.0	0.1	82.4	0.7	99.2	0.1
1355-201-14MGB	72.6	0.6	0.1	0.1	0.2	73.3	0.8	99.0	0.2
1355-201-16	65.9	0.8	0.6	0.2	0.8	67.5	1.1	97.7	1.2
1355-201-2	56.8	0.0	0.0	0.0	0.0	56.8	0.0	100.0	0.0
1355-201-7	24.1	1.4	0.0	0.0	0.0	25.5	5.5	94.5	0.0
1355-210-1	62.4	0.6	0.0	0.0	0.0	63.0	1.0	99.0	0.0
1355-210-10	73.8	0.0	0.0	0.0	0.0	73.9	0.0	100.0	0.0
1355-210-11	42.9	0.1	0.2	0.1	0.3	43.3	0.3	99.0	0.7
1355-210-12	66.8	0.1	0.0	0.0	0.0	66.9	0.2	99.8	0.0
1355-210-13	-6.1	54.3	0.0	0.0	0.0	48.2	112.6	-12.6	0.0

Table F-1 cont. Calculated Sulfide Concentrations

Sample name	%pyS	%cp	%tetSb	%tenAs	tot%tet	totSulf	rel%cp	rel%py	rel%tet
1355-210-14	66.0	22.5	0.0	0.0	0.0	88.5	25.4	74.5	0.0
1355-210-15	1.5	14.1	0.0	0.0	0.0	15.6	90.5	9.5	0.0
1355-210-16	68.3	0.0	0.0	0.0	0.0	68.3	0.0	100.0	0.0
1355-210-2	70.0	0.3	0.4	0.1	0.5	70.8	0.4	98.8	0.7
1355-210-3	50.5	5.3	0.0	0.0	0.0	55.8	9.5	90.5	0.0
1355-210-4	90.7	0.0	0.0	0.0	0.0	90.8	0.0	100.0	0.0
1355-210-5	44.1	5.5	0.0	0.0	0.0	49.6	11.0	89.0	0.0
1355-210-6	41.5	33.5	0.1	0.0	0.1	75.1	44.6	55.3	0.1
1355-210-7	58.6	0.0	0.0	0.0	0.0	58.7	0.1	99.9	0.0
1355-210-8	77.9	0.1	0.0	0.0	0.0	78.0	0.1	99.9	0.0
1355-210-9	82.3	0.0	0.0	0.0	0.0	82.3	0.0	100.0	0.0
1355-227-1	74.6	0.0	0.0	0.0	0.0	74.6	0.0	100.0	0.0
1355-227-2	74.4	0.0	0.0	0.0	0.0	74.5	0.1	99.9	0.0
1355-227-3	59.6	0.0	0.0	0.0	0.0	59.6	0.0	100.0	0.0
480ACESS-1CG	13.2	0.9	0.0	0.0	0.0	14.1	6.1	93.9	0.0
480ACESS-1MG	21.2	0.5	0.0	0.0	0.0	21.7	2.3	97.7	0.0
480N-1	37.9	0.0	0.0	0.0	0.0	37.9	0.0	100.0	0.0
480N-3A	26.6	0.0	0.0	0.0	0.0	26.6	0.0	100.0	0.0
480N-3B	23.8	0.0	0.0	0.0	0.0	23.8	0.0	100.0	0.0
480N-3C	31.2	0.0	0.0	0.0	0.0	31.3	0.0	100.0	0.0
555-152-1A	78.0	0.1	0.0	0.0	0.0	78.2	0.1	99.8	0.0
555-152-1B	60.8	0.1	0.0	0.0	0.0	60.9	0.1	99.8	0.0
555-152-1C	71.6	0.1	0.0	0.0	0.0	71.7	0.1	99.8	0.0
555-152-2	55.8	0.0	0.0	0.0	0.0	55.8	0.0	100.0	0.0
555-160-1B	39.7	0.0	0.0	0.0	0.0	39.7	0.1	99.9	0.0
555-160-1C	36.7	0.0	0.0	0.0	0.0	36.8	0.1	99.9	0.0
555-160-2	82.4	0.1	0.3	0.1	0.3	82.8	0.2	99.4	0.4
555-160-3	86.2	0.1	0.1	0.0	0.2	86.4	0.1	99.7	0.2
555-160-5 MG	39.5	0.0	0.0	0.0	0.0	39.6	0.0	99.9	0.0
555-160-5FG	32.2	0.0	0.0	0.0	0.1	32.3	0.1	99.8	0.2
555-160-6A	68.5	0.1	0.4	0.1	0.5	69.1	0.2	99.1	0.7
555-160-6B	73.4	0.1	0.3	0.0	0.3	73.9	0.1	99.4	0.4
555-160-7	50.7	0.0	0.1	0.0	0.1	50.8	0.1	99.8	0.1
555-160-8	30.9	0.3	0.9	0.1	1.1	32.2	0.8	95.9	3.3
555-176-1	81.9	0.2	0.0	0.0	0.0	82.1	0.3	99.7	0.0
555-188-3	64.1	0.9	0.0	0.0	0.0	65.0	1.4	98.6	0.0
555-188-4	72.7	0.8	0.0	0.0	0.0	73.5	1.1	98.9	0.0
555-188-5	23.8	36.6	0.0	0.0	0.0	60.3	60.6	39.4	0.0
555-188-6	66.8	0.0	0.0	0.0	0.0	66.8	0.0	100.0	0.0
555-188-7	42.6	0.0	0.0	0.0	0.0	42.6	0.0	100.0	0.0
555-188-8	37.1	5.1	0.0	0.0	0.0	42.2	12.0	88.0	0.0
555-188-9	45.3	0.0	0.0	0.0	0.0	45.3	0.0	100.0	0.0
555-204-1	34.1	0.1	0.0	0.0	0.0	34.2	0.2	99.8	0.0
555-204-2	33.5	0.2	0.0	0.0	0.0	33.7	0.5	99.5	0.0
555-204-3	64.7	0.0	0.0	0.0	0.0	64.7	0.0	100.0	0.0
555-204-5	45.2	0.1	0.0	0.0	0.0	45.3	0.2	99.8	0.0
555S-1	47.7	0.0	0.0	0.0	0.0	47.7	0.0	100.0	0.0
555S-10	35.5	0.0	0.0	0.0	0.0	35.5	0.0	100.0	0.0
555S-11	67.5	0.0	0.0	0.0	0.0	67.5	0.0	100.0	0.0
555S-13	58.2	0.0	0.0	0.0	0.0	58.3	0.1	99.9	0.0
555S-14	47.0	14.0	0.0	0.0	0.0	61.1	23.0	77.0	0.0
555S-15	75.9	0.0	0.0	0.0	0.0	75.9	0.0	100.0	0.0
555S-16	77.3	0.0	0.0	0.0	0.0	77.3	0.1	99.9	0.0
555S-17	47.6	0.0	0.0	0.0	0.0	47.6	0.0	100.0	0.0
555S-2	64.9	0.1	0.0	0.0	0.0	65.0	0.1	99.9	0.0
555S-3A	13.1	0.0	0.0	0.0	0.0	13.1	0.1	99.9	0.0
555S-3B	13.8	0.0	0.0	0.0	0.0	13.8	0.1	99.9	0.0
555S-3C	9.1	0.0	0.0	0.0	0.0	9.1	0.1	99.9	0.0
555S-4	59.9	0.1	0.1	0.0	0.1	60.1	0.1	99.7	0.1
555S-5	74.2	0.1	0.0	0.0	0.0	74.2	0.1	99.9	0.0
555S-6A	77.8	0.0	0.0	0.0	0.0	77.8	0.0	100.0	0.0
555S-6B	72.7	0.0	0.0	0.0	0.0	72.7	0.0	100.0	0.0
555S-6C	76.6	0.0	0.0	0.0	0.0	76.7	0.0	100.0	0.0
555S-7	69.0	0.0	0.0	0.0	0.0	69.0	0.0	100.0	0.0
555S-8	75.2	0.0	0.0	0.0	0.0	75.2	0.0	100.0	0.0
555S-9	82.4	0.0	0.0	0.0	0.0	82.4	0.0	100.0	0.0
630-1	26.9	0.0	0.0	0.0	0.0	26.9	0.0	100.0	0.0
630-224-1	62.3	0.1	0.0	0.0	0.0	62.4	0.1	99.9	0.0
630-224-2	19.4	0.0	0.0	0.0	0.0	19.4	0.0	100.0	0.0
630-224-3	34.2	0.0	0.0	0.0	0.0	34.2	0.0	100.0	0.0
630-224-4	30.3	0.0	0.0	0.0	0.0	30.3	0.0	100.0	0.0

Table F-1 cont. Calculated Sulfide Concentrations

Sample name	%pyS	%cp	%tetSb	%tenAs	tot%tet	totSulf	rel%cp	rel%py	rel%tet
705-184-1	51.6	0.0	0.0	0.0	0.0	51.6	0.1	99.9	0.0
705-184-2	27.7	0.0	0.0	0.0	0.0	27.7	0.0	100.0	0.0
705-PASTE-2	57.6	0.1	0.0	0.0	0.0	57.7	0.2	99.8	0.0
705-PASTE-3	56.7	0.0	0.0	0.0	0.0	56.7	0.1	99.9	0.0
705-PASTE-4	35.1	0.0	0.0	0.0	0.0	35.2	0.0	100.0	0.0
780-176-1	35.9	0.0	0.0	0.0	0.0	35.9	0.1	99.9	0.0
780-176-2	57.9	0.1	0.0	0.0	0.0	58.0	0.2	99.8	0.0
780-184-1	79.7	0.0	0.0	0.0	0.0	79.8	0.1	99.9	0.0
780-200-1	67.5	0.1	0.0	0.0	0.0	67.6	0.1	99.9	0.0
910N-2	24.6	0.0	0.0	0.0	0.0	24.6	0.0	100.0	0.0
910N-4	66.2	0.0	0.0	0.0	0.0	66.2	0.0	100.0	0.0
K12-10	23.8	0.0	0.0	0.0	0.0	23.9	0.1	99.9	0.0
K12-12-<100	1.8	0.0	0.0	0.0	0.0	1.9	1.4	98.6	0.0
K12-12-100-250	1.0	0.0	0.0	0.0	0.0	1.0	1.6	98.4	0.0
K12-13	30.7	0.0	0.0	0.0	0.0	30.7	0.1	99.9	0.0
K12-13-<100	1.0	0.0	0.0	0.0	0.0	1.0	1.9	98.1	0.0
K12-14	1.8	0.0	0.0	0.0	0.0	1.9	1.0	98.2	0.7
K12-19	85.2	0.0	0.0	0.0	0.0	85.2	0.0	100.0	0.0
K12-20	21.8	0.0	0.0	0.0	0.0	21.8	0.0	100.0	0.0
K12-21	5.5	0.0	0.0	0.0	0.0	5.5	0.3	99.5	0.2
K12-4	76.1	0.1	0.0	0.0	0.0	76.1	0.1	99.9	0.0
K12-5A	79.2	0.2	0.0	0.0	0.0	79.4	0.2	99.8	0.0
K12-5B	75.0	0.2	0.0	0.0	0.0	75.1	0.2	99.8	0.0
K12-7	84.4	0.1	0.0	0.0	0.0	84.5	0.1	99.9	0.0
K12-8	7.4	0.0	0.0	0.0	0.0	7.4	0.1	99.9	0.0
K12-8-<100	0.7	0.0	0.0	0.0	0.0	0.8	3.2	96.8	0.0
K12-9	7.0	0.0	0.0	0.0	0.0	7.0	0.1	99.9	0.0
K13-10A	4.2	0.7	0.0	0.1	0.1	5.0	14.8	83.6	1.6
K13-10A	4.8	0.7	0.0	0.1	0.1	5.5	12.3	86.6	1.0
K13-10B	3.2	0.5	0.0	0.0	0.0	3.7	12.9	85.8	1.3
K13-10C	4.6	0.7	0.0	0.1	0.1	5.3	12.4	86.3	1.3
K13-11	54.4	6.4	0.0	0.0	0.0	60.8	10.6	89.4	0.0
K13-12	51.5	0.0	0.0	0.0	0.0	51.6	0.0	100.0	0.0
K13-14	70.9	0.0	0.0	0.0	0.0	70.9	0.1	99.9	0.0
K13-15	79.0	2.6	0.0	0.0	0.0	81.6	3.2	96.8	0.0
K13-16A	60.3	2.1	0.0	0.0	0.0	62.4	3.4	96.6	0.0
K13-16B	76.1	3.1	0.0	0.0	0.0	79.2	3.9	96.1	0.0
K13-16C	41.0	1.8	0.0	0.0	0.0	42.8	4.2	95.8	0.0
K13-17	67.2	8.7	0.0	0.0	0.0	75.8	11.4	88.6	0.0
K13-18	62.4	0.0	0.0	0.0	0.0	62.4	0.0	100.0	0.0
K13-19	84.5	0.4	0.0	0.0	0.0	84.9	0.5	99.5	0.0
K13-21	38.4	0.0	0.0	0.0	0.0	38.4	0.0	100.0	0.0
K13-22	32.1	0.0	0.0	0.0	0.0	32.1	0.0	100.0	0.0
K13-24	53.9	0.0	0.0	0.0	0.0	53.9	0.0	100.0	0.0
K13-25	54.3	0.1	0.0	0.0	0.0	54.4	0.2	99.8	0.0
K13-4	69.5	0.0	0.0	0.0	0.0	69.6	0.0	99.9	0.0
KEN-02	27.8	0.0	0.0	0.0	0.0	27.8	0.2	99.8	0.0
KEN-04	64.0	0.0	0.0	0.0	0.0	64.0	0.0	100.0	0.0
KEN-04A	74.1	0.0	0.0	0.0	0.0	74.2	0.0	100.0	0.0
KEN-05	72.1	1.2	0.0	0.0	0.0	73.3	1.6	98.3	0.0
KEN-05L	71.4	1.2	0.0	0.0	0.0	72.5	1.6	98.4	0.0
KEN-05M	60.6	2.9	0.0	0.0	0.0	63.5	4.6	95.4	0.0
KEN-07	54.6	0.0	0.0	0.0	0.0	54.6	0.0	100.0	0.0
KEN-07B	74.4	0.0	0.0	0.0	0.0	74.5	0.0	100.0	0.0
KEN-07C	22.4	0.0	0.0	0.0	0.0	22.4	0.0	100.0	0.0
KEN-08	22.6	0.2	0.0	0.0	0.0	22.8	0.7	99.2	0.1
KEN-08A	38.4	0.1	0.0	0.0	0.0	38.6	0.4	99.6	0.0
KEN-08B	46.0	0.1	0.0	0.0	0.0	46.1	0.2	99.8	0.0
XCUT4-2	75.0	0.0	0.0	0.0	0.0	75.0	0.0	100.0	0.0
XCUT4-3	46.3	0.0	0.0	0.0	0.0	46.4	0.0	100.0	0.0
XCUT4-4	56.3	0.0	0.0	0.0	0.0	56.3	0.1	99.9	0.0

Table F-2. Total Sulfide Normalized Metal XRF Data with Samples < 20 wt% Total Sulfide Removed

Sample name	Cu	As	Ag	Te	Bi	Au	W	Mo	Pb	Zn	Sb	Ni	Hg	Co	Se	totSulf
1065-189-1	103	0	0	1221	7	953	0	8	68	10	7	34	0	111	36	74
1065-189-2A	59	0	0	72	0	43	19	8	0	39	0	40	0	348	37	79
1065-189-2B	47	0	0	85	0	58	25	9	0	49	0	35	0	259	37	70
1065-189-2C	64	0	0	214	0	163	9	9	8	15	0	36	0	273	37	84
1065-189-3	67	0	0	128	0	93	19	12	0	73	0	25	0	120	33	54
1065-189-5	87	0	0	270	0	229	18	9	0	13	0	25	0	90	34	76
1065-189-6	59	0	0	149	0	116	9	10	0	13	0	32	0	108	43	76
1065-189-8A	820	0	9	558	0	459	21	8	0	14	0	31	0	315	50	75
1065-189-8B	761	0	0	619	0	512	12	7	0	9	6	32	0	286	45	87
1065-197-4	83	0	0	1114	6	1080	8	9	6	8	9	35	0	77	40	81
1065-197-6	2404	0	23	358	0	325	31	10	41	47	0	39	18	251	47	50
1065-197-7	77	0	0	270	0	212	16	8	0	9	0	35	0	92	47	85
1065-197-8	69	0	0	13	0	0	434	9	0	11	0	23	0	342	46	82
1065-206-1	1439	0	0	227	0	185	33	17	12	27	18	21	0	287	37	45
1065-206-2	157	0	0	165	0	125	23	9	10	14	0	30	9	553	40	65
1065-206-3	39937	0	13	343	0	273	13	8	6	17	9	25	12	170	52	76
1065-206-5	42403	0	13	423	0	325	0	6	0	57	0	24	5	176	52	88
1065-5	79	0	0	237	0	177	18	11	0	12	0	32	0	254	56	71
1140-189-1	80	0	0	165	0	142	40	117	0	63	0	26	0	172	48	40
1140-189-3	354	0	0	950	0	771	16	7	8	14	0	42	0	143	42	71
1140-189-4B	141	0	0	414	0	338	15	24	0	29	0	29	0	160	35	57
1140-189-4C	186	0	7	307	0	283	16	16	0	25	0	45	0	165	37	67
1140-189-5	226	0	0	148	0	153	41	73	0	157	0	0	0	499	29	24
1140-197-12	150	0	0	1165	10	890	0	81	0	12	0	37	0	471	47	66
1140-197-13	138	0	0	1114	11	878	19	48	0	29	0	41	0	320	32	55
1140-197-2	347	0	0	87	0	76	21	7	0	14	0	27	0	581	77	66
1140-197-4	94	0	0	287	0	263	40	21	0	55	0	34	0	231	33	51
1140-197-5	771	0	0	51	0	52	20	9	0	17	0	39	0	1152	99	64
1140-197-6	115	6	0	99	0	61	19	8	0	10	0	30	0	697	78	92
1140-197-6A	141	5	0	118	0	66	10	7	6	10	0	31	6	1233	81	94
1140-197-8	122	8	0	111	0	97	11	12	0	23	0	41	9	562	76	80
1140-197-X	85	0	0	177	0	136	29	30	9	12	0	40	0	305	49	90
1140-206-1	181	0	0	227	0	182	17	8	0	15	0	31	0	367	32	70
1140-206-10	170	0	0	83	0	85	28	15	0	25	0	27	12	764	83	66
1140-206-11	336	0	0	172	0	102	15	15	0	14	0	29	15	409	52	56
1140-206-12	158	0	0	357	0	264	9	21	9	13	8	46	0	313	57	66
1140-206-13	69	0	0	332	0	263	20	6	0	10	9	37	0	100	58	86
1140-206-14	322	0	0	128	0	113	35	9	0	20	0	23	10	342	93	54
1140-206-2	146	0	0	314	0	250	29	7	0	24	0	21	0	355	35	64
1140-206-3	122	0	0	570	0	443	15	77	0	66	0	15	0	474	32	32
1140-206-4	377	0	0	459	0	395	25	102	0	20	0	30	0	181	34	66
1140-206-5	97	0	0	161	0	122	16	6	0	20	0	29	0	110	44	88
1140-206-6	68	0	0	17	0	22	24	9	0	24	0	29	0	52	42	71
1140-206-7	83	0	0	317	0	228	16	8	0	27	0	37	0	114	44	77
1140-206-8	96	0	0	272	0	222	23	9	0	21	0	30	8	167	31	59
1210-223-5	83	0	0	215	0	156	30	11	0	18	0	36	0	244	46	69
1210-223-6	173	0	0	512	0	414	71	29	0	34	0	27	0	297	28	37
1210-233-1	75	0	0	271	8	200	0	6	28	17	0	34	9	442	36	80
1210-233-3	113	0	0	194	0	180	0	33	0	31	0	0	0	334	27	21
1280-201-1	312	0	0	156	11	130	19	8	0	17	0	32	0	598	45	81
1280-201-10	147	0	0	547	0	402	7	7	6	12	0	37	0	218	61	72
1280-201-2	211	0	0	100	0	86	11	10	0	34	0	23	0	740	45	59
1280-201-3	88	0	0	79	0	85	26	10	9	50	0	37	0	189	55	68
1280-201-4	184	8	0	191	0	136	22	5	29	23	0	32	6	158	50	89
1280-201-5	163	0	0	21	0	17	37	8	0	17	0	40	0	584	56	73
1280-201-6	776	0	0	1537	14	1237	17	24	0	18	18	41	10	751	27	47
1280-201-7	236	0	0	59	0	47	24	0	14	49	0	35	62	376	42	57
1280-201-8	103	0	0	855	0	699	0	13	0	12	17	27	0	114	37	63
1280-201-9	163	0	0	386	0	324	24	16	0	25	0	22	0	139	38	42
1280-235-10A	130	0	0	524	0	417	28	20	9	33	0	33	0	137	37	62
1280-235-10B	127	0	0	552	0	490	11	16	0	20	0	34	0	104	33	66
1280-235-11A	50	0	0	0	0	0	20	9	6	10	0	29	5	96	47	88
1280-235-11B	50	0	0	18	0	0	16	7	7	19	0	29	0	82	43	86
1280-235-11C	150	0	0	102	0	95	20	12	11	16	0	44	0	218	50	81
1280-235-2	77	0	0	161	0	146	0	15	14	22	0	22	0	133	30	45
1280-235-4	206	23	12	182	0	142	29	6	24	23	0	40	0	105	28	81
1280-235-5	163	0	8	1461	11	1257	10	41	0	50	9	35	0	126	34	69
1280-235-6	1041	0	13	755	0	660	22	467	13	33	0	36	10	407	40	48
1280-235-8	206	0	30	1074	18	960	11	12	0	52	0	34	0	364	17	51
1290-1	2455	13	0	80	0	60	15	9	17	13	0	41	0	101	38	78
1290-2	159	10	0	957	7	735	0	22	6	15	9	43	0	96	22	78
1290-3	1272	6	0	606	5	462	0	8	9	17	0	50	6	84	32	93
1290-4	1899	8	0	1169	8	797	20	13	13	47	0	132	0	134	26	60

Table F-2 cont. Total Sulfide Normalized Metal XRF Data with Samples < 20 wt% Total Sulfide Removed

Sample name	Cu	As	Ag	Te	Bi	Au	W	Mo	Pb	Zn	Sb	Ni	Hg	Co	Se	totSulf
1290-5	1770	0	0	257	0	208	66	83	10	20	0	55	11	173	29	49
1350-1	132	6	20	761	15	599	11	15	12	16	0	45	0	188	33	81
1350-10	85	0	0	177	0	138	10	8	8	15	0	44	8	172	39	92
1350-11	68	0	0	27	0	22	0	10	8	19	0	35	0	220	23	81
1350-12A	1599	0	0	146	0	107	26	22	12	12	0	41	0	149	59	85
1350-12B	1039	0	0	246	6	205	24	18	20	12	0	34	0	234	46	76
1350-12C	208	0	6	42	0	32	28	7	17	17	7	44	0	266	59	84
1350-13	219	78	77	359	90	260	0	4885	183	107	0	52	0	257	45	22
1350-13A	191	89	84	393	79	252	43	3549	155	102	0	39	0	153	39	25
1350-13B	183	85	74	376	80	227	23	3890	148	141	0	52	0	263	43	22
1350-17	148	0	0	228	0	191	11	28	0	16	0	37	14	318	46	45
1350-19	76	8	0	233	0	186	26	8	12	18	0	30	0	146	52	61
1350-21	68	8	0	277	0	213	0	8	18	11	0	29	10	77	34	80
1350-21B	94	9	0	783	12	638	31	30	39	22	0	29	0	73	33	57
1350-23	77	0	0	253	0	190	11	13	11	15	0	30	18	41	35	47
1350-2A	130	0	0	466	8	396	0	11	0	19	0	33	8	178	27	67
1350-2B	109	0	12	767	14	622	10	5	7	11	0	32	0	210	32	88
1350-3	268	0	0	897	9	684	0	10	0	11	9	34	0	228	34	80
1350-3A	1731	6	0	649	5	523	13	7	8	9	11	55	0	124	28	93
1350-4A	264	6	0	628	10	485	0	7	0	14	9	44	0	257	38	81
1350-4B	261	6	0	471	9	382	25	9	7	16	0	39	0	297	37	84
1350-4C	659	8	0	350	8	271	21	7	7	20	0	43	8	303	41	76
1350-5B	184	0	0	339	0	274	19	9	0	25	0	37	10	184	24	70
1350-6	54	0	0	86	0	53	17	8	0	10	0	27	0	111	46	84
1350-7	71	0	0	478	8	348	0	10	0	12	0	27	8	49	25	65
1350-8	87	0	8	723	24	532	31	24	9	16	0	43	0	220	25	77
1350-9	7501	0	0	804	0	706	0	10	0	31	0	50	0	179	32	47
1355-193-2	158	0	0	523	0	329	0	0	11	30	0	28	16	206	16	53
1355-193-3	392	0	0	586	0	490	48	22	0	99	0	0	0	539	0	25
1355-201-1	1417	17	0	197	0	182	18	0	0	17	0	39	16	826	44	54
1355-201-10	80	26	8	760	0	555	14	51	34	15	0	31	10	102	33	77
1355-201-11	318	64	27	1342	16	960	17	28	97	95	94	38	169	156	26	79
1355-201-12	1284	35	31	1011	8	736	11	25	78	143	41	41	37	212	39	70
1355-201-12B	1282	33	71	482	24	332	18	35	89	42	0	117	11	343	30	68
1355-201-12C	1076	33	63	456	22	302	21	51	82	28	9	127	10	385	28	70
1355-201-13	3469	325	29	1390	12	1127	9	95	140	523	1743	35	21	220	31	75
1355-201-14 FG	2362	165	26	462	8	266	17	395	226	396	326	25	141	263	23	55
1355-201-14 MG-F	976	97	24	285	7	155	20	379	179	145	179	34	99	214	23	73
1355-201-14MGA	2884	89	35	506	10	295	26	150	149	337	111	38	165	172	25	82
1355-201-14MGB	3540	172	0	174	6	76	10	32	204	360	380	35	34	202	27	73
1355-201-16	8676	663	78	761	40	382	24	1425	788	1079	2450	61	76	654	23	67
1355-201-2	75	0	0	715	9	718	14	23	15	20	0	28	0	231	22	57
1355-201-7	19007	19	19	1360	27	1013	18	140	0	43	22	0	0	184	46	25
1355-210-1	3385	12	22	191	25	123	18	13	38	25	20	26	8	187	50	63
1355-210-10	159	0	0	169	0	136	17	7	0	17	0	32	0	94	28	74
1355-210-11	3713	402	27	575	21	422	0	95	134	629	1360	26	30	311	30	43
1355-210-12	842	29	78	590	18	405	34	57	78	31	0	97	16	334	28	67
1355-210-13	347222	0	11	21	0	157	0	9	37	96	0	0	66	11	40	54
1355-210-14	88431	21	42	150	15	112	10	8	35	50	60	20	17	79	60	89
1355-210-16	147	10	22	550	9	504	7	12	81	17	26	31	19	507	32	68
1355-210-2	4365	342	0	99	11	79	14	8	14	633	1629	23	0	147	52	71
1355-210-3	32992	0	17	272	11	230	0	13	31	17	0	41	26	130	58	56
1355-210-4	92	0	0	299	0	236	21	6	0	10	0	23	0	82	30	91
1355-210-5	38313	11	48	232	14	224	0	14	64	36	46	16	16	67	48	50
1355-210-6	155438	72	29	162	11	155	7	8	28	138	264	15	29	82	66	75
1355-210-7	204	0	10	408	0	387	14	8	0	14	0	36	8	319	34	59
1355-210-8	396	13	24	717	11	531	14	10	22	18	0	28	7	161	37	78
1355-210-9	64	0	0	127	6	95	16	7	9	14	0	28	0	88	27	82
1355-227-1	75	0	0	568	0	469	8	14	0	14	0	31	0	156	26	75
1355-227-2	234	0	8	749	0	624	13	8	0	57	9	33	0	184	31	74
1355-227-3	87	0	0	39	0	32	24	0	0	14	0	22	0	432	40	60
480ACESS-1MG	8127	0	1706	2996	456	1907	57	36	0	80	0	33	84	327	40	22
480N-1	124	0	39	485	44	371	0	14	33	23	0	44	15	609	24	38
480N-3A	154	0	58	994	50	744	0	33	41	39	0	30	18	676	23	27
480N-3B	136	0	77	1133	62	799	0	63	53	40	0	26	30	582	26	24
480N-3C	139	0	36	717	44	543	0	31	45	30	0	25	17	636	27	31
555-152-1A	563	33	81	1970	30	1492	0	10	117	43	63	52	32	1153	51	78
555-152-1B	561	32	71	2064	27	1336	0	33	186	65	54	59	46	1229	47	61
555-152-1C	612	21	73	1263	21	812	11	0	86	91	72	47	33	965	45	72
555-152-2	150	0	0	732	0	563	58	20	0	19	0	38	0	215	41	56
555-160-1B	185	0	0	1187	0	885	242	30	0	24	0	27	0	383	34	40
555-160-1C	256	0	0	1273	0	908	2111	39	0	29	0	16	0	424	37	37

Table F-2 cont. Total Sulfide Normalized Metal XRF Data with Samples < 20 wt% Total Sulfide Removed

Sample name	Cu	As	Ag	Te	Bi	Au	W	Mo	Pb	Zn	Sb	Ni	Hg	Co	Se	totSulf
555-160-2	2146	131	11	667	8	129	14	23	6	341	952	31	921	274	45	83
555-160-3	993	59	0	523	0	23	17	8	8	158	421	26	798	238	46	86
555-160-5 MG	234	0	58	3983	17	451	0	15	0	33	48	39	5265	371	27	40
555-160-5FG	918	77	0	779	0	234	37	23	27	197	344	29	906	690	21	32
555-160-6A	3347	195	19	39	0	28	22	19	11	593	1717	20	15	270	36	69
555-160-6B	2100	118	31	126	0	52	19	20	16	376	1045	29	127	334	39	74
555-160-7	743	33	13	784	0	206	19	20	89	153	314	35	875	521	36	51
555-160-8	15470	794	397	427	0	309	18	95	0	2661	8300	19	14	416	27	32
555-176-1	931	0	6	222	6	182	11	6	7	39	0	40	0	193	60	82
555-188-3	4762	0	0	283	0	288	11	8	12	19	9	32	0	609	50	65
555-188-4	3871	0	7	535	7	446	13	9	8	11	6	27	0	441	45	74
555-188-5	210345	0	54	316	0	327	0	8	0	31	0	0	52	189	51	60
555-188-6	91	0	0	205	0	196	24	10	0	22	0	32	0	435	34	67
555-188-7	156	0	0	559	0	402	34	17	0	36	0	29	0	334	41	43
555-188-8	41674	0	0	49	0	87	0	13	0	76	0	0	15	246	41	42
555-188-9	140	0	0	13	0	32	18	15	0	33	0	29	14	451	70	45
555-204-1	732	0	0	0	0	61	50	17	0	23	0	25	26	650	87	34
555-204-2	1776	0	0	67	0	69	17	18	0	58	0	0	0	265	60	34
555-204-3	58	0	0	0	0	0	24	7	0	12	0	23	0	253	67	65
555-204-5	668	0	14	21	0	41	39	0	0	78	0	37	14	184	87	45
555S-1	89	0	0	915	0	722	0	72	0	17	13	27	0	223	33	48
555S-10	121	0	0	188	0	80	85	30	0	77	0	20	248	171	44	36
555S-11	152	0	0	18	0	14	23	7	0	12	0	33	0	217	77	68
555S-13	244	0	0	125	0	107	29	10	0	33	0	36	0	125	45	58
555S-14	79718	0	24	816	0	680	0	8	0	15	0	15	13	134	58	61
555S-15	105	0	0	120	0	98	22	13	0	21	0	30	8	143	52	76
555S-16	188	0	0	218	0	158	12	13	0	25	0	25	0	103	50	77
555S-17	131	0	0	84	0	69	282	21	0	33	0	21	0	267	49	48
555S-2	536	42	69	1978	33	1001	0	36	968	44	46	49	656	813	56	65
555S-4	948	82	7	22	0	29	31	8	11	128	247	28	13	588	97	60
555S-5	305	0	0	44	0	41	21	8	0	12	0	31	0	386	75	74
555S-6A	134	0	0	38	0	44	18	8	0	12	0	30	8	370	78	78
555S-6B	83	0	0	0	0	25	23	7	0	9	0	28	7	289	70	73
555S-6C	115	0	0	28	0	16	32	8	0	12	0	24	7	293	74	77
555S-7	69	0	0	464	8	399	14	10	0	14	13	27	0	186	51	69
555S-8	85	0	0	166	0	135	18	9	0	11	6	26	0	171	49	75
555S-9	66	0	0	66	0	54	23	8	0	15	0	29	0	135	54	82
630-1	96	0	47	91	0	99	36	32	18	78	0	0	0	371	29	27
630-224-1	493	0	34	45	0	46	18	13	11	14	0	31	0	514	27	62
630-224-3	113	0	0	254	0	259	93	398	0	28	0	29	18	1320	32	34
630-224-4	140	0	45	138	0	116	135	112	17	98	0	30	17	1541	33	30
705-184-1	317	0	0	62	0	73	15	13	0	22	0	30	14	803	80	52
705-184-2	125	0	0	386	0	320	0	0	0	25	0	0	26	452	21	28
705-PASTE-2	608	0	0	166	0	145	12	16	10	13	0	34	0	762	84	58
705-PASTE-3	190	0	74	636	9	502	26	154	51	16	0	29	16	1022	40	57
705-PASTE-4	97	0	0	654	0	557	81	33	0	51	0	17	0	887	36	35
780-176-1	270	0	0	389	0	327	0	20	0	20	0	0	16	558	42	36
780-176-2	537	0	0	1955	10	1846	42	11	0	12	8	48	0	455	57	58
780-184-1	188	0	0	261	0	285	62072	16	7	0	0	6	470	819	77	80
780-200-1	289	0	0	10	0	7	0	9	0	11	0	25	0	370	68	68
910N-2	116	0	0	162	0	168	0	39	0	31	0	0	0	262	19	25
910N-4	61	0	0	273	0	254	27	10	0	16	0	19	0	125	34	66
K12-10	175	0	0	74	0	143	0	45	0	30	0	0	23	686	61	24
K12-13	369	0	0	663	0	554	0	202	0	36	0	25	0	378	31	31
K12-19	52	0	0	143	0	122	22	12	9	26	0	38	0	124	39	85
K12-20	104	0	0	71	0	103	0	57	0	33	0	0	0	180	37	22
K12-4	229	0	8	846	7	614	18	13	0	11	0	53	0	193	35	76
K12-5A	809	0	0	595	0	499	8	10	6	11	0	40	0	242	37	79
K12-5B	780	0	8	955	7	741	14	14	0	11	0	38	0	294	31	75
K12-7	328	0	0	89	0	67	25	10	5	16	0	50	30	187	49	85
K13-11	36822	0	25	211	0	162	13	0	20	8	0	17	15	96	44	61
K13-12	128	0	0	122	0	97	67	18	10	106	0	172	0	428	24	52
K13-14	235	0	0	1093	0	955	7	11	0	12	17	72	0	165	28	71
K13-15	11057	0	0	521	7	402	23	36	10	11	10	39	0	126	33	82
K13-16A	11883	20	0	1239	7	1045	0	16	25	21	10	79	0	116	34	62
K13-16B	13534	11	0	1546	8	1323	0	7	12	7	13	46	0	120	36	79
K13-16C	14708	20	0	1188	0	994	0	18	18	28	0	68	13	131	36	43
K13-17	39672	0	8	89	0	89	22	7	14	20	0	28	15	128	43	76
K13-18	112	0	0	289	7	251	36	10	0	14	0	40	8	230	51	62
K13-19	1628	0	0	81	0	66	24	7	0	18	0	28	0	177	44	85
K13-21	72	0	21	37	0	68	0	24	15	31	0	14	21	202	36	38
K13-22	100	0	0	869	0	663	0	84	31	19	0	0	17	399	26	32
K13-24	91	0	20	953	14	771	0	17	10	236	0	24	11	208	44	54

Table F-2 cont. Total Sulfide Normalized Metal XRF Data with Samples < 20 wt% Total Sulfide Removed

Sample name	Cu	As	Ag	Te	Bi	Au	W	Mo	Pb	Zn	Sb	Ni	Hg	Co	Se	totSulf
K13-25	686	11	32	1309	23	864	9	10	13	44	9	37	193	1622	49	54
K13-4	215	31	73	1001	30	716	28	16	161	33	16	48	10	234	33	70
KEN-02	537	0	0	76	0	99	78	0	0	180	0	56	0	713	25	28
KEN-04	143	21	22	240	8	221	27	9	50	18	0	99	13	314	78	64
KEN-04A	111	14	24	219	0	173	24	9	32	11	0	68	11	356	58	74
KEN-05	5751	7	18	473	10	445	30	23	18	11	7	87	14	309	46	73
KEN-05L	5512	0	0	377	0	336	29	31	13	11	0	99	7	233	48	73
KEN-05M	15887	15	71	1166	49	933	17	336	68	10	0	80	17	249	54	63
KEN-07	77	0	0	1038	0	1125	0	10	9	24	17	102	10	129	40	55
KEN-07B	68	0	0	738	0	690	14	0	0	16	0	110	6	120	54	74
KEN-07C	156	0	0	2284	0	2039	0	252	0	223	0	215	0	256	28	22
KEN-08	2897	53	153	662	0	505	0	0	29	200	345	30	281	227	32	23
KEN-08A	1295	0	0	672	0	633	29	12	32	50	0	32	36	214	38	39
KEN-08B	662	0	0	232	0	240	27	0	0	48	0	31	14	180	43	46
XCUT4-2	86	0	20	1216	14	809	3072	12	13	0	0	0	31	247	42	75
XCUT4-3	142	0	14	410	0	333	54	22	28	35	0	18	0	1045	43	46
XCUT4-4	175	0	0	709	0	578	22	14	0	18	0	28	0	247	41	56

Table F-3. Oxide XRF Data (Un-Normalized) with Samples < 20 wt% Total Sulfide Removed

Sample name	Al_2O_3	CaO	K_2O	MgO	Na_2O	SiO_2	MnO	TiO_2	P_2O_5	Fe_2O_3
1065-189-1	1.29	1.22	0.29	0.13	0.18	18.78	0.01	0.06	0.02	47.57
1065-189-2A	0.90	3.69	0.07	1.28	0.11	4.79	0.10	0.02	0.01	59.81
1065-189-2B	1.04	4.49	0.08	1.40	0.12	12.76	0.12	0.02	0.01	53.84
1065-189-2C	0.65	3.73	0.13	0.33	0.14	4.86	0.07	0.03	0.01	59.51
1065-189-3	1.71	0.34	0.17	1.72	0.14	33.17	0.04	0.02	0.01	40.42
1065-189-5	0.69	5.77	0.14	0.21	0.15	12.38	0.11	0.04	0.02	50.94
1065-189-6	1.24	0.55	0.41	0.29	0.15	19.21	0.01	0.03	0.01	48.23
1065-189-8A	0.88	3.71	0.20	0.25	0.15	9.61	0.07	0.03	0.01	55.60
1065-189-8B	0.29	2.28	0.12	0.14	0.12	6.55	0.04	0.01	0.01	56.86
1065-197-4	0.05	2.15	0.03	0.09	0.11	4.76	0.04	0.01	0.00	58.48
1065-197-6	2.69	8.51	0.54	0.93	0.21	23.36	0.14	0.11	0.04	38.58
1065-197-7	0.00	4.29	0.01	0.09	0.11	1.33	0.06	0.01	0.00	63.86
1065-197-8	0.42	1.26	0.11	0.14	0.12	10.22	0.02	0.03	0.01	57.15
1065-206-1	2.13	2.14	0.27	0.38	0.26	42.96	0.04	0.13	0.06	31.92
1065-206-2	0.00	8.45	0.00	0.17	0.11	16.39	0.15	0.00	0.00	48.88
1065-206-3	0.00	4.75	0.02	0.10	0.10	9.95	0.07	0.01	0.00	53.52
1065-206-4	8.66	2.78	1.87	1.14	0.55	52.68	0.07	0.41	0.19	16.58
1065-206-5	0.04	1.33	0.04	0.08	0.10	3.11	0.03	0.01	0.00	60.01
1065-5	1.05	2.55	0.31	0.21	0.15	16.60	0.04	0.09	0.03	51.23
1140-189-1	7.56	1.94	1.46	0.68	0.55	35.45	0.04	0.23	0.13	31.16
1140-189-2	1.42	1.17	0.31	0.27	0.19	70.81	0.03	0.06	0.04	11.97
1140-189-3	4.49	0.65	1.37	0.32	0.25	10.75	0.01	0.20	0.09	52.71
1140-189-4B	7.77	1.90	2.36	0.80	0.32	18.51	0.03	0.19	0.09	43.26
1140-189-4C	3.78	2.74	1.23	0.53	0.22	11.16	0.04	0.12	0.04	48.05
1140-189-5	13.50	1.12	3.89	1.93	0.55	36.09	0.06	0.42	0.20	22.11
1140-197-12	0.18	6.45	0.06	0.14	0.12	25.85	0.12	0.02	0.01	44.88
1140-197-13	3.78	1.60	0.96	0.71	0.23	28.36	0.04	0.15	0.09	40.79
1140-197-2	0.48	0.48	0.12	0.10	0.14	24.92	0.01	0.03	0.01	43.29
1140-197-4	3.74	3.73	0.65	1.19	0.29	28.13	0.09	0.16	0.07	37.85
1140-197-5	1.72	1.89	0.47	0.26	0.16	22.84	0.03	0.08	0.04	45.98
1140-197-6	0.31	0.14	0.17	0.10	0.11	5.25	0.01	0.01	0.00	58.56
1140-197-6A	0.09	0.47	0.06	0.08	0.11	5.18	0.01	0.01	0.00	60.88
1140-197-8	1.49	4.94	0.31	0.83	0.14	10.06	0.11	0.09	0.03	54.73
1140-197-9	17.16	0.84	4.03	0.50	0.88	47.89	0.02	0.85	0.29	4.73
1140-197-X	0.72	4.49	0.26	0.23	0.11	1.50	0.08	0.12	0.01	60.73
1140-206-1	0.05	0.84	0.04	0.11	0.12	15.03	0.02	0.01	0.00	45.15
1140-206-10	4.76	1.08	1.50	0.64	0.23	18.62	0.03	0.13	0.04	46.18
1140-206-11	0.04	0.90	0.04	0.05	0.11	30.64	0.02	0.01	0.00	36.62
1140-206-12	0.27	9.81	0.10	0.21	0.11	10.76	0.16	0.01	0.00	50.85
1140-206-13	0.00	2.88	0.02	0.09	0.11	2.19	0.04	0.01	0.00	63.28
1140-206-14	0.51	0.44	0.18	0.17	0.13	35.54	0.02	0.03	0.01	35.90
1140-206-2	2.19	5.43	0.45	0.55	0.23	19.73	0.09	0.12	0.05	43.29
1140-206-3	5.06	1.94	1.04	0.86	0.35	49.09	0.05	0.27	0.12	24.58
1140-206-4	3.31	2.00	1.07	0.47	0.13	17.11	0.02	0.21	0.06	49.61
1140-206-5	0.39	0.64	0.06	0.49	0.11	1.76	0.03	0.01	0.01	64.55
1140-206-6	1.24	0.80	0.24	0.39	0.17	18.37	0.03	0.05	0.02	48.06

Table F-3 cont. Oxide XRF Data (Un-Normalized) with Samples < 20 wt% Total Sulfide Removed

Sample name	Al_2O_3	CaO	K_2O	MgO	Na_2O	SiO_2	MnO	TiO_2	P_2O_5	Fe_2O_3
1140-206-7	1.85	2.66	0.33	0.78	0.19	6.07	0.07	0.05	0.03	57.21
1140-206-8	2.31	7.58	0.59	0.44	0.19	19.11	0.16	0.08	0.04	45.85
1210-223-4	14.21	2.82	3.55	4.60	0.42	47.32	0.20	0.50	0.27	16.20
1210-223-5	3.63	0.42	0.99	0.38	0.25	15.69	0.01	0.12	0.06	48.07
1210-223-6	6.57	1.08	2.05	0.62	0.26	43.89	0.03	0.28	0.11	28.84
1210-223-7	1.69	1.07	0.69	0.19	0.14	80.49	0.03	0.10	0.05	7.46
1210-233-1	0.00	2.71	0.00	0.63	0.11	14.19	0.05	0.00	0.00	53.49
1210-233-3	0.15	0.70	0.09	0.00	0.11	75.47	0.02	0.01	0.01	13.83
1280-201-1	0.02	0.97	0.02	0.40	0.11	10.53	0.02	0.01	0.00	54.99
1280-201-10	0.44	4.72	0.13	0.11	0.13	13.24	0.07	0.02	0.01	53.28
1280-201-2	0.12	2.33	0.02	0.79	0.12	29.39	0.06	0.01	0.00	41.68
1280-201-3	1.22	0.24	0.30	0.15	0.14	16.61	0.01	0.07	0.02	49.00
1280-201-4	0.00	0.92	0.01	0.30	0.11	3.72	0.01	0.00	0.00	62.22
1280-201-5	1.69	1.40	0.37	0.33	0.19	12.62	0.02	0.08	0.03	53.92
1280-201-6	1.64	6.24	0.51	0.28	0.15	33.11	0.12	0.11	0.05	36.12
1280-201-7	0.00	21.23	0.00	2.25	0.11	2.08	0.31	0.01	0.00	49.80
1280-201-8	0.72	0.40	0.29	0.10	0.13	28.04	0.01	0.03	0.01	42.79
1280-201-9	4.15	0.37	1.07	0.34	0.29	45.42	0.01	0.09	0.04	31.13
1280-235-10A	1.50	2.13	0.53	0.89	0.11	23.14	0.03	0.16	0.06	43.97
1280-235-10B	0.60	0.92	0.16	0.37	0.12	25.90	0.02	0.03	0.02	45.02
1280-235-11A	0.22	1.38	0.08	0.25	0.11	0.73	0.02	0.02	0.01	65.42
1280-235-11B	0.98	2.27	0.30	0.66	0.11	1.62	0.04	0.02	0.01	62.61
1280-235-11C	0.64	4.14	0.23	0.46	0.11	2.19	0.06	0.05	0.01	61.21
1280-235-2	0.31	0.27	0.11	0.12	0.11	47.79	0.01	0.02	0.01	30.87
1280-235-4	1.08	4.59	0.22	0.47	0.11	10.26	0.08	0.02	0.00	59.50
1280-235-5	1.28	3.48	0.52	0.85	0.11	13.15	0.06	0.06	0.01	50.32
1280-235-6	1.52	0.83	0.63	0.31	0.11	40.74	0.02	0.13	0.01	34.49
1280-235-8	1.08	4.35	0.32	1.21	0.13	30.17	0.10	0.02	0.01	38.59
1280-235-9	14.03	7.66	4.02	3.92	0.41	37.02	0.23	1.26	0.39	14.43
1290-1	0.00	0.53	0.00	0.26	0.11	13.39	0.01	0.00	0.00	55.19
1290-2	0.00	0.75	0.02	0.27	0.11	20.01	0.02	0.02	0.00	49.36
1290-3	0.24	0.42	0.12	0.16	0.11	5.39	0.01	0.01	0.00	59.75
1290-4	1.62	4.08	0.57	1.61	0.11	20.04	0.10	0.15	0.02	45.91
1290-5	0.46	0.51	0.18	0.18	0.11	48.29	0.01	0.24	0.03	31.33
1350-1	2.17	0.38	0.68	0.34	0.12	15.60	0.01	0.10	0.04	53.96
1350-10	0.73	0.47	0.27	0.22	0.12	3.86	0.01	0.03	0.01	59.64
1350-11	1.09	1.13	0.42	0.47	0.12	12.78	0.03	0.04	0.01	53.41
1350-12A	0.75	0.16	0.31	0.10	0.12	4.98	0.01	0.10	0.01	58.93
1350-12B	1.44	0.09	0.51	0.14	0.13	10.64	0.01	0.07	0.02	53.34
1350-12C	0.06	1.16	0.04	0.48	0.11	6.29	0.04	0.01	0.00	61.53
1350-13	11.39	0.13	3.28	0.54	0.12	60.33	0.01	0.12	0.01	16.74
1350-13A	12.54	0.33	3.58	0.72	0.14	52.76	0.01	0.21	0.04	20.22
1350-13B	13.48	0.62	4.20	0.79	0.13	53.10	0.02	0.14	0.02	17.81
1350-14	4.18	6.39	0.54	0.41	0.12	67.27	0.06	0.19	0.03	4.38
1350-15A	4.07	9.08	1.08	0.89	0.13	61.70	0.15	0.24	0.07	4.95
1350-15B	1.27	5.84	0.38	0.18	0.11	81.74	0.09	0.04	0.01	5.12

Table F-3 cont. Oxide XRF Data (Un-Normalized) with Samples < 20 wt% Total Sulfide Removed

Sample name	Al_2O_3	CaO	K_2O	MgO	Na_2O	SiO_2	MnO	TiO_2	P_2O_5	Fe_2O_3
1350-15C	1.00	1.60	0.33	0.12	0.11	89.62	0.02	0.04	0.02	1.98
1350-16FG-A	9.93	3.07	2.53	1.14	0.16	62.61	0.06	0.50	0.20	6.15
1350-16FG-B	9.55	6.90	2.07	1.62	0.15	56.05	0.17	0.52	0.18	7.02
1350-16MG	4.47	1.57	1.39	0.52	0.14	62.71	0.03	0.14	0.06	7.52
1350-17	0.17	0.05	0.09	0.02	0.11	47.81	0.01	0.02	0.01	29.41
1350-18	13.22	8.28	3.56	1.78	0.30	46.62	0.21	0.66	0.24	7.44
1350-19	1.01	0.28	0.26	0.11	0.15	29.48	0.01	0.04	0.01	41.49
1355-193-2	0.30	0.18	0.19	0.07	0.13	42.79	0.00	0.01	0.02	25.85
1350-20	5.92	4.75	1.63	1.16	0.19	62.81	0.10	0.32	0.13	11.09
1350-21	0.16	0.89	0.09	0.11	0.11	14.90	0.02	0.01	0.00	50.87
1350-21B	7.55	0.42	2.35	0.41	0.21	23.64	0.01	0.28	0.14	42.16
1350-22	9.77	2.15	2.99	1.00	0.21	57.64	0.05	0.65	0.25	14.19
1350-23	0.22	0.42	0.10	0.01	0.11	51.30	0.01	0.01	0.00	30.06
1350-2A	0.07	0.15	0.03	0.10	0.11	27.90	0.01	0.02	0.00	43.49
1350-2B	0.00	0.09	0.00	0.04	0.11	10.31	0.01	0.01	0.00	56.63
1350-3	0.00	0.08	0.02	0.10	0.11	16.62	0.01	0.01	0.00	50.84
1350-3A	0.06	0.23	0.05	0.10	0.11	6.64	0.01	0.01	0.00	60.32
1350-4A	1.13	0.46	0.38	0.31	0.12	13.59	0.02	0.03	0.01	53.53
1350-4B	0.92	0.13	0.37	0.18	0.11	10.39	0.01	0.02	0.01	54.44
1350-4C	0.51	0.91	0.17	0.42	0.12	16.19	0.02	0.01	0.00	50.61
1350-5A	3.24	3.90	0.94	1.18	0.11	64.90	0.09	0.14	0.04	15.71
1350-5A	3.31	4.05	0.95	1.21	0.11	65.58	0.09	0.14	0.04	15.71
1350-5B	1.37	5.40	0.36	0.60	0.12	17.69	0.10	0.05	0.02	48.07
1350-6	0.53	1.38	0.16	0.17	0.13	5.67	0.03	0.05	0.02	59.84
1350-7	0.03	0.19	0.04	0.01	0.11	35.30	0.01	0.01	0.00	41.23
1350-8	1.29	2.73	0.38	0.49	0.14	12.44	0.05	0.17	0.07	52.13
1350-9	0.33	7.04	0.04	0.47	0.11	35.40	0.13	0.02	0.02	34.49
1355-193-3	12.59	2.88	4.02	1.43	0.39	40.50	0.07	0.42	0.22	24.23
1355-201-1	0.58	10.63	0.20	0.39	0.12	20.87	0.18	0.04	0.02	41.56
1355-201-10	0.41	0.79	0.12	0.33	0.11	11.49	0.02	0.03	0.00	56.14
1355-201-11	0.54	0.24	0.10	0.21	0.11	15.67	0.01	0.01	0.01	56.33
1355-201-12	0.00	0.00	0.02	0.06	0.11	19.94	0.00	0.01	0.00	51.06
1355-201-12B	2.81	3.65	0.66	1.01	0.11	10.02	0.07	0.09	0.07	53.72
1355-201-12C	2.46	2.65	0.58	0.84	0.11	11.72	0.05	0.10	0.11	54.06
1355-201-13	0.57	0.26	0.14	0.11	0.12	19.03	0.01	0.02	0.01	51.88
1355-201-14 FG	1.03	0.27	0.07	0.18	0.11	40.76	0.01	0.04	0.03	38.03
1355-201-14 MG-F	0.88	0.05	0.12	0.14	0.11	21.38	0.01	0.03	0.03	52.17
1355-201-14MGA	0.40	0.13	0.06	0.16	0.11	11.56	0.01	0.02	0.03	58.85
1355-201-14MGB	0.17	0.06	0.04	0.14	0.11	23.18	0.01	0.01	0.02	51.11
1355-201-16	2.54	0.67	0.56	0.30	0.14	25.11	0.01	0.12	0.11	45.87
1355-201-2	0.56	2.91	0.22	0.26	0.12	26.60	0.05	0.06	0.02	38.82
1355-201-7	4.08	0.20	1.43	0.34	0.12	62.07	0.01	0.21	0.06	19.27
1355-210-1	0.43	0.32	0.08	0.15	0.13	28.74	0.01	0.02	0.01	44.09
1355-210-10	0.93	1.78	0.19	0.27	0.14	14.14	0.03	0.04	0.02	54.48
1355-210-11	1.09	7.83	0.34	2.57	0.11	34.96	0.19	0.05	0.04	32.83
1355-210-12	3.30	2.12	0.85	0.61	0.12	14.63	0.04	0.23	0.07	52.23

Table F-3 cont. Oxide XRF Data (Un-Normalized) with Samples < 20 wt% Total Sulfide Removed

Sample name	Al_2O_3	CaO	K_2O	MgO	Na_2O	SiO_2	MnO	TiO_2	P_2O_5	Fe_2O_3
1355-210-13	0.00	0.00	0.00	0.00	0.06	60.98	0.00	0.00	0.00	18.94
1355-210-14	0.00	1.59	0.01	0.71	0.08	6.68	0.03	0.01	0.00	52.64
1355-210-15	0.00	0.42	0.00	0.08	0.10	82.64	0.02	0.00	0.00	8.22
1355-210-16	0.00	0.19	0.00	0.12	0.11	26.83	0.01	0.00	0.00	43.74
1355-210-2	0.00	0.63	0.01	0.23	0.11	18.74	0.02	0.01	0.00	47.36
1355-210-3	0.00	0.71	0.00	0.37	0.10	28.96	0.02	0.01	0.00	39.13
1355-210-4	0.00	0.34	0.01	0.15	0.11	3.07	0.01	0.01	0.00	63.48
1355-210-5	0.05	0.07	0.03	0.05	0.11	40.17	0.01	0.01	0.01	30.67
1355-210-6	0.00	1.86	0.00	0.67	0.08	17.17	0.04	0.01	0.00	44.97
1355-210-7	0.00	13.38	0.01	0.37	0.11	13.48	0.27	0.01	0.00	47.59
1355-210-8	0.65	2.13	0.16	0.46	0.11	7.80	0.03	0.03	0.01	58.91
1355-210-9	0.02	0.54	0.02	0.21	0.11	9.00	0.01	0.01	0.00	57.58
1355-227-1	0.54	0.18	0.21	0.17	0.11	21.64	0.01	0.01	0.00	47.70
1355-227-2	2.78	2.46	1.00	0.93	0.12	8.61	0.06	0.05	0.01	55.30
1355-227-3	0.36	22.02	0.16	0.41	0.11	1.04	0.54	0.01	0.00	49.05
480ACESS-1CG	3.11	3.33	0.76	0.93	0.28	64.97	0.10	0.17	0.09	11.43
480ACESS-1MG	7.54	1.80	2.25	0.64	0.36	52.53	0.05	0.56	0.19	16.92
480N-1	0.00	31.58	0.00	0.57	0.11	5.26	0.82	0.01	0.00	35.08
480N-3A	0.00	39.96	0.00	0.67	0.11	1.03	1.06	0.01	0.00	25.96
480N-3B	0.00	42.60	0.01	0.68	0.11	0.92	1.19	0.01	0.00	23.31
480N-3C	0.00	36.18	0.00	0.62	0.11	2.66	0.94	0.01	0.00	29.55
555-152-1A	0.00	12.21	0.01	0.76	0.11	4.84	0.15	0.01	0.00	56.49
555-152-1B	0.09	20.25	0.05	0.83	0.12	12.79	0.22	0.02	0.02	46.13
555-152-1C	0.06	17.79	0.01	1.24	0.11	11.89	0.21	0.01	0.01	51.77
555-152-2	2.79	4.62	0.65	0.43	0.23	26.81	0.09	0.18	0.07	43.39
555-160-1B	0.15	6.86	0.09	0.39	0.11	44.70	0.15	0.03	0.01	28.96
555-160-1C	0.48	8.97	0.15	0.47	0.12	44.06	0.19	0.05	0.01	27.50
555-160-2	0.00	1.95	0.00	0.69	0.11	9.72	0.06	0.00	0.00	54.43
555-160-3	0.00	2.43	0.00	0.94	0.11	5.32	0.06	0.00	0.00	57.89
555-160-5 MG	1.53	3.48	0.38	0.84	0.14	45.44	0.10	0.04	0.02	29.29
555-160-5FG	2.67	4.61	0.60	1.20	0.14	45.14	0.14	0.09	0.04	26.19
555-160-6A	0.00	6.52	0.00	2.33	0.11	12.33	0.14	0.01	0.00	52.20
555-160-6B	0.00	4.36	0.00	1.44	0.11	13.96	0.10	0.01	0.00	50.93
555-160-7	0.15	4.55	0.04	1.32	0.11	29.64	0.14	0.01	0.01	38.70
555-160-8	2.05	10.48	0.31	3.29	0.11	34.17	0.37	0.05	0.04	29.11
555-176-1	0.00	2.38	0.00	0.09	0.11	2.94	0.04	0.01	0.00	59.78
555-188-3	0.00	14.92	0.00	0.20	0.11	6.01	0.29	0.01	0.00	47.59
555-188-4	0.00	2.55	0.00	0.07	0.11	20.08	0.04	0.01	0.00	48.42
555-188-5	0.00	0.53	0.00	0.11	0.07	41.97	0.01	0.00	0.00	30.95
555-188-6	2.93	1.78	0.63	0.47	0.24	17.54	0.04	0.09	0.04	46.05
555-188-7	4.82	2.83	0.93	0.61	0.39	36.31	0.06	0.26	0.12	32.19
555-188-8	1.99	10.88	0.38	0.74	0.17	39.24	0.15	0.05	0.04	24.80
555-188-9	3.04	3.54	0.70	0.47	0.24	37.65	0.07	0.13	0.07	32.13
555-204-1	0.11	8.65	0.04	0.11	0.12	48.18	0.16	0.01	0.01	25.49
555-204-2	5.16	1.68	1.37	0.78	0.28	48.03	0.04	0.18	0.13	24.29
555-204-3	0.00	2.52	0.02	0.03	0.11	25.94	0.03	0.01	0.00	44.32

Table F-3 cont. Oxide XRF Data (Un-Normalized) with Samples < 20 wt% Total Sulfide Removed

Sample name	Al_2O_3	CaO	K_2O	MgO	Na_2O	SiO_2	MnO	TiO_2	P_2O_5	Fe_2O_3
555-204-5	4.89	7.77	1.23	1.85	0.30	25.21	0.18	0.18	0.09	37.72
555S-1	0.85	0.36	0.34	0.09	0.11	44.95	0.01	0.04	0.01	33.20
555S-10	8.67	3.12	1.85	1.18	0.49	34.34	0.07	0.32	0.14	29.50
555S-11	0.00	6.04	0.02	0.43	0.11	18.50	0.12	0.01	0.01	48.02
555S-13	4.27	2.06	0.87	0.74	0.30	22.90	0.04	0.15	0.07	43.67
555S-14	0.00	4.06	0.00	0.22	0.09	30.96	0.06	0.01	0.00	39.36
555S-15	0.23	0.89	0.06	0.44	0.12	17.52	0.01	0.01	0.01	50.18
555S-16	0.47	0.94	0.18	0.60	0.11	12.68	0.02	0.04	0.01	53.88
555S-17	5.21	4.66	1.31	0.53	0.34	28.99	0.09	0.19	0.10	36.67
555S-2	0.08	11.78	0.05	1.59	0.11	10.22	0.24	0.02	0.01	48.69
555S-3A	11.83	8.92	2.43	1.28	0.62	40.49	0.22	0.47	0.25	14.10
555S-3B	10.46	13.98	2.14	1.35	0.59	36.25	0.30	0.60	0.24	14.84
555S-3C	12.40	10.18	2.63	1.45	0.55	40.96	0.25	0.46	0.25	11.31
555S-4	0.00	1.79	0.00	0.80	0.11	30.62	0.03	0.01	0.00	42.90
555S-5	0.00	2.71	0.00	0.16	0.11	19.17	0.05	0.01	0.00	48.66
555S-6A	0.09	4.72	0.04	0.15	0.11	11.05	0.09	0.02	0.00	53.00
555S-6B	0.06	10.96	0.03	0.24	0.11	8.26	0.21	0.01	0.00	52.95
555S-6C	0.16	10.19	0.04	0.29	0.12	6.34	0.20	0.01	0.01	53.44
555S-7	0.00	11.90	0.01	0.56	0.11	10.72	0.24	0.00	0.00	49.35
555S-8	0.00	7.44	0.03	0.43	0.11	11.99	0.14	0.01	0.00	51.44
555S-9	0.73	3.28	0.17	0.44	0.14	7.89	0.06	0.04	0.02	56.58
630-1	1.99	8.90	0.67	1.13	0.13	49.98	0.19	0.08	0.03	22.41
630-224-1	1.01	0.64	0.32	0.08	0.14	32.75	0.01	0.02	0.01	39.65
630-224-2	10.87	4.56	3.51	1.08	0.40	43.87	0.09	0.46	0.21	17.21
630-224-3	4.99	24.96	1.21	0.49	0.35	12.82	0.47	0.36	0.07	28.92
630-224-4	5.51	9.72	1.92	1.24	0.16	40.44	0.18	0.35	0.08	25.18
705-184-1	0.22	6.51	0.04	0.26	0.11	35.59	0.12	0.01	0.01	34.81
705-184-2	0.00	35.41	0.00	0.50	0.11	13.25	0.99	0.01	0.00	21.38
705-PASTE-2	0.00	2.11	0.01	0.02	0.11	33.03	0.02	0.01	0.00	41.17
705-PASTE-3	1.98	4.07	0.53	0.18	0.20	29.83	0.05	0.13	0.05	38.47
705-PASTE-4	10.04	2.24	3.18	0.78	0.41	35.87	0.04	0.59	0.28	26.80
780-176-1	0.00	15.36	0.00	0.18	0.11	38.58	0.33	0.01	0.00	27.59
780-176-2	0.00	13.06	0.00	0.15	0.11	13.88	0.28	0.00	0.00	45.29
780-184-1	0.00	12.27	0.00	0.18	0.11	2.34	0.23	0.01	0.00	57.84
780-200-1	0.01	0.20	0.03	0.02	0.11	31.20	0.01	0.01	0.00	42.45
910N-2	0.10	2.33	0.03	0.03	0.13	70.40	0.05	0.02	0.01	18.09
910N-4	2.58	9.27	0.74	0.32	0.20	12.34	0.19	0.09	0.04	46.67
K12-10	0.65	0.00	0.24	0.01	0.13	72.28	0.01	0.03	0.01	17.10
K12-12-<100	1.96	1.39	0.46	0.54	0.12	81.46	0.21	0.20	0.10	5.79
K12-12-100-250	0.71	0.45	0.14	0.12	0.10	86.99	0.19	0.08	0.03	4.20
K12-13	2.55	0.84	0.66	0.31	0.23	55.92	0.03	0.15	0.04	22.99
K12-13-<100	3.64	0.72	0.98	0.25	0.12	82.46	0.19	0.17	0.08	4.53
K12-14	10.56	15.04	2.91	4.32	0.29	38.80	0.39	0.38	0.18	12.20
K12-19	0.07	3.41	0.04	0.83	0.11	4.44	0.09	0.01	0.00	58.50
K12-20	0.52	0.65	0.14	0.01	0.13	72.32	0.02	0.02	0.01	14.72
K12-21	12.24	5.18	2.74	1.63	0.24	56.82	0.11	0.72	0.11	7.69

Table F-3 cont. Oxide XRF Data (Un-Normalized) with Samples < 20 wt% Total Sulfide Removed

Sample name	Al_2O_3	CaO	K_2O	MgO	Na_2O	SiO_2	MnO	TiO_2	P_2O_5	Fe_2O_3
K12-4	0.00	0.00	0.02	0.02	0.11	21.45	0.01	0.01	0.00	50.40
K12-5A	0.22	0.00	0.10	0.04	0.11	22.96	0.01	0.01	0.00	52.32
K12-5B	0.08	0.00	0.05	0.03	0.11	27.49	0.01	0.01	0.00	49.74
K12-7	1.26	2.47	0.22	0.25	0.18	5.06	0.04	0.05	0.02	56.15
K12-8	15.12	3.58	4.71	2.27	0.56	44.99	0.11	0.63	0.35	10.67
K12-8-<100	1.67	1.29	0.29	0.53	0.14	83.55	0.21	0.10	0.08	5.33
K12-9	12.31	2.66	3.28	2.68	0.53	52.76	0.11	0.63	0.33	10.05
K13-10A	19.12	5.51	3.73	2.68	0.21	38.81	0.10	1.29	0.40	10.91
K13-10A	17.80	4.12	3.47	2.64	0.24	43.42	0.08	1.15	0.37	10.69
K13-10B	14.71	14.89	2.61	4.87	0.23	29.51	0.20	1.01	0.29	11.57
K13-10C	18.53	6.57	3.59	2.91	0.22	38.41	0.10	1.27	0.39	10.65
K13-11	0.49	10.06	0.08	0.30	0.13	19.16	0.12	0.02	0.01	45.65
K13-12	4.01	2.34	0.77	2.69	0.12	26.46	0.08	0.22	0.06	40.78
K13-14	0.16	0.19	0.07	0.13	0.11	26.81	0.01	0.03	0.01	44.76
K13-15	0.35	0.21	0.16	0.19	0.10	9.28	0.01	0.02	0.00	57.64
K13-16A	0.92	1.49	0.25	0.60	0.12	31.74	0.02	0.07	0.01	39.93
K13-16B	0.05	0.02	0.03	0.09	0.10	18.80	0.01	0.01	0.00	49.53
K13-16C	0.33	1.57	0.07	0.54	0.11	49.87	0.02	0.05	0.01	27.06
K13-17	0.90	8.31	0.14	0.36	0.13	7.30	0.11	0.03	0.01	52.49
K13-18	1.83	2.35	0.45	0.30	0.19	23.87	0.04	0.07	0.03	45.64
K13-19	0.97	0.91	0.25	0.44	0.13	7.50	0.02	0.03	0.01	56.67
K13-21	0.00	24.10	0.01	0.54	0.11	19.35	0.53	0.01	0.00	32.25
K13-22	0.04	0.39	0.04	0.00	0.11	62.76	0.01	0.01	0.00	22.78
K13-24	0.03	2.27	0.02	0.04	0.11	38.23	0.03	0.01	0.00	37.98
K13-25	0.00	23.31	0.00	0.40	0.11	3.59	0.47	0.00	0.00	46.33
K13-4	1.43	3.19	0.22	1.10	0.11	12.73	0.09	0.15	0.03	54.47
KEN-02	10.28	5.05	1.42	2.50	0.61	31.74	0.14	0.88	0.59	27.70
KEN-04	0.33	1.13	0.10	0.36	0.10	13.88	0.02	0.01	0.00	42.37
KEN-04A	0.46	0.96	0.08	0.20	0.10	14.55	0.02	0.03	0.00	51.93
KEN-05	0.02	0.00	0.01	0.03	0.10	19.71	0.01	0.01	0.00	47.59
KEN-05L	0.00	0.00	0.00	0.01	0.10	13.39	0.01	0.01	0.00	47.39
KEN-05M	0.00	0.01	0.00	0.00	0.09	31.09	0.01	0.00	0.00	39.90
KEN-07	0.90	0.79	0.25	0.53	0.11	28.61	0.02	0.07	0.01	34.87
KEN-07B	0.18	0.57	0.06	0.25	0.10	5.18	0.01	0.02	0.00	47.78
KEN-07C	7.06	1.86	1.98	1.86	0.24	45.29	0.05	0.62	0.05	17.48
KEN-08	12.50	1.82	2.61	0.99	0.74	42.08	0.03	0.53	0.30	17.76
KEN-08A	12.18	1.64	2.47	0.86	0.75	40.50	0.02	0.56	0.30	28.59
KEN-08B	8.21	1.15	1.56	0.94	0.51	41.67	0.03	0.27	0.15	32.66
XCUT4-2	0.06	13.47	0.04	0.24	0.11	0.77	0.28	0.01	0.01	55.14
XCUT4-3	6.62	6.14	1.63	0.47	0.42	26.74	0.09	0.27	0.15	33.76
XCUT4-4	1.84	6.93	0.47	0.32	0.19	22.90	0.14	0.09	0.04	43.24

Appendix G. Long Sections of Individual Metals Looking West

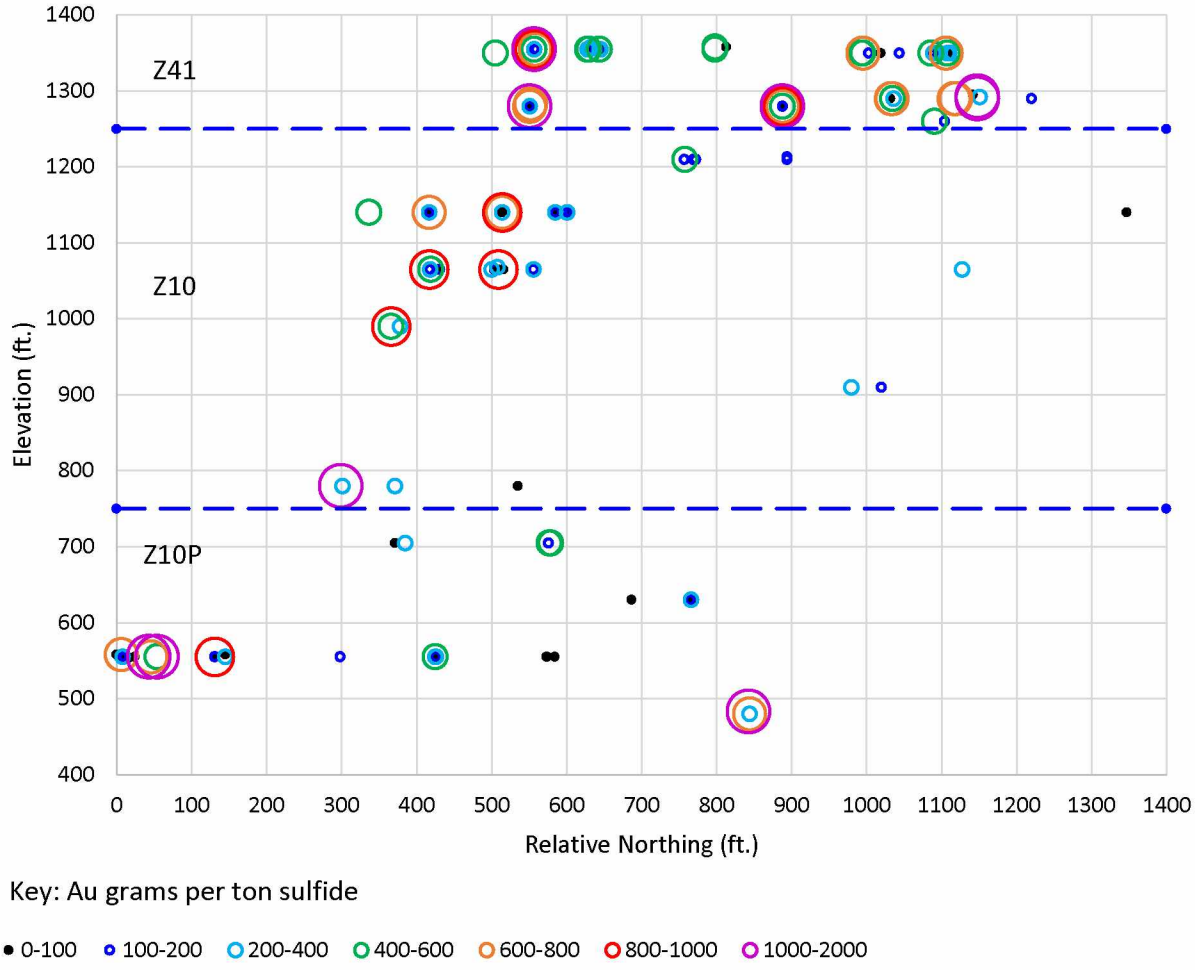

Key: Au grams per ton sulfide

● 0-100 ○ 100-200 ○ 200-400 ○ 400-600 ○ 600-800 ○ 800-1000 ○ 1000-2000

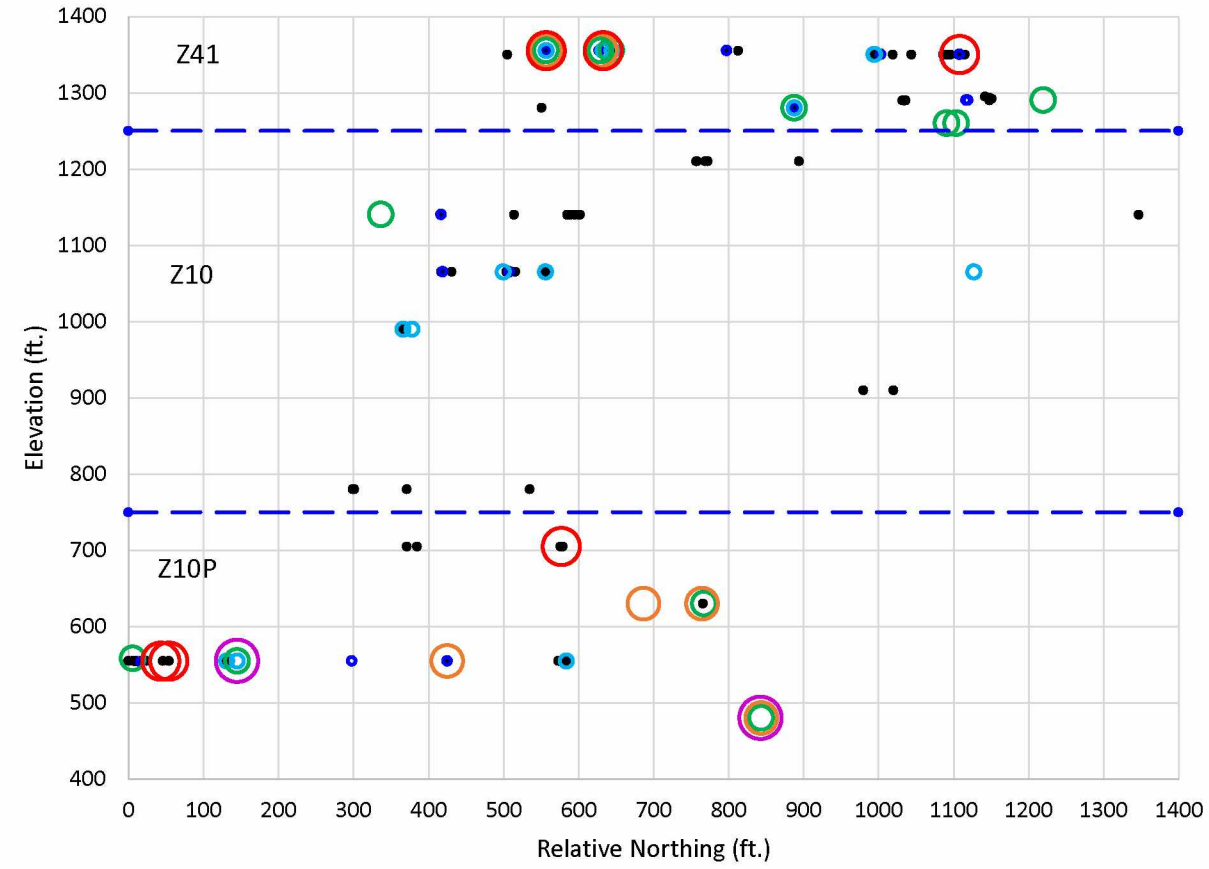

Key: Ag grams per ton sulfide

BDL '2-10 '10-20 20-40 40-60 60-90 90-1800

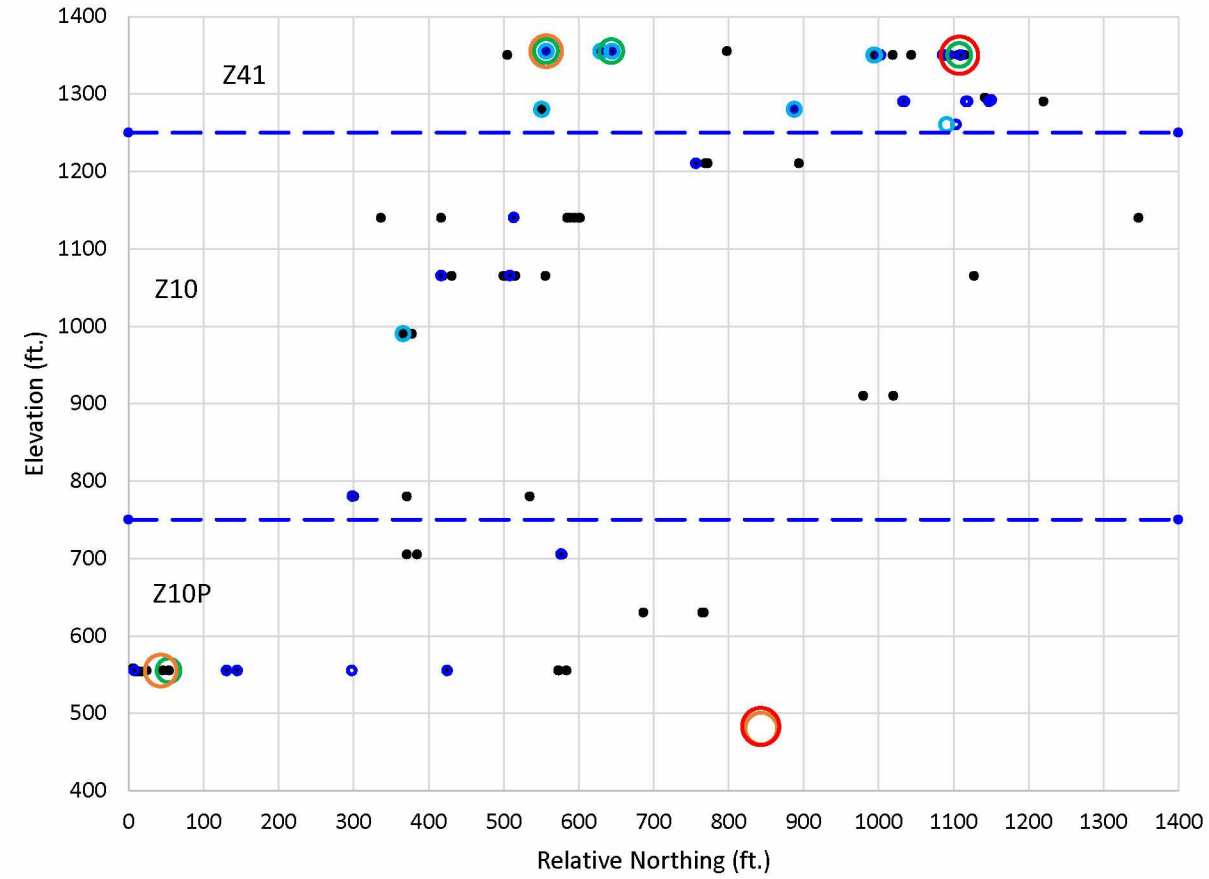

Key: Bi grams per ton sulfide

● BDL ○ '2-10 ○ '10-20 ○ 30-60 ○ 60-100 ○ 100-500

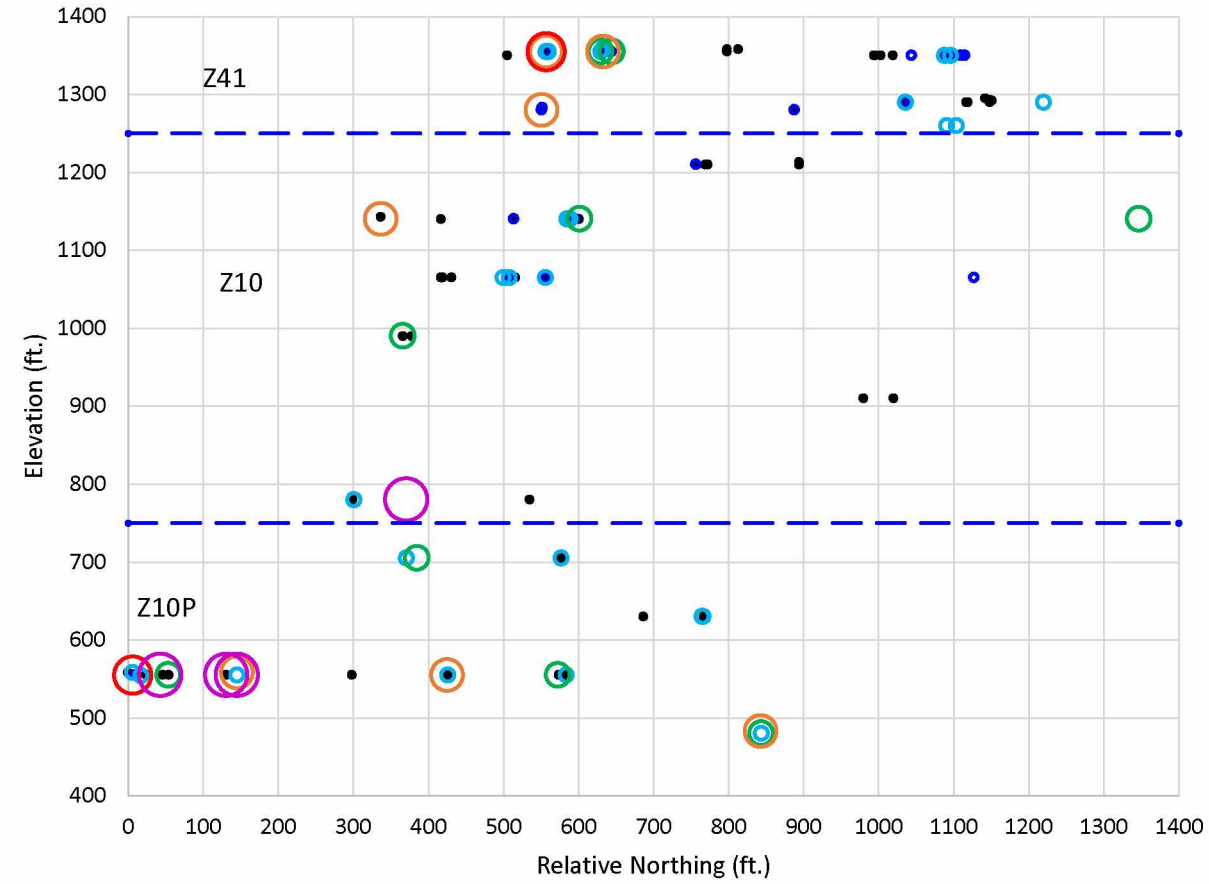

Key: Hg grams per ton sulfide

● BDL ○ '1-10 ○ '10-20 ○ 20-40 ○ 50-90 ○ 100-250 ○ 400-3500

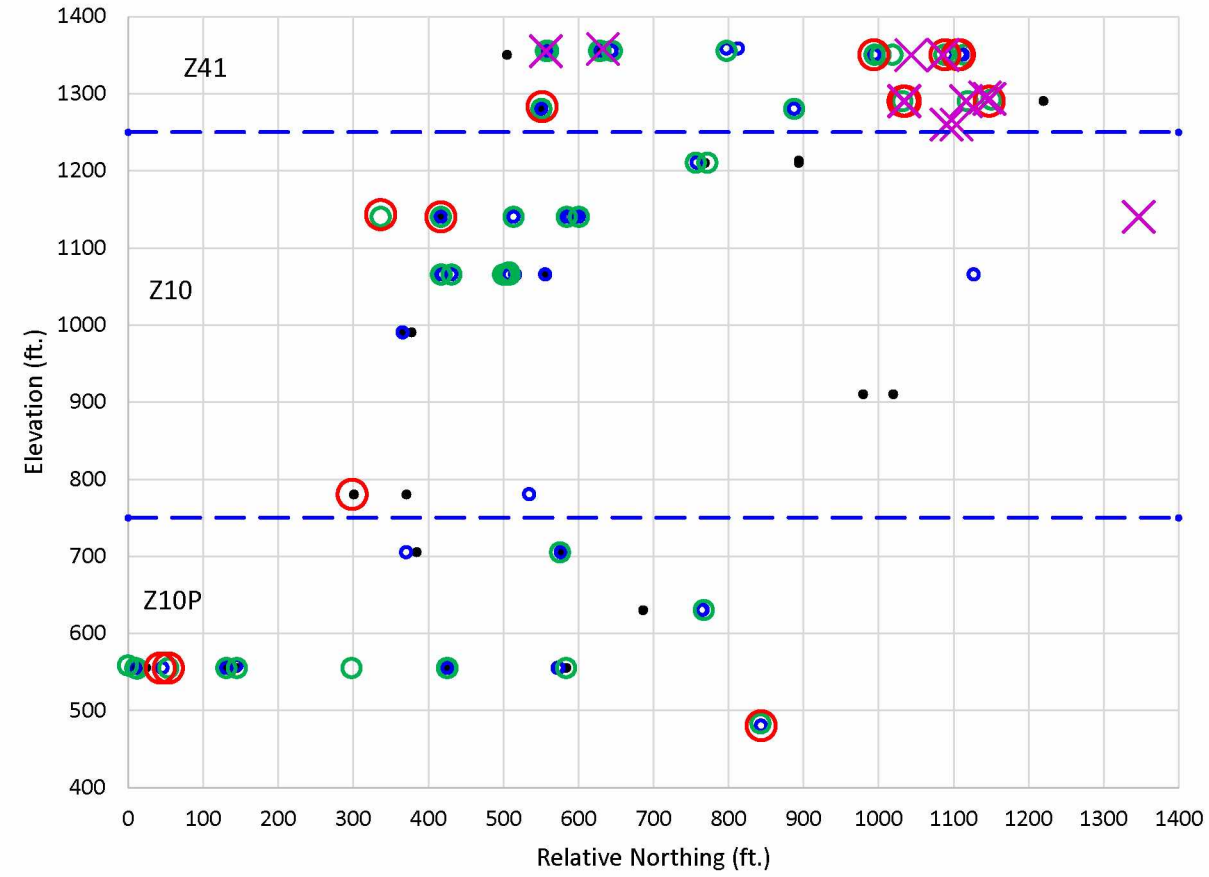

Key: Ni grams per ton sulfide

• BDL ○ 20-30 ○ 30-40 ○ 40-60 × NiTe

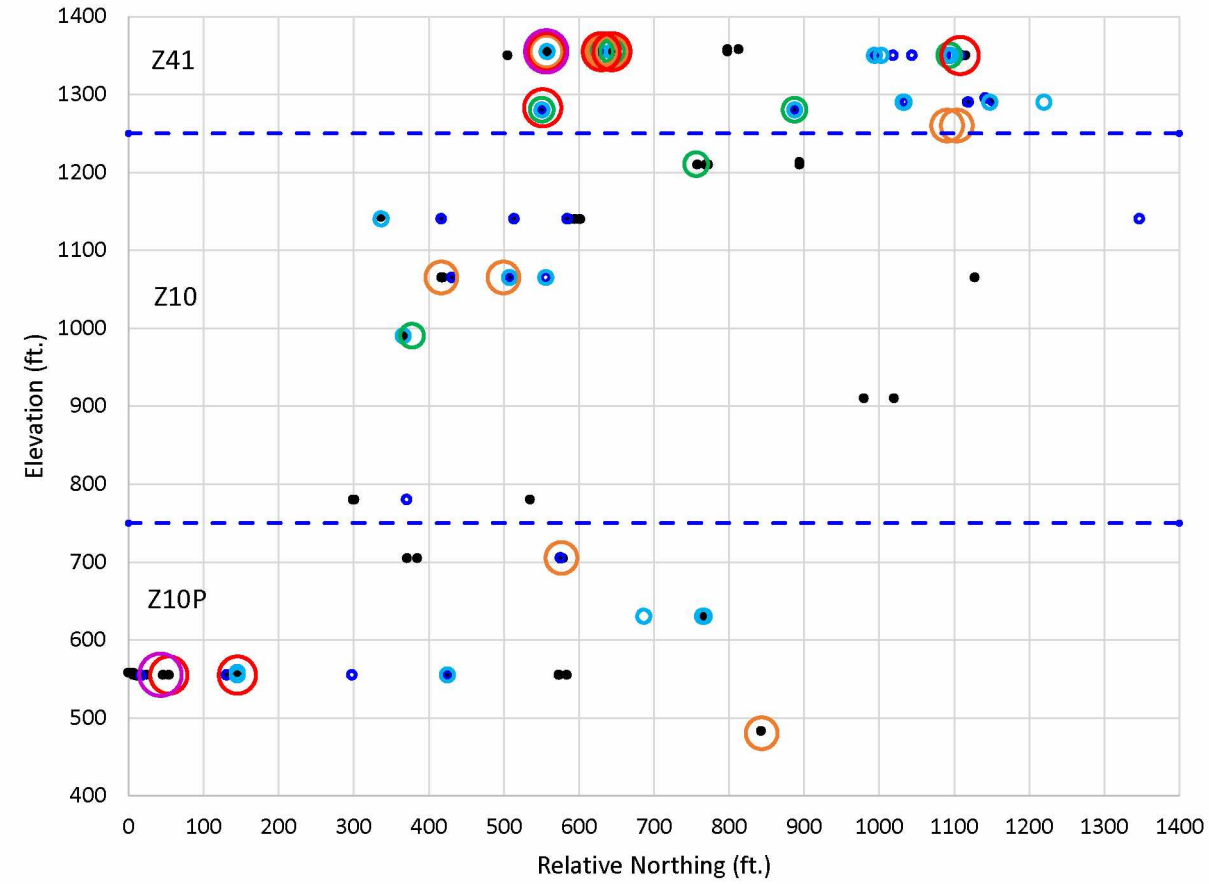

Key: Pb grams per ton sulfide

● BDL ○ '1-10 ○ '10-20 ○ 20-30 ○ 30-75 ○ 75-180 ○ 750-100

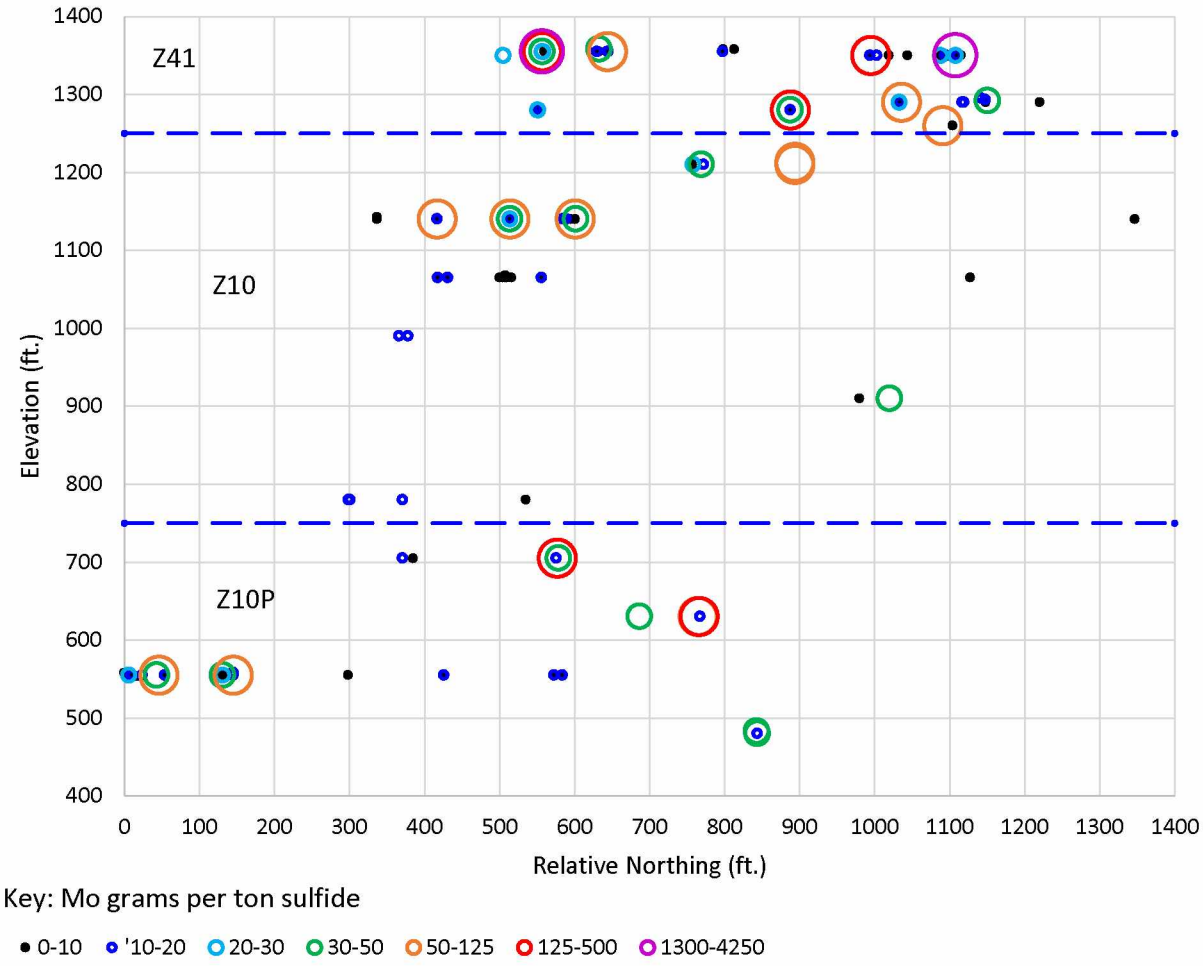
Z41
Z10
Z10P
Elevation (ft.)
Relative Northing (ft.)
1400
1300
1200
1100
1000
900
800
700
600
500
400
0
100
200
300
400
500
600
700
800
900
1000
1100
1200
1300
1400
Key: Mo grams per ton sulfide
0-10
'10-20
20-30
30-50
50-125
125-500
1300-4250

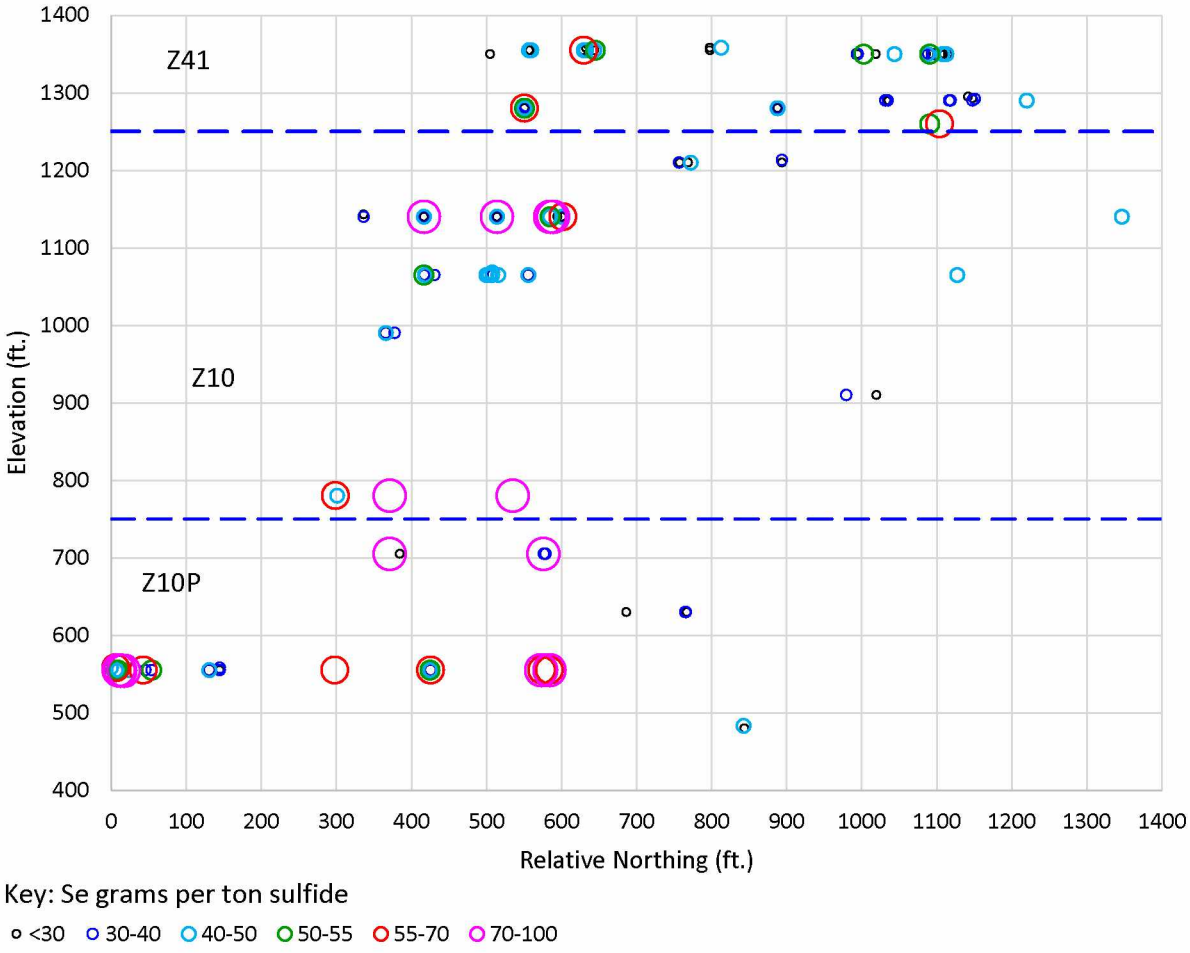
Z41
Z10
Z10P
Elevation (ft.)
Relative Northing (ft.)
1400
1300
1200
1100
1000
900
800
700
600
500
400
0
100
200
300
400
500
600
700
800
900
1000
1100
1200
1300
1400
Key: Se grams per ton sulfide
<30
30-40
40-50
50-55
55-70
70-100

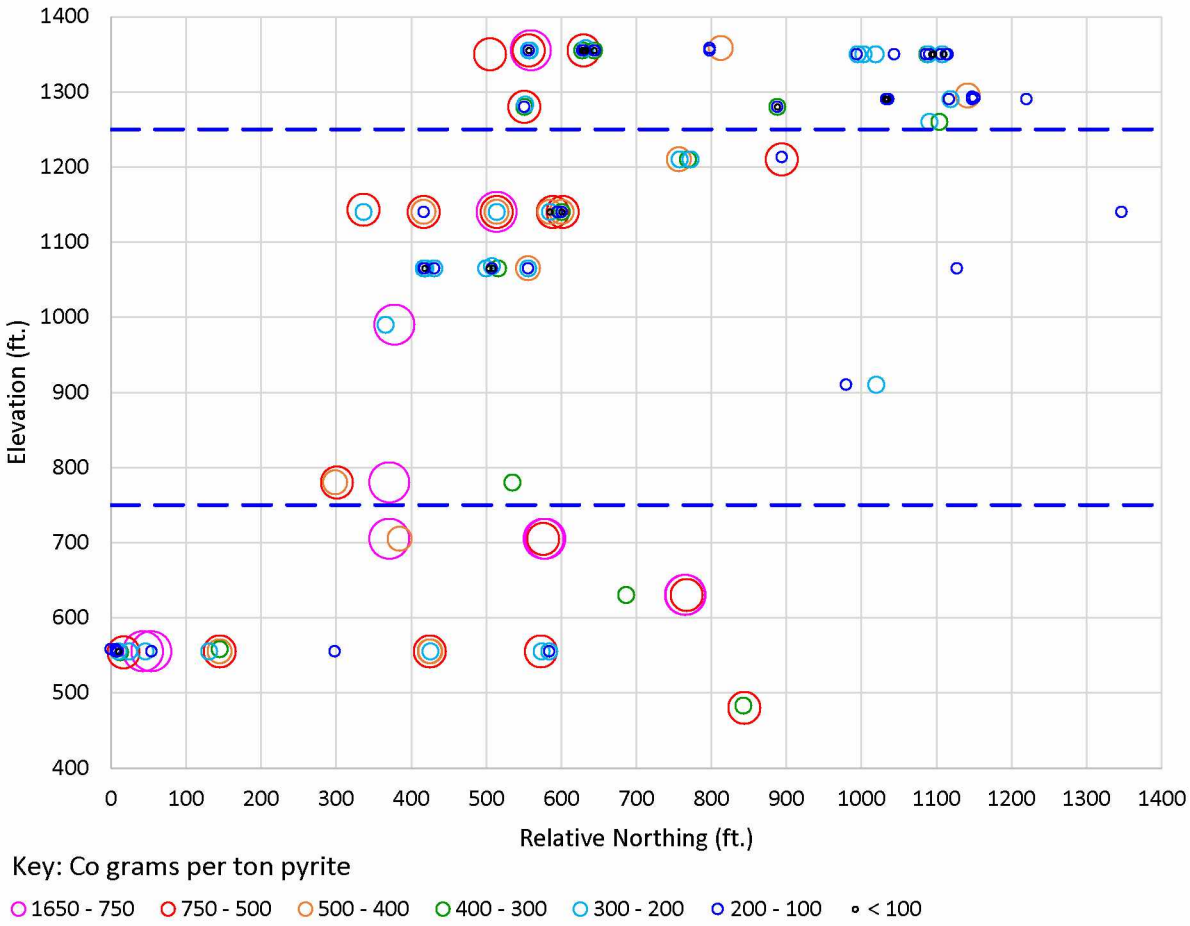
Elevation (ft.)
1400
1300
1200
1100
1000
900
800
700
600
500
400
0
100
200
300
400
500
600
700
800
900
1000
1100
1200
1300
1400
Relative Northing (ft.)
Key: Co grams per ton pyrite
1650 - 750
750 - 500
500 - 400
400 - 300
300 - 200
200 - 100
< 100

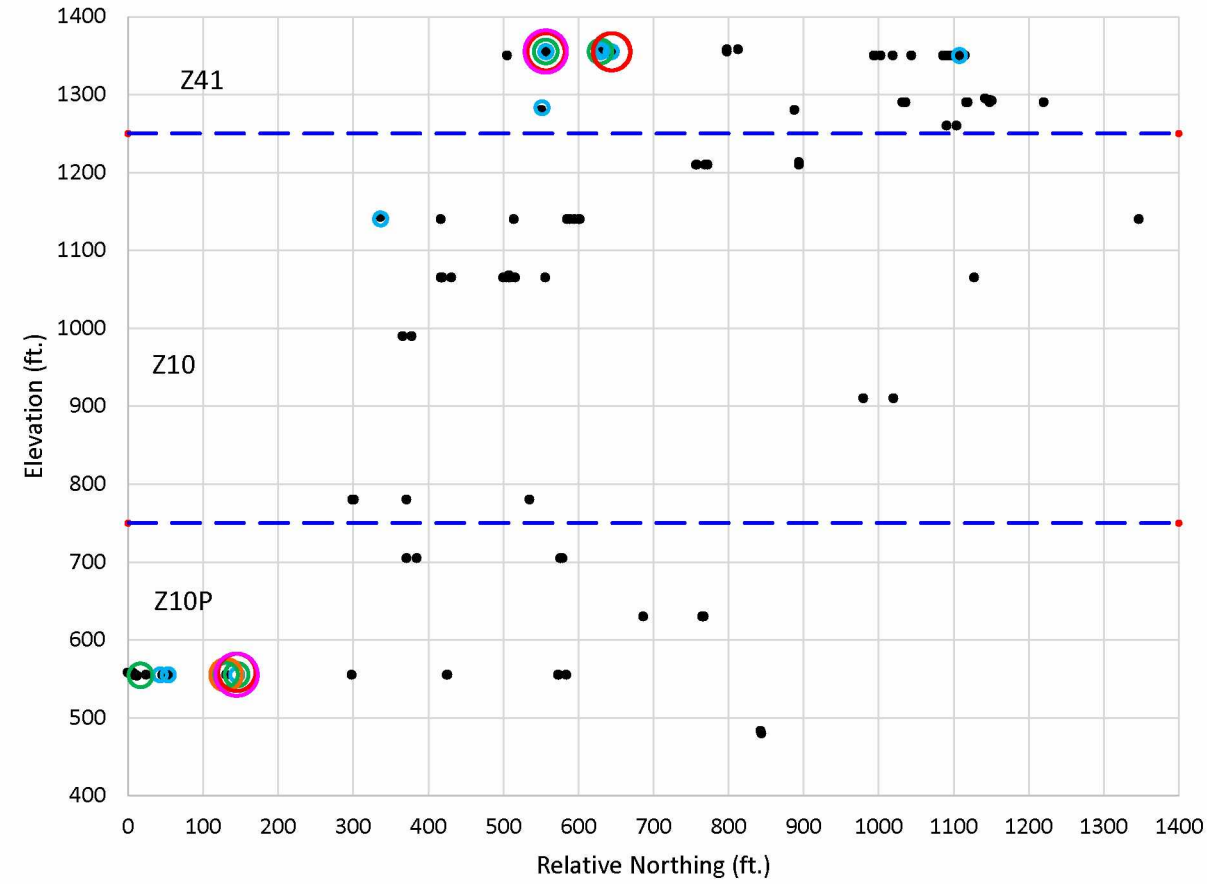

Key: Calculated relative % fahlore per ton sulfide

● no tet ○ 0.01-0.1 ○ 0.1-0.2 ○ 0.2-0.5 ○ 0.5-1 ○ '1-4

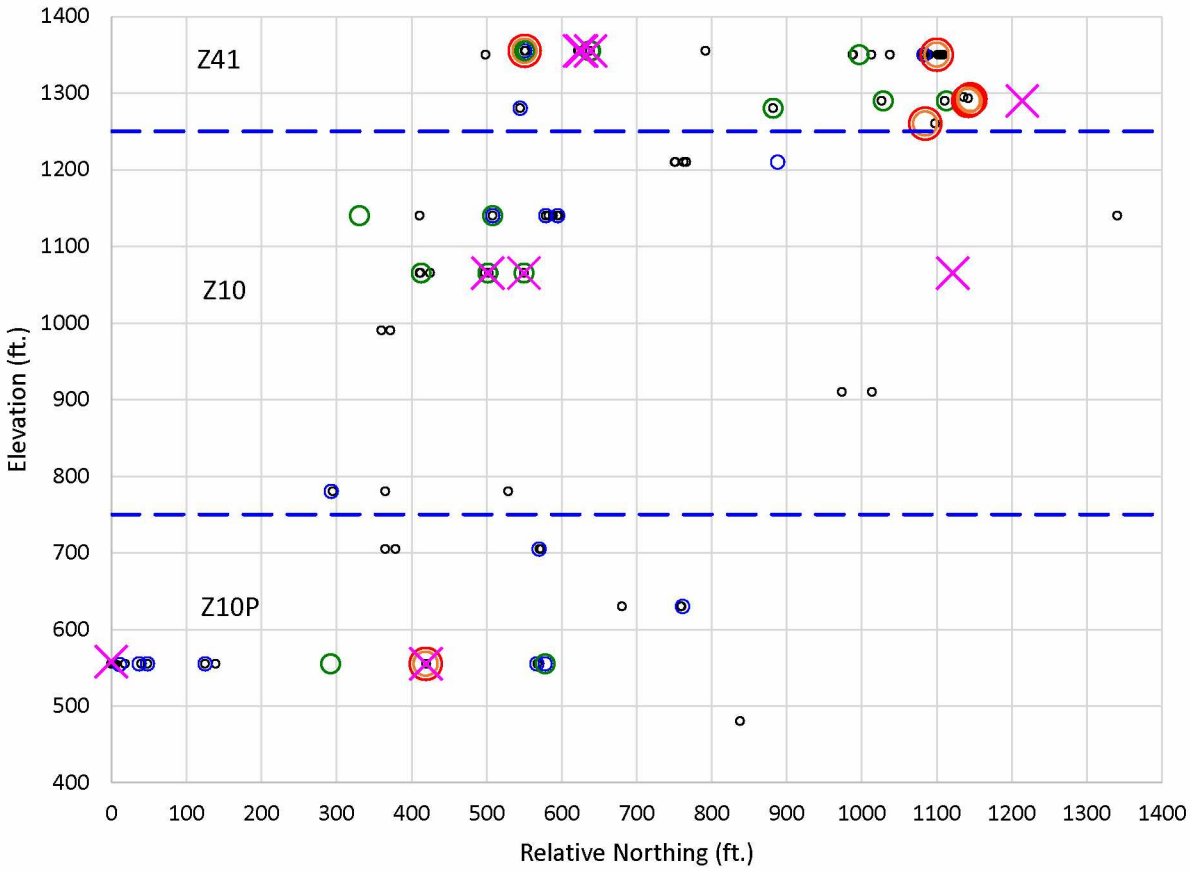

Key: Calculated relative % chalcopyrite per gram sulfide

<0.1 0.2-0.1 0.2-0.5 0.5-1 1-5 5-100

Appendix H. Polished Section Procedures and Descriptions

After all XRF results are processed, samples with anomalously high concentrations of metals are identified. The anomalous samples with enough sulfide rich material left after the XRF pellet was made are set aside. I then hand-picked sulfide grains to mount in epoxy on glass slides.

There are several polished sections that I made which were not used due to inability to get a suitable polish. Some sulfide rich material came from brecciated veins. This material could not be polished due to its softness.

One sample (KEN-01) was crushed and a magnet was used to separate out the magnetic material. Then non-magnetic material was then panned to concentrate the sulfides. This method was not effective and was not repeated for any other samples. Several samples have more than 1 polished section made due to varying sulfide texture or content. Below lists each polished section with a short description. Table H-1 lists the slide number and which hand sample it came from.

01-MAG: Made from the magnetically separated panned concentrates from a MSB. Small grains of magnetite, hematite, few pyrite and chalcopyrite. Magnetite is replacing hematite. Grains generally not fractured. Pyrite has inclusions of magnetite, but no tellurides or Au. The grains do not have any filled fractures or interstitial textures; this might be because the grains are too small in this sample.

01-1: Made from the non-magnetic leftovers from the panned concentrates of a MSB. The slide broke during polishing, requiring the slide to be epoxied to another glass slide for further polishing. This has not been done yet because there are not many sulfides in the samples. It is not worth the trouble.

01-2: Made from hand-picked grains from a MSB.

02-1: It is not fully polished because the epoxy started to get ripped off part-way through the polishing procedure. Only 2 pyrite grains are polished enough. Pyrite grains are generally not significantly fractured. Pyrite grains have inclusions of tellurides, quartz and/or calcite, and magnetite.

02-2: It is not fully polished because the epoxy started to get ripped off part-way through the polishing procedure. Several grains are polished enough to analyze. Pyrite grains are generally not fractured or included.

03-1: Fairly fractured pyrite grains with many and calcite inclusions. Not many tellurides, no Au, and few chalcopyrite inclusions.

05-PS1: Fairly fractured pyrite grains with many inclusions, interstitial, and fracture filling Au and telluride minerals. There is not much chalcopyrite and it is present as inclusions and fracture fillers. Strange intergrowths of Au and calaverite are present.

05-1: Very fractured pyrite grains filled with chalcopyrite and tellurides. Most fractured and filled pyrite grains also have inclusions of chalcopyrite and tellurides, but no inclusions of Au. Some of the inclusions are fairly large within these fractured grains.

05-2: Very fractured pyrite grains filled with chalcopyrite and tellurides. Most fractured and filled pyrite grains also have inclusions of chalcopyrite and tellurides, but no inclusions of Au. Some of the inclusions are cut by fractures, but not offset.

0-6, 06-2, 06-3: It was difficult to see the sulfide matrix in these samples because the matrix is very fine-grained and much softer than the quartz shards and the epoxy. As the slide was being polished the sulfides were being gouged out. Only occasional pyrite grains were visible and not well polished.

06-PS1: It was difficult to see the sulfide matrix in these samples because the matrix is very fine-grained and much softer than the quartz shards and the epoxy. As the slide was being polished the sulfides were being gouged out. Only occasional pyrite grains were visible. The pyrite grains were small and fractured with chalcopyrite fillings.

07-1: Pyrite grains moderately to weakly fracture with no chalcopyrite or Au. Many telluride inclusions.

07-2: Large pyrite grains moderately to weakly fracture with no chalcopyrite or Au. Many telluride inclusions.

08-1: Weakly fractured pyrite grains with a small amount of chalcopyrite present as inclusions, interstitial, and fracture filling. Most of the tellurides and Au are present as interstitial.

08-2: The pyrite grains are very weakly fractured with no Au or tellurides and almost no chalcopyrite.

08-3: It is not quite polished enough, but the pyrite grains are very weakly fractured with no Au or tellurides and almost no chalcopyrite.

08-4: The pyrite grains are very weakly fractured with no Au or tellurides and almost no chalcopyrite.

480Acess-1: Medium to fine grained pyrite bands (approx. 0.5 in.) in quartz. Fine grained pyrite bands have interstitial tetrahedrite. Abundant gold and non-Au telluride minerals in fractured pyrite.

555-160-2: Medium to coarse grained pyrite clots and fine-grained pyrite bands. Abundant gold and non-Au telluride minerals in fractured pyrite and grain boundary inclusions.

555-160-4:

555-160-5: Abundant gold non-Au telluride minerals in fractured pyrite and grain boundary inclusions.

555-160-8: Fractured pyrite grains with abundant chalcopyrite, tetrahedrite, and bornite veinlets filling fractured pyrite. The vein was vuggy.

555-188-3: Aggregates of intergrown pyrite with large (> 100 µm) grains of calaverite adjacent to pyrite in quartz. Multiple inclusion textures of calaverite and minor chalcopyrite.

555-188-5: Large grains of chalcopyrite (> 500 µm) grains in quartz and calcite. Minor pyrite inclusion in chalcopyrite. Large (> 100 µm) grains of calaverite and hessite adjacent to chalcopyrite and isolated in quartz.

555S-2: Aggregates of intergrown pyrite with multiple inclusion textures of calaverite and minor chalcopyrite. Significant calaverite filling fractured pyrite.

555S-3: Aggregates of intergrown pyrite with multiple inclusion textures of calaverite and minor chalcopyrite.

630-224-4: Aggregates of intergrown pyrite with multiple inclusion textures of calaverite and minor chalcopyrite. Minor magnetite inclusions in pyrite.

780-176-2: Aggregates of intergrown pyrite with large (> 50 µm) grains of calaverite adjacent to pyrite in quartz. Multiple inclusion textures of calaverite and minor chalcopyrite.

705PASTE-3: Minor pyrite with small fine grained calaverite inclusions.

1065-189-1: Aggregates of intergrown pyrite with multiple inclusion textures of calaverite and minor chalcopyrite.

1065-189-6: Aggregates of intergrown pyrite with multiple inclusion textures of calaverite and minor chalcopyrite.

1065-206-3: Fractured pyrite grains with abundant chalcopyrite, minor tetrahedrite, and abundant calaverite inclusions in chalcopyrite.

1140-197-6: Aggregates of intergrown pyrite with multiple inclusion textures of calaverite and minor chalcopyrite.

1280-201-6: Aggregates of intergrown pyrite with large (> 50 µm) grains of calaverite adjacent to pyrite in quartz. Multiple inclusion textures of calaverite and minor chalcopyrite.

1355-201-16a: Fractured pyrite grains with abundant tetrahedrite, chalcopyrite, and abundant non-Au telluride inclusions in tetrahedrite and chalcopyrite.

1355-201-16b: Large (> 500 µm) tetrahedrite grains in quartz and calcite with minor inclusions of chalcopyrite and pyrite. Large (> 50 µm) grains of calaverite adjacent to tetrahedrite in quartz.

1355-210-14: Fractured pyrite grains with abundant chalcopyrite, minor tetrahedrite, and abundant non-Au tellurides and calaverite inclusions in chalcopyrite.

1350-13: Fine grained sulfide material from brecciated vein. Few polished pyrite grains with small minor calaverite inclusions.

Table H-1. List of All Polished Sections with Corresponding Analysis Type

Polished Section Name	Hand Sample	Type of Data Collected		
		Reflected Light Survey	EDS	Co Maps
01-2	KEN-01			
04-1	KEN-04	x	x	x
05-1	KEN-05			
05-3	KEN-05			
05-PS1	KEN-05		x	
06-PS1	KEN-06			
07-1	KEN-07	x	x	
07-2	KEN-07	x		
08-1	KEN-08	x	x	x
08-2	KEN-08			
08-4	KEN-08			
480ACCES-1	480ACCES-1			
555-160-2	555-160-2		x	
555-160-4	555-160-4	x	x	
555-160-5	555-160-5	x	x	x
555-160-8	555-160-8	x	x	x
555-188-3	555-188-3	x	x	x
555-188-5	555-188-5	x	x	
555S-2	555S-2	x	x	x
555S-3	555S-3		x	
630-224-4	630-224-4	x	x	x
780-176-2	780-176-2	x	x	x
705PASTE-3	705PASTE-3		x	
1065-189-1	1065-189-1		x	
1065-189-6	1065-189-6			
1065-206-3	1065-206-3	x		
1140-197-6	1140-197-6	x	x	x
1280-201-6	1280-201-6	x		
1355-201-16a	1355-201-16	x	x	x
1355-201-16b	1355-201-16	x	x	x
1355-210-14	1355-210-14	x	x	
1350-13	1350-13	x	x	

Appendix I. Reflected Light Calaverite and Gold Survey Results

Table I-1. Calaverite ($AuTe_2$) Grain Textures and Average Size Observed in Reflected Light

Zone	Sample	Inclusions						Fracture Fill		Adjacent		Total #
		Round		Complex		GB						
		#	µm	#	µm	#	µm	#	µm	#	µm	
41	07-1	15	10	21	20	11	50					47
	07-2	22	20	11	30					10	70	43
	1355-210-14			15	10	7	20	36	30			58
	1355-201-16a	7	10	19	15			12	30			38
	1355-201-16b			8	10							8
	1350-13											0
	1280-201-6	16	10	32	40	35	70	31	500			114
	04-1	11	5	16	20	9	15					36
10	1140-197-6			18	20	9	60					27
	08-1	20	20					5	150			25
	1065-206-3							8	50			8
	1065-189-1	51	15	32	20	81	100	2	40	3	90	169
	780-176-2			11	20	10	400			3	100	24
10P	630-224-4			2	50							2
	555-188-3	3	10			9	20			11	200	23
	555-188-5	7	250									7
	555-160-4	16	20									16
	555-160-5	6	20									6
	555-160-8	3	10									3
	555S-2			40	30	61	40	35	30			136

Table I-2. Gold Grain Textures and Average Size Observed in Reflected Light

Zone	Sample	Inclusions						Fracture Fill		Adjacent		Total #
		Round		Complex		GB						
		#	µm	#	µm	#	µm	#	µm	#	µm	
41	1355-210-14			4	10			8	40			12
	1355-210-18							2	10	6	50	8
	1355-201-16a	11	10	2	10			10	15			21
	1355-201-16b	2	10									2
	04-1			4	20	1	15	1	30			6
10	08-1							4	100	2	15	6
	1065-189-1			4	15					3	20	7
10P	555-188-3	1	15									1
	555-188-5							13	40			13
	555-160-4							13	40	1	25	14
	555-160-5					3	60	6	60			9
	555-160-8	2	10					5	5			7
	555S-2			1	30	3	25	63	30			67
	555S-3							1	10	1	40	2

Appendix J. Non-Au Telluride Grain Textures Observed in BSE Imaging

Table J-1. Hessite (Ag_2Te) Grain Textures and Sizes Observed in BSE

Zone	Slide	Location	Point	Texture	Size (µm)
41	1350-13	w - close-up	1	round inclusion	5
41	1350-13	y	2	round inclusion	10
41	1350-13	y	3	round inclusion	5
41	1350-13	z - close-up	1	grain boundary	<2.5
41	1355-210-14	a	7	cp veinlet	5
41	1355-210-14	near a	2	cp veinlet	<5
41	1355-210-14	near a	12	cp veinlet	<5
10P	555-160-8	3 bright grains	1avg	round inclusion	10
10P	555-160-8	a	2	tet veinlet	>5
10P	555-160-8	f2 - high mag	1	tet veinlet	<5
10P	555-160-8	f3 high mag	1	tet veinlet	2
10P	555-160-8	w of c	2	round inclusion	10
10P	555-188-5	a2	2	in quartz	5
10P	555-188-5	a2	3	in quartz	5
10P	555-188-5	c	2	in quartz	100
10P	630-224-4	f	1	complex inclusion	<5

Table J-2. Petzite (Ag_3AuTe_2) Grain Textures and Sizes Observed in BSE

Zone	Slide	Location	Point	Texture	Size (µm)
41	05-PS1	h - closeup2	5	complex inclusion	<5
41	1350-13	u - high mag1	1	round inclusion	2
41	1350-13	u - high mag2	1	fracture fill	<5
41	1355-210-14	a	1	cp veinlet	5
41	1355-210-14	a	3	cp veinlet	10
41	1355-210-14	a	4	cp veinlet	5
41	1355-210-14	a	5	cp veinlet	5
41	1355-210-14	a	6	cp veinlet	5
41	1355-210-14	a	8	cp veinlet	5
41	1355-210-14	a - 25 kV	3	cp veinlet	10
41	1355-210-14	a - close-up	1	cp veinlet	<5
41	1355-210-14	a - close-up	3	cp veinlet	<5
41	1355-210-14	a - close-up	4	cp veinlet	5
41	1355-210-14	a - close-up	5	cp veinlet	5
41	1355-210-14	a - close-up	6	cp veinlet	5
41	1355-210-14	b	5	fracture fill	5
41	1355-210-14	b- close-up 25 kV	2	cp veinlet	<5
41	1355-210-14	b- close-up 25 kV	3	cp veinlet	5
41	1355-210-14	b- close-up 25 kV	4	cp veinlet	5

Table J-2 cont. Petzite (Ag_3AuTe_2) Grain Textures and Sizes Observed in BSE

Zone	Slide	Location	Point	Texture	Size (µm)
41	1355-210-14	d - near	4	cp veinlet	20
41	1355-210-14	f	5	euhedral inclusion	5
41	1355-210-14	h	2	cp veinlet	10
41	1355-210-14	h	5	cp veinlet	30
41	1355-210-14	h	6	cp veinlet	40
41	1355-210-14	h	7	cp veinlet	30
41	1355-210-14	h	8	cp veinlet	15
41	1355-210-14	h	9	cp veinlet	10
41	1355-210-14	near a	1	cp veinlet	<5
41	1355-210-14	near a	6	cp veinlet	15
41	1355-210-14	near a	7	cp veinlet	15
41	1355-210-14	near a	8	cp veinlet	15
41	1355-210-14	near a	9	cp veinlet	15
41	1355-210-14	near a	10	cp veinlet	15
41	1355-210-14	near a	11	cp veinlet	5
41	1355-210-14	near a	13	cp veinlet	5
41	1355-210-14	near a 25 kV	1	cp veinlet	15
41	1355-210-14	near a 25 kV	2	cp veinlet	15
10P	555-160-8	e	2	round inclusion	5
10P	555S-2	c	1	grain boundary	20
10P	555S-2	e2 - high mag	3	complex inclusion	5
10P	555S-2	f	2	grain boundary	25
10P	705paste-3	base2	1	fracture fill	20

Table J-2. Coloradoite (HgTe) Grain Textures and Sizes Observed in BSE

Zone	Slide	Location	Point	Texture	Size (µm)
41	1355-210-14	h	10	cp veinlet	10
10	08-1	a - closeup	2	adjacent	10
10	08-1	a - closeup	3	adjacent	5
10	08-1	b - closeup3	3	fracture fill	5
10	08-1	b - closeup3	4	fracture fill	<5
10	08-1	c	6	fracture fill	10
10	08-1	d	1	adjacent	100
10	08-1	d	5	round inclusion	50
10	08-1	d	6	adjacent	20
10P	555-160-2	run2	1	grain boundary	50
10P	555-160-2	run2	2	grain boundary	10
10P	555-160-4	b	1	fracture fill	50
10P	555-160-4	d	2	fracture fill	10
10P	555-160-4	d	3avg	fracture fill	30
10P	555-160-4	f	2	tet veinlet	10
10P	555-160-5	a	1	complex inclusion	5
10P	555-160-5	a	2	grain boundary	5
10P	555-160-5	a	3	grain boundary	40
10P	555-160-5	a	4	grain boundary	20
10P	555-160-5	a	5	grain boundary	10
10P	555-160-5	a - closeup2	2	tet veinlet	5
10P	555-160-5	a - closeup2	4	tet veinlet	<5
10P	555-160-5	c - closeup1	1	complex inclusion	15
10P	555-160-5	c-closeup2	1	grain boundary	5
10P	555-160-5	c-closeup2	2	adjacent	5
10P	555-160-5	c-closeup2	4	fracture fill	5
10P	555-160-5	c-closeup2	5	grain boundary	5
10P	555-160-5	c-closeup3	1	complex inclusion	10
10P	555-160-5	c-closeup3	2	grain boundary	50
10P	555-160-5	c-closeup3	5	grain boundary	10
10P	555-160-5	c-closeup3	9	grain boundary	50
10P	555-160-5	f	1	complex inclusion	15
10P	555-160-5	f	3	round inclusion	5
10P	555-160-5	f - closeup2	1	euhedral inclusion	10
10P	555S-2	a	2	grain boundary	20
10P	555S-3	c	1	tet veinlet	5
10P	555S-3	c - closeup1	2	tet veinlet	<5
10P	555S-3	c - closeup1	3	tet veinlet	<5
10P	555S-3	c - closeup1	4	tet veinlet	<5

Table J-3. Tellurobismuthite (Bi_2Te_3) Grain Textures and Sizes Observed in BSE

Zone	Slide	Location	Point	Texture	Size (µm)
41	05-PS1	g - closeup1	4	complex inclusion	5
41	05-PS1	g - closeup1	6	complex inclusion	<5
41	1350-13	y	1	round inclusion	5
41	1355-201-16b	n1 - closeup	2	tet veinlet	<5
41	1355-210-14	a	2	cp veinlet	5
41	1355-210-14	a - 25 kV	1	cp veinlet	10
41	1355-210-14	a - 25 kV	2	cp veinlet	10
41	1355-210-14	d	5	cp veinlet	30
41	1355-210-14	d	6	cp veinlet	30
41	1355-210-14	d	8	cp veinlet	20
41	1355-210-14	h	3	cp veinlet	40
41	1355-210-14	h	4	cp veinlet	40

Table J-4. Melonite ($NiTe_2$) **G**rain Textures and Sizes Observed in BSE

Zone	Slide	Location	Point	Texture	Size (µm)
41	05-PS1	a - closeup	1	fracture fill	3
41	05-PS1	h - closeup1	6	fracture fill	15
41	05-PS1	h - closeup2	4	fracture fill	5
41	05-PS1	h - closeup2	10	fracture fill	10
41	05-PS1	h - closeup2	6avg	fracture fill	20
41	05-PS1	h-closeup1	2avg	fracture fill	10
41	05-PS1	h-closeup1	4avg	fracture fill	35

Table J-5. Altaite (PbTe) **G**rain Textures and Sizes Observed in BSE

Zone	Slide	Location	Point	Texture	Size (µm)
41	1355-210-14	a - closeup	2	cp veinlet	<5
41	1355-210-14	f	2	cp veinlet	5
10P	555S-2	b1	4	grain boundary	15
10P	555S-2	c	4	grain boundary	<5
10P	555S-2	e - high mag	1	grain boundary	15
10P	555S-2	e2 - high mag	2	complex inclusion	20

Appendix K. Mineral Compositional Data (EDS)

Table K-1. Ag Concentrations in Calaverite ($AuTe_2$) from Energy Dispersive Spectroscopy

Slide	Site	Texture	Size (µm)	Point	Ag wt%
04-1	a	complex inclusion	40	1	0.6
04-1	a	round inclusion	10	2	0.4
04-1	a	round inclusion	20	3	0.42
04-1	a	fracture fill	10	4	0.3
04-1	a	round inclusion	10	5	0.41
04-1	a	adjacent	10	6	0.6
04-1	a closeup1	adjacent	5	1	0.7
04-1	a closeup1	fracture fill	5	2	0.4
04-1	a closeup1	fracture fill	10	3	0.9
04-1	a closeup1	adjacent	20	1	0.35
04-1	a closeup1	adjacent	5	2	0.74
04-1	a closeup1	adjacent	5	3	0.4
04-1	a closeup1	fracture fill	5	4	0.76
07-1	a	complex inclusion	20	1	0.33
07-1	a	grain boundary	40	2	0.11
07-1	a	round inclusion	15	3	0.04
07-1	a	round inclusion	15	4	0.08
07-1	b	fracture fill	40	1	0.08
07-1	b	fracture fill	40	2	0.05
07-1	b	round inclusion	25	3	0.18
07-1	b	fracture fill	30	4	0.24
07-1	b	adjacent	20	5	0.18
07-1	b	fracture fill	40	7	0.08
07-1	b	fracture fill	20	8	0.18
07-1	b	fracture fill	15	9	0.27
08-1	c	round inclusion	30	1	0
08-1	c	round inclusion	30	2	0.1
08-1	c	round inclusion	20	3	0
08-1	c	round inclusion	15	4	0
08-1	c	round inclusion	20	5	0
08-1	d	round inclusion	15	2	0.1
08-1	d	round inclusion	40	3	0.03
08-1	d	round inclusion	15	4	0.03
05-PS1	g - closeup1	complex inclusion	10	1	0.31
05-PS1	g - closeup1	complex inclusion	10	2	0.35
05-PS1	g - closeup1	complex inclusion	10	3	0.33
05-PS1	g - closeup1	complex inclusion	2.5	5	0
05-PS1	g - closeup1	complex inclusion	2.5	7	0.16

Table K-1 cont. Ag Concentrations in Calaverite ($AuTe_2$) from Energy Dispersive Spectroscopy

Slide	Site	Texture	Size (µm)	Point	Ag wt%
1065-189-1	c	fracture fill	30	2	0.2
1065-189-1	c	fracture fill	20	3	0.2
1065-189-1	c	fracture fill	30	4	0.2
1065-189-1	c	fracture fill	10	5	0.2
1065-189-1	c	fracture fill	5	6	0.2
1065-189-1	e	fracture fill	20	1	0.2
1065-189-1	e	fracture fill	20	2	0.2
1065-189-1	e	fracture fill	20	3	0.2
1065-189-1	e	round inclusion	5	4	0.1
1065-189-1	e	round inclusion	5	5	0.1
1065-189-1	e	round inclusion	5	7	0
1065-189-1	e	fracture fill	20	8	0.1
1355-201-16a	c1 - closeup1	tet veinlet	2.5	1	1.39
1355-201-16a	e1	complex inclusion	30	3avg	0.55
1355-201-16a	e2	cp veinlet	15	3	0.5
1355-201-16a	e2	round inclusion	2.5	5	0.4
1355-201-16a	f1	complex inclusion	25	1avg	0.6
1355-201-16a	f2	cp veinlet	40	1	0.7
1355-201-16a	f3	tet veinlet	25	1	0.6
1355-201-16b	m	round inclusion	5	1	0.01
1355-201-16b	m2 - closeup	round inclusion	2.5	2	0.17
1355-210-14	d - near	cp veinlet	60	2	1.1
1355-210-14	near a	cp veinlet	5	3	0.59
1355-210-14	near a	cp veinlet	5	4	0.32
555-160-8	3 bright grains	round inclusion	5	5	0.3
555-160-8	3 bright grains	round inclusion	10	3avg	0.15
555-160-8	isolated bright	round inclusion	5	1avg	0.195
555-160-8	w of c	round inclusion	10	1	0.2
555-188-3	a	fracture fill	200	1avg	0.6575
555-188-3	b	complex inclusion	50	1avg	0.49
555-188-3	c	adjacent	200	3	0.41
555-188-3	c	adj	200	1avg	0.42
555-188-3	c	adj	100	2avg	0.35
555-188-3	d	adjacent	300	4	0.17
555-188-3	d	round inclusion	60	1avg	0.346667
555-188-3	d2	in quartz	500	1avg	0.373333
555-188-5	a1	in quartz	125	1	0.4
555-188-5	a1	in quartz	200	2	0.6
555-188-5	a2	in quartz	20	1	0.5

Table K-1 cont. Ag Concentrations in Calaverite ($AuTe_2$) from Energy Dispersive Spectroscopy

Slide	Site	Texture	Size (µm)	Point	Ag wt%
555-188-5	c	adjacent	100	1	0.7
555S-2	a	grain boundary	10	1	0.5
555S-2	b1	grain boundary	20	6	0.6
555S-2	b1	grain boundary	25	2avg	0.85
555S-2	c	grain boundary	20	2	0.6
555S-2	d - high mag	fracture fill	100	3	0.5
555S-2	e2 - high mag	complex inclusion	20	1	0.7
555S-2	e2 - high mag	complex inclusion	5	5	0.6
555S-2	f	grain boundary	10	1	0.5
555S-2	h - very high mag	complex inclusion	2.5	1	0.38
555S-2	j	grain boundary	20	2	0.8
630-224-4	a	complex inclusion	40	1	0
630-224-4	b	round inclusion	30	1	0.6
630-224-4	g - high mag	round inclusion	2.5	1	0
630-224-4	g - high mag	complex inclusion	10	2	0
705paste-3	base1	round inclusion	10	1	0.45
705paste-3	base4	round inclusion	5	1	0
705paste-3	base5	round inclusion	5	1	0
780-176-2	a	grain boundary	80	1	0
780-176-2	a	fracture fill	100	3	0.1
780-176-2	c1 - high mag	complex inclusion	2.5	1	0
780-176-2	d	fracture fill	200	1	0
780-176-2	d	in quartz	60	2	0

Table K-2. Ag Concentrations in Gold (Au, Ag) from Energy Dispersive Spectroscopy

Slide	Location	Point	Texture	Size (µm)	Fineness
08-1	a - closeup	1	adjacent	10	903
08-1	a - closeup	4	adjacent	5	911
08-1	b-closeup3	1avg	fracture fill	40	908
05-PS1	a	1avg	fracture fill	30	899
05-PS1	a	2avg	fracture fill	20	897
05-PS1	a	3avg	fracture fill	10	841
05-PS1	a - closeup	2	fracture fill	7	905
05-PS1	a - closeup	3	fracture fill	7	908
05-PS1	a - closeup	4	fracture fill	7	925
05-PS1	h - closeup1	1	fracture fill	10	922
05-PS1	h - closeup2	11	fracture fill	15	911
05-PS1	h - closeup2	2avg	fracture fill	5	867.5
1065-189-1	c	1	fracture fill	15	955
1350-13	c - trial3 -22	1	complex inclusion	10	805
1350-13	c - trial3 -22	2	complex inclusion	5	730
1350-13	x	1	fracture fill	5	907
1350-13	x	2	fracture fill	10	907
1350-13	c - trial3 -24	1	tet veinlet	10	
1355-201-16a	c1	1	complex inclusion	15	941
1355-201-16a	c1	2	complex inclusion	5	937
1355-201-16a	e1	1	complex inclusion	10	940
1355-201-16a	e1	2	complex inclusion	10	936
1355-201-16a	e2	1	fracture fill	30	941
1355-201-16a	e2	2	fracture fill	30	938
1355-201-16a	a1	1	tet veinlet	<5	932.5
1355-201-16a	a1	4	tet veinlet	<5	931.8
1355-201-16a	a2	2	tet veinlet	<5	935.9
1355-201-16b	m2-closeup	1avg	fracture fill	5	910.75
1355-201-16b	x - closeup	1	round inclusion	5	915
1355-210-14	b	1	cp veinlet	10	938
1355-210-14	b	2avg	cp veinlet	10	938.5333
1355-210-14	c	1	cp veinlet	20	938.5
1355-210-14	d - near	1	cp veinlet	100	938.7
1355-210-14	d - near	3	cp veinlet	20	937
1355-210-14	h	1	cp veinlet	15	932
1355-210-14	f	4	euhedral inclusion	10	936.6
555-160-2	run1	2avg	fracture fill	100	869.5
555-160-4	e	1avg	adj	30	913.6667
555-160-4	d	1	fracture fill	5	922

Table K-2 cont. Ag Concentrations in Gold (Au, Ag) from Energy Dispersive Spectroscopy

Slide	Location	Point	Texture	Size (µm)	Fineness
555-160-4	f	1	tet veinlet	10	916
555-160-5	f	2	complex inclusion	5	909.6
555-160-5	a - closeup2	3	fracture fill	10	912.6
555-160-5	a - gold1	3	fracture fill	5	919
555-160-5	a-gold1	1avg	fracture fill	40	911
555-160-5	c-closeup3	3	grain boundary	5	904
555-160-5	c-closeup3	4	grain boundary	5	908
555-160-5	c-closeup3	7avg	grain boundary	30	916.5
555-160-8	a - closeup2	1	fracture fill	>5	838
555-160-8	a - closeup2	3	fracture fill	>5	829
555-160-8	c	2	fracture fill	30	846
555-160-8	c	3	fracture fill	10	864
555-160-8	c	4	fracture fill	10	862
555-160-8	c	5	fracture fill	10	849
555-160-8	many bright	1	fracture fill	<5	
555-160-8	many bright	2	fracture fill	<5	
555-160-8	many bright	3	fracture fill	<5	
555-160-8	many bright	4	fracture fill	<5	
555-160-8	tet & stuff	1	fracture fill	5	812
555-160-8	tet&stuff	2avg	fracture fill	5	835.5
555-160-8	w of c	3	fracture fill	15	837
555-160-8	w of c	4	fracture fill	5	841
555-160-8	e	1	round inclusion	25	840
555-160-8	e	3	round inclusion	15	850
555-160-8	a	1	tet veinlet	15	852
555-160-8	a - closeup2	2	tet veinlet	>5	812
555-160-8	f4 - high mag	1	tet veinlet	5	846
555S-2	e2 - high mag	4	complex inclusion	5	938
555S-2	k	1	fracture fill	30	938.5
555S-2	j	1	grain boundary	30	936
555S-2	j	3	grain boundary	5	934
555S-3	a	1avg	adj	50	943.98
555S-3	c - closeup1	1	tet veinlet	<5	934.1

Table K-3. Ag Concentrations in Tetrahedrite from Polished Section 1355-201-16a

Site	point	Element (wt%)						
		S	Fe	Cu	Zn	As	Ag	Sb
base 5	4	25.78	3.25	33.14	7.13	4.43	0.63	25.66
	5	25.77	3.14	32.84	7.46	5.42	0.62	24.76
base 6	1	23.89	2.12	34.95	8.4	3.26	0.64	26.75
	2	25.14	2.38	34.13	8.26	3.96	0.6	25.54
	3	25.02	2.08	34.03	7.24	2.39	0.6	28.64
	4	24.94	2.67	34.38	7.64	4.11	0.66	25.6
base 7 (e)	1	24.12	2.47	34.76	7.64	3.05	0.6	27.36
base 8 (g)	1	24.92	2	35.19	7.11	4.43	0.01	26.35
	2	25.4	1.79	35.36	6.94	4.2	0.01	26.3
	3	25.45	1.42	33.75	7.48	3.51	BDL	28.39
base 9 (g)	3	26.97	0.85	33.9	7.03	10	0.07	21.17
	4	26.1	1.19	34.06	7.22	4.43	BDL	27

Table K-4. Ag Concentrations in Tetrahedrite from Polished Section 1355-201-16b

Site	Point	Element (wt%)						
		S	Fe	Cu	Zn	As	Ag	Sb
N2-close up	1	23.72	0.3	40.47	6.99	2.33	0.51	25.67
	2	24.55	0.04	42.02	6.16	7.06	BDL	20.17
	3	24.4	0.32	41.89	6.3	7.46	BDL	19.63
N3-close up tetrahedrite 1	1	24.81	0.51	41.65	5.97	7.54	BDL	19.5
	2	23.92	0.34	41.02	6.18	1.94	0.72	25.88
	3	24.24	0.3	41.02	6.09	3	BDL	25.33
giant tet on slide edge	1	26.6	0.6	33.9	6.9	12.5	0.16	19.38
	2	26.51	BDL	33.88	6.91	4.91	0.16	27.62
	3	25.88	BDL	34.33	7.1	2.74	0.22	29.73
	4	26.21	0.66	34.02	7.75	9.09	BDL	22.17
	5	26.51	0.81	33.87	7.04	6.77	BDL	24.84
giant tet w/ cp	2	26.18	0.37	33.88	7.05	3.32	BDL	29.21
	3	26.78	0.75	33.7	7.56	13.3	0.08	17.81
	4	26.62	0.4	33.9	6.89	9.01	0.02	23.15
	5	26.52	0.39	34.03	7.09	8.01	0.08	23.87
giant tet w cp - area 2	1	25.74	0.37	33.71	7.64	5.25	BDL	27.29
	2	26.43	0.43	33.84	6.86	8.38	0.14	23.92
	3	26.13	BDL	34.39	6.69	4.04	BDL	28.75
big tet w/ multiple qtz incl (pic n)	1	26.25	0.81	34.09	6.66	6.35	0.09	25.76
	2	26.39	0.59	33.85	7.74	9.88	0.03	21.51
	3	26.39	0.57	34.45	6.52	8.1	BDL	23.97
	4	26.4	0.35	33.41	7.11	5.35	0.08	27.29
	5	26.72	0.44	32.94	7.2	9.75	0.11	22.85

Table K-5. Ag Concentrations in Tetrahedrite from Polished Section 555-160-8

Site	point	Element (wt%)						
		S	Fe	Cu	Zn	As	Ag	Sb
close up zoned tet	1	26.5	2.1	34.28	7.01	15.7	0.19	14.26
	2	27.25	2.15	34.33	6.32	15.4	0.13	14.43
	3	26.05	1.82	33.02	7.1	7.03	0.11	24.87
	4	25.41	1.72	33.56	7.1	4.03	0.04	28.14
	5	26.7	2.9	32.01	7.11	4.56	0.15	26.58
tet & stuff	4	26.82	2.6	32.32	7.03	12.6	0.2	18.42
	5	26.8	2.85	31.22	6.55	11.7	0.23	20.7
	6	27.15	2.95	32.72	6.62	16.1	0.18	14.28
slightly zoned tet	1	26.8	1.32	33.55	7.62	12.4	0.13	18.17
	2	26.53	1.25	33.92	7.11	8.96	0.16	22.07
	3	25.9	1.29	33.7	7.34	4.74	0.07	26.95
	4	25.76	1.6	32.52	7.68	3.92	0.18	28.33
	5	25.63	1.6	32.95	7.08	3.38	0.06	29.29

Table K-6. Tetrahedrite Compositional Data (Ag not measured)

Polished Section	Site	Texture	Size (µm)	Point	Element (wt%)					
					S	Fe	Cu	Zn	As	Sb
1350-13	A	Fahlore veinlet filling fractured pyrite	100 x 800	1	28.27	0.61	33.49	6.97	2.54	28.13
				2	28.71	0.82	33.02	6.78	3.25	27.41
				3	28.36	0.86	34.26	6.74	4.53	25.24
				4	28.45	1.12	34.54	6.73	6.12	23.03
				5	29.01	0.78	34.11	6.68	5.72	23.7
	A1	Fahlore veinlet filling fractured pyrite	100 x 800	1	29.33	0.94	33.34	6.59	3.89	25.92
				2	28.69	0.55	33.87	6.8	2.91	27.18
				3	28.52	0.76	33.97	6.94	3.71	26.1
				4	28.09	0.46	33.72	6.92	3.53	27.28
				5	29.1	0.68	33.52	6.98	3.91	25.81
	W	Fahlore matrix with pyrite	30 x 30	2	27.99	1.6	32.82	6.57	1.62	29.39
				3	28.13	2.14	32.83	6.91	2.36	27.63
				4	38.84	20.83	19.58	4.22	0.02	16.5
				5	27.72	2.63	33.24	6.61	2.51	27.28
	X	Fahlore veinlet filling fractured pyrite	25 x 150	1	27.4	1.9	33.09	6.74	1.64	29.23
				2	30.3	2.82	35.31	BDL	0.09	31.49
		inclusion in pyrite	25 x 25	3	28.43	3.8	31.8	6.62	4.19	25.16
	Y	Fahlore veinlet filling fractured pyrite	25 x 150	1	26.01	4.27	34.57	7.21	4.25	23.69
				2	27.56	4.25	32.84	6.55	2.47	26.33
				3	27.55	3.79	33.87	6.62	2.51	25.67
1355-201-16a	A1	Fahlore veinlet filling fractured pyrite	15 x 50	2	23.92	1.28	41.01	5.88	2.44	25.47
				3	23.71	1.41	40.5	6.61	2.75	25.02
	A2	Fahlore veinlet filling fractured pyrite	5 x 15	3	23.49	2.03	41.95	5.42	3.11	23.99
				4	24.86	2.45	40.58	5.91	4.01	22.2
				5	27.52	6.56	37.49	5.34	4.35	18.75
				6	23.74	2.23	40.83	5.81	3.14	24.25
	A3	Fahlore veinlet filling fractured pyrite	10 x 10	1	23.82	1.04	41.79	6.25	4.19	22.91
				2	23.95	1.1	41.97	5.73	3.9	23.34
				3	24.25	1.32	39.97	6.42	2.95	25.09
				4	24.02	1.07	42.01	5.79	3.76	23.36
	C1	Fahlore veinlet filling fractured pyrite	25 x 100	3	25.77	1.04	37.09	8.1	7.12	20.88
				4	25.23	1.41	36.75	7.41	4.57	24.64
				5	24.38	1.34	41.57	5.82	6.5	20.4
	C1-close-up	Fahlore veinlet filling fractured pyrite	20 x 30	4	25.49	1.4	37.18	7.41	6.4	22.11
				5	25.29	0.84	38.69	7.58	5.93	21.67
	C1-close-up2	Fahlore veinlet filling fractured pyrite	40 x 50	1	24.42	1.68	41.36	6.1	9.7	16.73
				2	24.92	1.27	39.22	7.11	5.18	22.29
				3	25.32	1.42	40.95	6.8	14.81	10.71
				4	24.94	1.27	41.04	6.67	12.83	13.24
				5	25.15	1.16	40.08	6.72	6.21	20.69

Table K-6 cont. Tetrahedrite Compositional Data (Ag not measured)

Polished Section	Site	Texture	Size (µm)	Point	Element (wt%)					
					S	Fe	Cu	Zn	As	Sb
1355-201-16a	E1	Complex inclusion in pyrite	< 10 x 10	5	23.95	1.87	40.8	6.48	3.26	23.64
				6	24.38	2.73	39.65	5.98	1.67	25.6
	E2	Fahlore veinlet filling fractured pyrite	5 x 25	4	24.15	1.03	36.05	7.33	2.55	28.88
	F1	Complex inclusion in pyrite	10 x 15	2	20.95	0.94	49.54	7.72	7.33	13.51
	F2	Fahlore veinlet filling fractured pyrite	20 x 125	2	24.47	1.07	41.1	6.36	7.33	19.67
				3	23.94	1.4	41.57	6.19	7.61	19.29
				4	24.55	1.3	41.3	6.02	7.95	18.9
	F3	Fahlore veinlet filling fractured pyrite	20 x 400	2	24.36	1.62	36.6	6.85	5.24	25.32
				3	23.59	1.94	35.05	7.66	3.24	28.53
				4	23.55	2.7	42.15	6.61	6.44	18.56
	F4	Fahlore veinlet filling fractured pyrite	40 x 40	1	26	4.31	40.1	5.82	7.84	15.92
				2	24.6	1.85	38.29	6.95	6.14	22.17
				3	24.39	1.69	41.13	5.93	5.97	20.9
1355-201-16b	J	Euhedral in quartz with pyrite and sphalerite inclusions	100 x 400	2	24.53	0.45	41.71	6.46	8.63	18.23
				3	24.57	0.14	38.64	7.01	4.41	25.24
				4	24.53	0.54	42.45	5.38	8.68	18.43
				5	24.08	0.3	41.55	6.17	5.03	22.88
	K	Euhedral in quartz	100 x 200	1	24.23	0.52	42.24	6.09	9.1	17.82
				2	23.82	BDL	42.5	5.95	3.14	24.6
				3	24.15	BDL	41.87	6.47	4.68	22.83
				4	23.96	0.45	43.18	5.69	6.32	20.4
				5	23.99	0.45	42.37	5.99	5.26	21.95
	M	Fahlore veinlet filling fractured pyrite	50 x 100	2	23.82	0.75	41.93	5.71	3.8	23.99
				3	23.94	0.61	42.03	6.41	5.4	21.6
	M-closeup	Fahlore veinlet filling fractured pyrite	50 x 200	1	24.03	0.78	41.69	5.8	3.52	24.19
				2	24.13	0.61	42.2	5.93	8.32	18.81
				3	24.33	0.72	41.53	6.44	6.35	20.63
				4	24.04	1	41.4	6.23	3.38	23.95
	N1	Euhedral in quartz and ankerite with chalcopyrite	500 x 500	2	24.5	0.81	40.58	7.25	6.89	19.96
				3	25.58	0.45	37.82	7.81	6.99	21.36
				4	23.94	0.33	42.36	6.35	7.08	19.93
	N2 closeup	Euhedral in quartz	200 x 200	1	24.15	BDL	41.98	6.17	3.77	23.92
				2	24.22	0.05	42.45	6.14	6.57	20.58
				3	24.13	0.1	39.29	6.84	1.9	27.73
	N2 closeup - closeup	Euhedral in quartz	200 x 200	1	23.72	0.3	40.47	6.99	2.33	25.67
				2	24.55	0.04	42.02	6.16	7.06	20.17
				3	24.4	0.32	41.89	6.3	7.46	19.63
	N3 very closeup	Euhedral in quartz	200 x 200	1	24.81	0.51	41.65	5.97	7.54	19.5
				2	23.92	0.34	41.02	6.18	1.94	25.88
				3	24.24	0.3	41.02	6.09	3	25.33
	giant tet on slide edge	Euhedral in quartz	75 x 300	1	26.6	0.6	33.9	6.9	12.45	19.38
				2	26.51	BDL	33.88	6.91	4.91	27.62
				3	25.88	BDL	34.33	7.1	2.74	29.73
				4	26.21	0.66	34.02	7.75	9.09	22.17
				5	26.51	0.81	33.87	7.04	6.77	24.84
	giant tet w/ cp	Euhedral in quartz	100 x 200	2	26.18	0.37	33.88	7.05	3.32	29.21
				3	26.78	0.75	33.7	7.56	13.33	17.81
				4	26.62	0.4	33.9	6.89	9.01	23.15
				5	26.52	0.39	34.03	7.09	8.01	23.87
	giant tet w cp - area 2	Euhedral in quartz	50 x 75	1	25.74	0.37	33.71	7.64	5.25	27.29
				2	26.43	0.43	33.84	6.86	8.38	23.92
				3	26.13	BDL	34.39	6.69	4.04	28.75
	giant tet w cp - area 2	Euhedral in quartz	50 x 75	1	25.74	0.37	33.71	7.64	5.25	27.29
				2	26.43	0.43	33.84	6.86	8.38	23.92
				3	26.13	BDL	34.39	6.69	4.04	28.75
	big tet w/ multiple qtz incl (pic n)	Euhedral in quartz	400 x 400	1	26.25	0.81	34.09	6.66	6.35	25.76
				2	26.39	0.59	33.85	7.74	9.88	21.51
				3	26.39	0.57	34.45	6.52	8.1	23.97
				4	26.4	0.35	33.41	7.11	5.35	27.29
				5	26.72	0.44	32.94	7.2	9.75	22.85

Table K-6 cont. Tetrahedrite Compositional Data (Ag not measured)

Polished Section	Site	Texture	Size (µm)	Point	Element (wt%)					
					S	Fe	Cu	Zn	As	Sb
555-160-8	A	Fahlore veinlet filling fractured pyrite	5 x 50	3	24.08	0.7	37.23	7.05	2.63	28.31
				4	23.98	2.69	36.99	7.51	2.82	26.01
				5	23.39	1.34	41.95	6.39	3.37	23.57
	A close-up	Fahlore veinlet filling fractured pyrite	5 x 15	2	25.51	5.25	40.87	6.41	2.64	19.33
	C	Fahlore veinlet filling fractured pyrite	15 x 25	1	24.02	1.06	40.07	6.74	2.91	25.19
	E	round inclusion	5 x 5	4	23.9	1.16	33.7	8.59	5.85	25
	F1	Fahlore veinlet filling fractured pyrite	5 x 50	1	24.14	1.38	41.21	6.22	3.21	23.84
				2	24.36	1.4	38.65	7.28	4.91	23.41
				3	23.78	1.46	40.76	6.86	3.71	23.42
	F2	Fahlore veinlet filling fractured pyrite	5 x 20	2	23.45	1.92	41.8	5.97	2.77	24.09
	F3	Fahlore veinlet filling fractured pyrite	5 x 10	2	23.87	2.4	41.5	6.24	3.01	22.98
	F4	Fahlore veinlet filling fractured pyrite	10 x 10	2	23.49	0.59	41.58	6.3	2.97	25.06
	G	Fahlore veinlet filling fractured pyrite	10 x 10	2	23.6	1.43	40.53	6.91	1.3	26.24
555-160-2	run 3	inclusions in pyrite	5 x 5	1	26.63	2.68	34.67	6.88	BDL	29.15
				2	27.16	2.07	32.5	8.66	4.75	24.86
555-160-4	B	inclusion in pyrite	100 x 100	2	24.52	1.19	40.05	6.19	3.53	24.52
				3	24.44	1.41	38.77	6.67	3.82	24.89
	F	Fahlore veinlet filling fractured pyrite	10 x 50	3	24.95	3.26	40.93	5.26	3.06	22.37
				4	24.27	1.78	41.73	5.43	3.3	23.49
				5	24.12	1.25	41.77	5.34	3.45	24.08
				6	24.41	1.34	41.21	5.83	3.61	23.6
555-160-5	D	grain boundary inclusion in pyrite	10 x 10	1	26.04	6.21	35.41	7.02	3.18	22.14
			10 x 10	3	27.88	9.17	29.85	10.57	0	22.53
			30 x 50	4	25.54	2.25	37.3	8.04	2.87	23.99
				5	25.84	1.4	39.71	6.83	3.19	23.03
				6	27.67	6.72	34.46	6.43	3.29	21.43
				7	25.48	1.95	35.42	8.86	3.56	24.74
				8	25.19	2.71	36.24	8.15	4.39	23.31
555S-3	C	Adjacent to pyrite	10 x 10	4	25.19	3.31	40.73	7.47	9.51	13.79
				5	26.07	1.79	43.16	7.11	9.38	12.49
				6	26.73	5.4	39.46	7.32	9.85	11.25

Appendix L. Co Map Routine

Co maps were done by scanning the designated area with a circle-shaped beam (2 µm diameter) with varying dwell times depending on size of scanned area.

Table L-1. Co Map Conditions for Each Map

Polished Section	Map	Dwell Time (s)	Volt	XRF ppm	BG Counts	Corresponding Map Color			
						red counts	yellow counts	green counts	lt blue counts
04-1	a	30	30	327	60	140	120	103	83
07-1	a	30	30	159	55	120	103	89	72
08-1	c	30	30	185	65	140	118	100	77
08-1	d	30	30	185	65	155	132	112	90
1355-201-16a	b1	10	30	640	24	40	33	30	
1355-201-16a	b2	30	30	640	55	140	118	100	80
1355-201-16a	e	10	30	640	20	66	51	40	27
1355-201-16a	f	10	30	640	18	75	59	45	31
1355-201-16a	f-slow	20	30	640	45	140	112	90	58
1355-201-16a	slow1	30	30	640	58	158	127	105	80
1355-201-16b	m	10	30	640	22	70	57	50	35
1355-201-16b	n	10	30	640	20	54	42	34	25
555-160-5	a	30	30	334	60	150	126	104	80
555-160-5	c	30	30	334	60	225	173	135	96
555-160-5	x	30	30	334	70	190	150	116	80
555-160-8	c	30	30	356	65	250	192	150	105
555-160-8	e	30	30	356	55	230	175	135	90
555-188-3	b	30	30	553	50	168	135	110	82
555-188-3	h	30	30	553	55	230	180	141	100
555-188-3	i	30	30	553	55	275	223	173	124
555S-2	e	30	30	723	85	900	680	530	370
555S-2	m	30	30	723	57	175	143	114	78
630-224-4	a	10	30	1233	21	130	95	71	48
630-224-4	b	10	30	1233	26	105	82	63	42
630-224-4	f	10	30	1233	28	105	82	63	42
630-224-4	g	10	30	1233	37	155	125	96	70
780-176-2	b	30	30	419	63	110	96	81	65
780-176-2	c	30	30	419	50	200	160	128	95
780-176-2	a	30	30	419	50	250	205	157	110
1140-197-6	X	10	25	1271					
1140-197-6	a	10	25	1271					
1140-197-6	c	10	25	1271					

Appendix M. Co Maps and Corresponding BSE Images

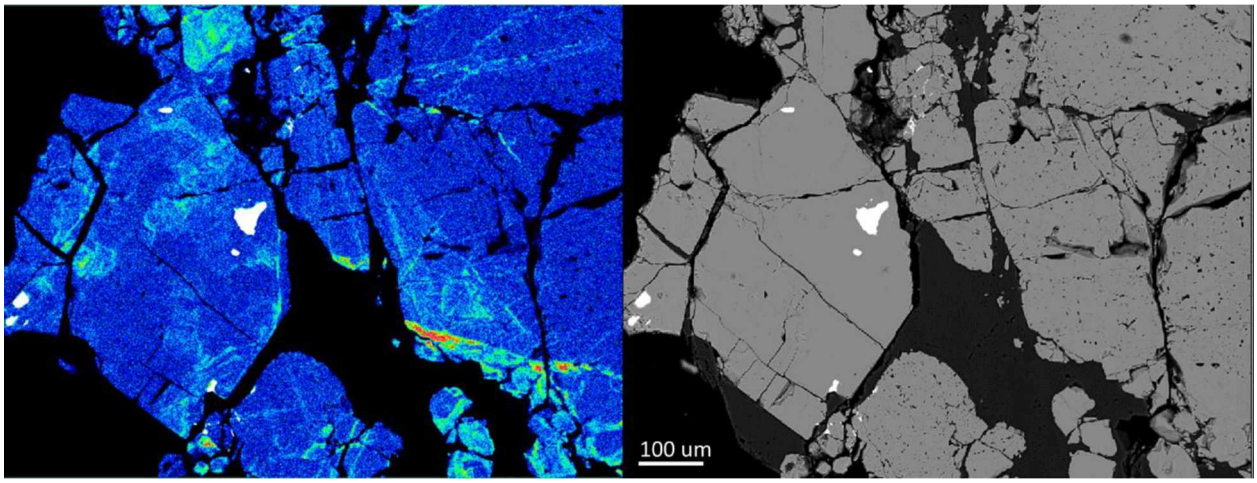

Polished section 04-1, map a. All bright inclusions are calaverite.

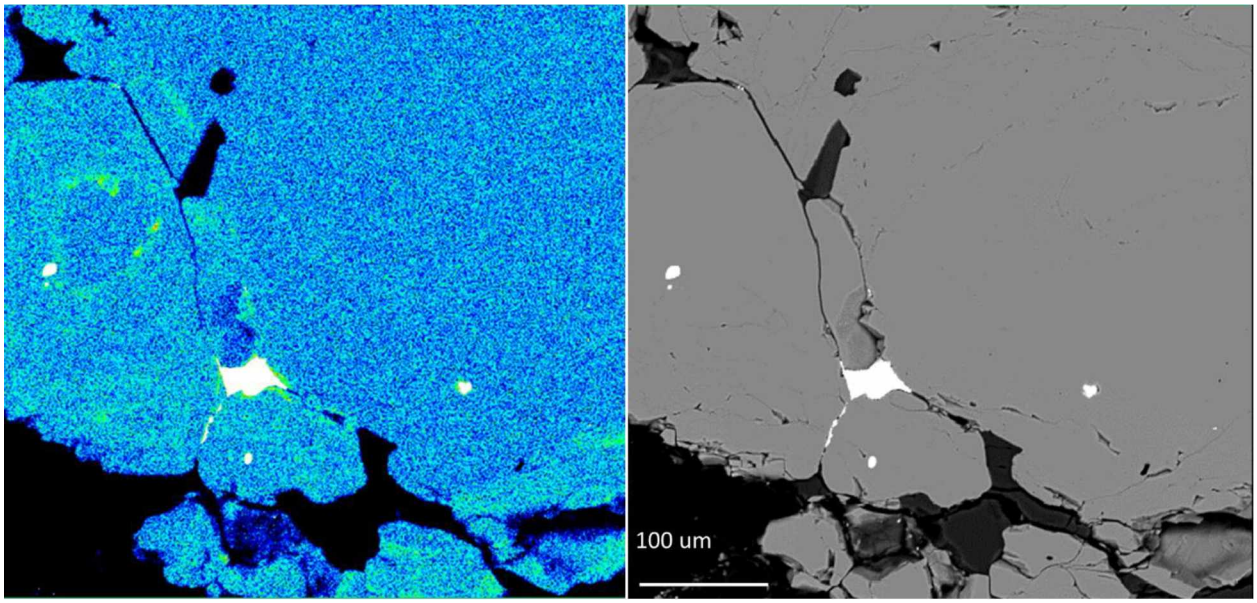

Polished section 07-1, map a. All bright inclusions are calaverite.

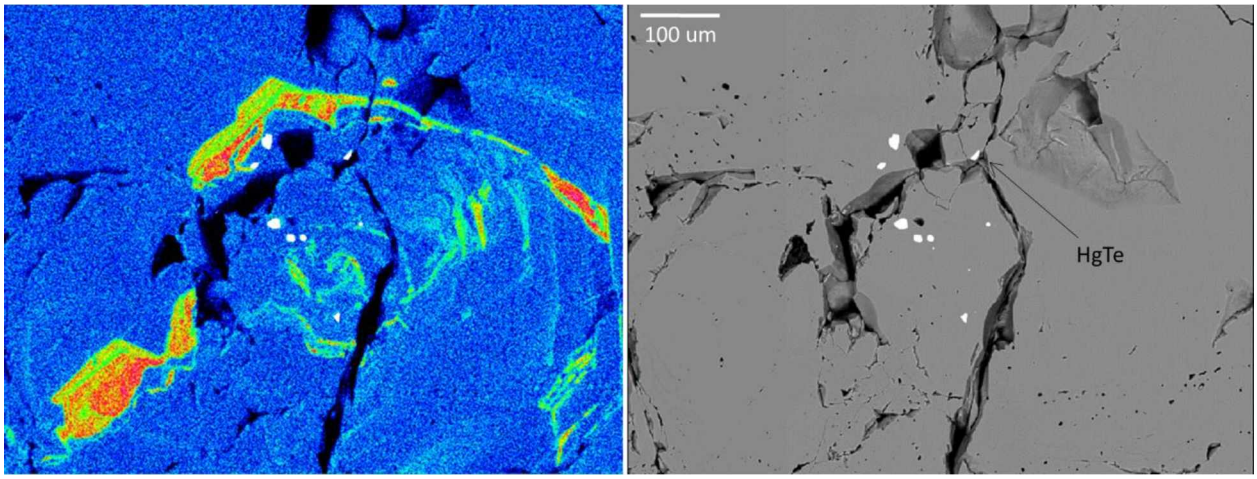

Polished section 08-1, map c. All bright inclusions are calaverite, except for 1 coloradoite (labeled).

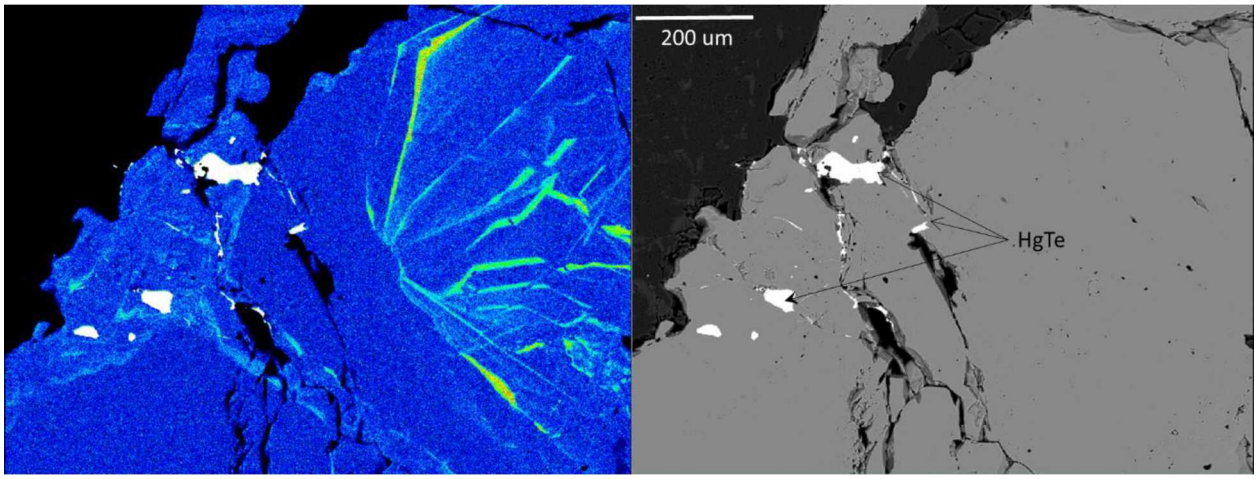

Polished section 08-1, map d. All bright inclusions are calaverite, except for 3 coloradoite grains (labeled).

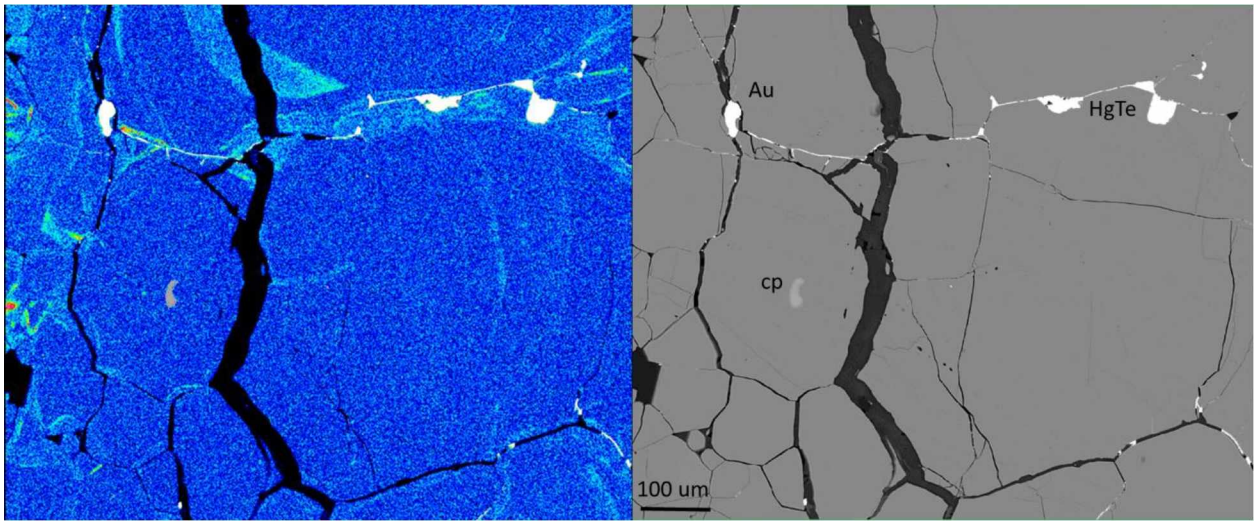

Polished section 555-160-5, map a. All bright inclusions are coloradoite, except for 1 gold grain (labeled).

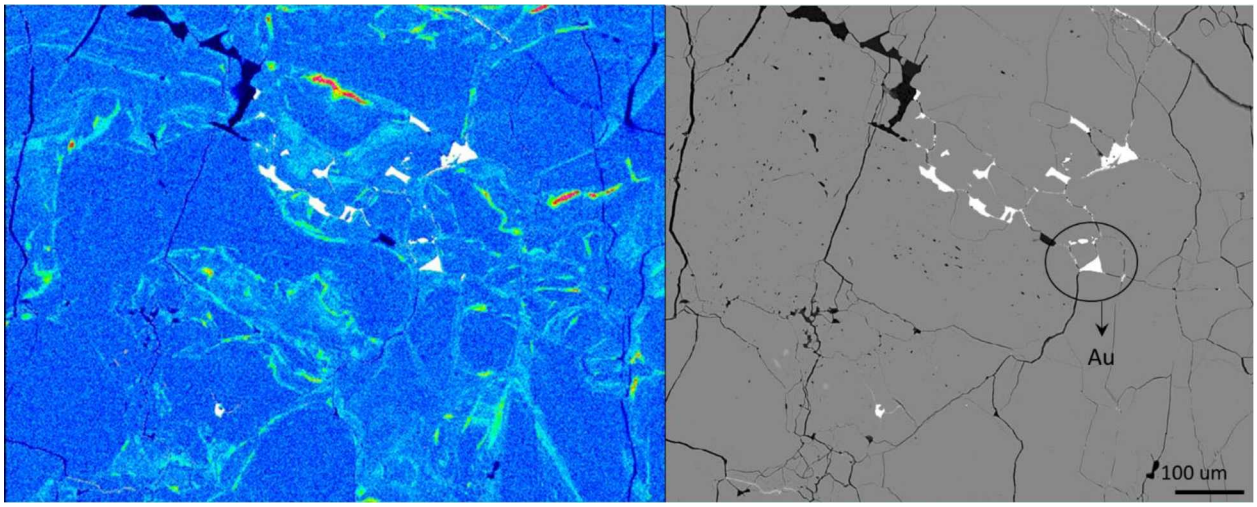

Polished section 555-160-5, map c. All coloradoite, except gold in circle.

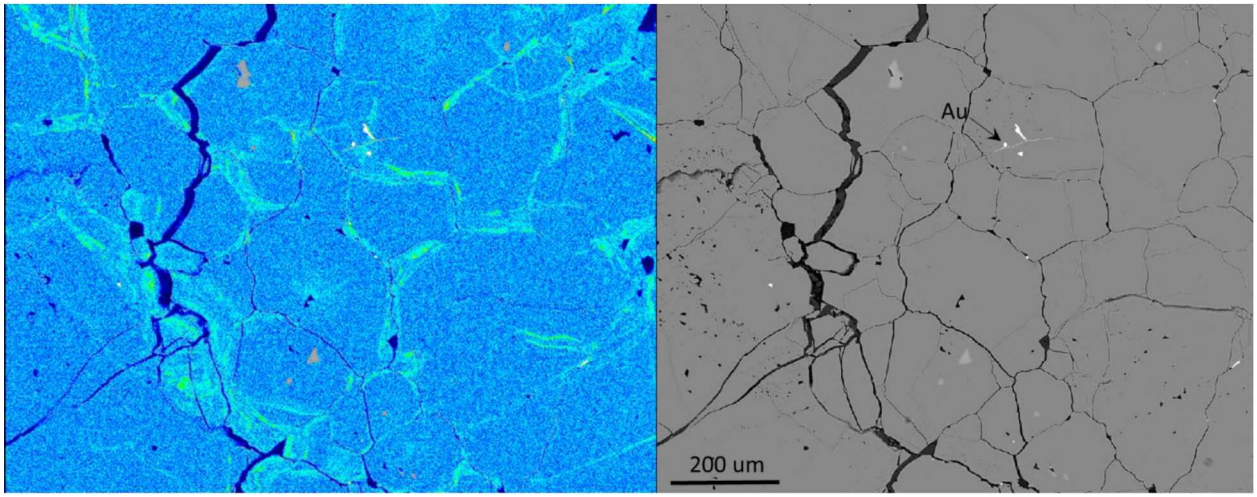

Polished section 555-160-5, map x. All bright inclusions are coloradoite, except for 1 gold grain (labeled).

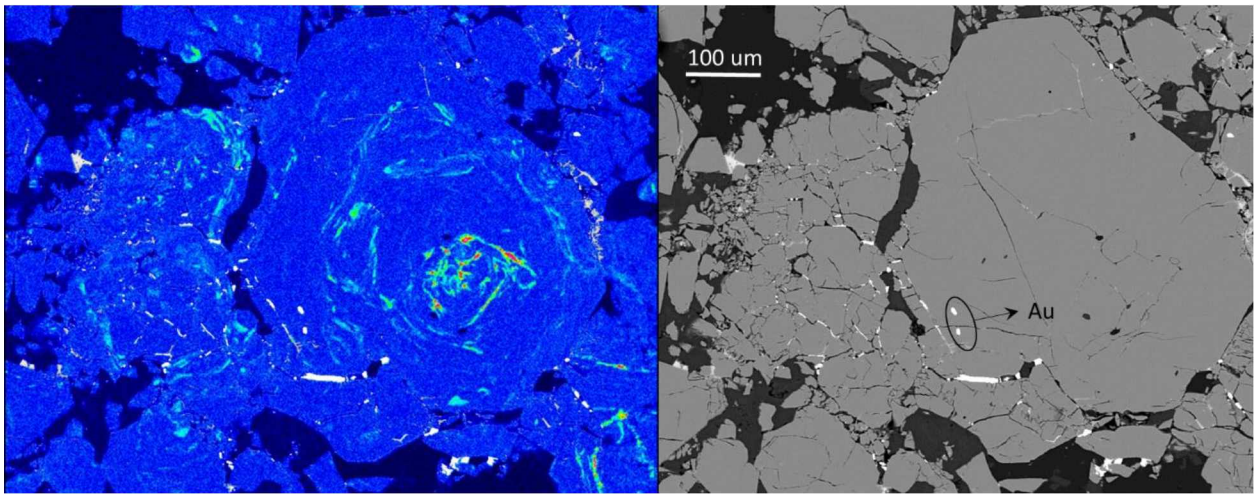

Polished section 555-160-8, map c. All calaverite, except for 2 gold grains (labeled).

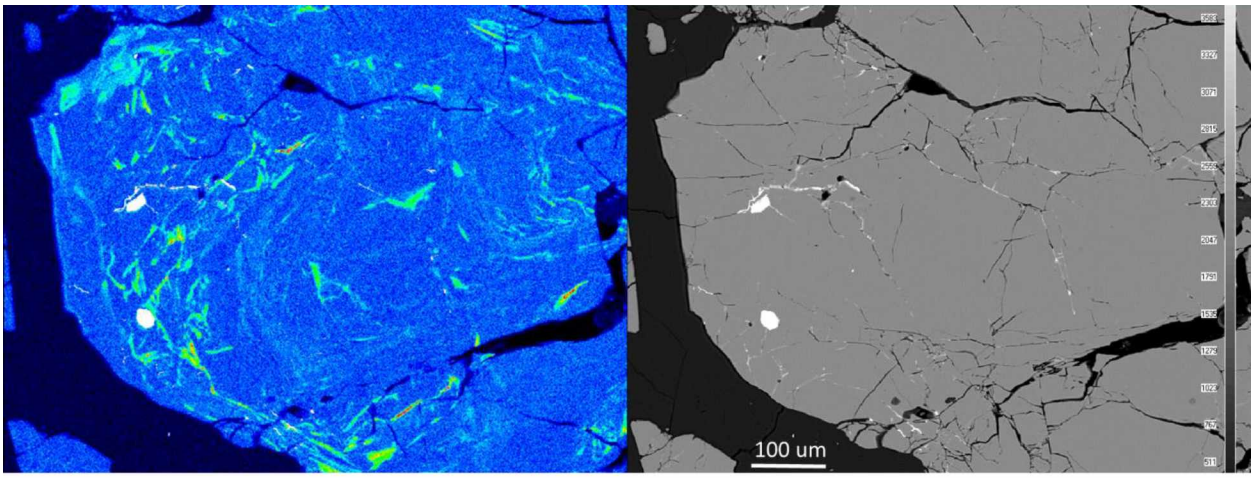

Polished section 555-160-8, map c. All gold.

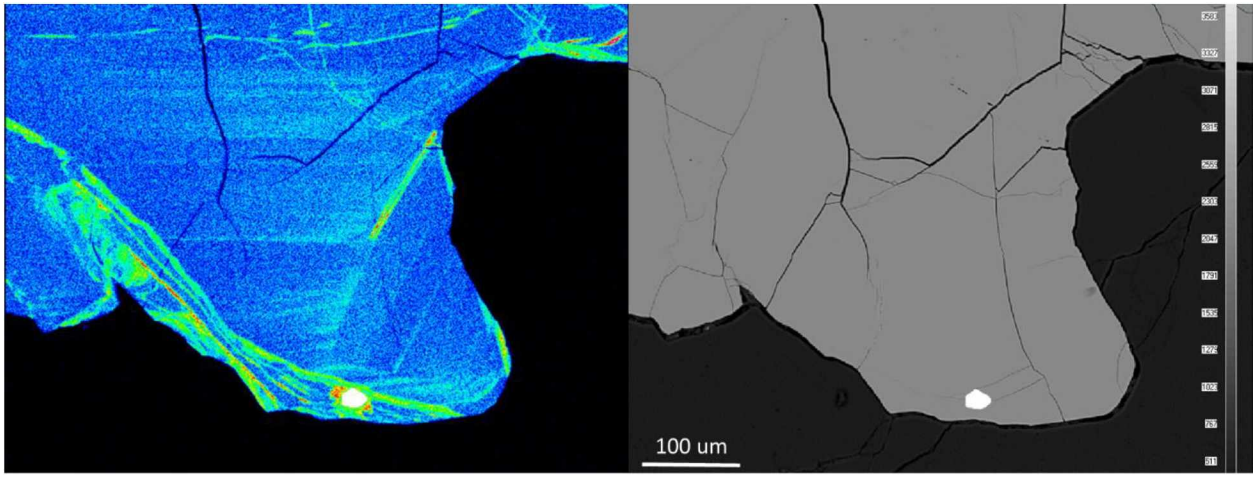

Polished section 555-188-3, map b. Calaverite inclusion.

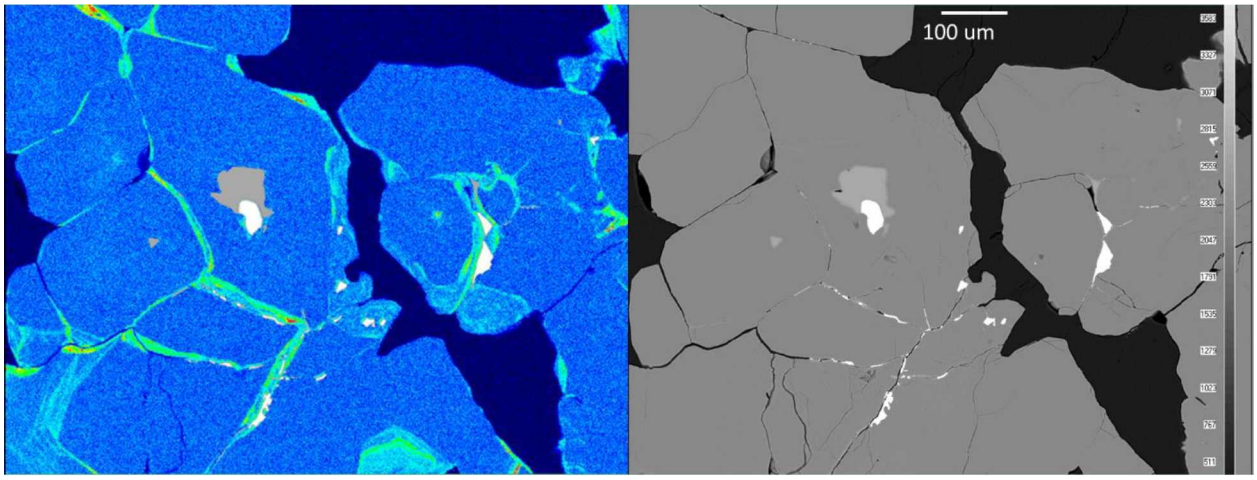

Polished section 555-188-3, map h. All inclusions are calaverite +/- chalcopyrite.

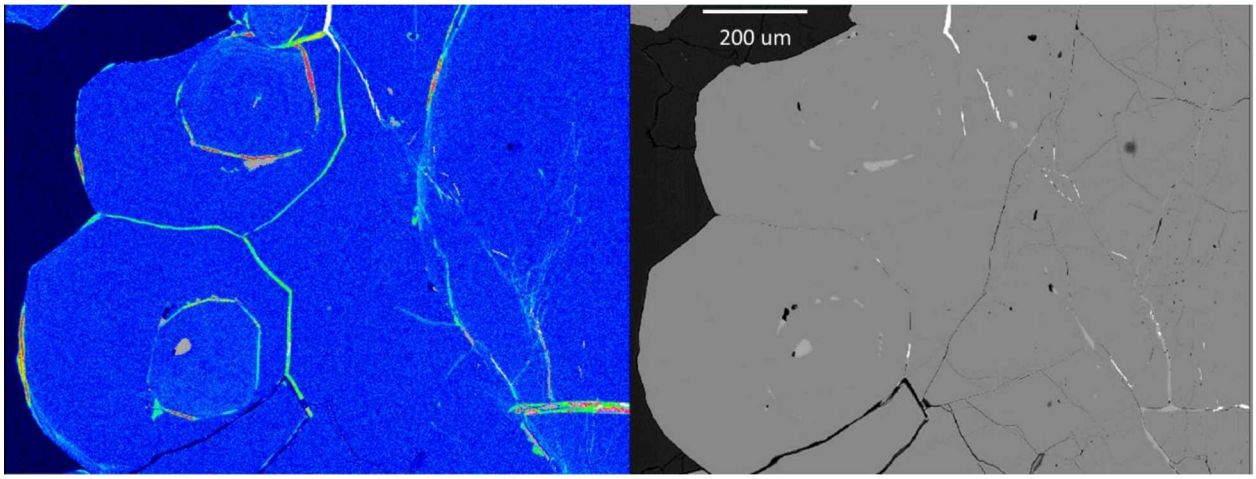

Polished section 555-188-3, map i. All inclusions are calaverite +/- chalcopyrite.

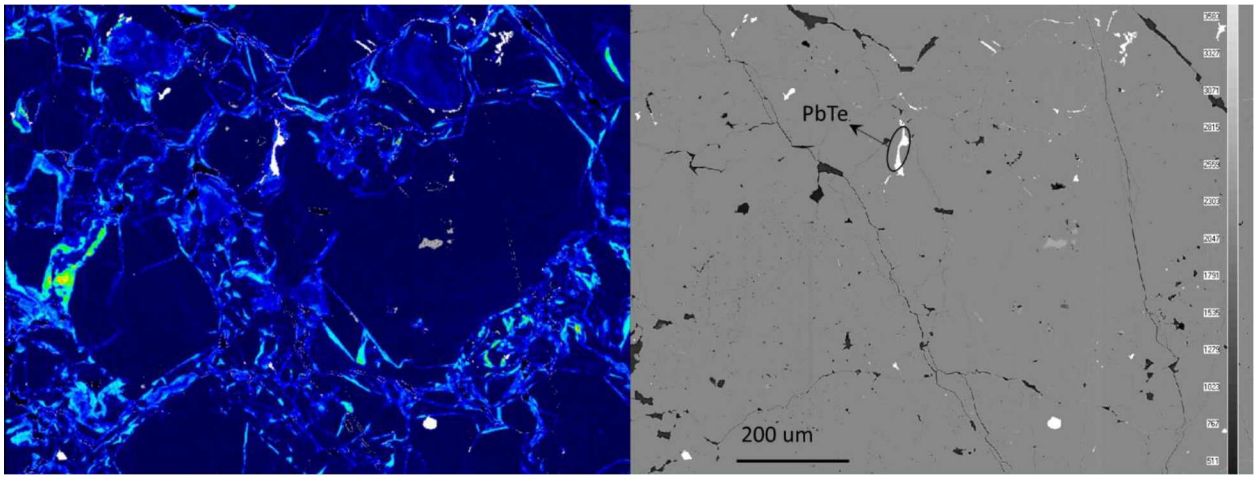

Polished section 555S-2, map e. All gold inclusions, except 1 altaite grain (labeled).

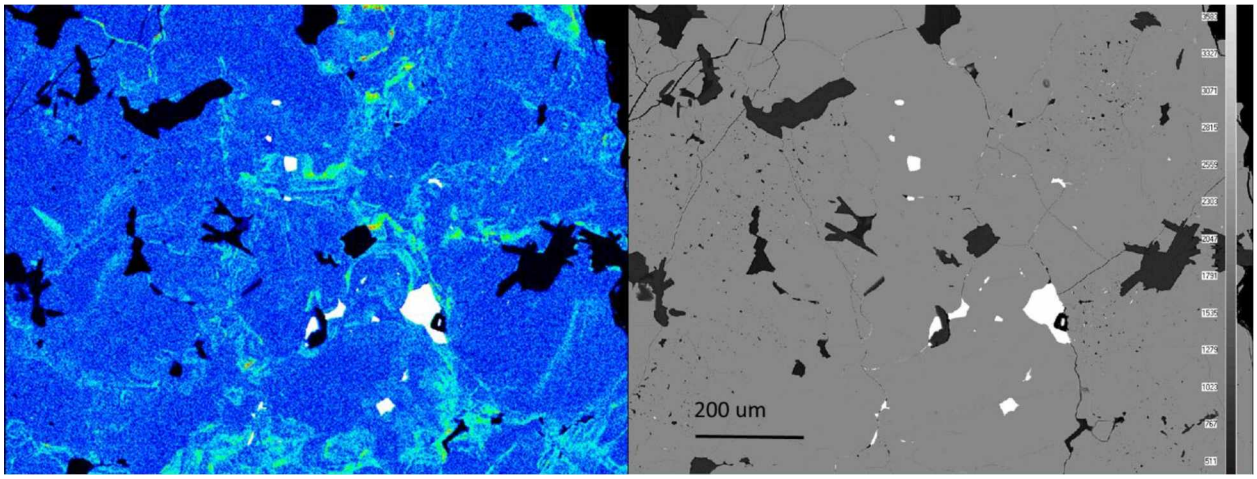

Polished section 555S-2, map m. All inclusions are calaverite.

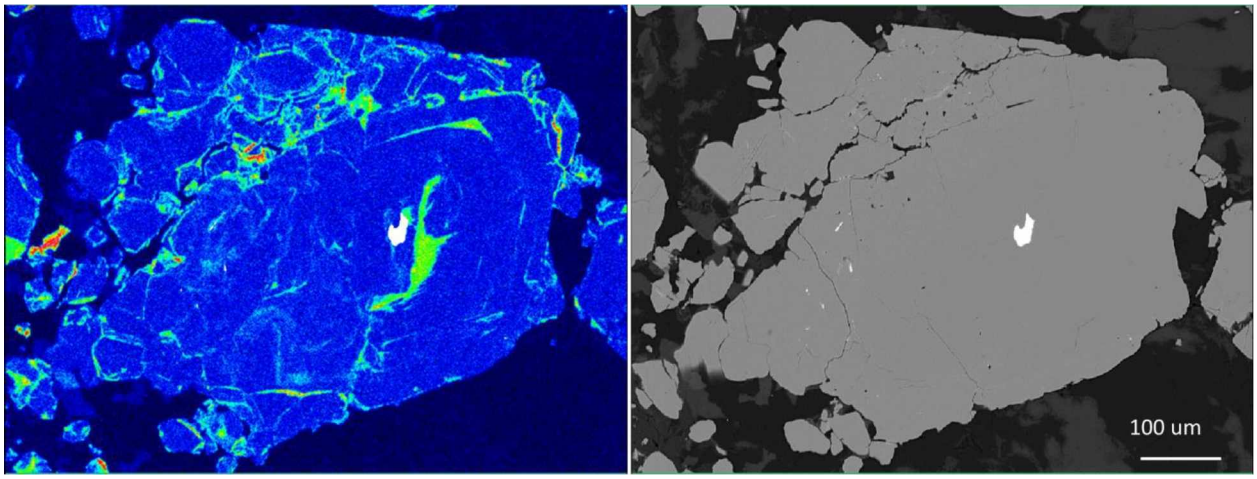

Polished section 630-224-4, map a. Calaverite inclusion.

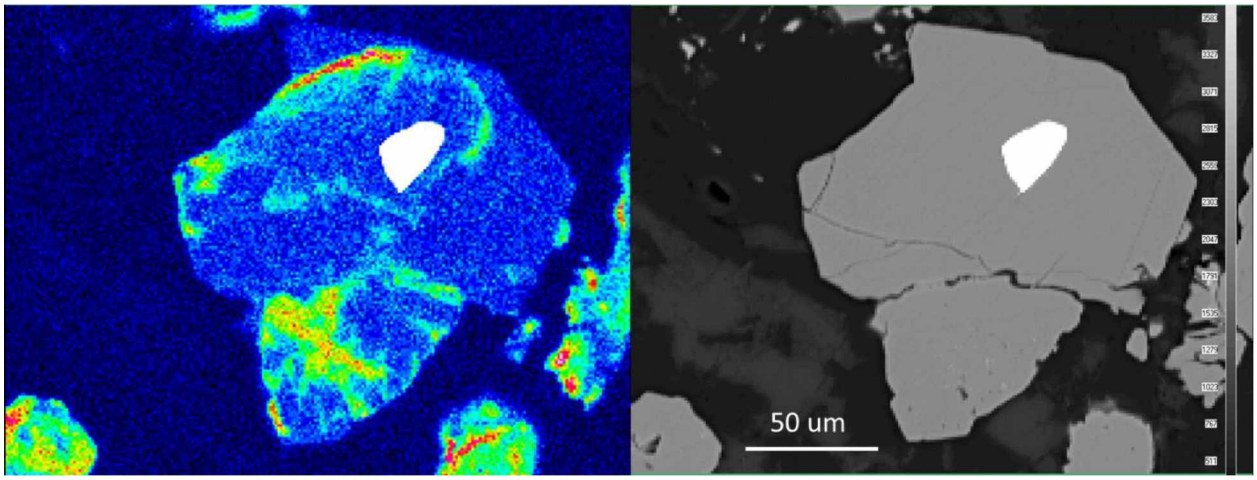

Polished section 630-224-4, map b. Calaverite inclusion.

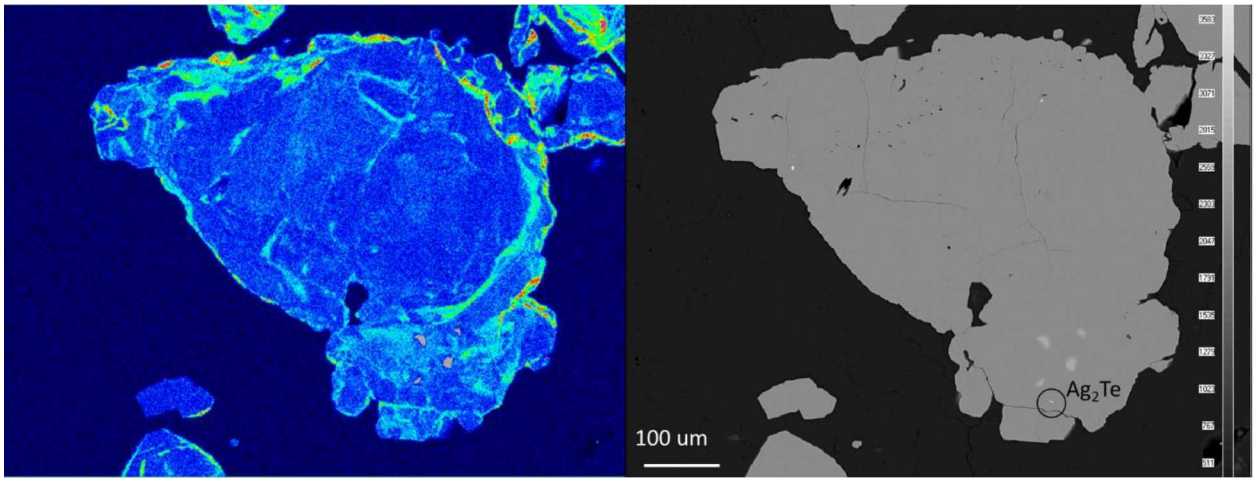

Polished section 630-224-4, map f. Hessite and chalcopyrite inclusions.

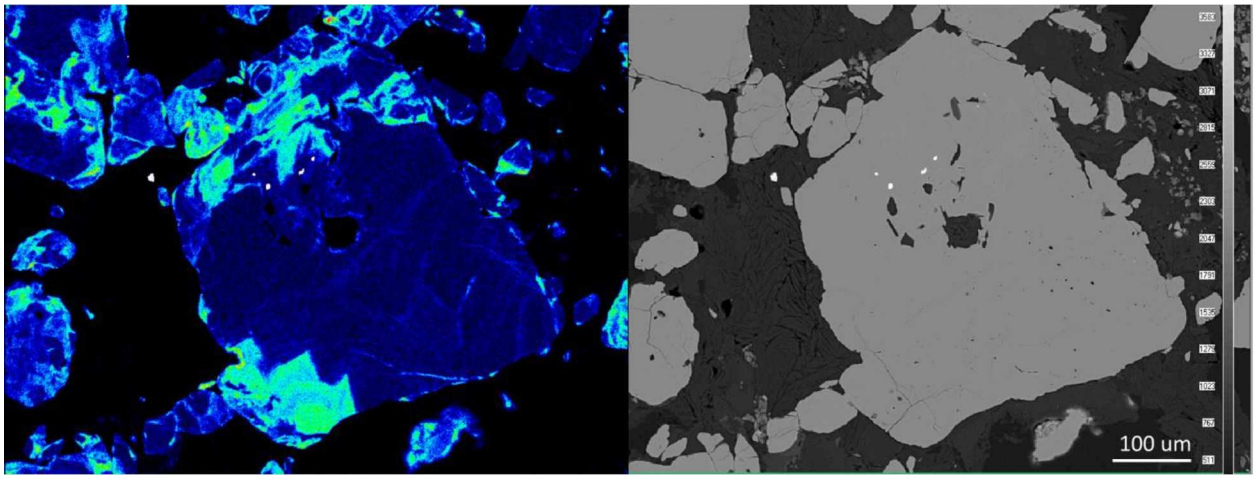

Polished section 630-224-4, map b. Calaverite inclusions.

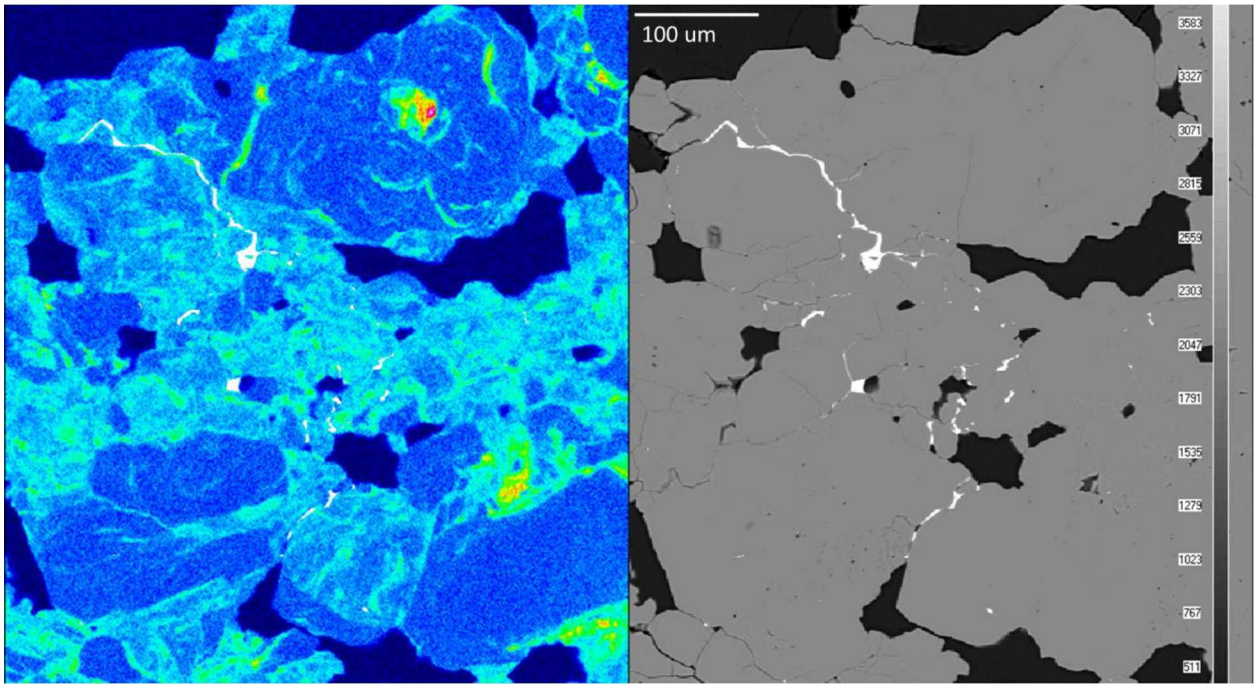

Polished section 780-176-2, map a. Unknown inclusion mineralogy.

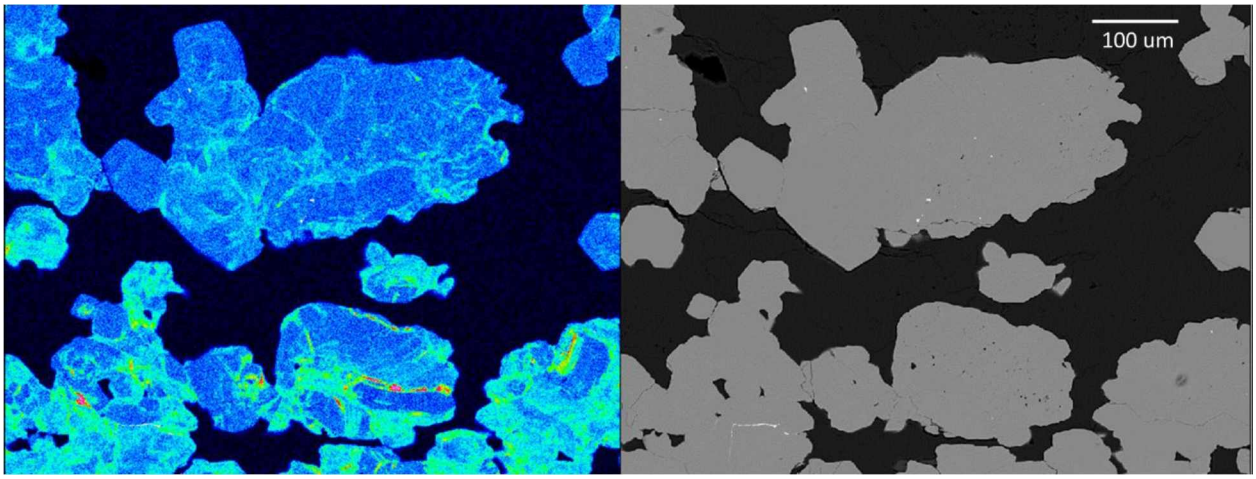

Polished section 780-176-2, map c. All calaverite inclusions.

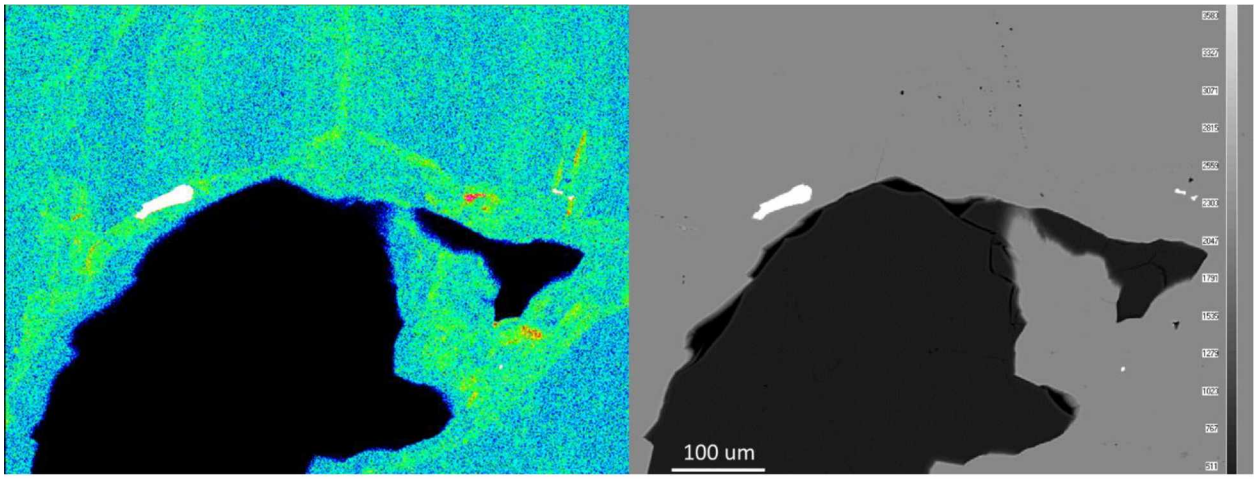

Polished section 780-176-2, map c. Calaverite inclusion.

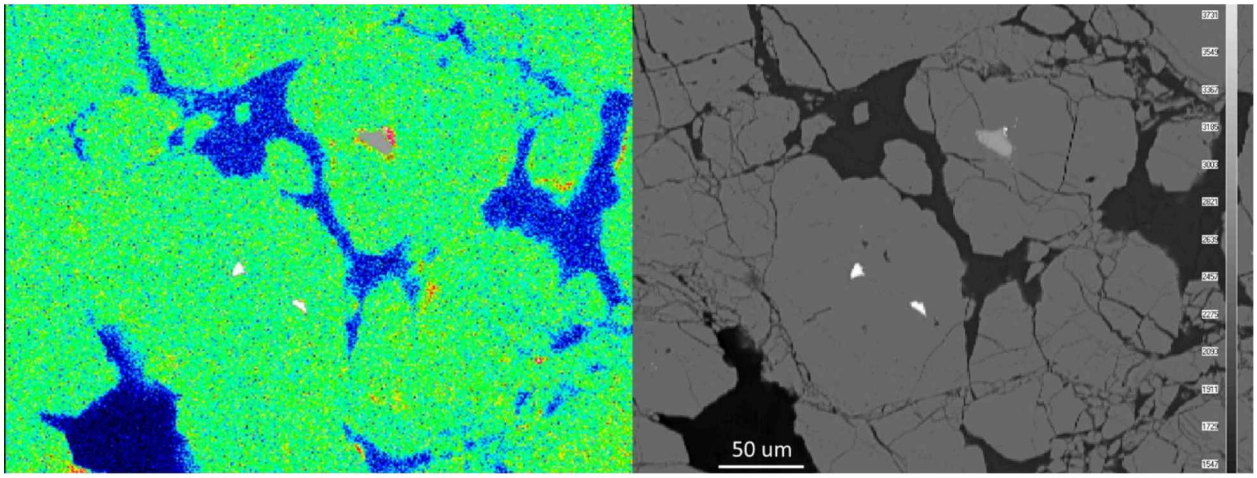

Polished section 1355-201-16a, map b. Calaverite and chalcopyrite inclusions.

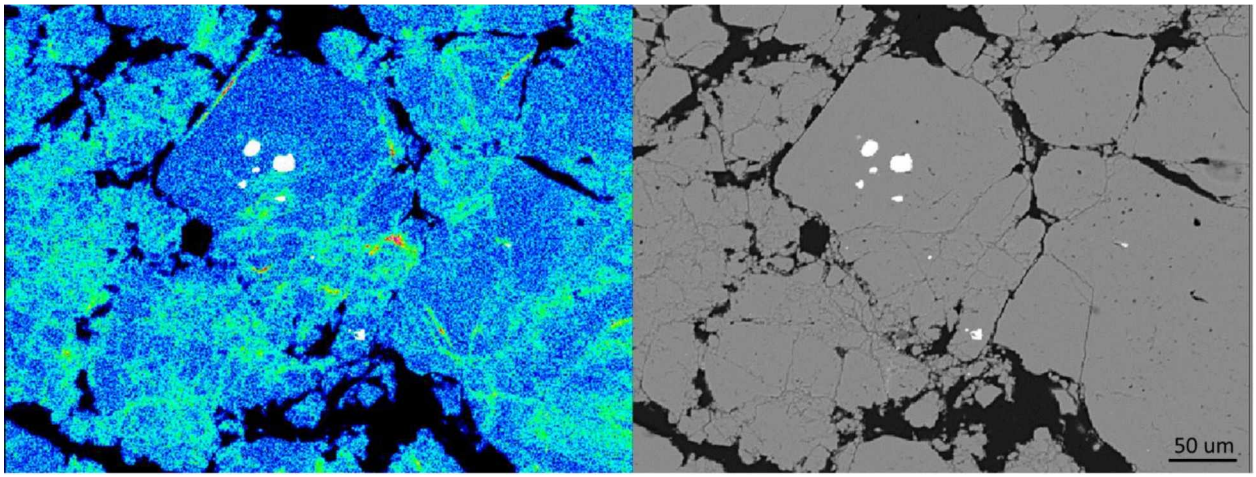

Polished section 1355-201-16a, map b2. All calaverite inclusions.

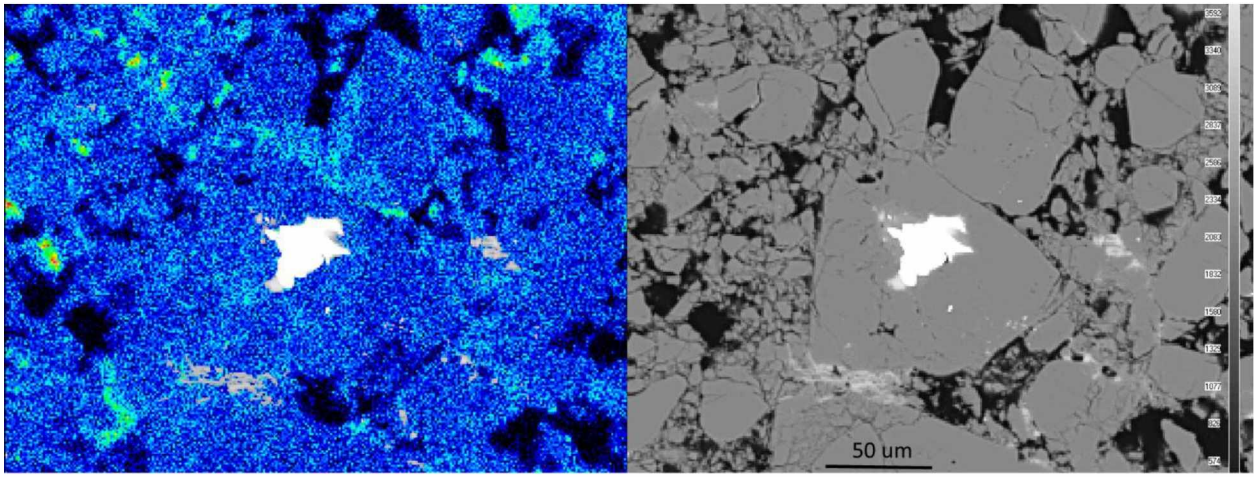

Polished section 1355-201-16a, map e. Tetrahedrite fracture filling pyrite. Large multi-mineral inclusion (gold, calaverite, tetrahedrite, and chalcopyrite)

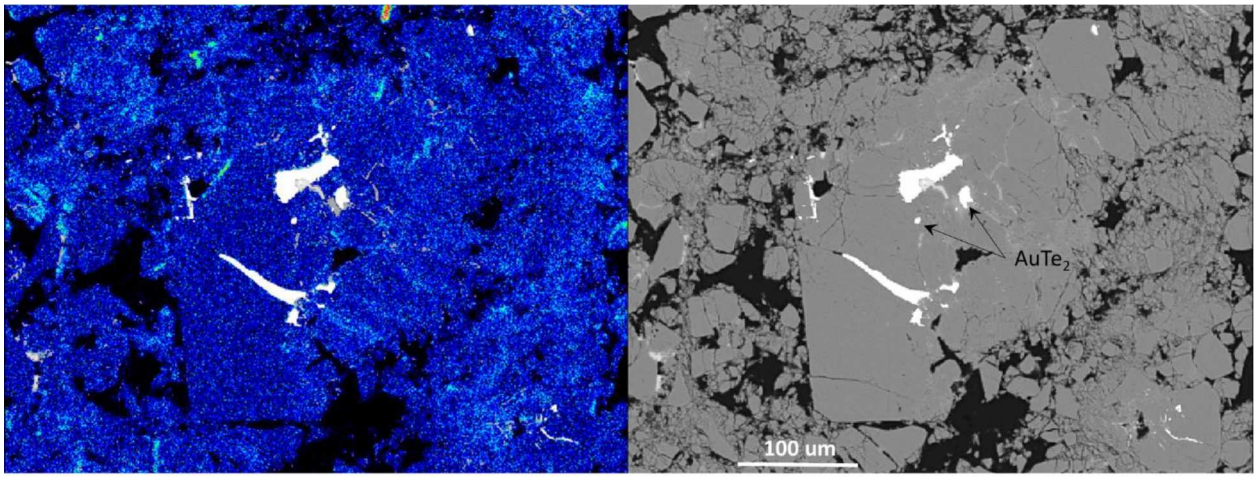

Polished section 1355-201-16a, map d. Gold and calaverite (labeled).

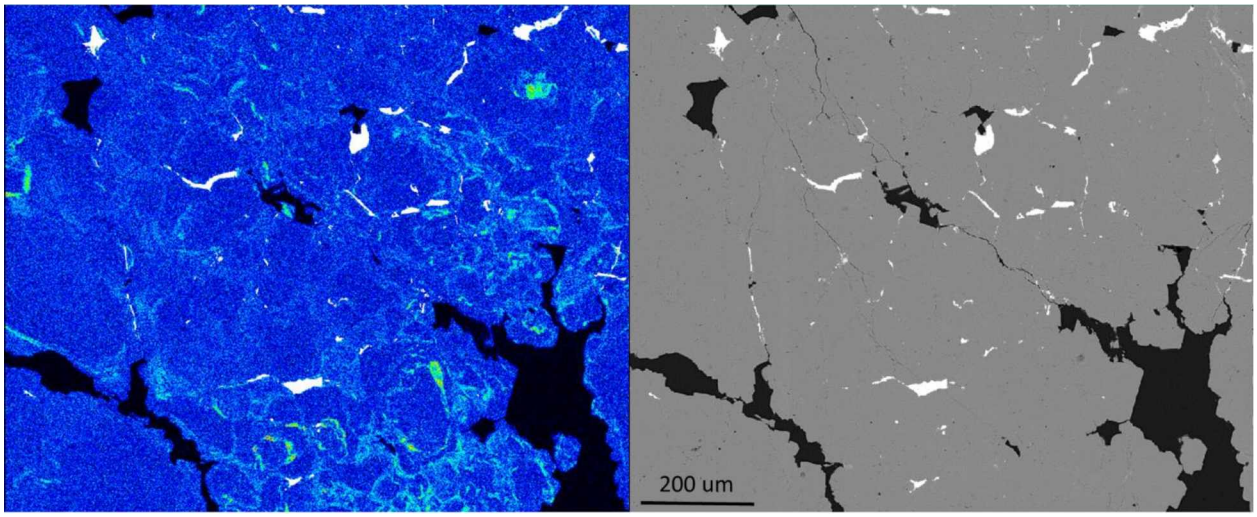

Polished section 1355-201-16a, map f. All calaverite inclusions.

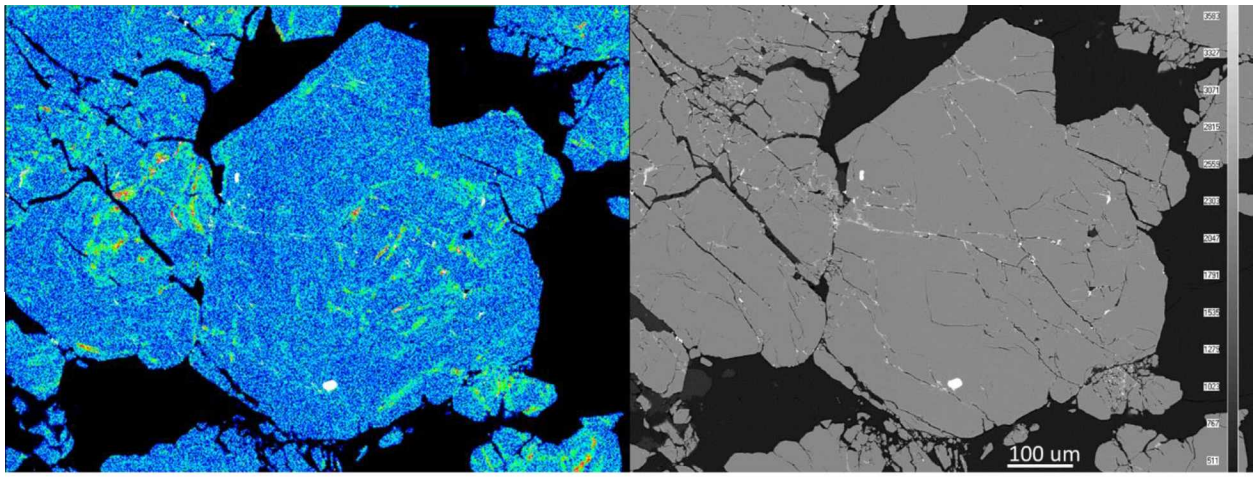

Polished section 1355-201-16a, map slow1. Unknown inclusion mineralogy.

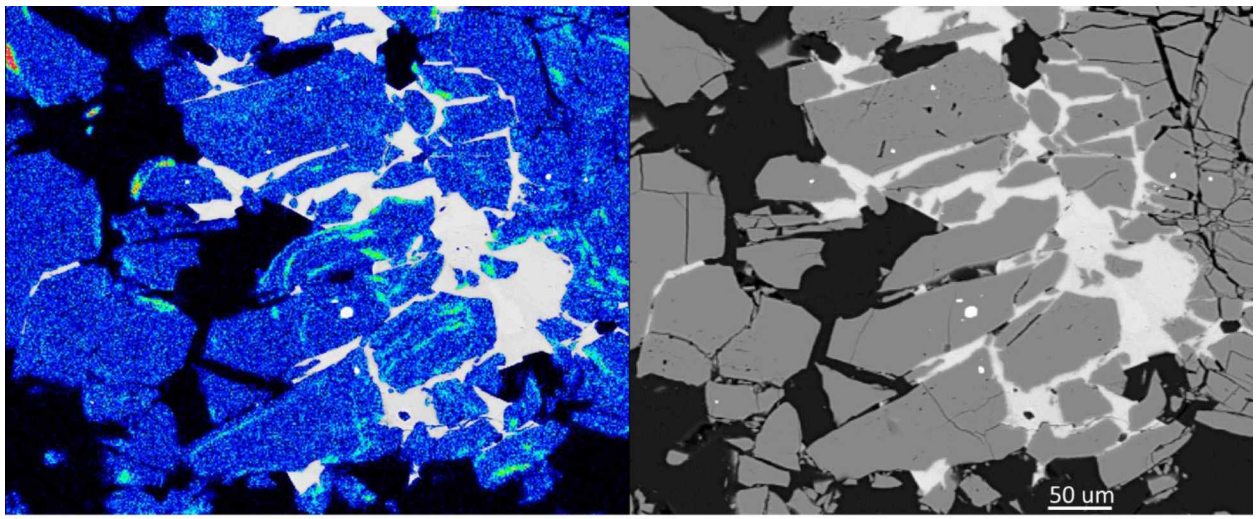

Polished section 1355-201-16b, map m. Rounded calaverite inclusion with tetrahedrite filling fractures.

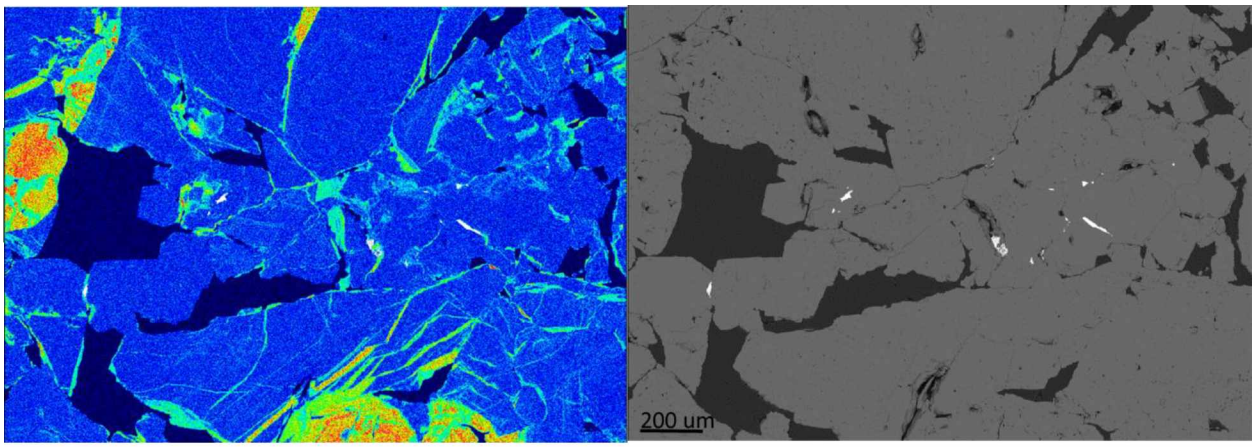

Polished section 1140-197-6, map x. Unknown inclusion mineralogy.

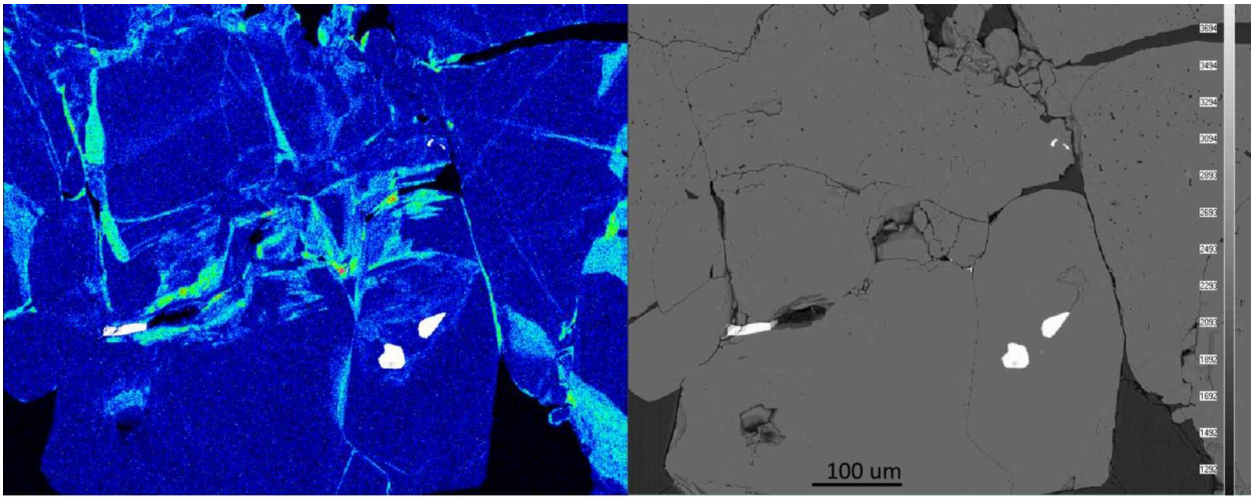

Polished section 1140-197-6, map c. Calaverite inclusions.

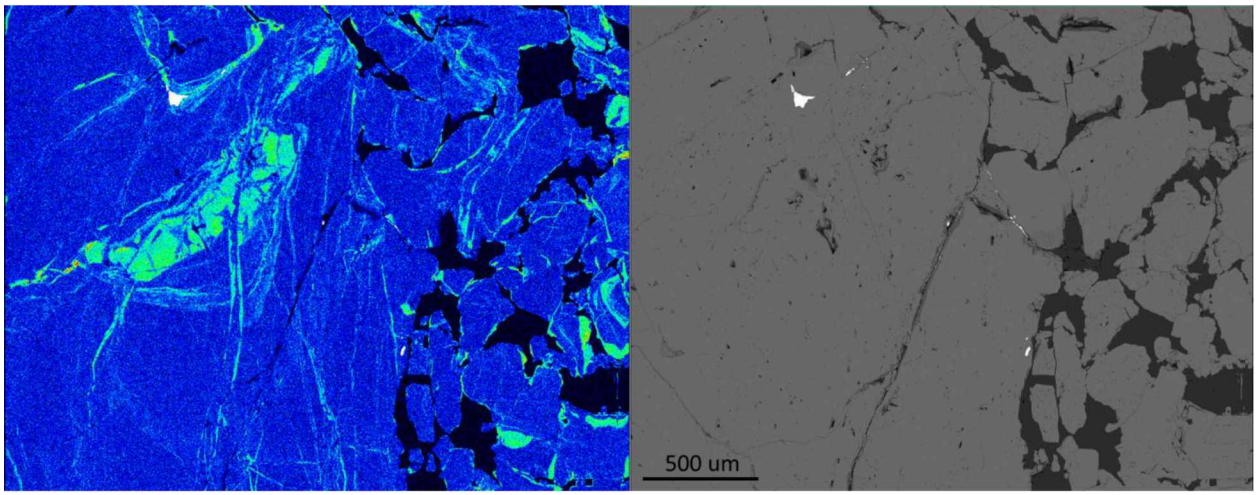

Polished section 1140-197-6, map a. Calaverite inclusion.